THE INFLUENCE OF ROLLER DRESSING AND ABRASIVE GRIT SHAPES ON GRINDING PERFORMANCE

Jack Palmer

A Thesis Submission for the degree of Doctor of Engineering

Industrial Doctorate Centre in Machining Science

Department of Mechanical Engineering

University of Sheffield

[Jan 2020]

All work presented was supported by Rolls-Royce plc. under agreement EP/I01800X/1 and is Private.

ABSTRACT

Grinding is a widely used manufacturing process in the production of aerospace engine components, such as turbine blades, due to its ability to cut difficult-to-machine materials and achieve tight quality tolerances (less than 50 μm). With an increasing number of orders for engines in industry, there is a strong drive to increase the productivity of the process which has led to the development of novel, engineered abrasive grit shapes to be used in grinding wheels. However the behaviour of these different shapes during dressing and grinding is not fully understood, from the impact of dressing on wheel topography to how that topography grinds and wears. Therefore the aims of this research were to better understand the effect of novel abrasive grit shapes on grinding performance to enable industry to make more informed manufacturing decisions when grinding Ni-base superalloy aerospace components leading to reduced costs and improved productivity.

Three types of abrasive wheels were tested, conventional (standard, approximately spherical grit shape), hybrid (mixture of conventional and engineered, triangular sintered grits) and elongated (extruded, spaghetti-shaped grits). These were dressed under a range of roller dressing infeed rates and speed ratios to measure the wheel surface topography as this directly influences the grinding behaviour. A series of grinding trials were then conducted on CMSX-4 single crystal Ni-base superalloy comparing the response of the different abrasive grit types. Continuous dressing cuts (at fixed grinding parameters and varied dressing conditions) were performed to assess the grinding behaviour whilst minimising the wear effects on the grits. These were followed by a wheel breakdown study to establish how different dressed topographies on the wheel wear by initially dressing the wheels then taking nine repeat grinding cuts (not continuously dressed). Finally, the grinding parameters were varied (over different dressing conditions) to assess the response of the topographies to different material removal rates.

These experiments demonstrated that the conventional wheel undergoes a transformation in dressing mechanism from low dressing infeed rates to high. Infeed rate was the most influential dressing parameter and that at high infeed rates and synchronous speed ratios, the roughest wheel surface was generated and these parameters should be used, for all grit shapes, when rough grinding due to sharp cutting points ensuring a larger chip size. The engineered, triangular grits dominated the dressing process in the hybrid wheel due to their microfracturing behaviour, reducing dressing forces which could increase dressing times. The orientation of the elongated grits was shown to restrict the impact of different dressing parameters on those wheels. The hybrid wheel showed improved performance at high material removal rates as the triangular grits became more influential. The

microfracturing behaviour of these grits also caused the most stable grinding process leading to longer wheel lifetime and increased productivity. The elongated grit wheel demonstrated the lowest grinding energy at high material removal rates but also dulled very rapidly meaning more regular dressing would be required. The best surface quality was achieved by the more uniform topography of the conventional grit wheel.

ACKNOWLEDGEMENTS

I would firstly like to thank my supervisors for all their help in enabling this thesis to come together. Thank you to Dr Hassan Ghadbeigi who pushed me to get the most out of my EngD and whose door was always open. Thank you to Dr David Curtis for the many technical discussions at his desk and facilitating most of the experimental work. Thank you to Dr Donka Novovic for believing in me and providing the connections that enabled this research.

A special thank you to the Advanced Manufacturing Research Centre (AMRC) Grinding Team, particularly Jim Kelsey, Andy Winder and Gary Mckee, for putting up with my many questions and providing willing practical support. Thanks as well to the AMRC Knowledge Transfer Centre Workshop for my access to vital machines to complete this work and providing a helping hand when required.

I would like to thank all my colleagues in the Industrial Doctorate Centre in Machining Science for making my EngD an enjoyable experience and for keeping me motivated. Thanks especially to Nikita Pietrow, Yosuf Faizi and Tom Gibbons. Thank you to Dr Jamie McGourlay, Clare Clarke, Dr Francesca Breeden and Dr Pete Crawforth for the support and administrative help.

Finally, thank you to my parents without whose love I would not be where I am today and to whom I would like to dedicate this thesis.

Psalm 121 v 1 - 2

PUBLICATIONS

Palmer, J., Ghadbeigi, H., Novovic, D., Curtis, D., An Experimental Study of the Effects of Dressing Parameters on the Topography of Grinding Wheels during Roller Dressing, *Journal of Manufacturing Processes, 31, 2018, pp 348-355.*

Palmer, J., Curtis, D., Novovic, D., Ghadbeigi, H., The Influence of Abrasive Grit Morphology on Wheel Topography and Grinding Performance, *Procedia CIRP, 77, 2018, pp 239-242.*

CONTENTS

LIST OF FIGURES

LIST OF TABLES

NOMENCLATURE

#80 / #120 etc.	Wheel grit size indicating wires per sq. inch in a mesh
μ	Friction coefficient
a_d	Dresser infeed rate
a_e	Depth of cut
ANOVA	Analysis of Variance
c	Number of active grits per mm^2
CD	Continuous Dressing
d_g	Average grain size (μm)
DoE	Design of Experiments
EDX	Energy Dispersive X-ray spectroscopy
FEM	Finite Element Model
Fn	Normal grinding force (N)
Ft	Tangential grinding force (N)
GLM	General Linear Model
G-ratio	Workpiece material removal to volume of grinding wheel loss
h_{eq}	Equivalent chip thickness (μm)
Lc	Grinding wheel contact length (mm)
P_d	Net power consumption in dressing (kW)
P_f	Power consumption of wheel in free rotation (kW)
P_{net}	Net power consumption from grinding (kW)
Q'	Specific material removal rate ($Q' = (v_w \times a_e)/60$)
q_d	Dressing speed ratio
Ra	Arithmetic average of surface heights (μm)
Rv	Maximum surface profile valley depth (μm)
S/N	Signal to Noise ratio
S_{ds}	Summit density
SEM	Scanning Electron Microscopy
SS_{opt}	Optimum sample spacing in wheel topography measurement (μm)
t	Average chip thickness (μm)
u	Specific grinding energy (J)
v_c	Wheel surface speed (m/s)
VIPER	Very Impressive Performance Extreme Removal
v_r	Roller dresser surface speed (m/s)
v_w	Workpiece feed rate (mm/min)
γ	Ni-base superalloy austenitic fcc matrix
γ'	Ni-base superalloy bcc hardened precipitate
δ	Interference angle of dresser diamond on the abrasive wheel (rads)

CHAPTER 1

INTRODUCTION

1.0 INTRODUCTION

Grinding is a vital manufacturing process and makes up to 25% of all machining operations in global manufacturing [1]. Different from most other machining operations; grinding involves using small hard abrasive grits bonded together to remove material from a workpiece. It is these small grits that makes grinding very advantageous over other machining operations for certain manufacturing procedures.

Grinding is the chosen process for cutting difficult-to-machine single crystal CMSX-4 Ni-superalloy for the manufacture of high pressure gas turbine engine components. In a process known as VIPER grinding (Very Impressive Performance Extreme Removal), a high pressure coolant with a programmable coolant nozzle and highly porous vitrified abrasive wheels are used in a five axis CNC controlled machine [2].

1.1 RESEARCH NOVELTY

Research into abrasive wheel technology by wheel manufacturers has led to the development of grinding wheels with new novel abrasive grit morphologies being commercially available for the manufacturing industry. However, the effects of these engineered grits on the mechanics of cutting and resulting surface topographies and surface integrity have not been studied. Understanding topography of grinding wheels is critical as it affects the mechanics of cutting and consequently the grinding performance and quality of generated surfaces [1], [3]. Wheel topographies degrade and wear during grinding, therefore monitoring this degradation is also vital to maintain process performance.

Some research has been conducted on grinding wheel topography from determining topography measurement methods [4] to 3D wheel surface models [5]. However, none of these works have investigated the influence of abrasive grit morphology on wheel topography and grinding performance. Neither do they capture the behaviour of grinding wheel topography for the entire grinding process from initial dressing through to grinding and the impact on workpiece surface quality and material integrity. This work aims to provide novelty by closing the gap in understanding of the influence of abrasive grit morphology on dressing and grinding behaviour. A more accurate and expansive model of the grinding process can be developed as a result of the obtained knowledge.

1.2 INDUSTRIAL IMPACT

This project has been supported by Rolls-Royce plc, who due to a large order book have a requirement to increase production rates and maintain a continuous drive towards process optimisation. This is achieved by reducing process cycle time, consumable/operational costs and improving component quality for increased part life. Additionally, new engine designs create manufacturing challenges as the engine components become increasingly complex demanding better grinding capability including tighter dimensional tolerances and finer forms. Currently VIPER grinding is a dominant process for machining the main features of a turbine blade within Rolls-Royce. Although it is an established process [3], the mechanisms involved in dressing and grinding chip formation are still not fully understood, especially in relation to the application and behaviour of new abrasive wheel technologies (novel grit morphologies). Therefore, better scientific knowledge of the process will enable optimisation and ensure that Rolls-Royce can meet its production demands. Knowledge generated from this research will be used for process modelling of the industrial grinding process with the aim of better predicting the performance of the process. It will also provide a knowledge database to enable better informed decisions in the manufacturing facility.

1.3 RESEARCH AIMS/APPROACH

This research aims to:

- Understand the influence of three different grit morphologies on dressing abrasive wheels and grinding single crystal Ni-superalloy material.
- Develop deeper knowledge of the effects of grinding wheel topography in the VIPER grinding process. This will better inform manufacturing decisions in industry with the aim of reducing wheel consumable costs, dressing cycle time, grinding cycle time and improved product quality. It will provide extensive data for analytical models which will help optimise abrasive wheel selections and dressing/grinding parameter selection.

To achieve these project aims, four research questions were asked and an experimental investigation platform was designed to answer them:

1. How does grit morphology and dressing influence the grinding wheel topography?
2. How do different wheel topographies impact grinding on a workpiece?
3. How do different wheel topographies breakdown during grinding?
4. How do different wheel topographies respond to varied grinding conditions?

Three different, commercially available, abrasive grinding wheels with different abrasive grit shape were compared and the reasons for their behaviour analysed. The project structure is detailed in Figure 1.01. During each experimental trial, all three wheels were investigated and compared.
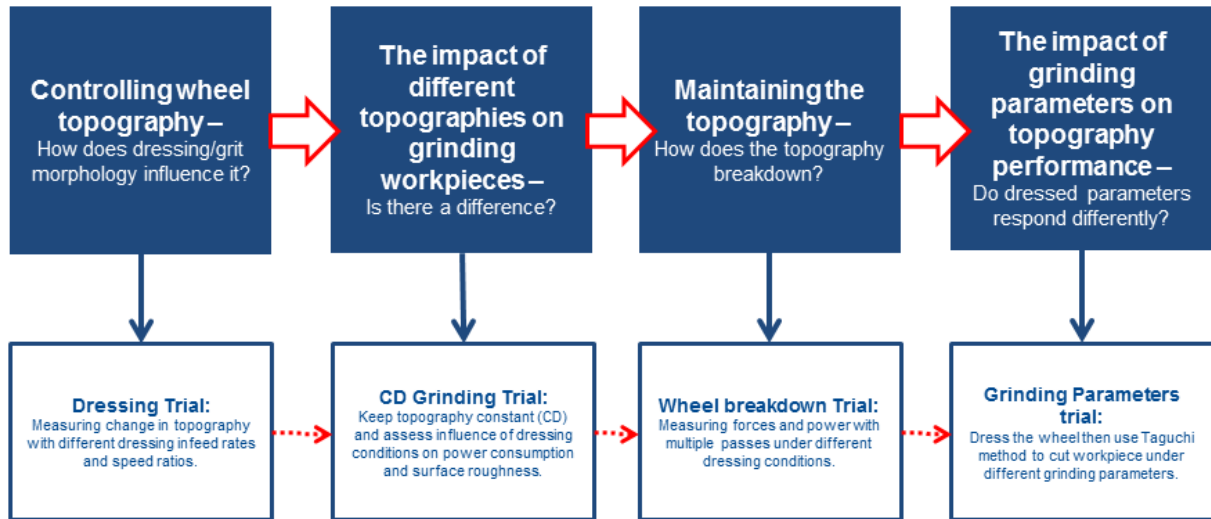
FIGURE 1.01 – ENGD EXPERIMENTAL PROJECT FLOW DIAGRAM.

1.4 THESIS CONTENT

This thesis explains the work undertaken to answer these research questions. All the work was performed at the University of Sheffield and the Advanced Manufacturing Research Centre for Rolls-Royce plc. A comprehensive literature review (Chapter 2.0) introduces the grinding process and abrasive wheel technology before assessing the state-of-the-art research for the grinding of Ni-superalloys. It critically assesses works studying the grinding and dressing performance as well as the influence of wheel topography and measurement techniques. The experimental framework section (Chapter 3.0) gives a detailed explanation of the experimental trials conducted, including determining and controlling the abrasive wheel topography, topography performance, topography breakdown and wheel performance under different grinding conditions. Each experiment is described in detail in an individual sub-section. The results of these trials are reported in Chapter 4.0 and analysed in the Discussion section (Chapter 5.0). Finally summarising conclusions based upon the points raised in the discussion of the data are given in Chapter 6.0. Future work (Chapter 7.0) as a result of this EngD project concludes the main body of the thesis before the references and appendices.

CHAPTER 2

LITERATURE REVIEW

2.0 LITERATURE REVIEW

This chapter reviews the relevant literature to the grinding process, materials used in this research and will highlight the current gap in the knowledge

2.1 GRINDING OVERVIEW

2.1.1 WHAT IS GRINDING?

Grinding has existed as a manufacturing process for centuries, from using abrasive stones to sharpen tools and weapons to contemporary application for finishing precision components [6]. Currently up to 25% of all global machining expenditure is in grinding [1], demonstrating its relevance in modern manufacturing. Grinding can be defined as a 'process by which hard, abrasive surface pressed against workpiece to remove material from workpiece' [7] and utilises hard, irregularly spaced and shaped grits lying on the circumference of a grinding wheel.

These grits are typically small (<1 mm in length) and act as cutting edges that remove material from the workpiece. They are held together by a bonding material that is softer than the abrasive grits [1] and depending on its quantity, controls the porosity of the wheel. Grinding can be characterised as a process with very small chip sizes, mostly negative rake angles and thousands of cutting points. It can also be described as having no defined cutting edge and being a very energy intensive process (explained further in Section 2.1.2).

Grinding is a high energy process which results in high temperatures in the cutting zone, therefore a cooling lubricant is applied to the cutting region to remove cutting chips and control the material response [8]. A dressing tool is also present to ensure accurate wheel form as well as sharpening the grits to create a good cutting surface. There are different forms of dressing tools available, but typically they consist of single or multipoint diamond tools to create a certain profile in the grinding wheel [6].

Grinding is a popular machining process because of its many advantageous properties. Due to its small and numerous cutting points, the chip size in grinding is extremely small which generates a workpiece with a very low surface roughness [6]. Reduced chip size also enables highly accurate dimensional tolerances to be achieved, which is why grinding dominates component finishing [9].

The high hardness of abrasive grits used in grinding, such as diamond or cubic boron nitride, mean difficult-to-machine materials (such as hardened steel, glass etc.) can be comfortably cut [10].

This enables parts to be formed out of a wider range of materials, therefore improving component performance. Grinding is not limited to finishing operations however, with large material removal rates achievable meaning that substantial stock material can be removed from the workpiece whilst still maintaining a high dimensional accuracy [6].

There are still challenges associated with grinding. It is an extremely inefficient process with as little as 0.17% of the abrasive grits actually cutting the work material [11]. Therefore the remaining grits in contact with the workpiece rub or plough the material, generating substantial heat in the contact zone. A problem well described by Malkin, "in applying the classic model of chip formation to grinding… virtually all the energy expended by grinding is converted to heat" [1]. As a result of this phenomenon, the metallurgical properties of the material can change in this heat affected zone, especially when conditions are particularly aggressive [12], [13].

Additionally, the grinding wheel itself is not considered to be geometrically defined and so maintaining control over the process can be difficult [14]. This is especially relevant for grinding wheels that use a friable bond (e.g. vitrified or resin) as during machining abrasive grits and the bond between them can fracture. This removes abrasive material from the wheel and so changes its form and causes the loss of workpiece dimensional accuracy. Friable wheels can be advantageous however as the fracturing reveals new sharp cutting points in a process known as 'self-sharpening' [6].

It is the lack of definition of a grinding wheel (consisting of thousands of randomly orientated grits) compared to other machining operations that makes understanding and predicting it extremely complex [15]. Hence much research is still conducted on developing the knowledge of grinding in order to better improve process performance.

2.1.2 GRINDING PROCESSES

There are many different types of grinding operations applied in industry that are defined based on the machine set up and components to be machined. The four common grinding operations are demonstrated in Figure 2.01.
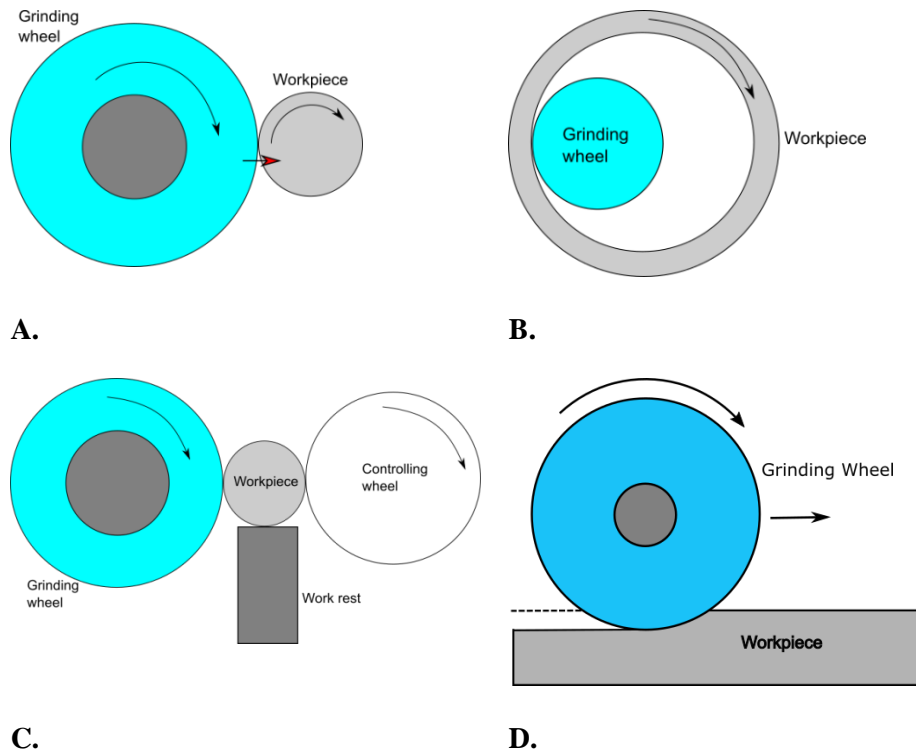
FIGURE 2.01 – THE FOUR COMMON FORMS OF GRINDING (A) EXTERNAL CYLINDRICAL GRINDING, (B) INTERNAL GRINDING, (C) CENTRELESS GRINDING, (D) SURFACE GRINDING.

External cylindrical grinding (Figure 2.01A) is a common machining and finishing process for generating external cylindrical surfaces. Both the abrasive wheel and the workpiece rotate in counter directions to each other with the abrasive wheel rotating much faster relative to the workpiece [10]. This method requires extensive workpiece clamping but has good surface finish due to the small contact length between the grinding wheel and the workpiece. Internal cylindrical grinding is reserved for machining internal surface however due to the long contact length compared to external, rubbing is increased during grinding which leads to instability [6]. For centreless grinding (Figure 2.01C), limited fixturing is required [9] and it uses large wheels so wheel wear is reduced [10]. There is limited control over component shape though. Surface grinding involves material removal on a (relatively) flat surface in which the workpiece does not rotate. Many aerospace turbine components are ground by this technique and is the focus of this thesis.

2.1.2.1 SURFACE GRINDING

Any abrasive machining on planar surfaces is known as surface grinding and like cylindrical grinding it has multiple forms that can occur in industry. A common configuration, often used for surface finishing is reciprocating table grinding in which the machine bed is moved back and forth across a fixed grinding spindle with a rotating abrasive wheel [9], [10]. Further development of these machines lead to the creation of speed-stroke grinders in which the table speed was greatly increased

and the cut depth per stroke reduced. This is advantageous as it reduces the grinding temperature and limits the wasted time from conventional reciprocating grinding when the stroke is reversed at the end of a pass [6].

Although conventional table grinding uses a small depth of cut, a technology was developed that greatly increased the cut depth coupled with slowing the table (feed) speed. This is known as Creep feed grinding and achieves material removal rates (Q') similar to that of milling [6]. Due to the configuration and parameters of creep feed grinding the contact length between the abrasive wheel and the workpiece is much longer than conventional grinding [16], as demonstrated by Figure 2.02.

A.   **B.**
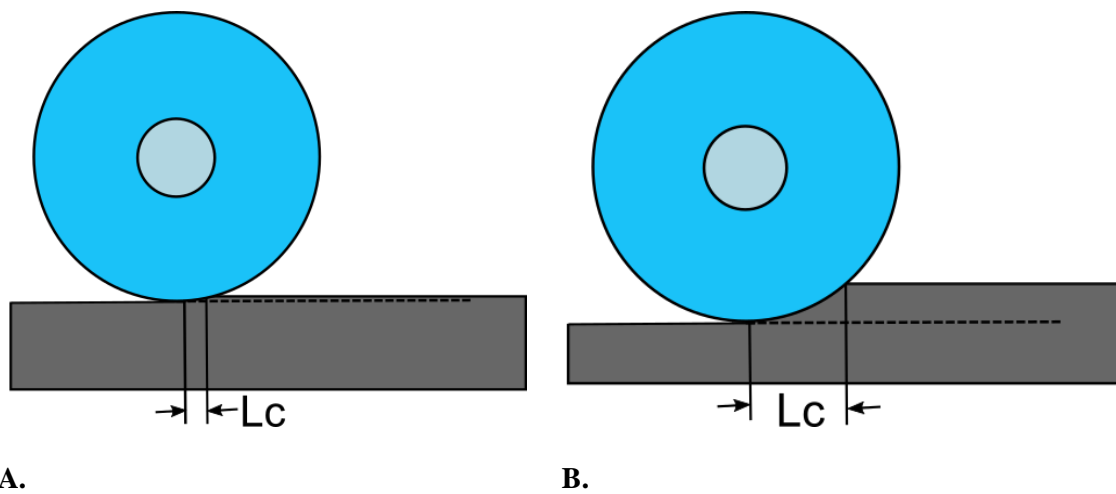
FIGURE 2.02 – (A) CONVENTIONAL GRINDING WITH A SHORT CONTACT LENGTH (L_C) (B) CREEP FEED GRINDING WITH A LONG CONTACT LENGTH [6].

A longer length of wheel in contact with the workpiece results in reduced wear per abrasive grit however there is greater rubbing contact. This increases the energy in the process and therefore the temperature in the cutting zone. With a low feed rate, more energy is transferred into the workpiece which greatly increases the risk of grinding induced defect such as thermal damage (surface burning) and metallurgical phase changes in the material [6]. In conventional grinding film boiling of the applied coolant occurs in the cutting zone, therefore reducing the heat transfer coefficient of the fluid and the wheel, limiting the transfer of heat from the workpiece [17].

However, the large contact length in creep feed grinding means that the power per unit area of the wheel is relatively low, ensuring that the coolant fluid remains liquid during grinding [17]. It is well known that vast amounts of coolant fluid must be applied during creep feed grinding and research has been performed in order to optimise the application of grinding coolant in the form of novel nozzle designs to increase the uniformity of the coolant velocity [18], a coolant 'shoe' to remove the damaging air curtain around the wheel, reducing grinding forces by over 40% [19].

However implementation of these methods can be difficult as they limit the flexibility of the process. Coolant application is a balance between reducing grinding normal forces (less coolant) and providing sufficient cooling (increased coolant) [20].

Further development of creep feed grinding led to the invention of VIPER (Very Impressive Performance Extreme Removal) grinding, a high performance process created by a collaborative group of Rolls-Royce, Tyrolit and Makino [21]. Using a highly porous, vitrified abrasive wheel with high pressure (70 bar) coolant directed into the wheel, coolant is able to access the cutting region on the workpiece whilst simultaneously cleaning the wheel [2]. Directing the coolant into the surface of the abrasive wheel, the pores carry coolant into the active region of cutting. Due to the indexable nature of the coolant nozzle, the process is able to perform creep feed grinding on multiple surfaces of difficult-to-machine components, such as turbine components in gas turbine engines. The research presented in this thesis is based upon VIPER grinding as the work was sponsored by Rolls-Royce in order to optimise their turbine blade grinding process.

2.1.2.2 OTHER PROCESSES

Beyond the primary forms of grinding (cylindrical and surface) there are other abrasive techniques that are used throughout industry. Classical methods include honing in which an abrasive stick is mounted on a mandrel and rotated whilst reciprocating over an unclamped workpiece. It is a low-velocity process meaning that the temperatures and forces generated are reduced and high dimensional accuracy can be achieved [9]. Lapping is a process in which loose abrasive, carried in oil or water, is sandwiched between the workpiece and a softer lapping tool [9]. It is commonly used for correcting surface imperfections and when a close fit is required between contacting surfaces.

More recent novel techniques include point grinding in which very small grinding wheels and abrasive points are attached to metal shafts [22], [23]. As the material removal rates for these techniques are limited they are mostly used for deburring and finishing using very high spindle speeds (up to 100,000 rpm) [10].

2.1.3 APPLICATIONS

As grinding has uniquely useful properties (excellent surface finish, cuts difficult-to-machine materials etc.) it is utilised in a wide range of industries. Materials such as advanced ceramics and glass are notoriously difficult to machine using standard processes because of their high hardness and brittle behaviour. However because of the very small penetration depths of the abrasive grits, microcracks form in the ceramic and enable controlled removal of material [24]. This has enabled the

highly accurate machining of optical glasses for microscopes and telescopes where high quality surface finish is required [25].

The automotive industry is a heavy user of abrasive machining processes because of their ability to combine high material removal with excellent surface finish. The development of improved grinding wheel technologies has led to vastly improved production times for many automotive components, such as cam shafts and valves, manufactured using a cylindrical grinding methods [14].

The aerospace industry uses grinding for a number of applications with many steels ground with cylindrical grinding for multiple components around the aircraft including aeroengine shafts and landing gear [2]. Superalloys (such as Inconel 718 or CMSX-4) are widely used in the production of jet engines for turbine and disk components [26] because of their high strength at high temperatures helping to achieve more efficient performance in the extreme conditions demanded in the engine [27]. However, machining these materials is very difficult, therefore grinding is the preferred machining operation over milling for many manufacturers in the aerospace industry. Hard abrasive carbides in the alloys creating a tendency for the material to adhere to the surface of cutting tools, making tool wear a major problem as high machining speeds are required in order to achieve a satisfactory material removal rate [28]. Grinding provides the optimum balance between the hard material challenge, tight dimensional and finish tolerances as well as cost rate.

Creep feed or VIPER grinding is usually employed for the machining of features on Ni-superalloy turbine blades (Figure 2.). These include the fir tree root forms and the top shroud of the blade, which require high dimensional accuracy and excellent surface quality (high pressure along the contact region on the fir tree between the blade and the disc) and are ground after being investment cast. Challenges include keeping a tightly controlled process to maintain high production rates, especially with increasingly complex blade designs.
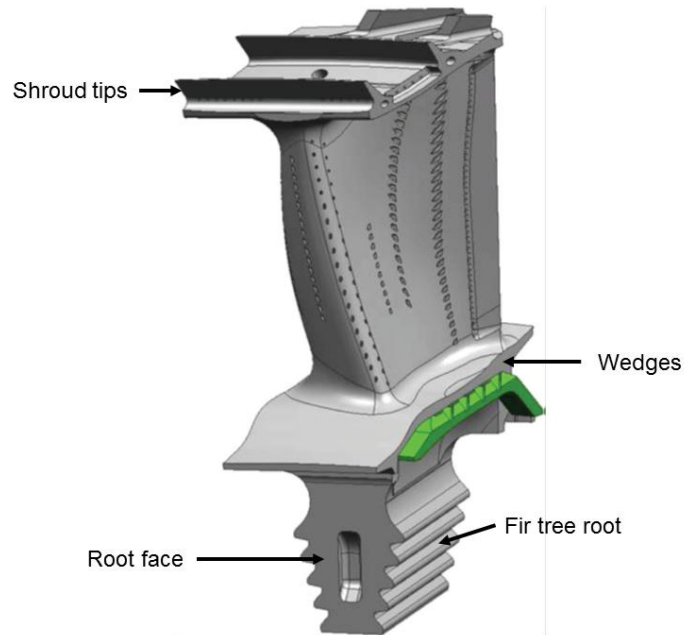
FIGURE 2.03 – THE TYPICAL FEATURES CREEP FEED GROUND ON A TURBINE BLADE [29].

Composite materials are also increasingly being used in aerospace applications due to their favourable strength-to-weight ratios. This family encompasses Ceramic Matrix Composites (CMCs) and Metal Matrix Composites (MMCs) [2]. CMCs are a particular area of growth for use in the turbine section of a jet engine because the matrix provides high wear, temperature and chemical resistance properties whilst the fibres give strength to the material [30]. Ceramics however are very difficult to machine with conventional methods. Hence much work is being conducted studying grinding of CMCs.

The work presented in this thesis is focused on the grinding Ni-superalloy material for use in the turbine section of the jet engine. The material studied is discussed further in Section 2.6.

2.2 GRINDING MECHANICS

2.2.1 CHIP REMOVAL FUNDAMENTALS IN GRINDING

The abrasive grits in grinding are irregular, blunt and often have a very negative rake angle, so there is a large compressive plastic zone ahead of the grain and three shear zones around the interface (Figure 2.04) [6]. Shear occurs when the shear stress in the shear zone is greater than the shear strength of the material.
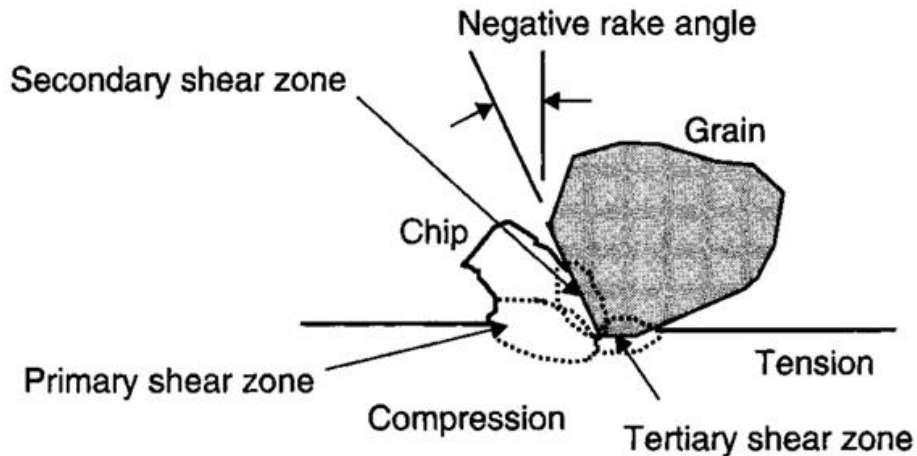
FIGURE 2.04 - THE INTERACTION BETWEEN AN ABRASIVE GRAIN AND THE WORKPIECE SHOWING THE THREE SHEAR ZONES AND A NEGATIVE RAKE ANGLE [6].

The specific grinding energy consists of three separate components [31]–[33] (Figure 2.05) and an abrasive grain can perform only one stage or a combination of them all [6], [34].

1. Cutting – the abrasive grain penetrates the surface and carves out a chip.
2. Rubbing – the grain gently rubs the workpiece surface causing some wear.
3. Ploughing – the grain penetrates the material and causes significant plastic deformation, without cutting (creates surface ridges).
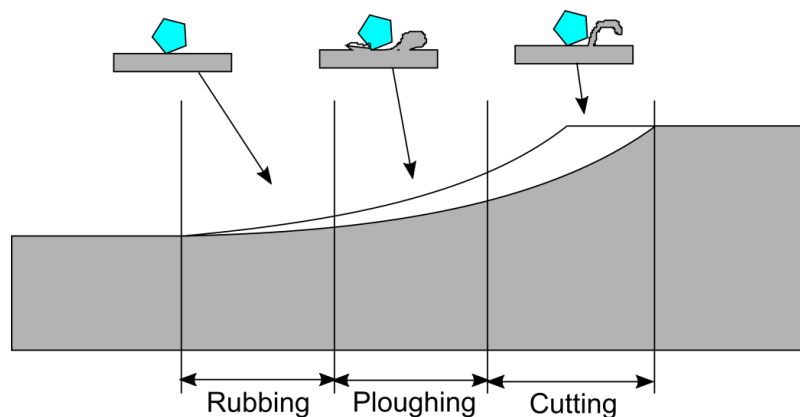
FIGURE 2.05 – SCHEMATIC OF THE 3 STAGES OF GRINDING. A RECREATION OF THE DIAGRAM BY MARINESCU [32].

Rubbing occurs when a grain first contacts the workpiece it typically slides along the surface, generating heat but only causing elastic deformation in the workpiece material [34]. An increase in stress eventually exceeds the yield stress of the material and plastic deformation occurs, this is the ploughing stage. With the plastic deformation, material piles up in front of the grain until the stress is sufficient that the material shears, creating a chip and entering the cutting phase [34].

Cutting in grinding is highly likely to occur with negative rake (the angle of the face of the tool, relative to the workpiece, Figure 2.04) grits. Experiments using tools with angles as negative as -75° have been shown to remove material [35]–[37] however with increased negative rake angle, the more plastic deformation that occurs. This is due to the fact that with high negative rakes, the compressive force on the surface is high and shear force is reduced. Rubbing and ploughing readily occurs in grinding and they are very difficult to prevent due to fabrication process of grinding wheels. Other works looking into negative rake angles [38]–[40] studied analytical assessment of tool-chip friction, finite element modelling of large negative rake orthogonal cutting and single grit grinding using CBN and diamond wheels respectively. These found that negative rake angles respond differently in cutting to positive rake and more negative angles lead to an increase in forces and affect the chip thickness.

The key process parameters in grinding are detailed in Figure 2.06 Workpiece feed rate (v_w) is the distance the grinding wheel traverses along the workpiece in one unit of time (mm/min), wheel speed (v_c) is the rotational surface speed of the outer edge of the abrasive wheel expressed in m/s. Depth of cut (a_e) is the distance into the workpiece from the top surface that the wheel penetrates in one grinding pass. The acting forces during grinding are the normal force (F_n) perpendicular to the direction of grinding and the tangential force (F_t) parallel to the direction of cut.
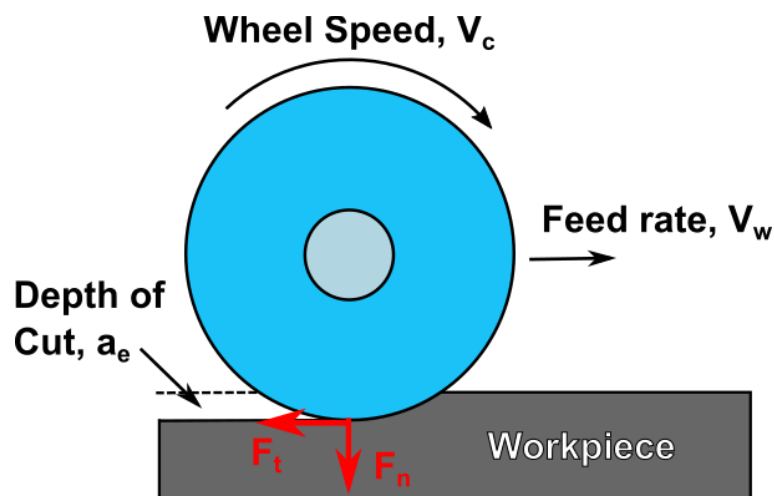
FIGURE 2.06 – DIAGRAM OF THE KEY PROCESS VARIABLES IN GRINDING.

Chip thickness in grinding is much smaller than for conventional machining due to the small abrasive grits performing the cutting (Figure 2.07) [1], [9]. The surface speed of the grinding wheel is very high compared to the feed rate of the workpiece so the average chip thickness value is small (Equation 2.1).
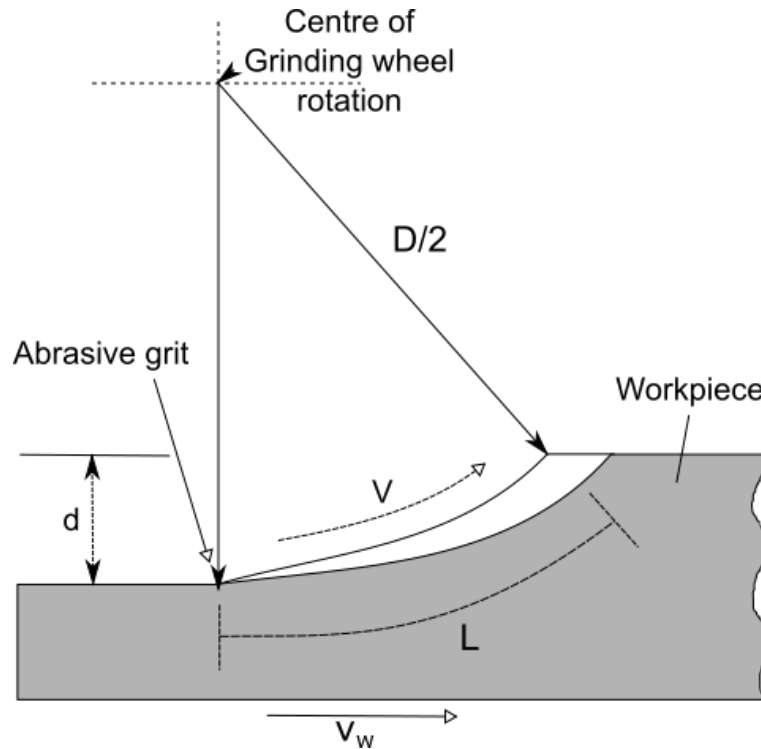
FIGURE 2.07 – (A) SCHEMATIC OF THE MOVEMENT OF A GRIT OVER A WORKPIECE [9].

$$t = \sqrt{\frac{4v_w}{rcv_c}\left(\frac{d}{D}\right)^{\frac{1}{2}}} \qquad \text{EQUATION 2.1}$$

Whereby t is the average chip thickness, r is the ratio of width to height of the abrasive grit and c is the number of active grits per mm^2. As c is not constant and is difficult to determine, equivalent chip thickness (h_{eq}) is a widely used term due to its simplicity to calculate [32](Appendix A). Work by Shaw [41] showed that the undeformed chip thickness is very small relative to the edge radius of the active grits. This can cause very negative rake angles along with the random orientation of the grits [10], [42] and so the volume of plastically deformed material is large compared to the volume of the chip that is formed (up to 75 times greater) [41].

Chip thickness in machining influences the energy consumed in the process by the relationship shown in Equation 2.2 [43].

$$u \propto \frac{1}{t^n} \qquad \text{EQUATION 2.2}$$

Whereby u is the specific grinding energy and n is 1 for precision grinding. In conventional machining, because of the positive rake angle and the large chip thickness, the extent of rubbing and ploughing is negligible and 75% of the consumed energy is transferred into the chip [1]. In grinding

the chip thickness is significantly reduced and so the energy consumed in the process is much greater [44].

Specific energy refers to the energy required to remove a unit volume of material [1]. It is defined by Equation 2.3 whereby u is specific grinding energy, P is grinding power which is derived from the tangential grinding force and the rotational wheel speed, a_e is the depth of cut and b is the width of cut.

$$u = \frac{P}{v_w a_e b} \qquad\qquad \textbf{EQUATION 2.3}$$

It is known that the specific energy of grinding increases with a reducing chip size with high shear stresses generated at very small depths of cut [1]. This phenomena is known as the 'size effect' [45] and was studied by Backer et al. [46] who examined the contact between abrasive grits and the workpiece using carbon-black on a glass plate to determine the number of contact grits per unit area. They suggested that the size effect could be caused by a decrease in stress-reducing defects in the material (such as grain boundaries and impurities), and therefore the reduced likelihood of the cutting tool encountering an specific energy reducing defect [47]. However this theory is doubtful because the density of defects (dislocations) is expected to increase in the shear zone [1].

As a result of the increase in dislocations, an alternative explanation for the size effect was proposed by Dinesh et al. [48]. It was suggested that an increase in the strain gradient occurs as chip size declines due to the formation of 'geometrically necessary' and 'statically stored' dislocations from plastic deformation (ploughing). As the scale of deformation declines, strain gradients increase and the density of geometrically necessary dislocations rises relative to the statically stored causing a strength increase in the material [49]. Indentation experiments by Stelmashenko et al. [50] on tungsten (W) and molybdenum (Mo) samples and work by Nix and Gao [51] on copper (Cu) and gold (Ag) showed that strengthening occurs in the surface material with an increase in dislocation density. Dinesh et al. [48] attempted to relate this dislocation and strain gradient feature from indentation to machining and proposed that undeformed chip thickness controls all deformation in machining [49]. This does not match exactly with research by Gerberich et al. [52] as they showed that at very small indentations on W, Al, Au and Fe-3wt%Si, hardness is unaffected by strain gradients.

The 'sliced bread' analogy by Rowe and Chen [53] is another explanation for the size effect which states that the specific energy increases as the surface area of the chip gets larger. As the number of chips required to remove the same volume of material increases, so does the total energy expended (like slicing a loaf of bread). Empirical and experimental results demonstrated the

relationship of depth of cut and cutting edge density on specific energy, indicating a link between wheel topography (Section 2.5) and grinding performance.

Grit shape (Section 2.3) is known to impact grinding specific energy and influence the size effect. Specific energy is inversely proportional to the chip thickness (t) (Equation 2.2), which itself is dependent on the dimensions (r) and number of active cutting points (c) (Equation 2.1). Both these parameters are controlled by the grit shape. Single grit scratch tests have shown substantial variation in the normal force and the level of workpiece pile-up ahead of the grit when varying grit shape [54]. It has been reported that specific energy and chip shape are both influenced by the shape of the cutting edge [55], [56]. This work demonstrates that although grit shape is known to influence the size effect, its true source of the effect is not yet fully understood. Therefore this EngD research aims to improve the understanding of grit shape and grinding behaviour which could further explain the size effect.

2.2.2 GRINDING PERFORMANCE

Extensive research has been conducted to understand grinding key process variables (depth of cut, feed rate and wheel speed) on process performance and how it can be optimised as grinding is widely considered a 'black art' due to its undefined cutting edge geometry [15].

Increasing depth of cut and feed rate has been shown to clearly increase normal and tangential grinding forces [57]–[59] (Figure 2.08A - B) because more material is removed in the cut as the chip size per grit is larger [60]. The relationship is linear as ploughing is the major deformation mechanism, however at extremely low depths of cut (< 2 µm) behaviour is parabolic as rubbing dominates and the shear stresses are insufficient for plastic deformation [61]. Increased wheel speed however causes a grinding force reduction [6], [58] because of the smaller chip size (Figure 2.08C).
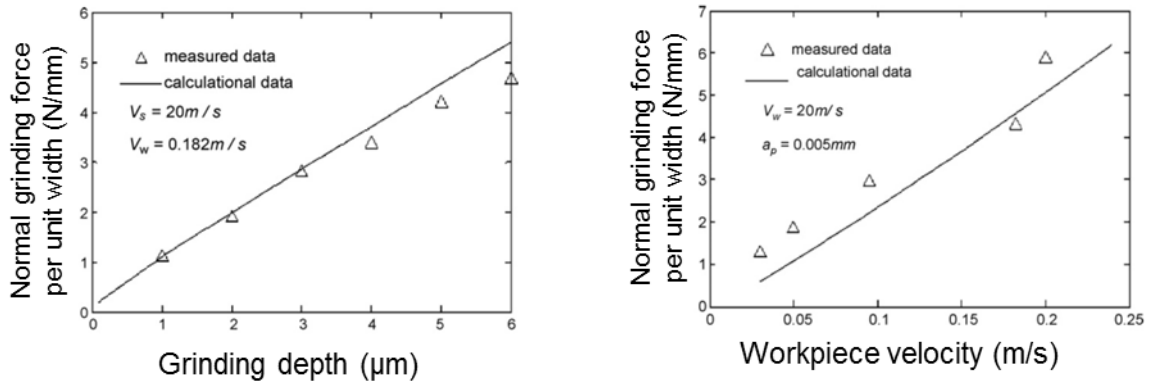
A.

B.
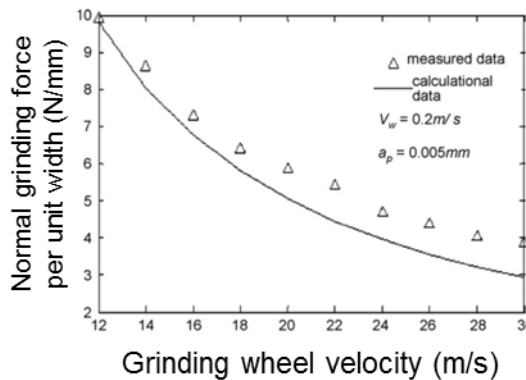
C.

FIGURE 2.08 - NORMAL FORCE INCREASING AS A FUNCTION OF (A) GRINDING DEPTH (B) WORKPIECE FEED RATE AND DECREASING (C) WHEEL SURFACE SPEED [58].

High levels of rubbing and ploughing mean that the friction coefficient (μ) is an important term in grinding. The friction coefficient is known to vary with wheel speed and feed rate and is related to the F_n and F_t force components in grinding, as shown by Equation 2.4 [1], [6]. Therefore a straight line graph of F_n against F_t gives an indication of the force ratio [62].

$$F_n = \frac{1}{\mu} F_t \qquad\qquad \text{EQUATION 2.4}$$

At low depths of cut the sliding and ploughing force (and therefore friction coefficient) is more dominant as penetration of the abrasive grits into the workpiece is less. Therefore forces are insufficient for material removal [63] and the friction is high. This has been demonstrated in work by Durgumahanti et al. [64] with single grit diamond scratch tests as well as alumina wheel validation trials.

Increasing wheel speed causes a decline in the friction coefficient as shown by Cai et al. [65]. Anderson et al. [57] performed Lagrangian and Eularian Finite Element formulations supporting this (Figure 2.09A) as well, demonstrating that friction mostly influences the tangential force as its value

increased by 58 % when it was included in the model (compared to a 6 % increase in the normal force). This does not agree with work performed by Durgumahanti et al. [64] who saw an increase in friction with wheel speed, however the authors explain this is likely due to wear (Section 2.3) of the abrasive grits, which was not considered by Anderson. As both Coulomb friction (adhesion between grit and workpiece) and ploughing friction (resistant to movement due to build-up of material ahead of the grit) were decreased [57], the force ratio (Ft/Fn) was reduced with an increase in cutting speed, an effect also seen by Cai et al. [65]. Anderson et al. [57] claimed that a decrease in the force ratio indicates a more efficient process as less friction reduces the tangential force component, an effect also reported by Subhash and Zhang [66] from single pass scratch tests. Also because of an observed increase in normal force due to greater strain hardening of the workpiece at higher cutting speeds. However this disagrees with Rowe [6] who reports that an efficient process has a high force ratio as the grinding wheel is expected to remove material, not slide over it. Marinescu [32] argues that a low force ratio demonstrates a well lubricated process, with a high force ratio the wheel cutting points are sharp and the grains penetrate deep into the workpiece (Figure 2.09B force ratio increase at greater depth).
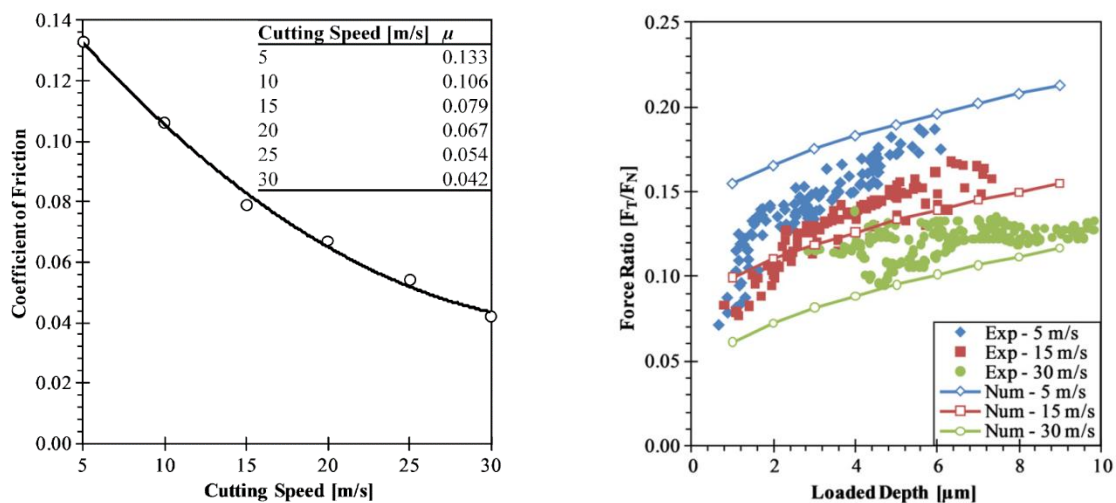
A.   **B.**

FIGURE 2.09 – (A) DECREASE IN COEFFICIENT OF FRICTION AS A FUNCTION OF CUTTING SPEED FOR SINGLE GRIT FINITE ELEMENT GRINDING MODELS (B) EXPERIMENTAL AND NUMERICAL DATA SHOWING INCREASING FORCE RATIO WITH CUT DEPTH [57].

The grinding power is closely related to the tangential force, as discussed in Section 2.2.2, and is therefore linked to chip thickness. Power consumption tends to increase as the depth of cut and workpiece feed rate increase (larger chip size) [67], [68]. Grinding power is also known as a good representation of wheel topography sharpness and is can be used to assess the impact of dressing [68].

Much of the literature assesses the grinding behaviour in respect to measured/calculated forces or energy. However much of the data is gathered from very low depths of cut for the grinding parameters. There is an opportunity for further grinding research analysing force and power monitoring in rough (large depth of cut) grinding.

2.2.3 GRINDING MODELLING

The random nature and large number of abrasive grits in contact with the workpiece at one time makes modelling grinding extremely complex, however many analytical and experimental models have been developed to describe the mechanics of the process. Grinding modelling work has developed significantly over the years with many early models being based on multiple linear regression to form analytical and empirical models. This has since developed more recently into Finite Element Analysis and geometric kinematic models [24], [69]. Many of these models consider the topography of the grinding wheel (Section 2.5.5), the grinding forces/energy and topography wear (breakdown) and the relationships between them.

As the grinding wheel topography directly influences grinding forces, many models consider this factor. Early models that considered 2D wheel topography include those by Reichenbach [70] and Shaw [71]. Warnecke and Zitt [72] used 3D synthetic models of abrasive wheels, based upon cutting point density and grit volume, to create a kinematic simulation of the tangential forces on individual grits. However this model assumed no ploughing effects in the process. Hecker et al. [73], [74] provided a similar 3D topography model of the wheel topography using cutting edge density and found a linear relationship for normal / tangential force per grit against grit penetration into the workpiece. This model did assume all abrasive grits were spherical or conical, which is not truly representative of the abrasive cutting edges. Chang and Wang [75] developed a stochastic grinding force model that factors the random grit distribution in a wheel. This model studied different grinding conditions but not variation in the wheel (grit size, porosity etc.). Snoeys et al. [76] used a chip thickness model to predict the tangential forces in grinding and other research has considered the forces for the three separate chip formation stages of grinding (rubbing, ploughing and cutting) [77], [78]. Durgumahanti et al. [64] also adopted this approach and established equations for both the tangential and normal force based on experimental coefficients and process parameters (wheel speed, feed rate and depth of cut). The results showed a clear increase in forces with increasing depth of cut and feed rate. Wheel speed increase was shown to reduce the grinding forces (Figure 2.10) which matches experimental data (Section 2.2.3).
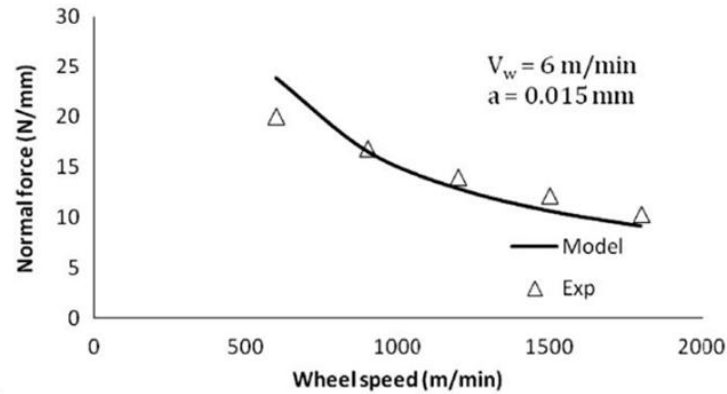
A.
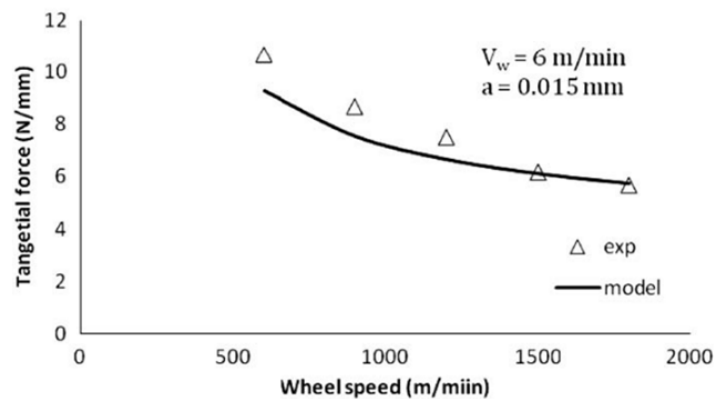
B.

FIGURE 2.10 – MODELLED (A) NORMAL AND (B) TANGENTIAL FORCES DECREASING WITH INCREASING WHEEL SPEED [64].

As grinding energy is related to the forces, many models predict energy and its distribution. Bifano and Fawcett [79] developed an analytical model relating the grinding depth to the specific grinding energy. However this was focused on brittle materials and the ductile-brittle transformation. Single grit scratch tests performed by Singh et al. [80] were used to develop an empirical model to predict specific ploughing energy, which was found to be very dependent on depth of cut. Hwang et al. [81] considered how the breakdown of cutting edges during grinding impacts the chip thickness and kinematic models found a linear relationship between forces and the area of 'flattened' cutting edges.

Grinding is a high energy process and understanding thermal behaviour is important. Hahn [82] was the first to suggest that high temperatures in grinding are a result of frictional rubbing between the abrasive grits and the workpiece. A thermal model by Hou and Komanduri [11], which considers the stochastic nature of the abrasive grit distribution found localised temperature spikes at the grit-workpiece interface resulting from a frictional response. Over 70% of the heat generated flows into

the workpiece [11] meaning that high temperatures in the grinding zone can cause metallurgical changes in the workpiece that could generate additional defects in the machined surface [2]. Analytical and experimental work [83], [84] has shown that work-surface temperature actually decreases with increasing depth of cut because more chips are generated so the heat is removed along with the chips before it can conduct away from the cutting path of the wheel on the workpiece. Grinding thermal energy modelling has shown that the energy partition (the fraction of cutting, ploughing and rubbing energy conducted as heat into the workpiece) is in the region of 60-85% for conventional grinding compared to 5% for creep feed [84], [85].

Experimental data is required to generate and validate process models and so this EngD work produces grinding data that can be utilised to create future empirical models. Small-scale general linear models will also be created to assist in the analysis of the grinding results.

2.3 GRINDING WHEEL TECHNOLOGIES

2.3.1 GRINDING WHEEL STRUCTURES

A typical grinding process uses abrasive grinding wheels to perform the cutting part of the grinding process. They consist of hard, ceramic grits which are bonded together. It is these grits which perform the cutting, whilst the bond material ensures the wheel maintains its shape and binds the hard grits together.

There are a number of key input variables for abrasive wheels, as demonstrated by Figure 2.11 which shows an example wheel specification code, which can greatly influence the grinding behaviour of a wheel. Bond type and hardness, grit material and size, as well as porosity are all customisable parameters of a grinding wheel whose impact is not fully understood [86].
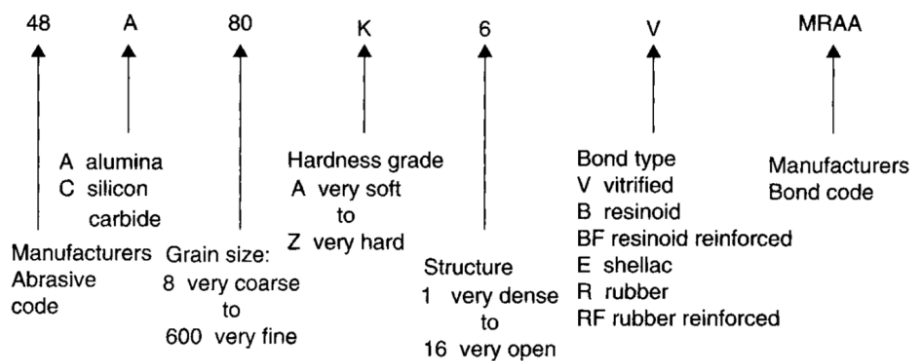
FIGURE 2.11 – WHEEL CODING FORMAT FOR CONVENTIONAL ABRASIVE GRINDING WHEELS [6].

2.3.2 ABRASIVE GRITS

The ideal cutting tool is much harder than the workpiece material so abrasive wheels consist of ceramic grits with a very high hardness which enable effective cutting of the workpiece material [87], [88]. Abrasive grits for grinding wheels can be split into two categories, 'conventional' which use aluminium oxide or silicon carbide grains bonded by either a vitreous or resin bond, and 'superabrasive' consisting of diamond or cubic boron nitride (CBN) grains with bonding including vitreous, metal or resin [1].

2.3.1.1 SUPERABRASIVES

The term superabrasives refers to diamond or Cubic Boron Nitride (CBN) as these are far harder than other abrasive materials but also significantly more expensive [6]. Diamond is the hardest known material as well as very thermally stable and resistant to mechanical wear. Hence it has become widely used when grinding very hard ceramics (such as for dressing vitreous bonded conventional wheels, discussed Section 2.4) [6]. However, as diamond is formed of carbon it cannot be used for grinding ferrous materials because carbon diffusion into the workpiece leads to extensive abrasive wear [1]. Both natural and synthetic diamonds are used, however, the latter has become more popular due to their reduced cost and ability to control their properties, such as friability (how easily the grit fractures under compression), in different directions along the crystals [1].

Cubic boron nitride (CBN) is a mono or polycrystalline superabrasive alternative to diamond that has largely filled the gap when machining ferrous materials (steels, certain nickel alloys etc.) due to its favourable mechanical properties (Table 2.1). Oil coolants are often preferred with CBN though as the protective boron oxide layer formed on the grits dissolves in water meaning that a scrubbing method has to be applied to reduce loading [1], [6]. CBN wheels have the potential to give improved process efficiency, low overall grinding costs (reduced consumable costs) and increased flexibility for low volume components [62]

TABLE 2.1 – HIGH HARDNESS AND THERMAL CONDUCTIVITY OF SUPERABRASIVES (YELLOW) COMPARED TO CONVENTIONAL (BLUE) AS ACCORDING TO ROWE ET AL. [6].

Abrasive	Knoop Hardness (kg/cm^2)	Thermal conductivity (W/m K)
Diamond	6500	600-2000
CBN	4500	240-1300
Silicon Carbide	2500	100
Aluminium Oxide	1370-2260	35

Much recent research has focused on CBN grinding wheels studying aspects including dressing [89], [90], coolant behaviour [91] and grinding performance [92]–[95]. However there are still research gaps for conventional abrasives to investigate.

2.3.1.2 CONVENTIONAL ABRASIVES

The vast majority of conventional abrasives are either aluminium oxide (Al_2O_3) or silicon carbide (SiC). The aluminium oxide grits are usually synthetic consisting primarily of hexagonal alumina with other oxide impurities (such as TiO_2), while the silicon carbide grits have hexagonal or rhombohedral crystal structures [1], [96].

The hardness (measured by Knoop hardness test) and friability are the key criteria for the abrasive grits. These properties can be modified by controlling chemical composition, size and geometrical factors of the crystals. It has been shown that smaller grits are less friable (fractured less easily) because of the reduction in the number of defects (such as pores) which can nucleate a crack [97]. Figure 2.12 demonstrates that friability is directly related to Knoop hardness, so the harder the grit the more friable it is. This behaviour is exponential for alumina but is more linear for SiC. High friability will lead to loss of form but can provide self-sharpening functionality to the wheel so hardness and friability must be balanced.
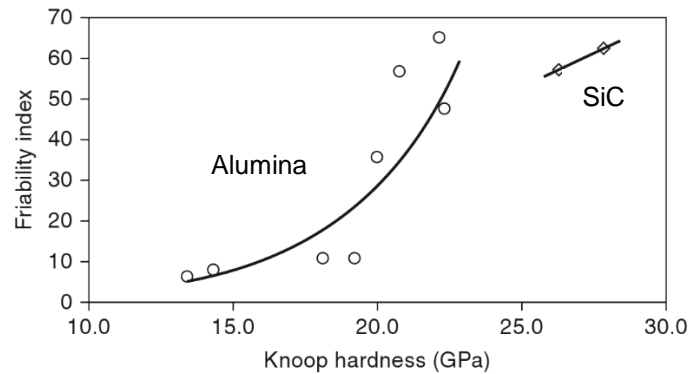
FIGURE 2.12 – INCREASING FRIABILITY AGAINST HARDNESS FOR ALUMINA AND SILICON CARBIDE ABRASIVES [1].

Alumina is manufactured through the smelting of aluminium alloys at 1260 °C and there are two common methods, electrofusion and chemical sintering. Electrofusion uses a bed of bauxite (raw material containing >80% alumina) in an electric furnace heated to 2600 °C (with coke or iron to remove impurities) as a high current is passed through carbon starter rods. The generated crystals are crushed by a series of mills to form abrasive grits which are then sorted by size through a series of sieves (creep feed grinding typically ranges from 300 µm to 45 µm grain size) [32]. The crushing process forms randomly shaped abrasive grits containing few crystals (3 – 4 per grit) which can mean a substantial loss of dimension when grain cleavage occurs [32]. These are conventional, fused abrasive grits and because of their blocky shape, are considered approximately spherical in form (Figure 2.13A).

Sintering is a more recent production technique for alumina compared to electrofusion. Compacted bauxite slurry is extruded in order to set the grain size and shape. The slurry is then sintered at over 1500 °C. Examples of sintered abrasives include those developed by 3M plc. called 'Cubitron' or Saint Gobain's 'Altos'. These are known as sol-gel (SG) abrasives and are precipitated with various materials (e.g. magnesia or yttria) to give abrasive grits with high microstructural strength and much smaller crystals (0.1 – 5 µm) than electrofused [98]. SG grits can also be extruded into shapes [32] such as the triangular Cubitron grit (Figure 2.B) or the elongated Altos grit (Figure 2.13C).

Grinding of AISI52100 steel was conducted by Madopothula et al. [99] with partially SG (30% SG and 70% fused) and 100% fused alumina wheels. Results demonstrated a higher toughness in the SG grits which also encouraged the formation of more dull grits so grinding forces increased. Godino et al. [98] performed a similar investigation when grinding tempered steel and found that although SG wheels were initially sharper, they had 23% more dull regions on the grits compared to the entirely fused wheel. Rubbing and ploughing was the dominant mechanism however the depth of cut was

extremely low (a_e < 20 µm). Selvakumaran et al. [100], saw contrasting results when comparing the wheel types for grinding steel and found a 21% reduction in cutting forces and 20% efficiency increase with the SG grits due to their high hardness maintaining sharpness. The depths of cut in all these trials were very small and no attention was paid to the abrasive grit shapes.

Krell et al. [101] studied the microstructure and mechanical properties of sintered SG grits and performed microindentations on the grit surfaces. Results indicated that the inherent hardness of the grits increases with a crystal size reduction, which supports findings by Badger [102] who measured grinding power of fused and SG wheels and saw a lower power in SG wheels due to hard, sharp cutting points. The author also proposes that certain manufactured SG wheels (such as Cubitron) be run at higher material removal rates to maintain sharp cutting points and remove dulling. A proposal supported by Frantisek et al. [103] who argued that these wheels perform better at higher grit engagement with the workpiece. Again however, little attention was focused on abrasive grit shape. Some work has been conducted on heat partition and surface roughness modelling for fused vs. SG wheels by Garcia et al. [104] and Nizankowski et al. [105] respectively however they both focused on model construction than grit performance. As raised by Wegener et al. [86], literature covers different abrasive materials however 'there remains a lack of understanding of the non-uniform orientation of shaped grains'.
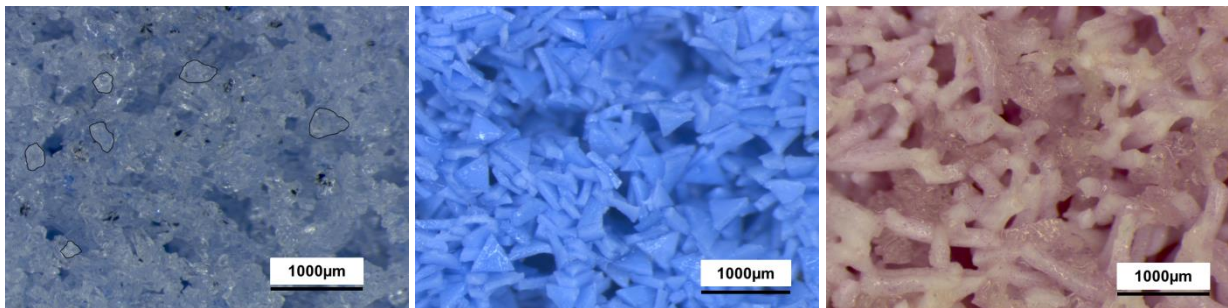
A.   **B.**   **C.**

FIGURE 2.13 – (A) CONVENTIONAL ELECTROFUSION MANUFACTURED ABRASIVE WHEEL (EXAMPLE SHAPES HIGHLIGHTED) (B) SOL-GEL CUBITRON SINTERED GRITS (C) SEEDED GEL ALTOS SINTERED ABRASIVE GRITS.

2.3.1.3 GRIT SIZE AND GRIT TYPE COMPARISON

Abrasive grit size in a grinding wheel is determined according to the American National Standards Institute (ANSI) US standard in which grain sizes are sorted by filtering them through a series of meshes of different sizes. A mesh number refers to the quantity of wires per inch in the sieve [6]. For example a wheel of grit size #60 has an approximate grit size of 250 µm. It is well known that the larger grit sizes are typically used for high stock removal rates whereas finer grit sizes are for finishing processes as they generate a lower surface roughness [32]. Kannappan and Malkin [31] were

some of the first to investigate the influence of grit size under constant grinding and wheel parameters. Surface grinding was performed on AISI1095 steel with vitrified alumina grinding wheels. Although the data showed improved surface roughness with finer abrasive grits (#120 to #30) the specific grinding energy appeared independent of grain size. This is because of a change in the chip dimension with grit size. Specific energy is known to be closely related to undeformed chip thickness (Equation 2.1). Therefore grinding with fine grits forms small, narrow chips from lots of cutting points. With larger grits then the chip dimensions increase but the number of cutting points declines [106], therefore there is little change in the undeformed chip thickness, and so specific energy.

Nan Li et al. [107] modelled the grain-workpiece interaction of individual grits, factoring in wheel randomness (including grit orientation), and applied it to the entire wheel. Rubbing, ploughing and cutting forces were considered separately rather than predicting an overall average force. The data showed that wheel grit size was the most influential parameter on rubbing, ploughing and cutting as a small grit size leads to a high level of rubbing (more contact points and smaller uncut chip thickness). Depth of cut was the second most impactful parameter on grinding forces. The model was validated on a surface grinder with an alumina wheel on AISI1055 workpiece material. The authors also highlight that rubbing, ploughing and cutting occur simultaneously during machining but that certain mechanisms dominate.

A wheel comparison study of three abrasive types (single alumina, white alumina and CBN) by Yao et al. [60] found that single grit alumina had the highest grinding forces and CBN the least. The resultant analytical model suggested that this is because the experimental coefficients related to frictional force (K_2 and K_4 , Equations 2.5 - 2.6) are very dependent on wheel type. This force is increased by adhesion phenomenon generated on surface of grain. For the CBN wheel, it has good chemical stability so the adhesion is reduced and so are the grinding forces. The chip formation coefficients (K_1 and K_3) however showed much smaller difference between the wheel types.

$$F_n = K_1 \frac{v_w}{v_c} a_e + K_2 (\frac{v_w}{v_c})^\alpha (a_e)^{\frac{1+\alpha}{2}} \qquad \text{EQUATION 2.5}$$

$$F_t = K_3 \frac{v_w}{v_c} a_e + K_4 (\frac{v_w}{v_c})^\alpha (a_e)^{\frac{1+\alpha}{2}} \qquad \text{EQUATION 2.6}$$

F_n is normal force, F_t is tangential force, v_w is workpiece speed, v_c is wheel speed, a_e is grinding depth and α is the exponential coefficient of edge distribution. The grit sizes used between each of the wheels was not consistent however (#80 grit size used for single alumina and #60 for white alumina) therefore this will influence the sharpness and chip size formed by the wheels.

2.3.3 BONDING

The hard, abrasive grits in a grinding wheel are held together by a bond material. There are many different variations but most bonding materials are either organic, metallic or vitreous.

Organic (or resin bonds) are thermosetting resins and plasticisers (such as epoxy or polyurethane) which are mixed, formed and cured with the abrasive grits to form a grinding wheel. The wheels have a high elasticity and are more commonly used for high speed or variable loading operations because they are far better at withstanding shock loads and reducing chatter [1], [6]. Organic bonding is used with superabrasive grits for machining hard materials, such as carbides as demonstrated by Namba et al. [108] and Inasaki [109]. However, organic bonds have a limited shelf life and wear rapidly at high temperatures [6].

Metal bonds are the hardest bonding system and exclusively used with superabrasive materials. They can be either single or multi-layer. Multi-layer wheels are formed by sintering powder metals (typically bronze or stronger options of iron or nickel) with the superabrasive and these wheels hold form excellently. However, because of the high bond strength, forming and dressing these wheels is an expensive and complex process [6], [110]. Single-layer metal bonded wheels consist of individual superabrasive grits bonded onto a metallic layer (copper, tin, iron, chromium and nickel alloys) using either an electroplating, in which Nickel particles are deposited on the tool body using a charged bath, or brazing technique, whereby the superabrasive is coated in a slurry which melts and fuses together at under high temperature (Figure 2.14)[111]. It is usually the type of superabrasive that influences what technique is employed. As superabrasives are both hard and expensive, these bonding methods ensure that the grits are utilised fully without using too many of them (only the outer layer of the wheel is used) which assists in lowering costs. Dressing cannot be performed on these wheels though and their unit cost is high.
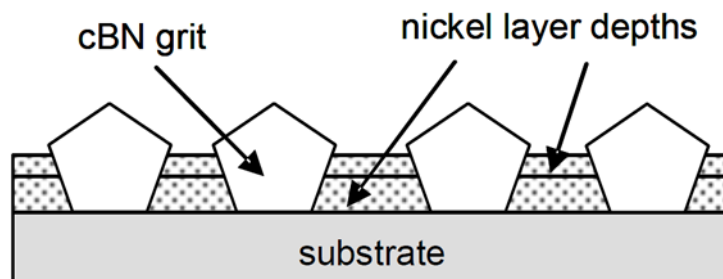
FIGURE 2.14 - DIAGRAM OF A SINGLE-LAYER METAL-BONDED WHEEL WITH ORIENTATED CBN GRITS HELD IN A NI BOND [15]. GRITS PROTRUDE APPROX. 50% ABOVE THE PLATED MATRIX.

Vitreous bonding is formed from feldspars, clays, glass frits (pre-ground glass with set oxide content) and mineral fluxes (silicon clay with low melting point) [15]. These minerals are then fired (or vitrified) at high temperatures causing glass melting and bonding all the abrasive grits together [1]. Different combinations and ratios of feldspars and glasses can be used in order to control the resulting wheel behaviour. Yang et al. [112] conducted 3-point bend tests on specially formed, rectangular samples of vitreous glass with CBN grits and demonstrated a variation in bending strength as the composition of glass oxide was varied. Similar results were seen by Kim et al. [113] also.

Vitreous bonded grinding wheels are advantageous as they are soft enough that they can be used for high material removal machining (like resinoid bonds) but also hard enough to achieve high levels of component accuracy and surface roughness [6]. Due to the friable nature of the vitreous bond, these wheels can be dressed to a form and also undergo a self-sharpening process during machining in which worn grits will be removed/fractured during grinding and replaced with a new sharp edge [1]. Vitrified wheels are also very porous which allows coolant to soak through the wheel and into the cutting area during grinding (Section 2.3.4).

The hardness of vitrified abrasive wheels is tightly controlled by the quantity of vitreous bond in the wheel [6] as the greater proportion of bond in the wheel forms more bridges between individual grits, giving the wheel increased hardness. This results in higher G-ratio as reported by Lin et al. [114]. The wear behaviour (Section 2.3.4) of wheels is also partially bond dependent as a soft bond will fracture more easily, releasing whole abrasive grits during grinding. Measurement of the elastic contact energy during single point dressing of grinding wheels of different hardness revealed that the elastic contact area depends on the hardness grade of the grinding wheel [115]. It has been shown that for higher hardness wheels, greater retention of the grits causes the formation of larger dull regions on the grain tips, resulting in higher grinding forces. It is also suggested that there are more active grits with the higher hardness wheel and that harder wheels reduced the elastic deflection of the grits [116]. Grinding experiments, wheel hardness tests and topography measurement by Herman and Krzos [117], on both a conventional vitreous bonded wheel and that with a fine crystallite phase addition in the bond, showed an increase in cutting points due to the high fracture toughness of the bond retaining abrasive grits.

These types of wheels (vitreous), with conventional abrasives, are widely used in the aerospace manufacturing industry and will be the focus of this thesis.

2.3.4   P="SMALLCAPS"OROSITY

In vitreous bonded wheels used for VIPER grinding, the porosity of the abrasive wheels are high. This is controlled by the proportion of the bond in the wheel with a dense grinding wheel containing a much higher proportion of bond than a low porosity wheel [6]. Not only this but pore-formers, such as hollow glass beads can also be used to control the level of porosity in a wheel. Porosity can greatly influence the behaviour of the wheel during grinding with higher porosity allowing greater volumes of coolant into the wheel, which is then directed into the cutting zone providing improved cooling [1], [6], [32]. Research by Engineer et al.[118] and Morgan et al. [119] has shown that increased porosity led to a higher fluid utilisation. However increased porosity means less support for the abrasive grits, hence the fracture force is reduced and the bond breaks down more easily [6] (mechanisms discussed in section 2.3.4). G-ratio is expected to increase for wheels with a higher weight percentage of bond content as noted by Jackson [96] and Chen et al. [120] who saw an increase of double when using higher porosity vitreous wheel for internally grinding Inconel 718 workpieces. Porosity of a vitrified wheel is not uniform from the outer surface to the centre [17] which can cause a difference in the grinding behaviour depending on the of different porosities. As grits protrude from the bond at the surface of the wheel (assisted by dressing), then the porosity is always less than in the bulk of the wheel.

2.3.5   WEAR MECHANISMS

It is well understood that during grinding the abrasive grits wear when in contact with the workpiece material. There are four mechanisms of wear that can occur on an abrasive wheel (Figure 2.15) which remove abrasive grain material and can alter the grinding behaviour.
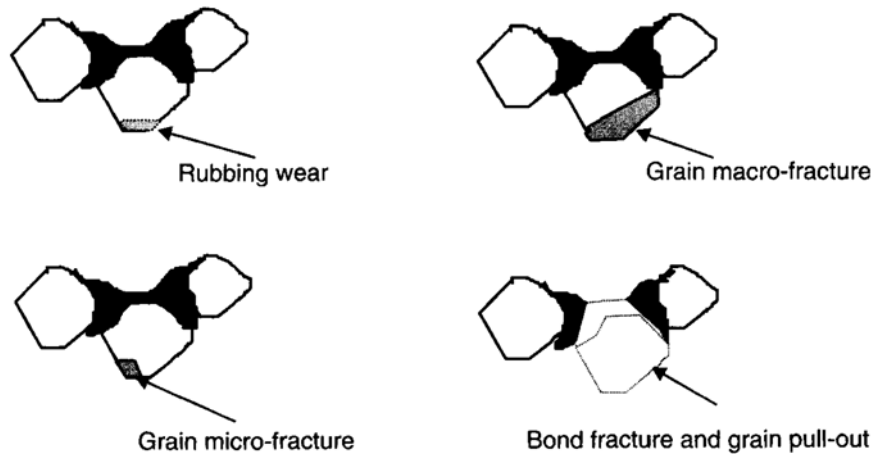
FIGURE 2.15 – THE FOUR WEAR MECHANISMS THAT OCCUR ON ABRASIVE GRITS [6].

Rubbing wear, also known as attritious wear, is generally caused on the grain by plastic flow of the workpiece and chemical reaction [121] which causes a dulling of the sharp cutting point. It often occurs when the stresses on the grain are low [6] and results in negative effects on the workpiece such as burn [102] and workpiece smearing. As shown by Malkin [122], attritious wear leads directly to the formation of wear flats on the active grits of the wheel with the wear flat area increasing linearly with grinding forces after a series of grinding cuts. Further work by Tso [123] supports this finding, by conducting similar trials, as well as suggesting that the loads on grits increase as they wear until the forces are sufficient to release a large grit volume. Chen et al. [124] factored attritious wear into an analytical model of grinding wheel wear which showed increasing influence as the total ground volume grew until macro-fracture could occur.

Macro-fracture wear on an abrasive is the cleaving of a substantial volume of individual grits [6]. This is a common feature in high stress conditions and is dependent on the crystal structure of the abrasive material [32]. Modelling of grit fracture by Jackson [125] indicated that this fracture is tensile and propagates from the maximum tensile stress at the rake face of the grit, generating a long crack. Brecker [97] performed roll crushing tests on individual abrasive grits to examine fracture behaviour and found it is also dependent on grit size with smaller grits containing less impurities and displaying a higher resistance to macrofracture.

Between macro-fracture and attritious wear is micro-fracture wear which involves very small volumes of the abrasive grit fracturing, generating new sharp cutting points whilst reducing macro wear of the wheel. This behaviour is dependent on the grain structure of the abrasive, as shown by Sunarto [126] who compared the wear response of CBN grain materials with poly and monocrystalline grain structures. The polycrystalline grains produced much smaller grit fractures than the monocrystalline alternative. Due to sintered abrasive grits typically containing a polycrystalline

structure, many wheels containing these engineered grits will see extensive microfracture on the wheel topography.

Finally, whole-grain pullout (bond fracture) is both beneficial and negative in grinding as it gives the wheel a self-sharpening ability, revealing new, sharp cutting points as the dull points are removed [127]. Typically when the bond strength of the wheel is reduced and grinding stresses are high, then increased bond fracturing occurs [6]. However, this can lead to significant loss in dimensional accuracy of the abrasive wheel as large volumes of abrasive are removed. Therefore by changing the hardness of the bond the dominant wear mechanism of the wheel can be transferred from attritious to whole grain pullout [121], [128]. Grinding tests on various steel grades by Badger [129] studied the sudden release of multiple abrasive grits (known as wheel 'collapse'). The author postulated that dulling (attritious wear) of the grits caused an increase in forces on the grits until the normal force was sufficient to initiate bond fracture. The paper highlights that this phenomenon can occur erratically.

All these mechanisms can occur on the abrasive wheel at once and influence how effective a grinding process is. In industry this can be economically defined as the G-ratio which is the ratio of volume of material removed from the workpiece (in mm³) to the volume removed from the abrasive wheel (in mm³) [130].

For vitrified abrasive wheels, both small micro-wear of the grits and whole grain pullout can occur. It is generally understood that under gentle grinding conditions, the wheel obeys the laws of attritious wear and there is the removal of very small amount of material from the individual abrasive grits, leading to grit dulling. As the grain penetration depth increases, then macro fracture mechanisms dominate as large abrasive particles are removed [6].

The volume of material removed from an abrasive wheel is often proportional to the normal grinding force and the hardness of the abrasive material. This is given as an equation developed by Archard (see Equation 2.7) [32].

$$V = K.\frac{F_n}{H}.L \qquad \textbf{EQUATION 2.7}$$

Wherein V is the volume of material removed from the asperities in adhesive wear, K is the adhesive wear coefficient, F_n is normal grinding force, H is hardness and L the sliding distance of the grit along the workpiece. This equation applies for slow, progressive wear of the abrasive under very gentle grinding conditions but it does not apply when fracture wear is present. As the equation shows, grinding wear is dependent on L as shown in Figure 2.16.

K : Wear constant

l_e : Contact length

N_s : Rotational wheelspeed

t : Contact time
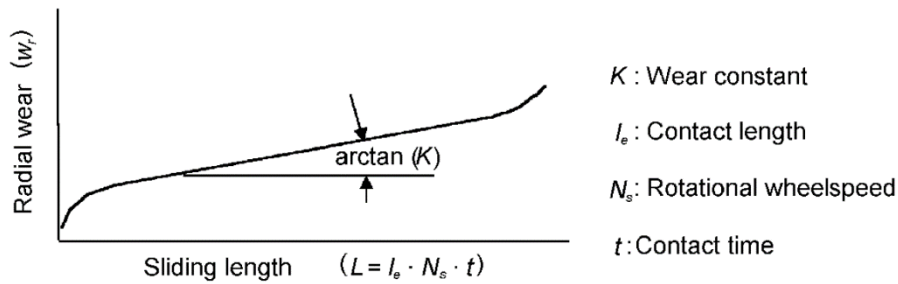
FIGURE 2.16 – RADIAL WEAR OF AN ABRASIVE TOOL IS DEPENDENT ON THE DISTANCE THE GRITS ARE IN CONTACT WITH THE WORKPIECE [32].

Kinematic analysis of single grit wear by Novoselov et al. [131] has led to the development of expressions to define dulling. These indicate that as cutting depth increases then the abrasive grits penetrate deeper into the cutting zone, increasing the path length and probability of grit contact with the workpiece. This causes more extensive wear at the top of the grit, creating a dull cutting point so future penetration becomes slower.

With the development of sintering and SG grain manufacturing processes, the abrasive grits can be formed to shapes (Figure 2.13) which can change the wear mechanism of the grit. Studies on the influence of grain morphology (shape) on grinding behaviour have been somewhat neglected. As mentioned earlier, Badger [102] conducted grinding trials comparing fused alumina, sintered alumina (Cubitron) and seeded-gel (Norton) abrasives grinding high speed tool steel and discussed three regimes of grinding wear (Figure 2.17). In regime I there is excessive grit dulling and high grinding energies, in regime II grit and bond fracture occurs and new sharp cutting points are revealed, and in regime III there is excessive bond fracture and the wheel readily breaks down. SG grits were revealed to be tougher than the fused alumina, therefore a higher grinding aggressiveness (a term that indicates chip thickness using factors under the direct control of the operator) must be used for these engineered grits in order to utilise the wheel in the favourable regime II. The work indicated that the SG Cubitron grits had a lower power and higher G-ratio throughout the grinding process due to smaller grit fracture (micro fracturing) compared to the fused grits. This supports work by Krueger et al. [132] who from cylindrical grinding of steel found that shaped Cubitron grits also have shown the smallest increase in surface roughness as material removal rate is increased compared to fused grit wheels. For both these papers however, there is limited analysis of the mechanisms of why this behaviour occurs and the impact of grit shape.
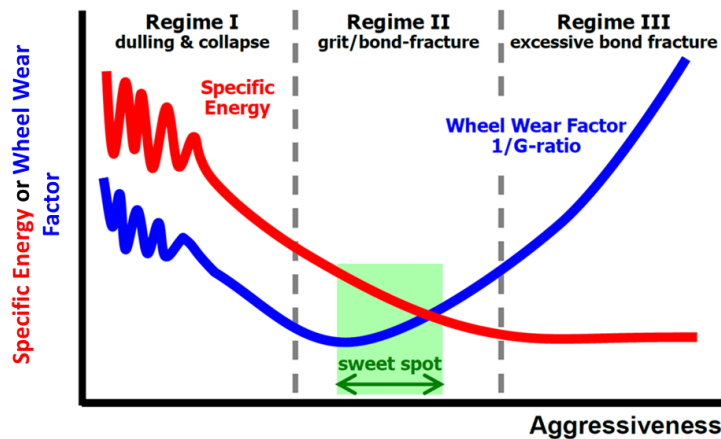
FIGURE 2.17 – THE THREE REGIMES OF GRINDING [102]**.**

Some grinding models have attempted to understand the influence of abrasive grit shape by including the rake angle of the contact point with the workpiece in the calculations. Cooper and Lavine [133] considered all the grits on the surface of a grinding wheel to be identically shaped as the frustum of a cone and varied the size of the wear flat on the cone tip (ratio of wear flat radius to abrasive grain radius). The model indicated that for sharper grits (0.1 % wear flat ratio compared to 1 %), the grinding zone sliding length is reduced. Ohbuchi [39], [134] created FEM models of the influence of rake angle on chip formation and found that negative rake angles influence the undeformed chip thickness and therefore grinding forces and mechanisms. The work did not discuss the level of impact of rake angle or different workpiece materials though. Single grit grinding tests with just diamond and CBN grits of different shapes on steel and alumina by Matsuo et al. [54] showed a significant difference in normal grinding force between the different grit shapes with a dull grit also producing a higher normal force than a sharp grit.   However a model developed by Liu et al. [135] comparing three different abrasive grain geometries argued that the dressing conditions primarily influenced the workpiece surface roughness over the abrasive grain shape.

2.4 DRESSING

2.4.1 TYPES/APPLICATIONS

Dressing is a vital stage in the grinding process. Primary objectives are to ensure certain wheel straightness (truing), to cut a certain form into the wheel, to generate a particular wheel structure (open or closed) and to remove workpiece material clogged in the wheel.

There are two primary methods of dressing an abrasive wheel:

- Point dressing
- Roller dressing

A.   **B.**
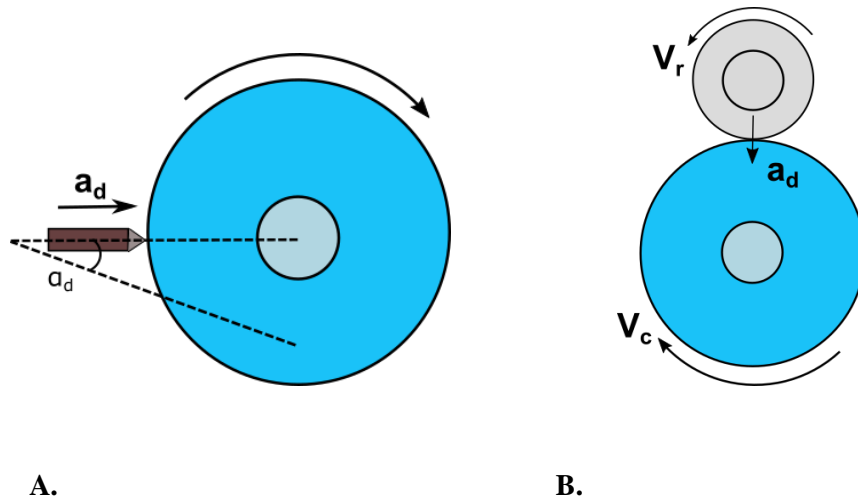
FIGURE 2.18 – (A) POINT DRESSING WHEREBY A_D IS INFEED RATE AND A_D IS DRAG ANGLE OF THE POINT RELATIVE TO THE WHEEL CIRCUMFERENCE (B) ROLLER DRESSING WHEREBY A_D IS INFEED RATE, V_R SURFACE SPEED OF THE DRESSER, V_C SURFACE SPEED OF THE ABRASIVE WHEEL.

Point dressing involves the use of a stationary tool, usually a single or multi-point diamond which is traversed across the face of a wheel in order to prepare the cutting surface (Figure 2.18A). As the grinding wheel is rotating the dressing tool cuts into the wheel at a predefined depth whilst moving axially across it at a distance per revolution known as the dressing lead [1].

Several papers have also attempted to model the impact of the single point dressing process on grinding wheel topography or workpiece surface roughness. A grinding power model by Chen et al. [68] showed that dressing lead and depth values have a strong consequence on grinding power and forces for early cuts, but all dressing conditions eventually converge to a steady state of attritious wear. Torrance and Badger [136] performed grinding trials to validate a dressing analytical model and highlighted that literature is contradictory regarding the effect of dressing lead on wheel sharpness. The data used did suggest however that a higher dressing depth did increase the number of active grits on the wheel surface although the focus of the paper is on model accuracy. A good summary of some of the other models created was compiled by Brinksmeier et al. [69] and Saad et al. [137], who has examined both point and roller dressing.

Single point dressing is a much simpler technique to understand and model, compared to roller dressing, as it only typically involves a single point of contact on the abrasive wheel. Although the

technique enables almost any form to be dressed into the abrasive wheel, wear can be a significant issue due to the low number of diamond grits. This can cause loss of dimensional accuracy in the ground workpiece as well as not generating an adequate wheel topography for the process [6]. Research, such as that by Pombo et al. [138], has been performed on the wear of these diamonds.

Roller dressing consists of a rotating diamond wheel which moves into contact with the abrasive wheel, removing abrasive grits and bond (Figure 2.18B). The rotating action means that not only must infeed rate be considered during dressing, but also the speed ratio (rotational speed between dresser and wheel) and rotational direction.
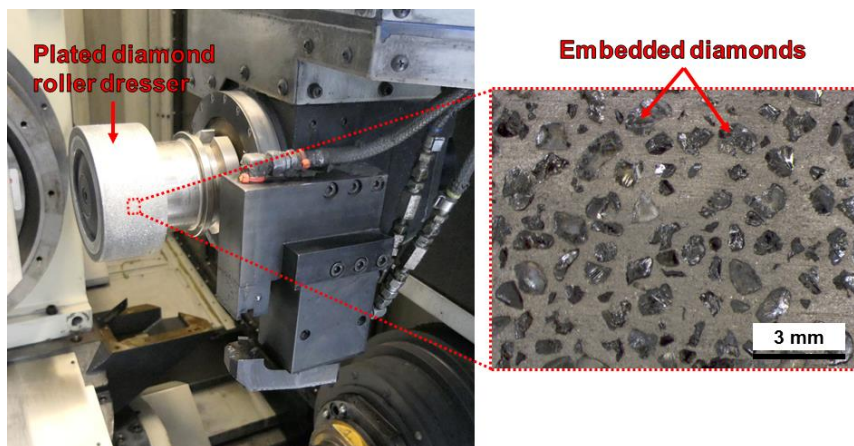
FIGURE 2.19 – MICROGRAPH OF DRESSER SURFACE WITH PLACED DIAMONDS IN AN ELECTROPLATED MATRIX.

Roller dressers (Figure 2.19), like electroplated wheels, consist of an asymmetric body with a single layer of diamond particles impregnated in a metal matrix or similar (typically nickel). This roller can also have a form which is generated on the abrasive wheel which enables the grinding of features onto the workpiece [1]. The main advantage of roller dressers is increased lifetime compared to single point [139] due to far more diamond points in contact with the wheel which distributes the loading so tip dulling is decreased. As this means the dressing run can complete much faster, roller dressers are greatly preferred in some industries, such as gas turbine engine production, as complex forms can be generated at reduced production times [2], [6]. As roller dressing is typically applied in the manufacture of turbine blades for gas turbine engines, this thesis focuses on this technique and its mechanisms.

Intermittent dressing is the most popular dressing method whereby the wheel is dressed occasionally (and separately) between grinding passes to generate a desired wheel topography and profile [32]. In this case it is often used to generate a rough topography on the wheel for large stock removal or to ensure dimensional form accuracy before finishing. Continuous dressing (CD) is an alternative dressing technique in which the abrasive wheel is continually dressed whilst grinding a

workpiece [140], [141]. This ensures the wheel form and sharpness is maintained and enables high productivity, which is very important when removing large volumes of material [2], [32], [142]. However CD can result in a rapid wheel volume consumption leading to higher consumables costs if not adequately implemented.

2.4.2 ROLLER DRESSING MECHANISMS

As discussed earlier there are three key parameters that must be considered when roller dressing which will influence wheel topography and grinding performance [1]:

- Infeed rate (a_d) – this is often referred to as a depth of feed of the dresser per revolution of the abrasive wheel.

- Speed ratio (q_d) – the ratio of the peripheral surface speed of the dresser (v_r) to the surface speed of the abrasive grinding wheel (v_c). Equation 2.8.

$$q_d = \frac{v_r}{v_c} \qquad \text{EQUATION 2.8}$$

- Dresser velocity – the direction that the dresser roll turns relative to the abrasive wheel. This can be either positive or negative and is known as synchronous or asynchronous respectively (Figure 2.20).

A.   **B.**
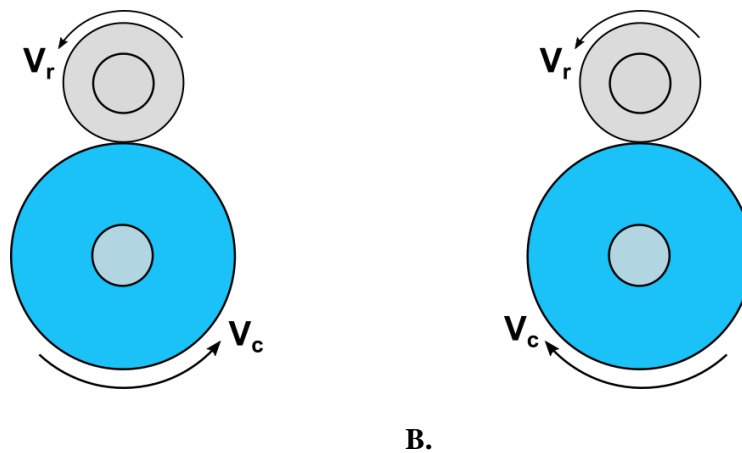
FIGURE 2.20 – THE DIFFERENT DRESSING VELOCITIES DURING DRESSING (A) ASYNCHRONOUS (B) SYNCHRONOUS.

As discussed earlier, single point dressing is relatively well covered [68], [69], [136], [143], [144]. However there is less focus on the mechanisms involved in roller dressing owing to the process complexity. It is known that when the dresser ratio equals +1 (i.e. the dresser and grinding wheel surface speeds are at unity) then crush dressing occurs as this is the only mechanism that will cause

fracturing (and therefore dressing) of the abrasive wheel as the surfaces of the wheel and dresser are moving at the same speed relative to each other [43]. This also results in high normal forces on the wheel and dresser [6]. These high forces can cause extensive fracture which can 'open' a wheel surface creating sharp cutting peaks (Figure 2.21). However they can also create concentricity deviations (run-out) on the wheel as well as extensive diamond wear on the dresser [32].
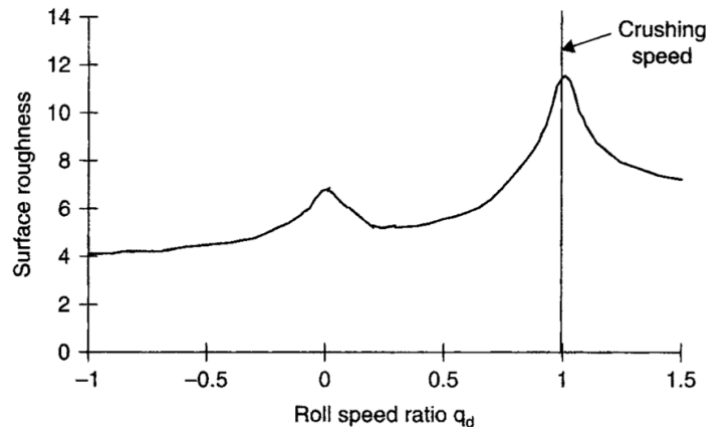
FIGURE 2.21 – THE MOST AGGRESSIVE ABRASIVE WHEEL TOPOGRAPHY IS GENERATED UNDER CRUSH DRESSING WHEN THE SPEED RATIO IS AT UNITY [6].

It is generally understood that the particles dressed off the wheel are much bigger than the dressing infeed, but smaller than the original whole grits [121]. Therefore the abrasive wheel material must be removed by brittle fracture when colliding with the dresser diamonds through a number of mechanisms such as grit fracture and bond fracture (Figure 2.22) [1]. Therefore the bond hardness of the wheel can greatly influence its dressing behaviour with harder or denser wheels typically generating a much finer wheel topography compared to softer wheels [1][145].
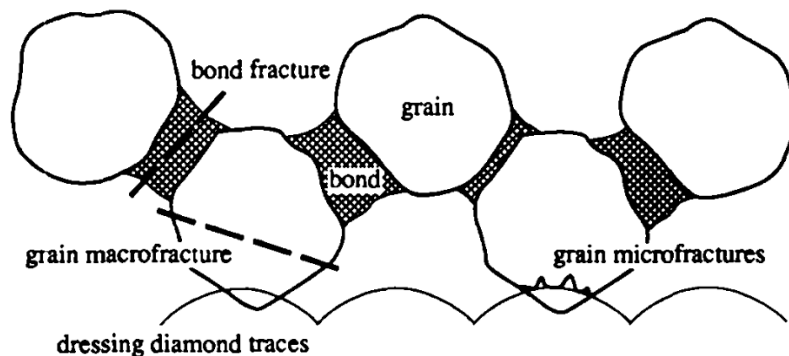
FIGURE 2.22 – THE FRACTURE MECHANISMS THAT OCCUR ON A VITRIFIED ABRASIVE WHEEL DURING DRESSING [146].

A critical concept in roller dressing is the interference angle (δ) which defines the angle of the trochoidal path of the diamond relative to the surface of the abrasive wheel [147] and can be calculated as according to Equation 2.9.

$$\delta = tan^{-1}\frac{a_d}{|v_w - v_r|}$$

EQUATION 2.9

Whereby a_d is the infeed velocity of the rotary dresser, v_w is the surface speed of the wheel and v_r is the surface speed of the dresser. This angle determines the angle of approach of the dresser diamonds onto the abrasive wheel and so the steeper this angle then the more aggressive the dressing conditions (Figure 2.23).

A.   **B.**
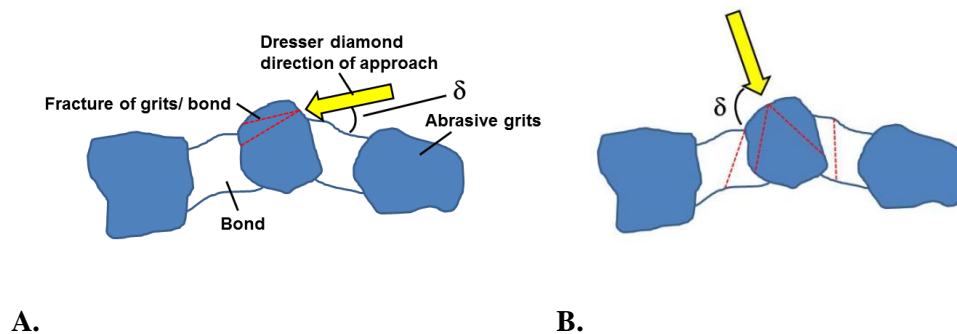
FIGURE 2.23 – (A) SHALLOW ANGLE OF APPROACH FOR LOW INTERFERENCE ANGLE (B) STEEP ANGLE OF APPROACH WITH HIGH INTERFERENCE ANGLE.

Typically in fine dressing, less aggressive dressing parameters are employed (reduced infeed and speed ratio) which reduces the sharpness of the abrasive grits and 'closes' the wheel surface. This reduces the surface roughness of the ground workpiece and also often causes an initial drop in grinding power as some dressed grits fracture and pull-out [6]. For aggressive dressing then macro-fracture and bond fracture is higher and the abrasive wheel grits are often damaged which increases their susceptibility to cracking during grinding. This reduces the power of the grinding process as when they are in contact with the workpiece material, they fracture revealing new cutting points [6]. However grits will eventually blunt, reducing the efficiency of the grind and increasing the power consumption of the process.

Dresser wear can influence grinding performance as the diamond grits will begin to wear immediately from use. A worn dresser can cause various issues (such as vibration, loss of form and blunting of the abrasive wheel) as the fracturing mechanism of the abrasive wheel grits is diminished [6]. Dresser wear comprises a three stage process (Figure 2.24) in which there is high initial wear from first use (stage I), steady wear (stage II) whereby the dresser behaves as expected and the degree of wear is small and linear. The final stage is end-of-tool life (stage III) in which there is rapid wear

and failure of the tool [32]. To the best knowledge of the author, research into roller dresser wear is limited.
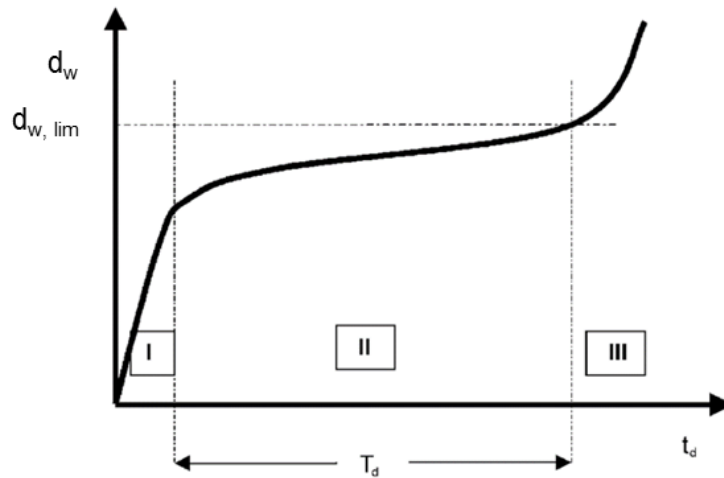
FIGURE 2.24 – DRESSER WEAR AS A FUNCTION OF TIME WITH THE THREE STAGES OF DRESSER WEAR HIGHLIGHTED WHEREBY T_D IS THE DRESSER TOOL LIFE AND d_W IS THE LEVEL OF WEAR (SPOT DIAMETER) [32].

2.4.3 INFLUENCE OF DRESSING PARAMETERS

Malkin and Murray [147] were one of the first to focus on the roller dressing of aluminium oxide grinding wheels. Their results showed that for a range of dressers (with different diamond set patterns) an increased infeed caused a decrease in specific dressing energy. SEM images indicated flat regions on the alumina abrasive grits when dressed at low interference angles. A peak in dressing forces was seen when the dresser surface speed was the same as the wheel (ratio of 1). Follow up research [148] showed that the interference angle is a controlling factor in dressing/grinding performance with low angles causing more deformation of the abrasive grits compared to fracture (at high angles). There appeared a negative linear response in the grinding forces as the interference angle increased although the explanation of this response is limited. Surface roughness increased linearly with interference angle. The same response was also seen by Saad et al. [137].

The length of trajectory of dresser diamond grits on the working surface of the grinding wheel is closely related to the interference angle and describes the approach of the diamond onto the abrasive wheel. Simulations have demonstrated that trajectory length increases with increased dressing depth and contact length of dressing grits (Figure 2.25). The length is reduced in down (synchronous) dressing compared to up (asynchronous) dressing [149] meaning a steep approach of the dresser diamond generating a rough workpiece surface [6].
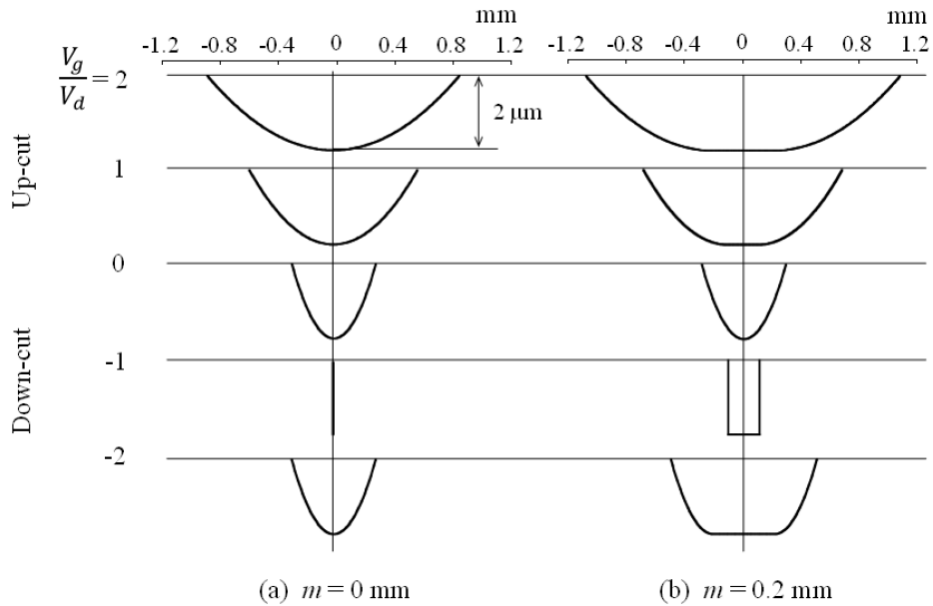
FIGURE 2.25 – DIAGRAMS OF THE DIFFERING TRAJECTORY OF THE DRESSER DIAMONDS FOR UP AND DOWN DRESSING. V_g IS THE PERIPHERAL SPEED OF THE GRINDING WHEEL, V_d IS THE PERIPHERAL SPEED OF THE ROLLER DRESSER AND m IS THE LENGTH OF DIAMOND GRITS ON THE DRESSER [149].

Many models have been created in order to better understand and predict the dressing behaviour of vitrified grinding wheels. These have indicated that the diamond pattern on does not dominate the profile of the wheel surface [150]. Modelling the influence of dressing parameters has also indicated that speed ratio is more influential on specific energy during grinding than depth of dressing. This is because at high speed ratios there is increased grit fracture and a rougher wheel surface generated [151]. Using a neural network and simulated annealing algorithm, validated with an alumina wheel under different dress depths and speed ratios, Baseri [144] demonstrated a reduction in tangential grinding force at high dress depths and speed ratio. The workpiece surface roughness showed an almost positive linear response to increasing speed ratio (Figure 2.26).
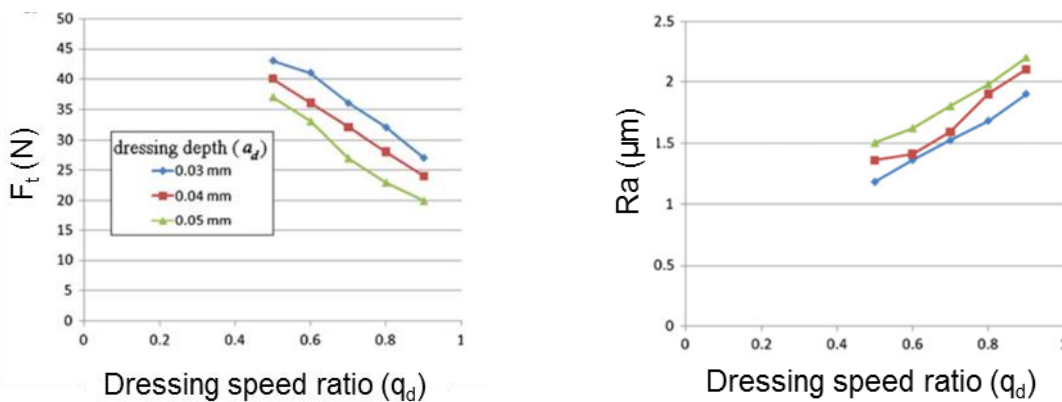
A.   **B.**
FIGURE 2.26 – VALIDATION DATA FOR BASERI'S DRESSING MODEL SHOWING THE INFLUENCE OF SPEED RATIO AND DRESSING DEPTH ON (A) TANGENTIAL FORCE AND (B) SURFACE ROUGHNESS [144].

Models using chip mechanics in dressing, or considering the process as a tribological system, have improved the understanding of roller dressing. Dressing has been shown to alter the cutting edge density on the topography of a grinding wheel [68]. A particular dressing model developed by Linke [152] suggested that high normal forces causes shattering of the grinding layer and increased wheel wear due to grits breaking off the surface. Further work also indicated that previous dressing strokes can weaken the abrasive wheel bond and result in high wheel wear directly after dressing. This is even after a 'finishing' dressing stroke [153]. This matches behaviour seen by Chen [154] who saw a power reduction initially in grinding due to damaged grits from coarse dressing being susceptible to fracture.

Linke's dressing model [152] has been developed further by Klocke et al [155], to predict the influence of dressing on the wear of the grinding wheel during operation, a largely neglected research area. Dressing load was seen to be directly related to the mean dressing chip cross-section and the smaller the chip then the less force in dressing. Reduced dressing forces lead to less damage to the grinding wheel structure and so less grain breakout during grinding. At low dressing chip sizes (chip cross sectional area <3000 μm^2, q_d 0.6 and depth of dress 10μm) then the wear response is parabolic, but beyond the threshold chip size then the relationship is linear (Figure 2.27). Dressing greatly influences the initial wear of a grinding wheel. However, once steady-state grinding (in which the wheel self-sharpens) is reached then the impact of dressing is minimal. Warkentin et al. [156] saw a similar response with low initial power until a steady-state grinding power was achieved after a number of grinding passes.
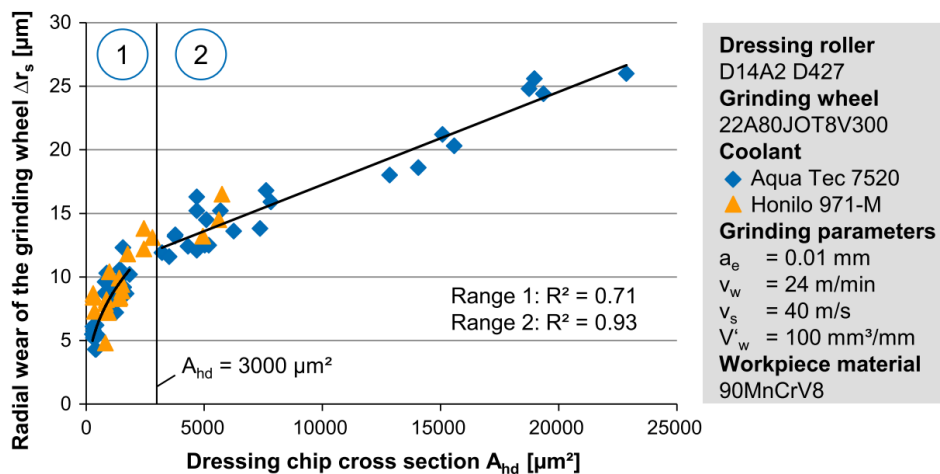
FIGURE 2.27 - EFFECT OF DRESSING CHIP SIZE ON RADIAL WHEEL WEAR [155]**.**

The number of fully experimental studies on the dressing of vitrified abrasive wheels, in the literature, is not as extensive. Azizi et al. [90] performed rotary cup dressing (dressing disc perpendicular to grinding wheel) on vitrified CBN wheels and ground Inconel 738 material. The topography measurement showed that an increase in the number of cutting points reduced the

grinding energy, an observation that is contrary to general understanding of the process. It was concluded though that the shape of the abrasive grits is more important than the number of active cutting points. Liu et al. [135] studied the influence of grit shape on dressing response and modelled single point dressing for different defined grit shapes (sphere, cone and truncated cone). Dressing parameters (tip geometry, dress depth of cut and overlap ratio) were predicted as the primary influencers on workpiece surface roughness over grit shape. Without dressing significant differences between the wheels were visible. However all the experimental validation for the model was performed on a single alumina wheel with conventional grit shape. Therefore dressing parameters will inevitably appear more influential.

Prusak et al. [157] measured grinding and dressing forces, over a wide range of dressing parameters, for vitrified CBN and seeded gel wheels in order to avoid the typical break-in period (wheel acts dull immediately after dressing) in superabrasive wheels. The work identified optimum dressing parameters. It also indicated that more aggressive dressing conditions did not generate a significantly sharper wheel and lead to a decreased useful wheel life (defined as loss of wheel profile, measured using a soft replica coupon which was ground). Guo et al. [140], [141] performed continuous dressing whilst grinding with an abrasive wheel with the aim of reducing the process cycle time for forming turbine blades for gas turbine engines. Models were constructed based upon grinding principles of sliding, ploughing and cutting and clearly showed the significance of dressing infeed reducing the grinding power. This led to a 40% reduction in the process cycle time.

Although the investigation of roller dressing on vitrified grinding wheels is extensive, the literature is very limited on the impact of engineered grit shapes on dressing and grinding performance for superalloy workpieces. This thesis focuses on the comparison between conventional and engineered grit morphologies and how their dressed abrasive wheel topographies behave in grinding.

2.5 GRINDING WHEEL TOPOGRAPHY ASSESSMENT

To better understand the grinding and dressing response of the different grit morphologies the topography of the wheel must be captured. It is widely known that the topography of a grinding wheel directly influences its grinding response as it is the region in contact with the workpiece. There are a number of techniques used in literature which are discussed in this Section.

2.5.1 CONTACT METHODS

The most common method for studying grinding wheel surfaces is a profilometry technique in which a stylus is dragged over the surface in a similar way to roughness measurement [1]. Blunt and Ebdon [4] were the first to examine the use of 3D profilometry for wheel measurement and they used a Somicronic Surfascan with a 2 µm stylus on the wheel directly. The wheel was analysed in terms of cutting edge density (the number of peaks per square area of wheel surface) and defined a peak as a point in the data array higher than its eight nearest neighbours. Although a successful method that aligned with other research, a highlighted drawback was that two peaks close together would be counted separately but in reality, when grinding, they will more likely behave as one. Also the technique resolution is limited by the size of the stylus.

Nguyen and Butler [158] and Butler et al. [159] conducted extensive work on stylus methods for wheel topography analysis. A Talyscan 150 stylus system was used to test the grinding performance of a SiC grinding wheel on IN718 by measuring the topography of the wheel in two locations and averaging. The focus of the work [158] was the parameters used to define the wheel, namely the root-mean-square roughness (Sq) to quantify wheel coarseness and density of summits (Sds) and summit curvature (Ssc) to give cutting point density and sharpness. It was shown that 3D surface scans are an effective method of measuring wheel topography (Figure 2.28).
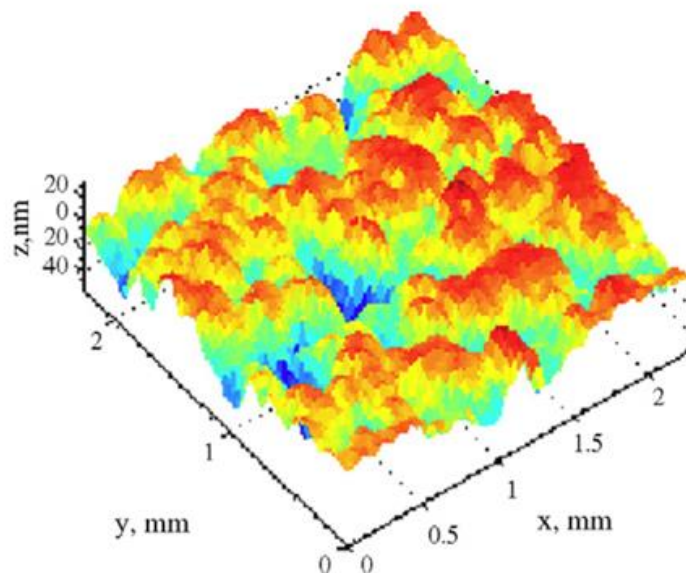
FIGURE 2.28 - AN EXAMPLE OF THE TOPOGRAPHICAL MAP GENERATED FROM A 3D STYLUS SCAN [158]**.**

Salisbury et al. [160] used a similar profile method to validate a wheel topography model as a result of grinding and found good agreement between the stylus and the model for a small section of

the wheel. Koziarski and Golabczak [161] used a 2D profilometry technique to scan across the surface of the wheel to capture the number of active and static edges on the grits. This experiment was performed to assess the influence of single point dressing on wheel cutting edge topography. Stylus transducers measured the level of glazing (dulling of the grits) and gross breakdown (whole grain pull out) on vitrified alumina wheels under different dressing conditions by Baul, Graham and Scott [162]. The probability density functions generated by the transducers were able to detect a noticeable difference between the fine and coarse dressing conditions.

Maximum grain protrusion height (h_{max}) is another parameter measured using a 3D stylus technique, on vitreous bonded wheels, which was applied to a model by Zhou and Xi [163] to predict workpiece surface roughness. This was a useful parameter as it captures the random grain protrusion height that occurs in vitreous bonded wheels. A contact stylus method was employed by Brinksmeier and Glwerzew [164] to measure the average spacing between the grits on an abrasive wheel. This was ultimately used in a wheel topography model to better understand the chip formation process at low cutting speeds.

Cai and Rowe [165] conducted a study comparing different topography measurement techniques for CBN wheels (stylus, interferometry and laser triangulation). This showed that stylus methods were not recommended for very hard grits due to the high level of wear on the stylus tip. This is an issue as the size and shape of the tip can greatly influence the final measurement [128]. A profilometry technique however did prove to be effective at revealing wear flats on the grits.

Overall, profilometry is a favoured technique because it measures the wheel directly to get a clear profile of the wheel. However resolution of the measurement is limited by the size of the stylus and careful selection of the sample spacing must be made in order not to miss any peaks on the surface. Also the penetration depth of the stylus is restricted and often penetrates less than the operating depth of the wheel [1].

2.5.2 IMPRINT METHODS

An imprint technique involves creating a replica or copy of the surface of the wheel. This is usually achieved by rolling or pressing the wheel into a secondary material. The first imprint technique developed was by Backer et al. [46] by covering a glass plate in soot and rolling an abrasive grinding wheel across it to determine the number of active grits. As the grits contacted the glass they removed the soot, enabling a count of the active grits on the wheel [45].

Cai and Rowe [165], [166] conducted a thorough investigation into different wheel analysis techniques for CBN comparing both stylus and replica methods. Both soft lead and silicon-based impression materials were trialled and rejected. Ultimately, Microset 101 synthetic rubber compound was the most successful when analysed with an optical interferometer. An example of a synthetic imprint material is shown in Figure 3.14. Analysing these replicas with SEM and stylus however were unsuccessful due to high temperatures causing melting under the electron beam and the softness of the replica causing issues with the stylus.

Plastic, tapered roller methods have also been investigated whereby a carbon paper is inserted between the wheel and the roller in order to generate the high point imprints [1]. Hecker et al. [73] used a polished metallic sample (lead, due to its softness and ability to be viewed under an optical microscope) to press into the surface of vitrified seeded gel/alumina wheels. A white light optical interferometer was then used to measure the imprinted lead for cutting edge density. Baseri [167] used a gel-type material into which an abrasive wheel was pressed. After addition of the hardener the sample was sectioned and a profile of the wheel gained from a high resolution scanner. The resulting data was applied in a neural network model to predict grinding wheel sharpness from different disc dressing parameters.

The advantage of imprint techniques is their flexibility to take a snapshot of the wheel when wheel removal or direct measurement is difficult. With high resolution replication materials available, a highly representative replica of the wheel surface can be gathered with much better resolution than a stylus technique.

The drawbacks of this method however are how to analyse the replica as they must be rigid if to be measured by a profilometer and temperature resistant if analysed under an SEM. Not only this but any shrinkage issues must be considered during replica setting or elasticity of the material if a hard replica is used.

2.5.3 MICROSCOPY METHODS

Microscopy technique involves using either an optical or electron microscope to measure the wheel surface. For optical techniques the incidence of light is critical as this impacts the angle of reflection from the grits. If the light is applied normal to the wheel surface then flat regions of the grits will be much brighter than others [1]. This can then be used to give information about wear and fracture of the abrasive grits using various image analysis software [168]. A good example is provided by Hwang et al. [81] who used optical microscopy to directly observe grit wear flats on electroplated diamond wheels.

Inasaki [169] applied an optical profilometry technique in order to capture the topography of a grinding wheel. The method measured the height of the surface of the wheel using an auto-focus system which varied the height of the optical lens. This movement corresponded to the height on the wheel. These measurements determined the cutting edge distribution which was used to model the output workpiece topography after grinding. Woodin et al. [170] used a similar technique, employing an Alicona variable height microscope to capture the topography of an abrasive wheel (Figure 2.29). A vitrified, seeded-gel alumina grinding wheel was single-point dressed under different conditions and the peak height and skew of the height distribution investigated. Due to the type of Alicona system available to the authors, the entire wheel was able to be placed under the microscope for direct measurement.

A.   **B.**
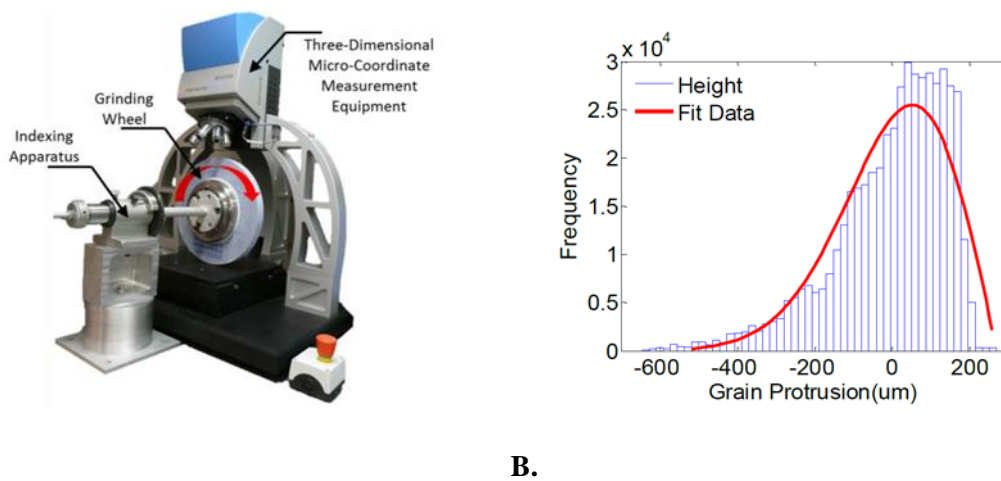
FIGURE 2.29 - (A) DIRECT GRINDING WHEEL MEASUREMENT UNDER ALICONA VARIABLE HEIGHT MICROSCOPE (B) MEASURED DISTRIBUTION OF TOPOGRAPHY HEIGHTS [170]**.**

A similar set up was used by Yan et al. [171] to measure topography on alumina wheels of #60 and #120 grit size. The authors used a white light interferometer to directly measure sections of the vitreous bonded wheels and measured the 'Birmingham set' of 3D surface parameters [172] including root mean square roughness (S_q), summit density (S_{ds}) and average principle curvatures of the summits (S_{sc}). A Fourier filter was applied to remove high frequency noise and the paper focused on finding the optimum sampling interval for the technique. It did require sacrificial samples of the abrasive wheels to take measurements however.

Other direct optical methods include that used by Arunachalam and Ramamoorthy [173] who applied a charge couple device (CCD) camera to capture images of the wheel condition during grinding. An alumina wheel was measured when grinding mild steel and images taken of the wheel at regular time intervals during operation (30, 60 and 90 minutes). The Grey level co-occurrence matrix (GLCM) statistical approach was applied to the gathered images, measuring the grey level of the

pixels and its frequency of occurrences. The purpose of this paper was to determine which parameters using this technique recorded a change in the texture of the grinding wheel as a function of time.

Brinksmeier and Werner [3] developed a laser triangulation method which applies a laser beam perpendicular to the wheel surface. A second lens then collects the scattered light and focuses it on a position sensitive detector. If the distance of focus changes then the detector position also changes. The technique was able to measure both macroscopic properties of the wheel (waviness) and microscopic (grain breakage and wear flats). However it found that there was little correlation between the measured wheel topography and workpiece surface quality.

There are issues with optical microscopy methods as they are often dependent on an accurate incident angle of light onto the grinding wheel, therefore ensuring this is correct can cause issues. Not only this but it can only capture a small region of the wheel at once, therefore several images of the wheel should be taken to be representative of the wheel topography.

Not only optical but scanning electron microscopy (SEM) is also a valid technique for examining abrasive grain morphology. The high resolution and depth of field enables the capturing of high quality images. However wheel structure greatly impacts the ease with which this technique can be conducted. For example, Nguyen and Butler [158] used the method to study the topography of the diamond conditioning pads used in a grinding system. For this case the diamond grits were placed in a single layer of electroplated metal, therefore making the system conductive and easy to achieve a vacuum.

Due to the high porosity and non-conductive nature of ceramic vitrified wheels, achieving a vacuum is extremely difficult. The wheel section also has to be coated with a conductive coating to obtain an image but again porosity reduces the effectiveness of this process meaning not all of the wheel coats. Using an SEM is also a sacrificial method as the wheel must be sectioned to create a small enough piece to fit in the chamber of the microscope [166]. This makes the process expensive, especially if a wide number of test conditions are investigated. Coated replicas of the wheel surface have been placed in the SEM although sample melting becomes an issue [165].

2.5.4 OTHER TECHNIQUES

Other techniques for studying wheel topography include scratch methods which isolate single scratches on the workpiece rather than the ground surface as a whole with multiple scratches. To achieve this the workpiece is moved quickly along a slowly rotating grinding wheel. The separate

scratches can then be analysed to give a good indication as to the cross-sectional shape of the grits and their cutting motion [1].

In-process methods have also been developed using dynamometers to give an indication as to the topography of the wheel. Azizi [90] used a dynamometer to measure the dressing forces as a function of speed ratio and found a relationship between overlap factor of the rotary cup and the forces generated. The problem with this method however is in most roller dressing situations, forces cannot be measured during the dressing stage and so dyno techniques can only indicate wheel topography when the abrasive wheel is cutting a workpiece.

Table 2.2 shows a summary of some of the different topography measurement techniques used in literature for measuring abrasive consumables.

TABLE 2.2 – SUMMARY OF SOME OF THE DIFFERENT GRINDING WHEEL TOPOGRAPHY MEASUREMENT TECHNIQUES IN LITERATURE.

Author	Title	Technique Type	Method	Technical Details
Altintas & Gungor [174]	Alternative Surface Roughness Measurement Technique for Inaccessible Surfaces of Jet Engine Parts Using the Rubber Silicon Replica Method	Replica	Repliset T3 - For measuring inaccessbile regions of Jet engine parts and analysed using white light optical microscope.	Used Fowler roughness comparators to validate technique measuring the distance between the peaks as well as Ra. Replica of the actual parts were performed on 10mm sq area and measured with a light microscopy tool.
Aspinwall, Soo, Curtis & Mantle [22]	Profiled superabrasive grinding wheels for the machining of a nickel based superalloy	Replica/Stylus	Graphite replica cut to measure tool wear. 3D stylus profilometry were used to record grinding tool roughness.	Profiled superabrasive grinding wheels used to machine firtree root forms on Ni-base superalloy. Graphite replica was 3mm thick and used to capture wheel wear.
Azizi, Rezaei & Rahimi [90]	Study on the rotary cup dressing of CBN grinding wheel and the grinding performance	Replica/Stylus	Replica taken of the grindign wheel surface and measured using Talysurf CCI stylus instrument.	Studying the influence of rotary cup dressing on the topography of a grinding wheel using the replicant material to measure the density of active grits and the gradient of their slope.
Backer, Marshall & Shaw [46]	The Size Effect in Metal Cutting	Soot-Track method	Soot on glass - Developed to provide a value for number of cutting points per area.	Used to calculate undeformed chip thickness.
Baseri [167]	Modeling of grinding wheel sharpness by using neural network	Replica	Vitrified alumina wheel imprinted into gel-type material with hardener.	Hardened gel replicant measured under a high resolution scanner to record profile and skewness. Data used to feed a neural network to determine whether skewness acceptable term to define wheel sharpness.
Bhaduri, Soo, Novovic et al. [175]	Ultrasonic Creep feed Grinding of Inconel 718	Replica	Microset - Used to measure impact of ultrasonic grinding on topography of the wheel.	Graphite block used to get average, negative profile of the wheel. Microset utilised to get a positive replica grinding wheel and was measured using a form Talysurf Measure density of cutting points Sds. Examined under SEM. Sa value measured on Graphite blocks
Blunt & Ebdon [4]	The Application of Three-Dimensional Surface Measurement Techniques to Characterizing Grinding Wheel Topography	Stylus	Somicronic 3D stylus - 2 different grinding wheels dressed and the topographies compared.	2um stylus tip, 1um increments used to measure the shape of the cutting edges. Measuring Sds and Sa as well as no. active grits above a certain height.

Author	Title	Technique Type	Method	Technical Details
Brinksmeier & Werner [3]	Monitoring of Grinding Wheel Wear	Triangulation Sensor	Laser triangulation sensor - Used to monitor cutting capacity of grinding wheels	Developed internally
Butler & Blunt [159]	The characterisation of grinding wheels using 3D surface measurement techniques	Stylus	Somicronic 3D stylus - Further development of 3D profilometry technique on grinding wheels.	Studied density of summits and summit curvature as well as rms roughness (Sq). Performed over 2.4mm sq area on grinding wheel.
Cai & Rowe [165]	Assessment of vitrified CBN wheels for precision grinding	Replica	Microset 101 - Testing different CBN wheels wwith varying porosity on different materials (internal grinding). Microset proved to be the best replicant material. 4 parameters were measured, active cutting edge density, cutting edge dullness, effective porosity volume, wheel scratch hardness.	Resolution 0.1um, cartridge dispensal. Didn't work with SEM or stylus analysis but no problems under optical interferometry. Found did not penetrate the full depth of the pores. Rt surface roughness of the replica 60-90% of the wheel roughness. Error estimated <20% fine-grain wheels.
Cai & Rowe [165]	Assessment of vitrified CBN wheels for precision grinding	Stylus	Talysurf 3D - Paper comparing different analysis techniques for CBN wheels	Vertical range and resolution limiting factors. Must account for curvature of the wheel. Good technique as can scan over a large area and measuring wheel directly.
Darafon [176]	Measuring and Modelling of Grinding Wheel topography - PhD Thesis	White-light axial chromatic scanning	Nanovea CHR150 white light chromatic sensor with 1200um optical pen - part of validation of grinding models to simulate surface topography change.	Wheel horizontally mounted on system with Zaber actuator to control the axial movement of the sensor. Custom built rotary stage constructed with rubber contact wheel to rotate the grinding wheel. Used hole-filling method on Nanovea software.
Herman & Krzos [117]	Influence of vitrified bond structure on radial wear of CBN grinding wheels	Stylus	Hommel-Tester 8000 Profilometer - Comparing different bonds on the wear of super hard CBN wheels	Single pass scan to give 4.8mm x 2.5mm size 3D scans.
Inasaki [169]	Grinding Process Simulation Based on the Wheel Topography Measurement	Optical	3D optical measurement of the wheel directly on CBN wheels.	CBN wheels have reduced wear so easier to predict wheel topography and so resulting workpiece surface and grindign forces.
Klocke, Thiermann & Mattfield [155]	Influence of the dressing process on grinding wheel wear	Replica	Replicant applied to the wheel to measure wheel wear.	Validation experiment of analytical-emprical model to assess the impact of dressing parameters on the grinding wheel wear.

Author	Title	Technique Type	Method	Technical Details
Nguyen & Butler [158]	Correlation of grinding wheel topography and grinding performance: A study from a viewpoint of three-dimensional surface characterisation	Stylus	Talyscan 150 - varied truing operations to examine its impact on grinding wheel topography. Discusses sample spacing and features to measure (Sds, curvature and Sa).	Sampling interval for grinding wheel was 15um and over a 3mmx3mm area. Trials conducted on Inconel 718.
Nilsson & Ohlsson [177]	Accuracy of replica materials when measuring engineering surfaces	Replica	Araldite SV40, Microset 101F and Technovit 3040 - Replica performance tested on a range of engineering surfaces (crankshaft, steel plate etc.).	Araldite - Cast material with cure time of several hours. Microset - known, Technovit - cold curing resin methylmethcrylate for roughness replication on fine surfaces. Cure time 15mins. Paper examines various S parameters (Sa, Sv etc.). All had error <10%.
Oliveira,Coelho & Neto [178]	Development of an Optical Scanner To Study Wear on the Working Surface of Grinding Wheels	Optical	Optical scanner records reflected light off flat regions on the abrasive grits to determine grit dulling.	Reflected light passes through 0.4mm receptor tube to identify flat regions tangential to the wheel surface.
Prusak, Webster & Marinescu [157]	Influence of Dressing Parameters on Grinding Performance of CBN / Seeded Gel Hybrid Wheels in Cylindrical Grinding	Coupon	Thin, hardened steel coupon ground to capture wheel wear.	Study on trueing and dressing of CBN grinding wheels using thin steel coupons to measure the wear of abrasive grits. Captured 2D image of the wheel surface.
St Gelais [168]	Investigation into the Characterisation and Generation of Grinding Wheel Sharpness in Diamond Roll Plunge Dressing	Replica	polyvinylsiloxane dental ISO 4823 type 1 - Create replicas of grinding wheel to see how sharpness changes with diamond rolls dressing.	Pneumatic cylinder used to apply putty onto wheel with force of 10 psi. Replicas measured used laser scanning microscope with replicas taken at 4 locations on each wheel. 5mm x 5mm size scan. Also measured wear flats using Matlab imTool (imaging tool)
Sunarto [126]	Creep feed profile grinding of Ni-based superalloys with ultrafine-polycrystalline CBN abrasive grits	Replica/SEM	Acetyl-cellulose film used to take a replica of the wheel and observed under an SEM.	Measuring wear behaviour on CBN grits after grinding Nimonic 80A Ni-base superalloy.
Young & Chen [179]	Online dressing of profile grinding wheels	Optical	Non-contact optical measurement system to record wheel form after dressing.	Optical measurement system used to measure the profile of the grinding wheel and capture deviation from the designed wheel form.

2.5.5 IMPACT OF WHEEL TOPOGRAPHY ON GRINDING BEHAVIOUR

The topography of a wheel can be described as the shape and sharpness of the abrasive grinding surface and a number of parameters are employed in order to quantify it.

Active grit count (abrasive grits involved in cutting workpiece material) has been used in literature to describe wheel topography and has been shown to be greatly influenced by the abrasive wheel type. The number of active grits has been seen to increase with a higher depth of cut in grinding due to a greater contact length [106]. This means the chip size per grit is smaller and therefore more energy (and grinding power) is required to achieve the same total volume of material removal as with a larger chip [68]. Hecker et al. [73] noted the dependence of active grit density on chip thickness when measuring the topography of two alumina grinding wheels. As expected, the grit density was also higher for a fine grit wheel than a coarser wheel, an effect also seen in 3D topography measurements by Blunt and Ebdon [4]. Azizi et al. [90] measured a decrease in the active grit density at fine dressing conditions. This contradicts the opposite behaviour seen by Rowe and Chen [53], Buttery et al. [128] and Marinescu et al. [43] as coarser dressing lead to increased fracture and higher loss of active grits through bond and grit fracture. The investigation by Azizi et al. however was rotary cup dressing on CBN wheels using a stylus to measure 2D peaks, a technique which as discussed in Section 2.5.1 has limited resolution. Work by Hamdi et al. [180] on single grit scratch tests has shown that individual abrasive grits can have multiple cutting points rather than one as assumed by literature [90]. Depending on the fracture behaviour of the grit type, far more cutting points may be present than expected thus demonstrating the relevance of studying different abrasive grit types.

Grit shape has also been used to describe wheel topography with Klocke et al. [181] using rake and wedge angle to define the grain shape. Modelling work and validation trials with CBN wheels indicated that smaller negative rake angles led to reduced tangential forces and therefore grinding energy. This is because the 'sharper' grits caused an earlier occurrence of plastic deformation and chip formation as the grit moved along the workpiece. Chip formation tests by Xie and Willaims [182] supported this behaviour with higher levels of plastic deformation at less negative rake angles. However experiments were performed with single point steel tools rather than abrasive grits. CBN single point grinding tests on hardened steel conducted by Rasim et al. [183] furthered this work showing that higher penetration depth of the grit into the workpiece is required at more negative rake angles to form a chip (Figure 2.30). This is due to more downward material displacement.
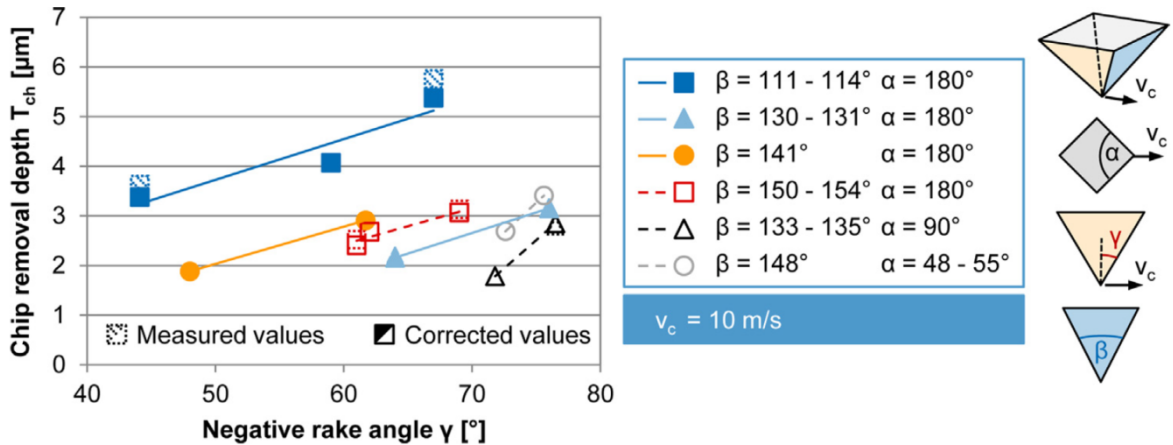
FIGURE 2.30 – INCREASE IN PENETRATION DEPTH OF THE GRIT REQUIRED FOR CHIP REMOVAL AS THE NEGATIVE RAKE ANGLE INCREASES [183]**.**

Not only grit shape and distribution but flat regions (tangential to the wheel surface) on the wheel topography can affect grinding performance and as discussed in Section 2.3.5, are caused by dressing or attritious wear on the grits [122]. Flat grit regions are often captured using optical techniques (Section 2.5.3) with the level of reflected light used to indicate the number of flat regions. It has been measured that as the material removal in grinding increases then so does the level of reflected light, indicating an increase in the amount of wear flats on the wheel topography (Figure 2.31) [178]. Therefore the abrasive grits are duller and the level of cutting to ploughing and rubbing in grinding declines, raising the energy of the grinding process (hence the force increases in Figure 2.31) [124]. High energy causes higher grinding temperatures which risks thermal damage of the workpiece, as shown in thermal partition measurement during grinding of steel by Zarudi and Zhang [184]. In the same dataset, increased depth of cut also raised the level of wear flats.
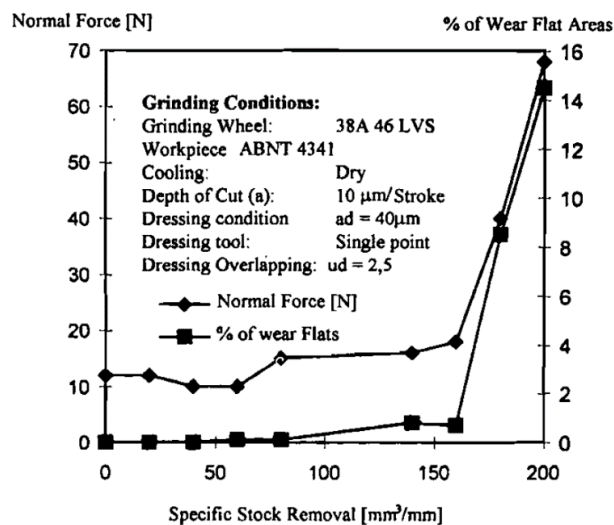
FIGURE 2.31 – FORCE AND WEAR FLAT AREA FOR INCREASING GRINDING MATERIAL REMOVAL [178]**.**

Further in-process topography monitoring research has been conducted by Liao [185]–[187] which focused on using acoustic emission signals and extensive data processing in order to understand wheel topography breakdown including abrasive grit dulling. Liao [185] reported an extensive review of acoustic emission methods to monitor grinding wheel topography breakdown.

Few examples were found in literature of multiple topography measurement techniques used simultaneously to understand abrasive grit behaviour and there was a clear gap linking dressing, grinding and breakdown.

2.6 NI-BASE SUPERALLOYS

2.6.1 APPLICATIONS

Ni-base superalloys have extremely desirable properties such as high temperature resistance, strength and fatigue resistance which makes them useful for a range of applications. including nuclear reactors, reciprocating parts in gasoline engines and rocket engines [188], [189]. The primary application of Ni-base superalloy though is for gas turbine engines, for both aerospace and power generation.

Due to their high temperature performance Ni-superalloys are mostly employed in the rear section of the engine (Figure 2.32), in the turbine, whereby hot air (approx. 1600 °C) from the combustion section flows over the turbine blades which drive the fan at the front. A turbine section consists of blades (mounted in rotating discs) which turn the engine shaft, static nozzle guide vanes to redirect air flow and casing plates surrounding the entire section. In most modern designs, Ni-superalloys accounts for over 50 % of the total mass of the engine [26].
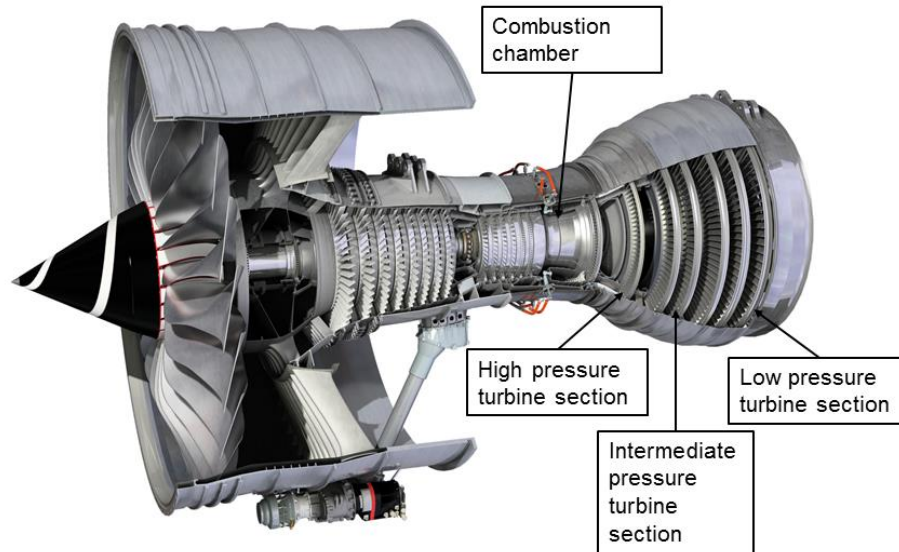
FIGURE 2.32 – ROLLS-ROYCE TRENT 900 GAS TURBINE ENGINE. NI-BASE SUPERALLOY COMPONENTS ARE IDENTIFIED [IMAGE COURTESY OF ROLLS-ROYCE PLC].

Single crystal superalloy materials are primarily reserved for high and intermediate pressure turbine application as this is where the conditions of the turbine are most extreme and the greatest benefit of the superior mechanical performance of the material can be utilised [190]. In the low pressure section, the conditions are less arduous and so the performance requirements of the turbine blades are reduced, hence directionally solidified Ni-superalloys are used.

This thesis focuses on CMSX-4 single crystal alloy, which is currently used for high temperature turbine blade and nozzle guide vane applications [191], [192]. This advanced superalloy was developed by Rolls-Royce plc and its chemical composition can be seen in Table 2.3. Different mechanical properties of this material have been studied in detail, including fatigue [193]–[197] and creep [191], [198], [199]. Much less attention however has been given to the grinding of this alloy using different abrasive wheels and its subsequent interaction with surface and sub-surface integrity.

2.6.2 METALLURGY

Unsurprisingly Nickel (Ni) is the primary constituent material in Ni-base superalloys. Typically these alloys contain approximately 50% Ni with 10-20% Cr and Co. They also contain other alloying elements such as aluminium (Al) and titanium (Ti) which provide strengthening as well as small amounts of other elements such as boron (B) and zirconium (Zr) which help separate grain boundaries [27], [200]. The percentages of these elements can vary between manufacturers and depending on the desired properties of the material. The chemical formulations of two industry-used Ni-base superalloys are shown in Table 2.3.

TABLE 2.3 - THE PERCENTAGES OF ALLOYING ELEMENTS IN TWO NI-SUPERALLOYS, CMSX-4 AND INCONEL 718 [201]**.**

Alloy	Cr	Co	Mo	W	Ta	Re	Nb	Al	Ti	Hf	C	B	Fe
CMSX-4	6.5	9	0.6	6	6.5	3	-	5.6	1	0.1	-	-	-
IN718	19	-	3	-	-	-	5.1	0.5	0.9	-	-	0.02	18.5

The microstructure of Ni superalloys consists of two phases, γ and γ'. The first of these (γ) has an austenitic face centred cubic crystal structure and forms the matrix in the material. The γ' phase has a Ni_3Al (or Ni_3Nb) composition and has a body centred tetragonal structure which is coherent with the matrix (Figure 2.33) [202]. This is the main cause of the alloy strength as the γ' phase is precipitate hardened (held at high temperature) to produce cube-shaped regions of the phase, with high carbide concentration at the grain boundaries, within large γ grains. These regions provide excellent resistance to dislocation movement, forcing the dislocations to bend through the γ channels in between (Figure 2.34) in an effect known as particle strengthening [203]. Dislocation movement is critical for plastic deformation of a metallic material, therefore the γ' phase gives the alloy superior tensile strength
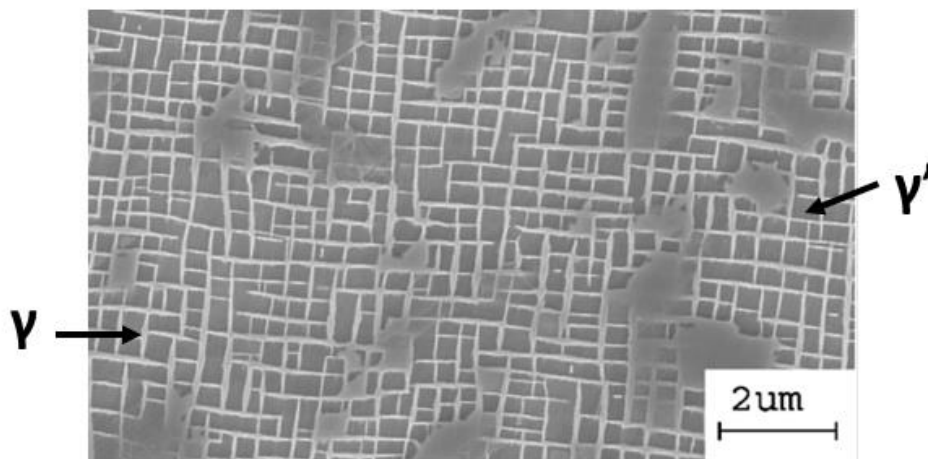
FIGURE 2.33 – MICROSTRUCTURE OF THE NI-SUPERALLOY WITH THE CUBOIDAL GAMMA PRIME CLEARLY VISIBLE AND GIVING THE MATERIAL HIGH TENSIONAL STRENGTH [201]**.**

Elements such as molybdenum (Mo) or tungsten (W) are also added to provide extra strengthening. Due to the significant atomic radius differences between Mo/W and Ni, they give excellent solid-solution strengthening of the γ phase. Ti and Nb are also used for strengthening of the γ' phase whilst carbon is used to form hard carbides on the grain boundaries [201].
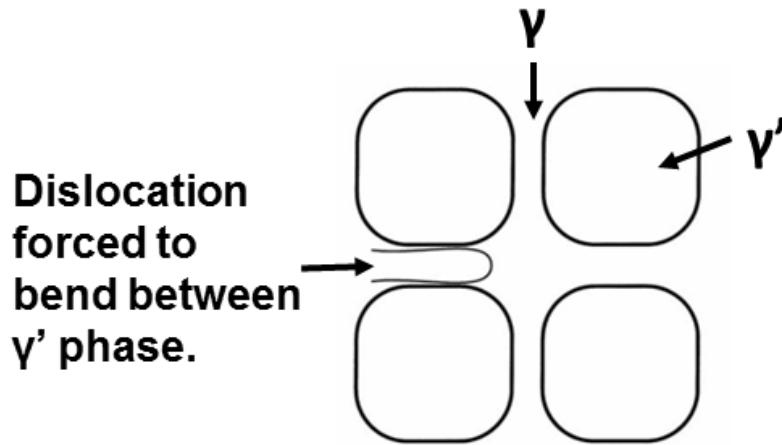
Due to the high operating temperature of Ni-superalloy components, the material must have a high resistance to oxidation. Although this is not natural for Ni alloys, Chromium (Cr) is added in volumes up to 20 % to enable the formation of a protective Chromium oxide (Cr_2O_3) layer in high temperatures [189]. This prevents any further metallurgical damage to the Ni component.

Adding more alloy elements alone does not necessarily achieve the required performance for Ni-superalloys in aerospace applications. In the high pressure section of a gas turbine, temperatures are at an extreme (>1600 °C) and components are more prone to damage. Literature suggests that high-angle grain boundaries can be sites for failure under these conditions [201] and are defined as grains with a misorientation angle above 15° [204]. Issues such as grain boundary sliding, in which there is displacement of grains against one another, can be a cause of creep failure in superalloy materials [205].

This desire for increased creep-resistance led to the development of directionally solidified components in the mid-1960s with the aim of removing high-angle grain boundaries [188]. Carefully designed casting methods ensured that as solidification occurred in the component, only those dendrites with a <001> orientation grew quickly. This formed a component with several, aligned columnar grains [201], [206]. However with increasing operating temperatures, even better operational performance was required of the blades leading to the evolution of single crystal superalloys which have the best properties, at high temperatures, of any structural material. These properties include the removal of grain boundaries which can initiate failure and the higher melting temperature allowing a refined γ' phase microstructure, improving creep strength [188].

Investment casting with directional solidification is typically used to form single crystal superalloy components because it enables high complexity and near-net shape to be achieved. Initially a wax template of the component is formed using injection moulding. The wax template is then dipped in a mobile ceramic slurry consisting of a refractory filler system, colloidal binder and a coarse stucco. The coated template is then dried and the wax melted out leaving a hollow mould into which molten superalloy is poured in a furnace [207], [208]. The mould is drawn steadily out of the furnace from the base causing the material to solidify directionally. Defects in the material can be reduced by increasing the thermal gradient during solidification [209]–[211]. A single crystal is achieved using a multiple-turn constriction in the base (Figure 2.35). The sharp turns in the mould constriction prevent the growth of less favourable grains so that the grain most aligned with the <001> plane is the one that grows for the entire component [206].

A.   B.   C.
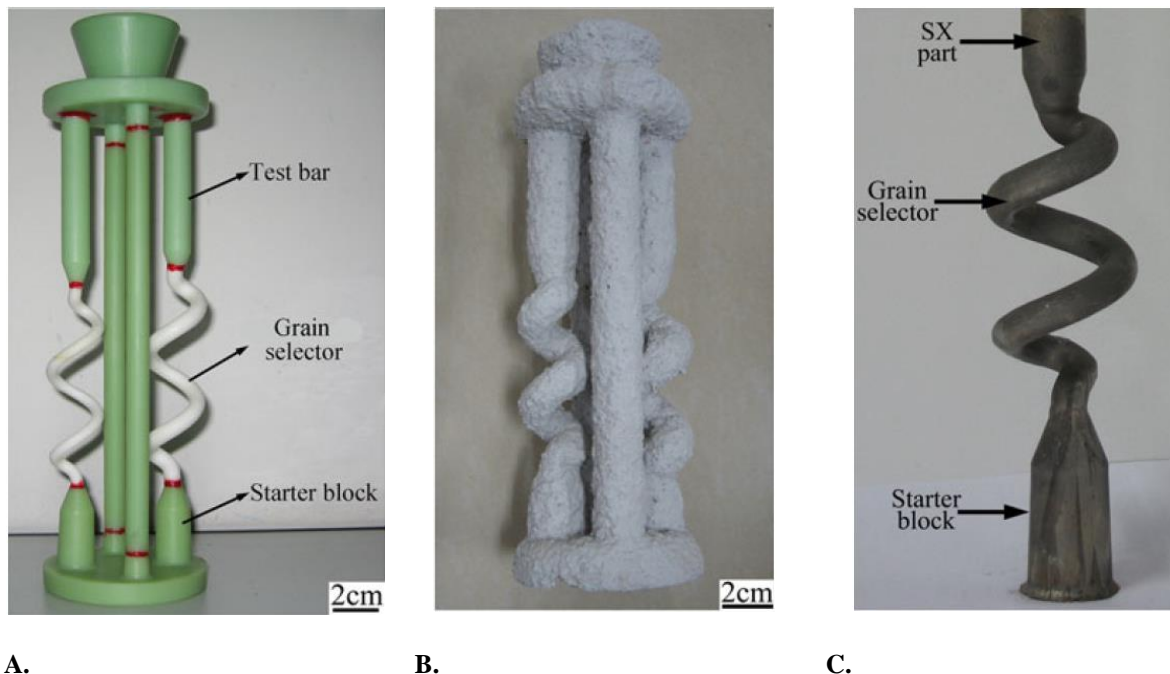
FIGURE 2.35 – (A) WAX PATTERN WITH CONTRICTION GRAIN SELECTOR, (B) CERAMIC MOULD AFTER COATING THE WAX PATTERN AND (C) CAST COMPONENT WITH SINGLE CRYTAL (SX) STRUCTURE [212]**.**

2.6.3 MATERIAL REMOVAL

Ni-base superalloys are extremely hard materials with a low thermal conductivity, thus limiting their machinability. Hard abrasive carbides in the alloy and a tendency for the material to adhere to the surface of the cutting tool also make tool wear a major problem as high machining speeds are required in order to achieve a satisfactory material removal rate [28].

The produced surface generated during machining of Ni superalloys must be of a specified high quality in order to ensure desired performance in a jet engine. It is reported that Ni-based alloys tend

to work harden which results in surface changes such as residual stresses and microcracking [213], [214]. Wear has a significant impact on the surface integrity of Ni alloys as well as cutting tool shape, due to the dulling of the cutting edge [189], [215]. High temperatures at the interaction between the cutting tool and workpiece induce residual stresses in the surface, an effect that can be reduced with coolant. However this greatly increases costs to the manufacturing process because of the energy required and disposal issues [216].

Understanding the response of Ni-superalloys to machining parameters helps understand the behaviour in grinding. At low cutting speeds (125 m/min) a great amount of heat accumulates in the chip however the ability to dissipate heat is less (as slower cutting head speed). Therefore more heat flows into the machined surface and deformation becomes thermally driven. Hence tensile residual stresses generated in the surface. The inverse occurs at higher cutting speeds [217]–[219]. Also the deeper the machining cut, the greater the compressive stresses in the surface due to a work hardening effect in the superalloy as a result of machining [217].

Higher temperatures in the cutting zone of Ni-base superalloys results in a poorer quality surface, which is assisted by the inefficient thermal conductivity of Ni superalloys. Therefore temperature control in machining Ni-base superalloys is vital, as shown in Figure 2.36, as in the presence of coolant the high tensile residual stresses at the surface of the workpiece were reduced [220].

A.   B.
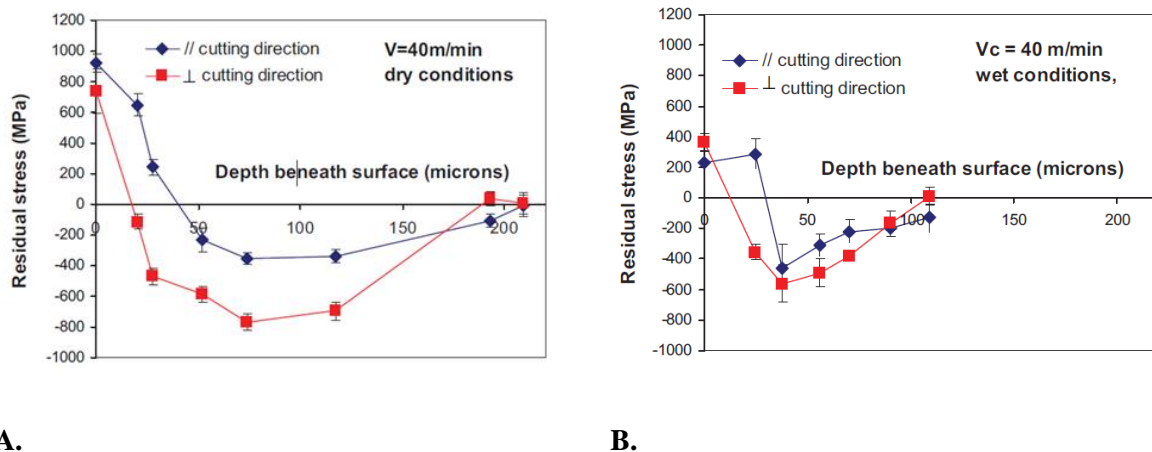
FIGURE 2.36 – REDUCED SURFACE RESIDUAL STRESSES MEASURED FROM THE MACHINED SURFACE OF NI-BASE SUPERALLOY IN (B) WET CONDITIONS COMPARED TO (A) DRY [220].

2.6.4 Grinding of Ni-base Superalloys

Due to the high hardness of Ni-base superalloys grinding is a dominant machining method for cutting these materials for the manufacture of blades and vanes in gas turbine engines (Section 2.1.3).

The grinding of these components mostly involves creep-feed grinding using porous, vitrified alumina (Al_2O_3) wheels with intermittent or continuous dressing (CD) [2].

White layer is a common defect that can occur in the sub-surface of Ni-base superalloys and consists of small, nanocrystalline, equiaxed grains that appear 'white' and amorphous under optical microscopy (Figure 2.37). It is suggested that this forms due to a combination of severe plastic deformation of the material as well as heating (to the material melting temperature) and rapid quenching of the material at the surface. This demonstrates the excessive temperatures that are generated during grinding [221]. Research has indicated that grinding temperatures can be reduced and therefore white layer, by better wheel topography control and liquid cooling.
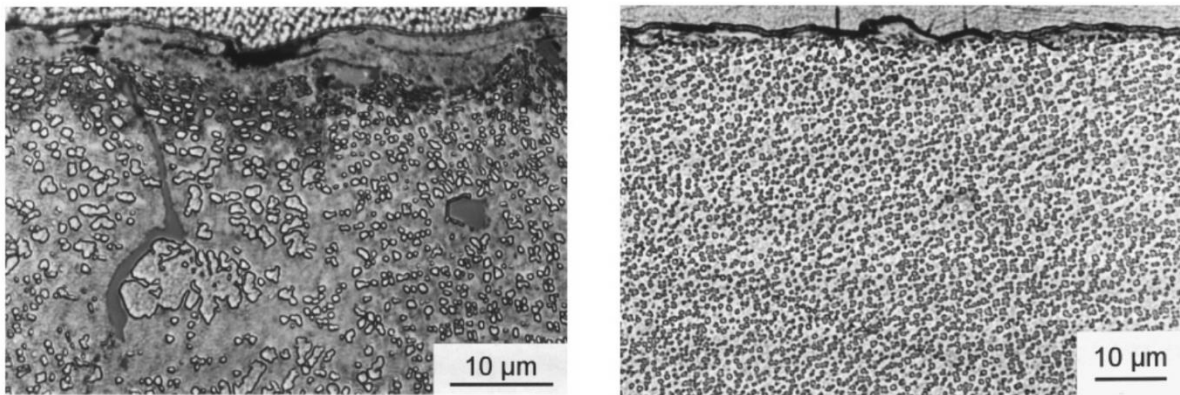
A. **B.**

FIGURE 2.37 – (A) VISIBLE WHITE LAYER FROM CREEP FEED GRINDING IN738LC ALLOY (B) REDUCED WHITE LAYER FROM HIGH INFEED CD GRINDING [221]**.**

White layer is an issue in Ni-base superalloys because it increases the risk of mechanical failure. As the white layer is very hard and contains very small grains, it can fracture easily and nucleate cracks in the material [222]. It can also reduce the surface finish quality of the workpiece and fatigue strength [223].

High grinding temperatures can also cause a surface colour change (known as 'burning') and is a result of oxidation of the workpiece surface [32], [102]. Greater burning leads to higher surface roughness, as seen by [224] on K417 alloy, and this is because of increased plastic deformation and surface micro-cracks. It is also reported that the grinding induced surface burning is not detrimental to surface integrity as long as microcracks are not formed at the surface [224].

Temperature in grinding directly influences the occurrence of burning on the workpiece. Work conducted by Liu et al. [93] on CMSX-4 and IN718 material, measuring forces and temperature in grinding, clearly demonstrated that the temperature increases with material removal rate, which

impacts grinding force (Figure 2.38). Similar research by Chen et al. [225] on DZ4 Ni-base superalloy showed that the force ratio during grinding was closely related to whether burning was seen on the workpiece surface. During cutting, a 'jump' was observed in the measured force ratio which corresponded to burn on the workpiece. This is explained as softening of the material due to high temperature, which leads to severe adherence of the material to the abrasive wheel. Hence there is an increase in the friction coefficient and the force jumps. Therefore reducing frictional forces is vital to control grinding temperature and workpiece burn. SEM images of the ground surface (Figure 2.39) showed substantial plastic flow of the material around the abrasive grits when extensive burn was observed. Not only this but small spheres of remelted DZ4 material are deposited on the surface due to high grinding temperatures. When there is extensive plastic deformation on a workpiece surface then there is high thermal expansion which generates tensile residual stress in the surface. Tensile residual stress can limit the fatigue performance of the component and so burn is to be avoided [226].
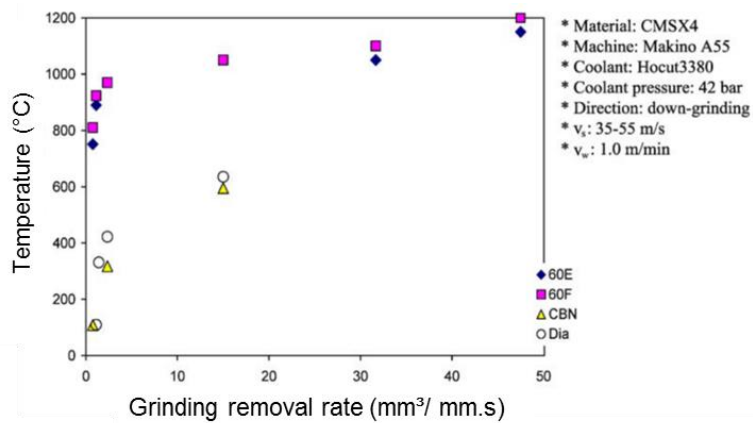
FIGURE 2.38 – INFLUENCE OF MATERIAL REMOVAL RATE ON GRINDING TEMPERATURE IN CMSX-4 [93]**.**

A. **B.** **C.**
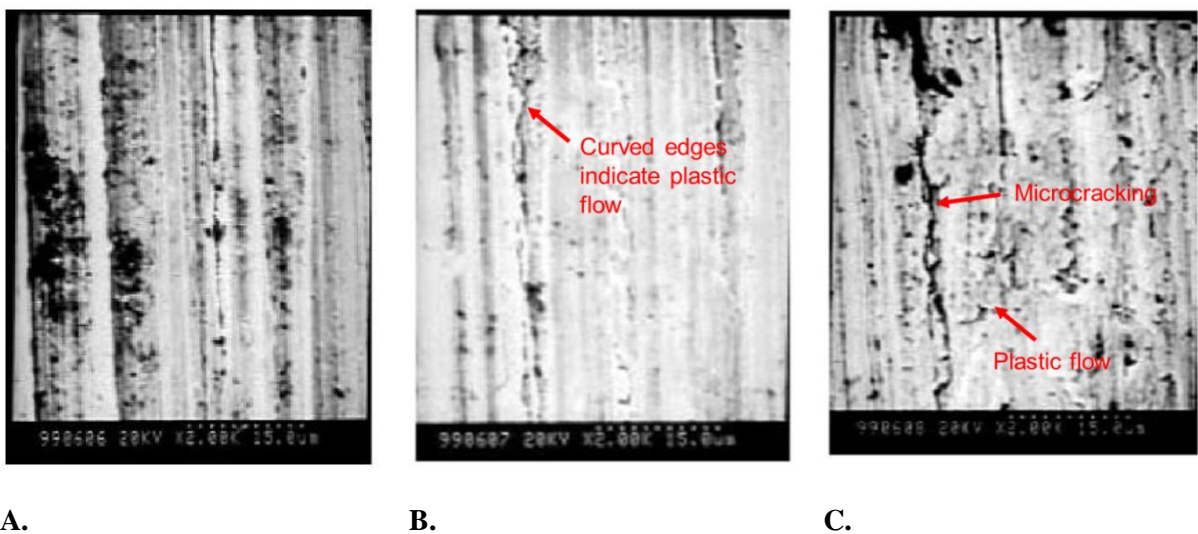
FIGURE 2.39 – SEM IMAGES OF GROUND SURFACES (A) NORMAL SURFACE (B) LIGHT BURN (C) SEVERE BURN
[227]**.**

Plastic flow of material on the ground surface around an abrasive grit (also known as smearing or side flow) is suggested to be a result of multiple factors in grinding. It has been seen by Zeng [228] that when the depth of cut increases, the degree of smearing increases (also with surface roughness) as the grits penetrate deeper into the workpiece so more material is deformed. Vibration also directly impacts the level of smearing with Bhanduri et al [175] showing clear side flow when ultrasonic vibration was applied to grinding of IN718 (Figure 2.40). It is also known that increased dulling of abrasive grits reduces the cutting effect and ploughing becomes a more dominant mechanism [159].
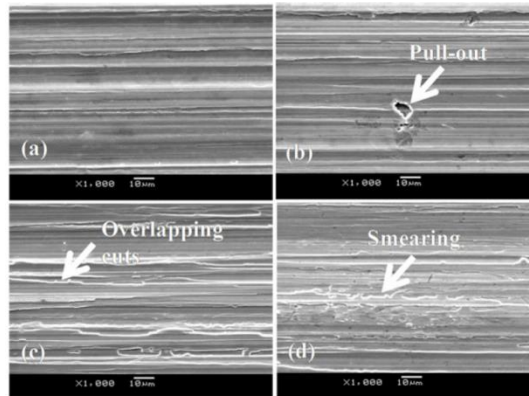
FIGURE 2.40 – (A) – (B) GRINDING IN718 WITHOUT VIBRATION (C) – (D) CONTROLLED VIBRATION APPLIED [175]**.**

Surface quality (roughness) must be considered when machining superalloys for aerospace application as the machined surface can be an origin for failure [229]. Surface roughness is a main factor in the fatigue response of Ni-base superalloy, particularly for low cycle fatigue [226]. At high feed rates and cut depths, chip size per grit is increased and there is greater plastic deformation on the workpiece. Resulting grinding forces and temperatures rise and a rougher workpiece surface is generated (Figure 2.41A). This has been seen on IN718 with alumina grinding wheels by Yao et al. [230]. Temperature was shown to decline with wheel speed due to increased coolant flow into the contact area (using porous grinding wheels) causing a decline in surface roughness (Figure 2.41B). The CBN wheel however showed the opposite behaviour for feed rate, due to is relatively higher hardness meaning that high feeds increase the wheel sharpness. Also at wheel speeds beyond 25 m/s, the surface roughness increased again (Figure 2.41B) due to adhesion wear on the wheel. Guo et al. [62] showed a similar behaviour by studying the grinding behaviour of single-layer CBN grinding wheels on Ni-base superalloy. It was shown that surface roughness increased with material removal rate, an inverse behaviour to the power consumption. Similarly Tso and Zhong et al [123], [231] found that reducing wheel speed increased the surface roughness of IN718 due to the increase the in chip size.
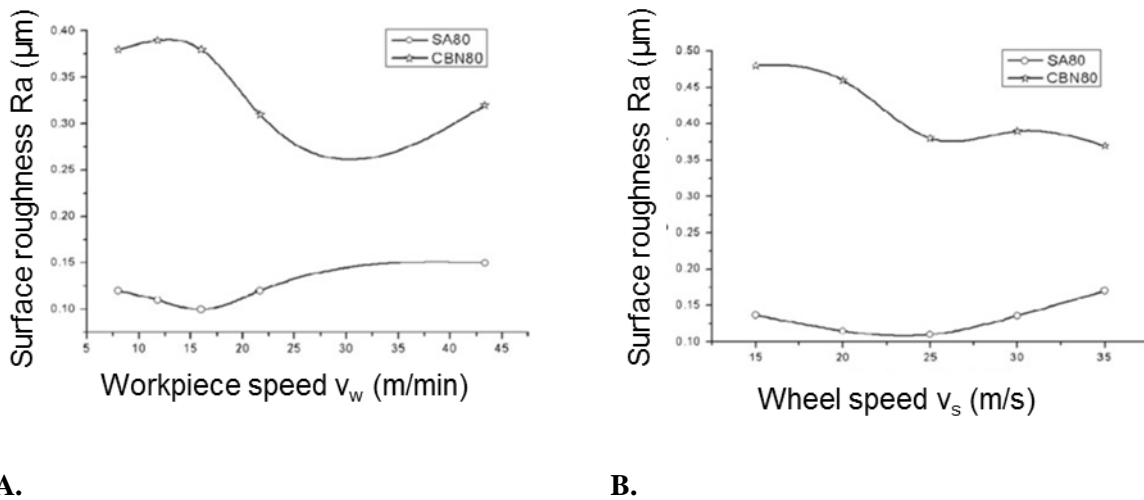
A.   **B.**

FIGURE 2.41 – (A) SURFACE ROUGHNESS VS WORKPIECE FEED RATE FOR ALUMINA AND CBN WHEELS (B) SURFACE ROUGHNESS VS WHEEL SURFACE SPEED FOR ALUMINA AND CBN WHEELS [230]. **ALL OTHER PARAMETERS CONSTANT.**

There are many input parameters in grinding that are known to affect grinding force and workpiece roughness. An experimental investigation on the measured surface roughness and grinding force of IN718 as a result of various input parameters (wheel grit size, lubricant type, feed rate and depth of cut) was performed by Huddedar et al. [232]. Grit size was show to have the largest impact on the workpiece roughness whilst infeed (depth of cut) proved to be statistically significant (Figure 2.42). Also ultrasonic assisted creep feed grinding of IN718 indicated the significance of vibration in grinding [175]. A 24 % increase in surface roughness was detected when ultrasonic vibration was applied during grinding compared to no ultrasonic assistance.

Models, such as those by McDonald et al. [233], have studied the link between grinding wheel topography and surface quality. By predicting the wheel topography (randomised grit shape, distribution and protrusion) and grit interaction with the workpiece, generated data showed increase in surface roughness with an increase in feed rate. Roughness also decreased with increasing wheel speed, corroborating with experimental data in literature. Other models [234], [235] have shown that as the depth of cut in grinding increases then so does the chip thickness, contact length and percentage of active grits on the wheel surface generating a rougher workpiece. This is because at greater cut depths, more grits with a smaller height protrusion from the wheel surface participate in the cutting operation.
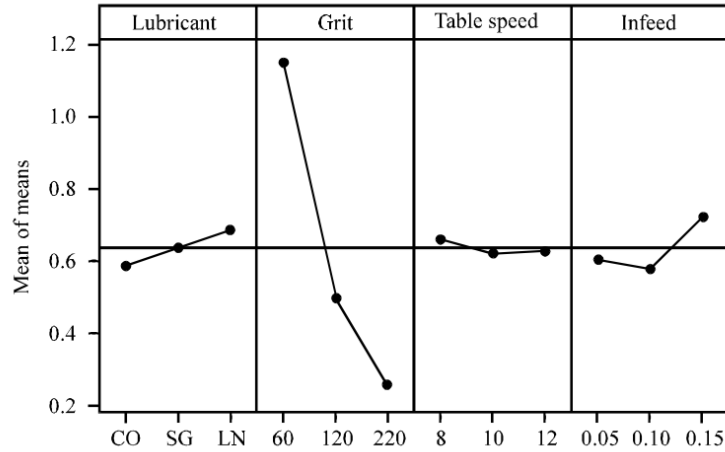
FIGURE 2.42 – MAIN EFFECTS PLOT FOR FOUR DIFFERENT GRINDING INPUT PARAMETERS ON WORKPIECE SURFACE ROUGHNESS [232].

Residual stresses are common features in the generated surface of a machined workpiece and controlling them is vital to ensure reliable performance of a component [226]. Often it is desired that a surface contains compressive residual stresses as this resists the opening of cracks on the surface and helps prevent failure, particularly for fatigue.

Research has shown that creep feed grinding generates tensile stresses at the surface of a component [228], [236]. The application of continuous dressing and coolant has been shown to reduce the width of the tensile zone, supporting data from previous work [221] that residual stress is temperature dependent.

Finite element analysis of residual stress formation in grinding by Gangaraj et al. [237] has indicated that whilst workpiece velocity controls the level of residual stress in the material, the depth of cut influenced the depth of tensile stress from the surface. This phenomenon is related to temperature gradient between the surface and material bulk as the high workpiece velocity generates a large gradient and therefore a peak tensile residual stress (Figure 2.43A). It has been suggested that tensile surface residual stresses are a result of thermal expansion and contraction, as well a plastic deformation from the cutting points on the abrasive grits [238].
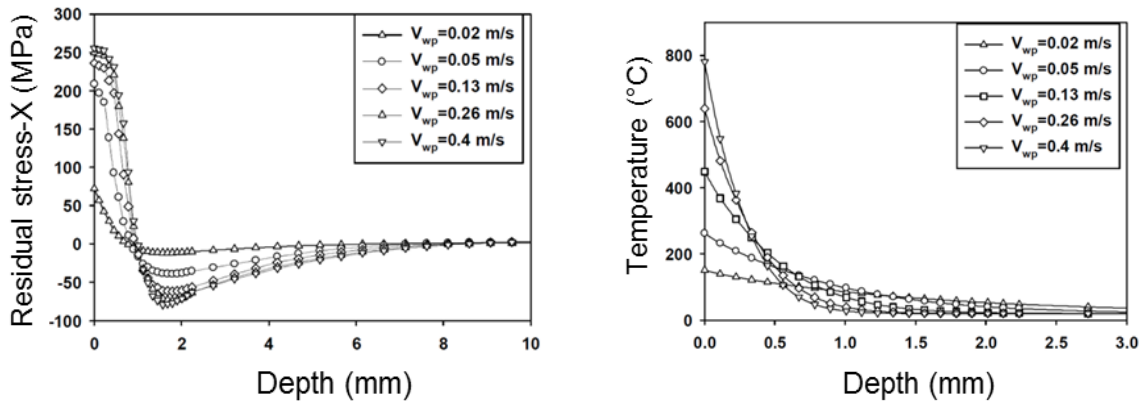
A.   **B.**

FIGURE 2.43 – (A) FINITE ELEMENT ANALYSIS OF THE RESIDUAL STRESS GENERATED FROM GRINDING (B) THE MODELLED GRINDING TEMPERATURE [237].

If the residual stress is dependent on the thermal behaviour of grinding, it is also dependent on the grinding forces. In work by Tso [123] an increase in grinding wheel wear flats, with more grinding passes, led to a rise in grinding forces. Thus the topography of the abrasive wheel becomes very influential in controlling the grinding process.

This thesis focuses on the impact of abrasive wheel topography on the grinding of single crystal Ni-base superalloy (CMSX-4). Although much literature has examined this process it is primarily targeted at polycrystalline alloys and machining with superabrasives grits. This work aims to better understand the grinding process for CMSX-4 Ni-base superalloy using conventional abrasive wheels with novel grit shapes. Metallurgical cut ups gathered in this research are compared against the Rolls-Royce Surface Condition Standards for Chip Forming Machining of Turbine Blades (CME5043 Section 2) [239]. This standard gives detailed examples of common defects created during the grinding of single crystal Ni-base superalloy as well as defining the tolerance bands and potential causes for these defects. Examples of these defects are shown in Appendix B.

2.7 SUMMARY

This section has given an assessment of the state of the research with regards to dressing of abrasive wheels and grinding of Ni-base superalloys. Although much work has covered the influence of wheel topography on grinding there is a substantial lack of research into the impact of abrasive grit morphology. As a result there is very little current data on the dressing and grinding response of abrasive wheels consisting of engineered grit shapes, compared to conventional abrasives, specifically in VIPER grinding of Ni-base superalloy material.

Much literature focuses on a specific aspect of grinding including workpiece metallurgical damage, grinding mechanics, dressing response etc. There is a gap in the research to link all these aspects together from initial dressing and wheel topography generation to final grinding. This research aims develop the understanding of abrasive wheel topography and how it can be controlled in order to optimise aerospace component grinding by conducting a series of experimental investigations to answer the research aims detailed in Section 1.3. To achieve this the following objectives were set.

1. Capture the most influential parameter in dressing on the wheel topography by measuring spindle power during dressing and analysing the generated topography including the number of cutting points and average roughness.

2. Define the dressing mechanisms for different abrasive grit shapes and how they impact the grinding behaviour of the different abrasives by measuring grinding power, surface roughness and ground surface imaging.

3. Compare the response of the generated topographies after multiple grinding passes by measuring spindle power and grinding force as well as determining when bond fracture and substantial breakdown occurs.

4. Grind with a range of parameters to compare the behaviour of abrasive grit shapes under different grinding conditions to assess optimum parameters for different abrasive wheels (balance between surface quality, wheel breakdown, efficiency and sub-surface material damage).

5. Identify the most suitable grit shape for industrial application including dressing and grinding technique.

The following Chapter details the experimental trials to meet these objectives and the motivation behind each.

CHAPTER 3

EXPERIMENTAL FRAMEWORK

3.0 EXPERIMENTAL FRAMEWORK

This section details all the experimental methods performed during this research. A series of experimental trials were performed, as explained in Section 3.1, with the knowledge gained from each used to build on the subsequent experiments.

3.1 EXPERIMENTAL OVERVIEW

3.1.1 EXPERIMENTAL STRATEGY

In order to understand the dressing mechanisms of different abrasive grit shapes and their subsequent grinding performance, three different wheels were selected. These were selected based upon the differences in the grit morphology and what is currently available for use in industry, as explained in Section 3.1.3. Figure 3.01 details the overall experimental plan.
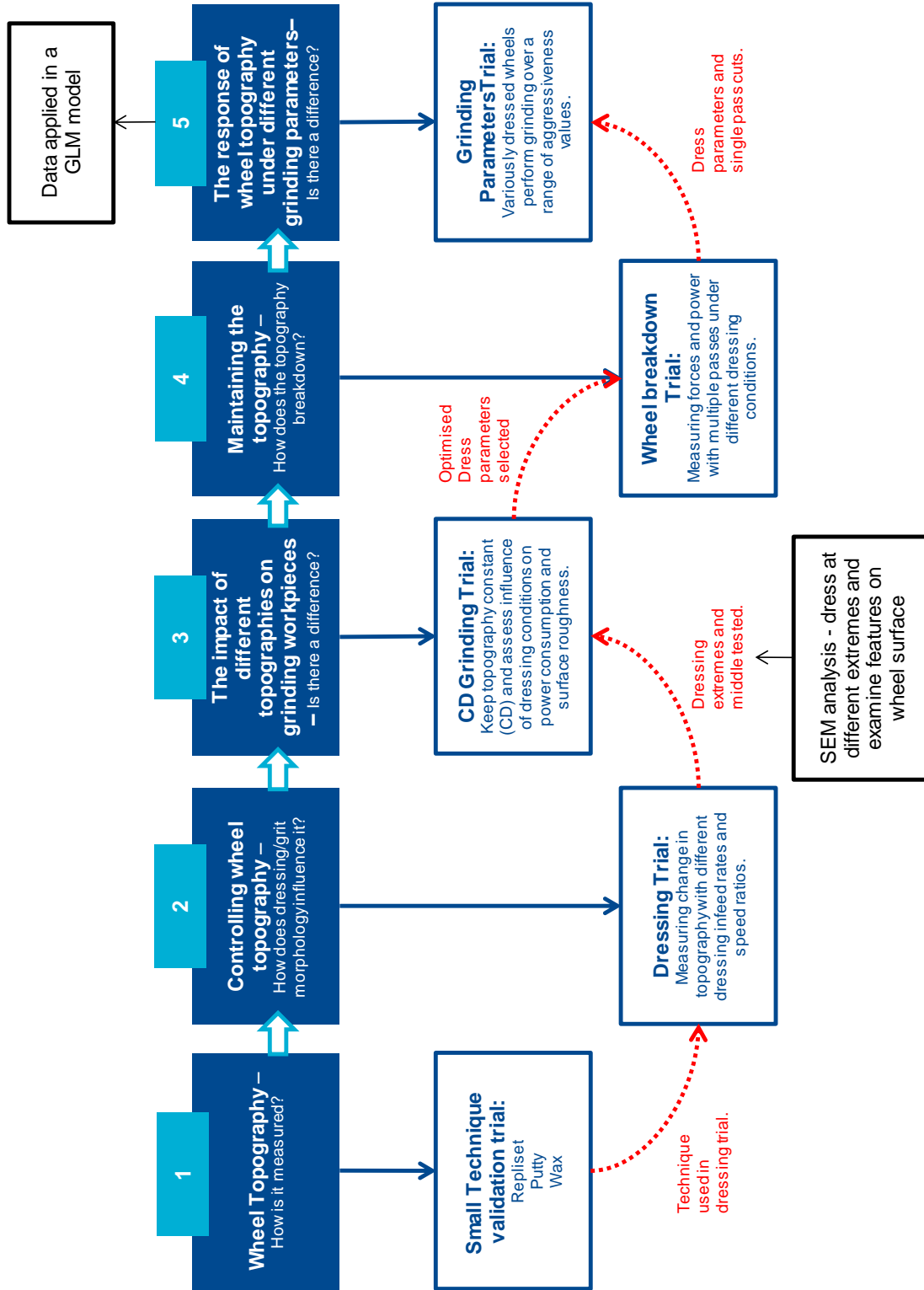
FIGURE 3.01 – FLOW DIAGRAM DETAILING THE EXPERIMENTAL APPROACH TO THE THESIS.

Characterisation of the grinding wheel topography is the first step to determine the influence of abrasive grit shape on the grinding performance (Figure 3.01 – step 1, Section 3.2.3). An extensive review of the literature (Section 2.5) was performed to identify possible techniques to use in this context. Different techniques were tested and a wheel surface replica was selected to determine the wheel topography (Appendix C).

Once a wheel surface topography characterisation method had been defined a dressing investigation was conducted (Figure 3.01 - stage 2). As discussed in Section 2.4, dressing is a vital stage of the grinding process and has been shown to have significant consequences on the subsequent grinding performance. Although work has been conducted on this for conventional abrasive wheels, the research is limited for vitrified wheels with engineered grit shapes. Using the techniques in Figure 3.01 (stage 1) for the different grit morphologies, the response of the wheel topography to different dressing parameters was captured.

The effects of the dressing process on the grinding performance of different abrasive wheels was then studied (Figure 3.01 – stage 3, Section 3.3). There is a gap in the literature linking the measured surface topography to the resulting grinding performance, especially for novel abrasive grit shapes. A set of dressing parameters were used whilst grinding CMSX-4 alloy samples with continuous dress (CD) grinding. The CD technique assumes wheel wear effects are eliminated (such as grit dulling, as it is shown in Section 2.3 and 2.6) due to constant sharpening of the grinding wheel, thus isolating the impact of the dressed topography on grinding behaviour. The full experimental method for this study is detailed in Section 3.3.

After analysing the effect of dressed topography on grind performance without wear (process driven), it was then introduced (Figure 3.01 – stage 4, Section 3.4) to understand the significance of the dressing conditions on the grinding performance after several passes. Each abrasive wheel was initially dressed then several repeat grinding passes conducted on CMSX-4 samples. Grinding parameters were kept constant and three dressing parameters tested (coarse dressing and two conditions that generate the lowest grinding power and surface roughness). Process monitoring such as force and power measurement was employed to compare dressing and grit shape performance. The full experimental method for this study is detailed in Section 3.4.

Previous trials used constant grinding parameters so the topography response under a range of grinding parameters was investigated (Figure 3.01 – stage 5). A Taguchi design of experiments was applied to understand how the grinding and breakdown behaviour of the wheels, under different dressing conditions, changes with various grinding feed rates, wheel speeds and depths of cut. This reveals the significance of engineered grit morphologies under different grinding conditions. The aim

of this trial was to link machining and dressing parameters and use the obtained information to develop a regression model to quantify the significance of different grinding conditions. The full experimental method for this study is detailed in Section 3.5.
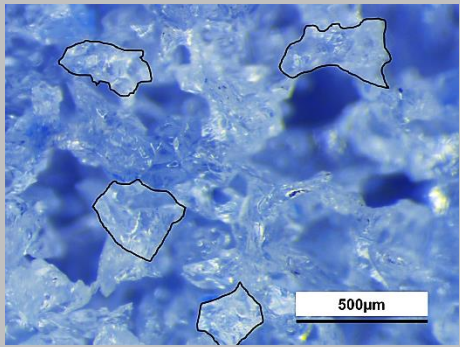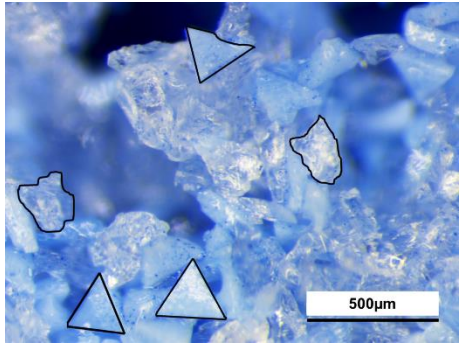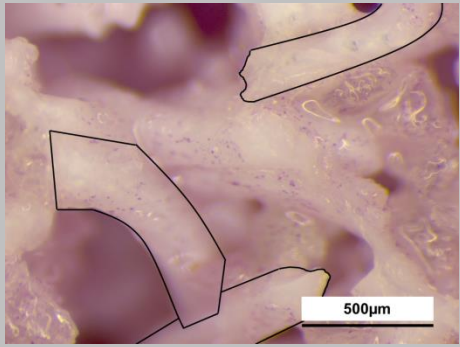
3.1.2 ABRASIVE WHEEL SPECIFICATIONS

For turbine component grinding in Rolls-Royce, porous, alumina grit, vitreous-bonded grinding wheels are typically used and so this type of wheel is the focus of this EngD research. Novel, engineered grit shapes have been developed for vitreous wheels but little research has been done to compare the behaviour of these with conventional abrasive grits. Three different abrasive grit morphologies were investigated as they are commercially available and there is little knowledge about their dressing and grinding mechanisms:

- Conventional (random, spherical)

- Hybrid (combination of conventional and triangular)

- Elongated

To obtain the different grit shapes, each wheel type was supplied by a different abrasive wheel manufacturer which also enables effective cost comparison together with the grinding performance. Apart from the geometry and morphology of the grits, other wheel specifications including grit size, bond strength and porosity were aligned with each other as closely as possible. The hybrid wheel type was investigated as these are favoured in industry over wheels containing just engineered, triangular grits due to reduced costs. Table 3.1 shows an overview of the selected grinding wheels, the grit morphologies and wheel specifications. The wheel brand and manufacturer is shown in square brackets.

TABLE 3.1 - VITREOUS ALUMINA ABRASIVE GRINDING WHEELS USED IN THIS RESEARCH WHERE THE HIGHLIGHTED REGIONS SHOW THE GRIT SHAPE.

Wheel specification	Abrasive grit shape	Optical micrograph	ID
VU33A802HH10VB1 **[Viper Ultra]** **[Tyrolit]**	Conventional		Conventional
93DA80/120 H15VPHH901W **[Cubitron Hybrid]** **[3M]**	Triangular (30%, #120 grit size)/ Conventional (70% #80 grit size) hybrid		Hybrid
IPX80H13VCF5 **[Altos]** **[Saint Gobain]**	Elongated		Elongated

The conventional wheels consist of crushed alumina grits which have a random, irregular morphology. This is the typical grit shape of most alumina grinding wheels and most literature considers a sphere as the closest geometrical definition. These grits are manufactured in the standard crystallisation technique and consist of a large crystal structure of 3-4 crystals per grit.
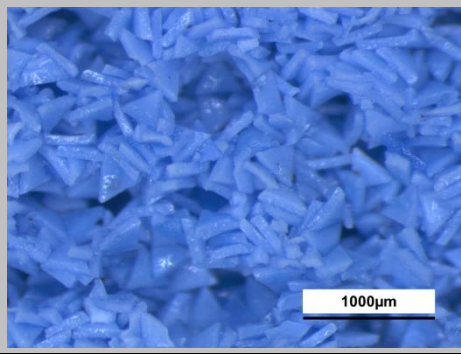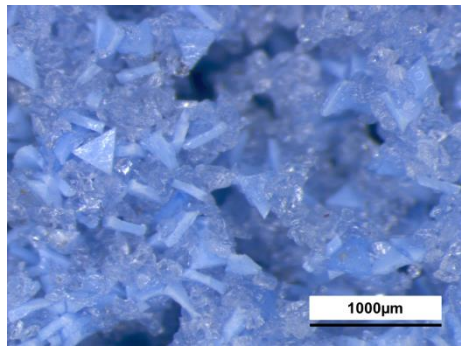
The triangular hybrid wheels consist of a mixture of sintered engineered grits (triangular grits, manufactured according to the process outlined in Section 2.3) and crushed conventional grits. The sintered grits contain small crystals (<0.2μm) whereas the conventional grits have a much larger crystalline structure. The wheels tested from Table 3.1 used #120 grit size triangular grits as these had a comparable size to the conventional (#80) grits.

To understand the level of contribution of the engineered grits in the hybrid wheel, some testing was performed on a wheel containing 100% triangular grits. A hybrid wheel (30% triangular grits) was tested alongside the 100% wheel to serve as a comparison as the grit size of the 100% triangular wheel was larger than those used in Table 3.1 (#80 and #120 respectively). The behaviour of these wheels was investigated in Sections 3.2 and 3.4 and their specification is shown in Table 3.2. Both wheels detailed in Table 3.2 contained a grit size of #80, larger than those described in Table 3.1. This was due to availability restrictions from the supplier. All comparisons using these larger grit size wheels was only between the wheels in Table 3.2 to assess the impact of increased triangular grit content.

The wheel containing elongated grits consist of seeded gel abrasive (Section 2.3) formed into extruded grits. These are colloquially known as 'spaghetti' grits and also contain crystals of a few microns.

TABLE 3.2 – WHEEL SPECIFICATIONS OF VITREOUS WHEELS CONTAINING TRIANGULAR GRITS FOR EXPERIMENTAL COMPARISON. THE GRIT SIZES OF THE TRIANGULAR GRITS IN BOTH WHEELS ARE LARGER THAN THOSE IN TABLE 3.1.

Wheel specification	Abrasive grits shape	Image	ID
93DA80 H15VPHH901W	Triangular (100%)		100% Triangular
93DA80/80 H15VPHH901W	Triangular (30%)/ Conventional (70%) hybrid		30% Triangular

3.1.3 MACHINE TOOL

The VIPER grinding process was used as the grinding process in this research due to its industrial application for machining turbine components formed of difficult-to-machine Ni-based

superalloys. As explained in Section 2.1.2, a high pressure coolant (70 bar) together with porous wheel structures are used to achieve high material removal rates.

All grinding trials were conducted on a 5-axis Makino A100e universal horizontal machining centre with VIPER grinding capability (Figures 3.02 - 3.03). The full machine specifications are detailed in Table 3.3.
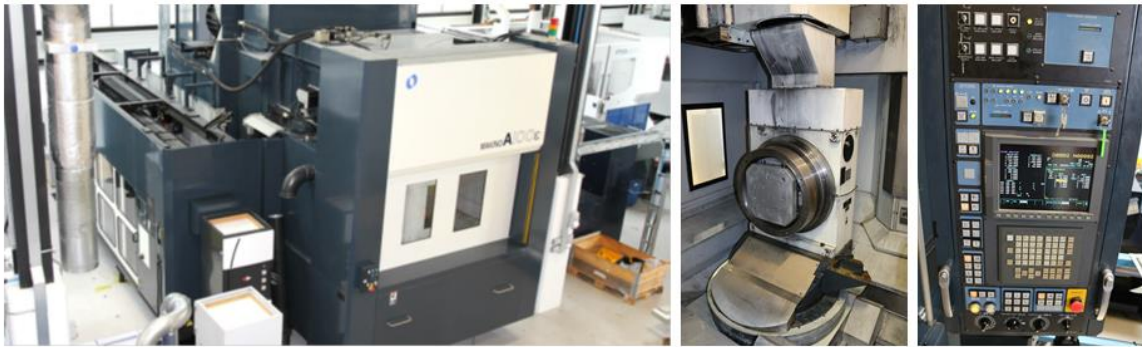
FIGURE 3.02 – MAKINO A100E 5-AXIS VIPER GRINDING MACHINE WITH CD CAPABILITY, TOOL CHANGER AND FANUC CONTROL PANEL.
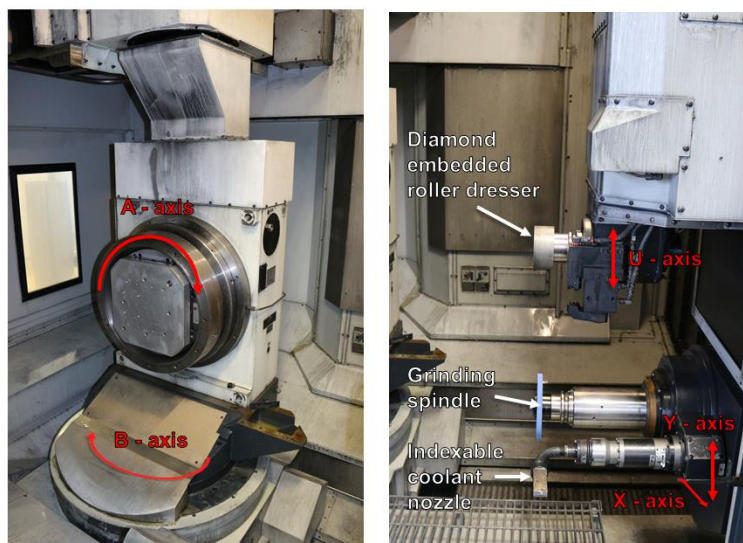
FIGURE 3.03 - INTERNAL SET UP OF THE MAKINO A100E INCLUDING THE 5-AXES OF MOVEMENT PLUS THE DRESSER AXIS (U).

TABLE 3.3 - MAKINO A100E MACHINE SPECIFICATIONS

x-axis travel	1700mm
y-axis travel	1050mm
z-axis travel	1400mm
a-axis travel	360°
b-axis travel	270°
Max spindle speed	12000rpm (spindle), 8000rpm (CD spindle)
Max spindle power	50kW (spindle), 11kW (CD spindle)
Max traverse speed	50000mm/min at 0.4G acceleration
Spindle interface	BT50 (spindle), HSK63A (CD spindle)
Max workpiece size	1900mm x 1500mm
Max workpiece weight	3000kg

The coolant applied in the machine was water-based Hocut 768 kept at a constant concentration percentage of 6-8% and a pH of 8.5-9.5. It was applied using a hook-in nozzle set at 70° PU and 147° PV (Figure 3.04) ahead of the point of contact between the workpiece and the wheel at a pressure of 70 bar. These parameters were set based upon a fixed process used in Rolls-Royce machining facilities.
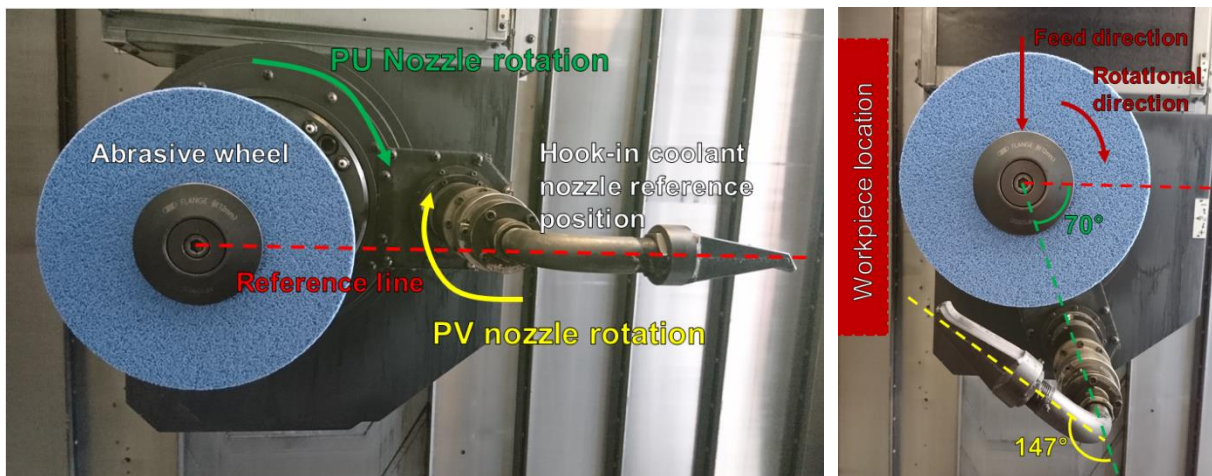
A.   **B.**

FIGURE 3.04 – (A) COOLANT NOZZLE REFERENCE POSITION (B) COOLANT NOZZLE POSITIONING FOR GRINDING. THE ANGLE IN YELLOW IS ADJUSTED AS THE WHEEL DIAMETER REDUCES DUE TO WEAR AND DRESSING TO KEEP THE DISTANCE TO THE WHEEL CONSTANT.

3.1.4 WORKPIECE MATERIAL

All grinding trials were performed on single crystal blocks of CMSX-4. This is a common material in Rolls-Royce for turbine applications wherein the components are investment cast and then ground in order to achieve the required dimensions and surface finish. Every used slab was from the

same cast batch ensuring consistency in the material. The nominal material chemistry is shown in Table 2.3.

All the slabs were investment cast, heat treated and blasted to the same dimensions (Figure 3.05) at Europea Microfusioni Aerospaziali S.p.a. facility in a condition ready for autofinishing in the Rolls-Royce turbine production process. The raised spots on the casting surface (circled, Figure 3.05) were a result of the casting process and were ground off prior to measured experimental activity.
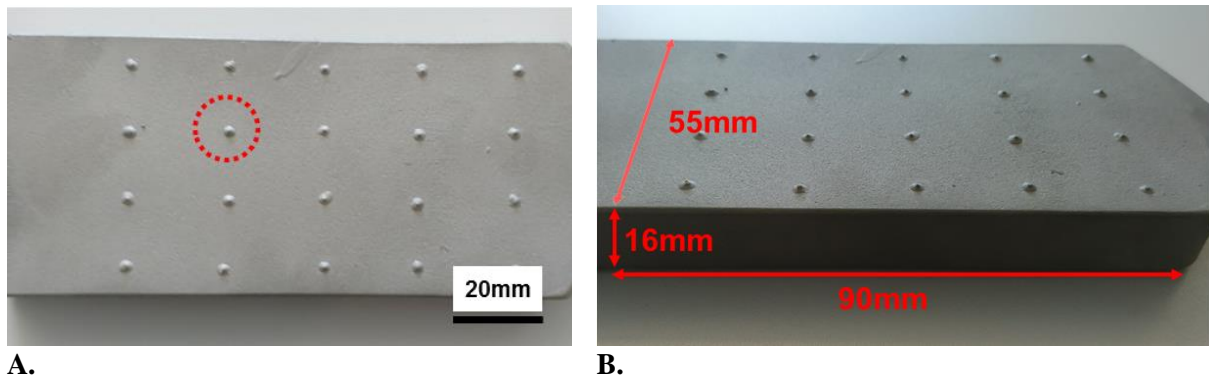
A.   **B.**

FIGURE 3.05 – CMSX-4 WORKPIECE SLAB DIMENSIONS IN (A) TOP VIEW WITH CASTING SPOTS CIRCLED (B) ISOMETRIC VIEW.

3.1.5 POWER MONITORING

To capture the behaviour of the abrasive wheels during dressing and grinding, power monitoring of the grinding spindle was performed. A Load Control Incorporated Power Monitoring kit (4 - 20 mA output) was installed on the Makino A100e and a National Instruments 9201 DAQ box was connected to interpret the output signal. A sampling rate of 20 kHz was used during the measurements and each recorded reading was an average of 1000 data points. The reported power measurements in the results were calculated as an average of the measured points during wheel contact with the workpiece (Figure 3.06).
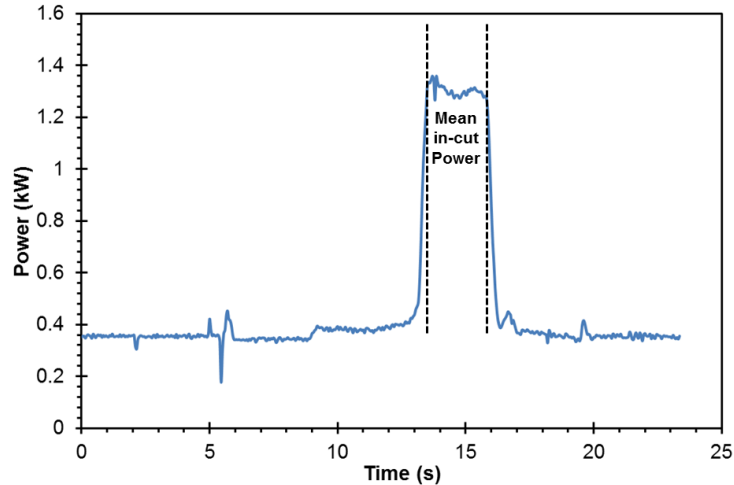
FIGURE 3.06 – DEMONSTRATION OF THE DATA USED FOR IN-CUT POWER MEASUREMENT.

3.1.6 FORCE MEASUREMENT

To measure the forces during grinding a Kistler Type 9139AA force dynamometer was used that could measure a range up to 30 kN and sensitivity of -8.2 pC/N in *x* and *z* and -4.2 pC/N in the *y* direction. A full drawing of the dynamometer is given in Appendix F. Figure 3.07 shows the test setup in which the force dynamometer was fixed vertically to the Makino A100e EROWA fixture plate and a Type 1698AA armoured cable fed from the dyno, through a covered hole in the machine wall, to a Type 5070A charge amplifier with Type 5697A DAQ box. The entire dynamometer was covered in several plastic sheets to provide waterproofing from the high pressure coolant supplied during grinding. Each workpiece block was attached on top of the dynamometer using hardened steel clamps at either end of the workpiece to minimise vibration.
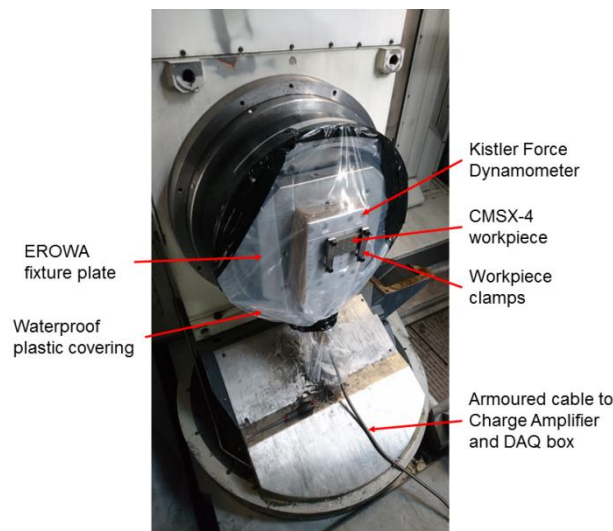
FIGURE 3.07 – TEST SETUP FOR SECTION 3.4 AND 3.5 FORCE MEASUREMENT DURING GRINDING.

The normal (F_n) and tangential (F_t) forces (Figure 3.08) were measured for each grinding cut at measurement range of -1000 to 1000 N. A sampling rate of 1000 Hz was used to capture the average force for each pass which was recorded in the overall *x, y* and *z* directions. All the data was captured in Kistler Dynoware software and was used to calculate the average force by finding the mean in the constant force region where the maximum length of the abrasive wheel is in contact with the workpiece (Figure 3.09A). The measured force in *z* and *y* directions were reported as the normal and tangential forces respectively and determined as the force of both grinding and coolant on the workpiece.
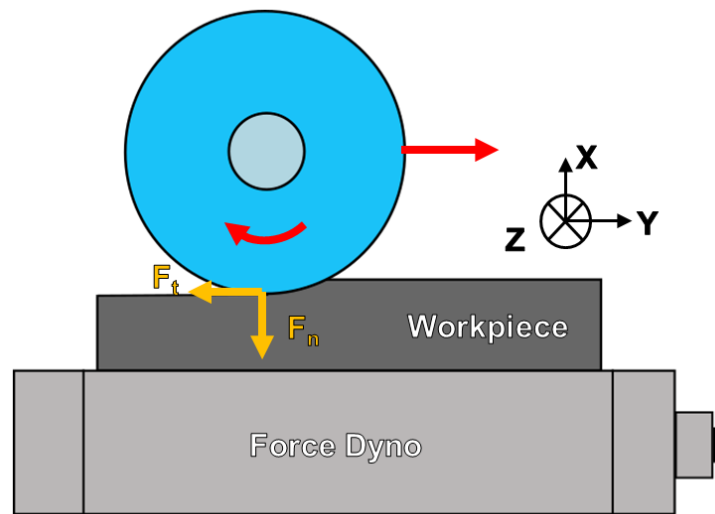
FIGURE 3.08 – DIAGRAM OF THE FORCES ACTING ON THE EXPERIMENTAL SET UP.

A.   B.
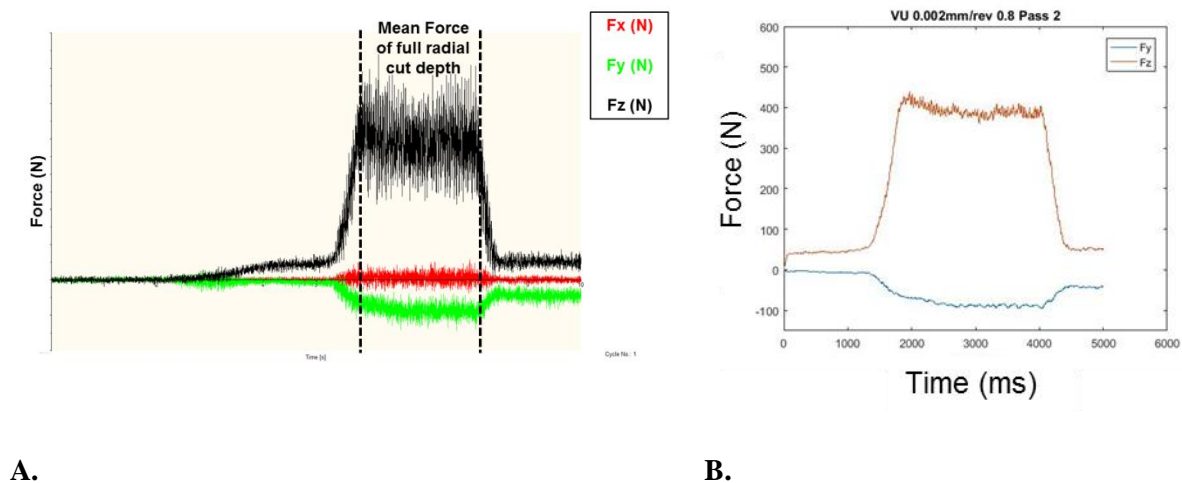
FIGURE 3.09 – (A) MEASURED FORCE DURING GRINDING IN DYNOWARE SOFTWARE (B) MOVING AVERAGE FORCE PLOT OF THE DATA (USING MATLAB) TO DEMONSTRATE THE IN-CUT FORCE RESPONSE.

3.1.7 SURFACE ROUGHNESS MEASUREMENT

All ground metal surfaces were assessed with an Alicona InfiniteFocusSL 3D non-contact profilometer to measure surface roughness. This optical system was selected as it provided more data about the workpiece surface through increased surface assessment parameters (e.g. Kurtosis) compared to a portable roughness stylus (Mitutoyo SJ301). Measurements were conducted using both the probe and the Alicona to ensure the system was comparable (Appendix E).

A vertical and lateral resolution of 100 nm and 4 µm were used respectively as it was sufficient to measure the surface roughness range studied, without greatly extending the measurement time. The cut off wavelength was set at 0.8 mm and each measurement was taken perpendicular to the cutting direction at a minimum length of 4 mm according to EN ISO 4287 & 4288. Five measurements were taken on each ground surface and averaged to give the reported surface roughness.

3.1.8 METALLURGICAL ANALYSIS

In some experimental trials, workpiece samples were sectioned, mounted and prepared for optical and SEM analysis to assess the metallurgical response of the CMSX-4 to grinding. Samples were sectioned using a Buehler AcuThin blade (product code 102501) of width 1.0 mm on an AbrasiMet 250 Cut off machine then mounted in conductive Bakelite to enable analysis under the SEM (Figure 3.10). The following grinding and polishing sample preparation method was employed using a Buehler Automet grinding/polishing machine (Table 3.4).

TABLE 3.4 - GRINDING AND POLISHING SAMPLE PREPARATION PROCESS.

Step	Paper/Pad	Lubricant	Force (N)	Time (mins)	Platen Head Direction	Platen speed (rpm)	Head speed (rpm)
1	P800	Water	20	1	Complimentary	240	50
2	P1200	Water	22	1	Complimentary	240	50
3	P2500	Water	27	1	Complimentary	240	50
4	Chemomet	Colloidal Silica	27	5	Contrary	140	30

After polishing the samples to a mirror finish the samples were etched using Kallings Reagent (Copper (II) Chloride 5 g, HCl 100 ml, IMS 100 ml) [240] in order to highlight the different phases in the material as well as any metallurgical changes such as recrystallisation. Each sample was submerged in the etchant for 4 seconds then immediately washed in water. Selected samples were checked under an optical microscope to ensure the microstructure had been sufficiently revealed.
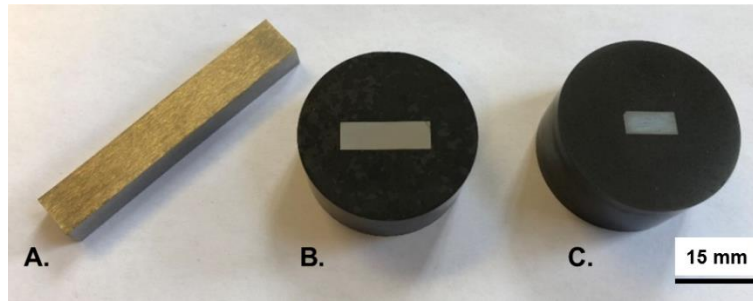
FIGURE 3.10 – (A) GROUND CMSX-4 TEST CUT FROM WHICH SAMPLES (B) ACROSS THE CUT AND (C) ALONG THE CUT WERE TAKEN.

The metallurgical assessment was carried out on an optical microscope, in unpolarised bright field light. The entire ground surface was scanned at a magnification of 100x and any features were imaged and measured from the surface to the maximum depth of influence. All analysis was conducted in accordance with the Rolls-Royce CME5043 metallurgical surface condition standard [239] in which only samples from along the grinding (longitudinal) direction were compared to the CME and defects were measured and compared to the defined limits.

3.2 CHARACTERISATION AND CONTROL OF WHEEL TOPOGRAPHY MEASUREMENT

To understand the grinding performance of different abrasive grit morphologies, first the topography of the different wheel types was captured. The grit shape response to the dressing conditions was also determined in order to explain the subsequent grinding performance. Figure 3.11 shows the experimental flow diagram wherein the grinding wheels topography were measured before and after the dressing processes. The grinding wheel was dressed while the power consumption of the grinding spindle was measured. A graphite coupon was cut to capture the 'average' roughness of the wheel using a stylus measurement. Replicating material was applied to the wheel at three points and the samples measured under an Alicona microscope to record peak density (Section 2.5.1) and grit shape. Finally micrographs of the wheel were taken under an optical microscope to capture the fracture flats on the wheel surface, as described in Section 3.2.3.
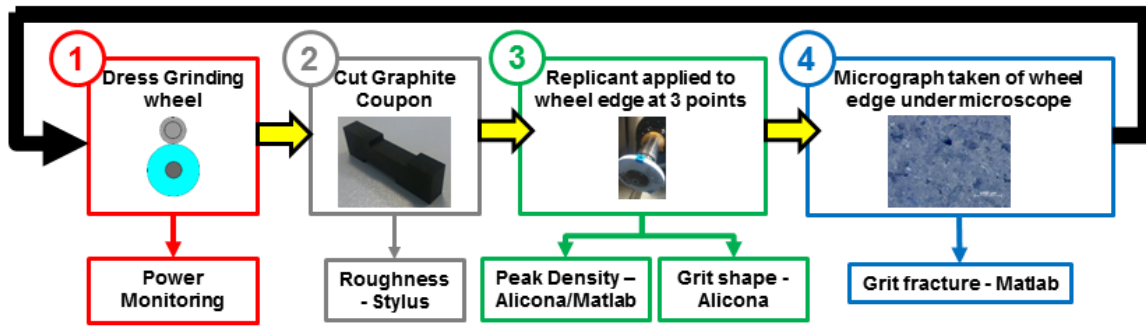
FIGURE 3.11 – EXPERIMENTAL STEP FLOW DIAGRAM FOR WHEEL TOPOGRAPHY MEASUREMENT TRIAL.

3.2.1 EXPERIMENTAL PLAN

The three different abrasive wheels detailed in Section 3.1.2 were dressed under a range of roller dressing parameters including two different infeed rates (0.0005 mm/rev and 0.002 mm/rev) and seven speed ratios (-0.8, -0.6, -0.4, 0.4, 0.6, 0.8, 1) using a flat roller dresser. These were selected to capture a wide scope of speeds and the infeed extremes. The dresser was a single layer, diamond grit which had been partially used and sat in stage II of overall dresser wear (Section 2.4). Wear on the dresser was therefore considered minimal but was monitored by visual observation under an optical microscope (Appendix Di).

Minitab statistical software was used to generate a full factorial design (Levels$^{\text{Factors}}$) limited to two replicates due to time and wheel quantity constraints. The order of testing was split into two blocks with respect to the replicates (1 – 14, 15 - 28) and randomised to reduce the influence of any uncontrolled, time-dependent factors. This test was repeated for each of the abrasive wheels making a total of 74 tests. Table 3.5 shows the complete dressing parameters test plan for the experiment.

TABLE 3.5 - EXPERIMENTAL TEST PLAN WITH RANDOMISED PARAMETER ORDER

Test ID no.	Infeed rate (mm/rev)	Speed Ratio, q_d
A1	0.002	1
A2	0.002	-0.4
A3	0.002	0.8
A4	0.0005	0.8
A5	0.002	0.4
A6	0.0005	-0.6
A7	0.0005	0.4
A8	0.0005	0.6
A9	0.0005	-0.4
A10	0.002	-0.6
A11	0.0005	1
A12	0.002	0.6
A13	0.002	-0.8
A14	0.0005	-0.8
A15	0.0005	-0.8
A16	0.0005	1
A17	0.0005	-0.4
A18	0.0005	0.6
A19	0.002	-0.4
A20	0.002	0.4
A21	0.002	1
A22	0.002	0.8
A23	0.002	0.6
A24	0.002	-0.6
A25	0.0005	0.4
A26	0.0005	-0.6
A27	0.002	-0.8
A28	0.0005	0.8

Before each test, the wheel was dressed to a radial depth of 0.3 mm to remove any defects from the previous dress. The wheel was then dressed again according to the experimental design parameters and the power output of the grinding spindle recorded. A small graphite coupon was then ground with the newly dressed wheel to measure the average roughness (Section 3.2.3). All dressing was performed to a constant volume of 2×10^3 mm^3 material removal after each dress, meaning increased dress depths as the wheel radius reduced.

A single grinding cut was made into the graphite coupon at a constant wheel surface speed of 50 m/s and feed rate of 1200 mm/min (Figure 3.12C).
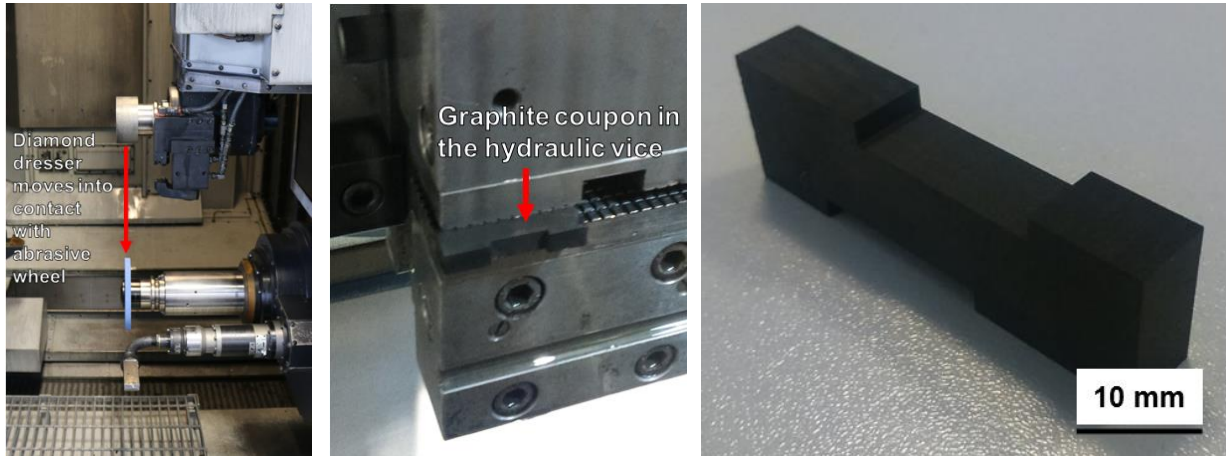
A. **B.** **C.**

FIGURE 3.12 – EXPERIMENTAL TEST STEPS (A) ROLLER DRESSER MOVED INTO CONTACT WITH WHEEL (B) MOUNTED GRAPHITE COUPON AFTER GRINDING (C) ISOMETRIC VIEW OF GROUND GRAPHITE COUPON.

To understand the influence of the engineered grits in the hybrid wheel the 100% triangular grit wheel (Table 3.2) and the hybrid comparator were also tested. The wheels were dressed at two different infeed rates (0.002 mm/rev and 0.0005 mm/rev) and three speed ratios (0.8, 0.4, -0.8) according to the method described above. Power monitoring was performed during dressing and graphite coupon roughness measured. The full factorial experimental test with two replicates is shown in Table 3.6.

TABLE 3.6 – EXPERIMENTAL TEST PLAN WITH 100% TRIANGULAR GRIT ABRASIVE WHEELS.

Test ID no.	Infeed rate (mm/rev)	Speed Ratio, q_d
B1	0.0005	0.4
B2	0.002	0.4
B3	0.002	-0.8
B4	0.0005	-0.8
B5	0.002	0.8
B6	0.0005	0.8
B7	0.002	0.8
B8	0.0005	-0.8
B9	0.0005	0.8
B10	0.0005	0.4
B11	0.002	-0.8
B12	0.002	0.4

To measure the power consumption during dressing the equipment and sampling technique described in Section 3.1.5 was applied. The power was monitored when the grinding wheel was in

free rotation (not in contact with the dresser) with coolant applied. It was then measured whilst the dresser roller was in contact with the abrasive wheel. The reported net power consumption in the results is the power during dressing minus that measured whilst the wheel was in free rotation (Equation 3.1). This is to ensure the reported power is only a result of dressing response.

$$P_d = P_s - P_f \qquad \textbf{EQUATION 3.1}$$

Whereby P_d is the net power consumption of dressing, P_s is power during dressing and P_f is the power consumption when the wheel is in free rotation.

3.2.2 WHEEL TOPOGRAPHY MEASUREMENT

The aim of the trial was to investigate the impact of dressing parameters on the topography of different abrasive wheels, therefore a sensitive method needed to be designed to capture changes in the topography as a result of dressing. The selected method must accurately capture any variation in the topography, be repeatable and practical to be performed on a large number of experimental tests.

After the second dressing cut was performed a graphite coupon (Grade GD4430, full specification in Appendix Dii) was cut by the wheel at a speed of 50 m/s and feed rate of 1200 mm/min. The graphite material is very soft and cut easily and can therefore provide a direct snapshot of the 2D average topography of the wheel after each cut. The coupon roughness was measured in the lay direction (perpendicular to the cutting feed rate) using a Mitutoyo SJ301 portable roughness probe under ISO1997 standard. A force of 5 N with an evaluation length of 4.0 mm were used. The probe applied a Gaussian filter and the cut off wavelength set to 0.8 mm. Five measurements were taken per coupon and the average value calculated. The output measurements of this equipment were Ra (average roughness), Rz (height between max peak and lowest valley) and Rq (root-mean-square roughness).

A.   **B.**
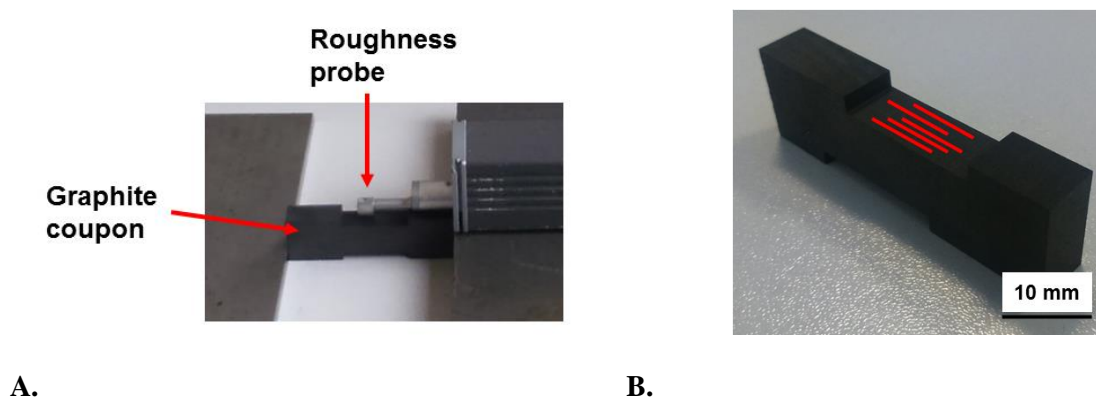
FIGURE 3.13 – (A) PORTABLE ROUGHNESS PROBE MEASURING THE RA OF THE GRAPHITE COUPONS AFTER DRESSING (B) DIAGRAM OF THE ROUGHNESS MEASUREMENT POSITIONS (RED LINES) ON THE COUPON.

There are many techniques that have been used to capture grinding wheel topography in literature (Section 2.5). Based upon the equipment available, accuracy of the measurement and processing time the replica method was the most fit-for-purpose. Struers Repliset T3 two-part silicon rubber replicate material was selected as to take the copy of the abrasive wheel surface (see Appendix C for the selection study) which was then measured under a variable height microscope.

3D printed plastic jigs were designed to fit onto the outer surface of the abrasive wheel to ensure a consistent volume of replica material was applied (Figure 3.14). These jigs were evenly spaced at three locations around the circumference of the wheel and the replica material applied using a dispenser gun enabling thorough mixing of the replicate. The samples were allowed to cure for 10 minutes before being removed and scanned under an Alicona InfiniteFocusSL 3D non-contact profik lometer (see Appendix Diii) to take a 3D surface scan of the wheel replica samples. Vertical and lateral resolutions of 1 µm and 10 µm were used, respectively, and an area of 5.7 mm² scanned at the set magnification of the lens (i.e. x100). A 3D representation of the replicate surface was generated which is an inverse of the wheel surface. Any overall tilt on the samples was removed using form removal algorithms in the software.
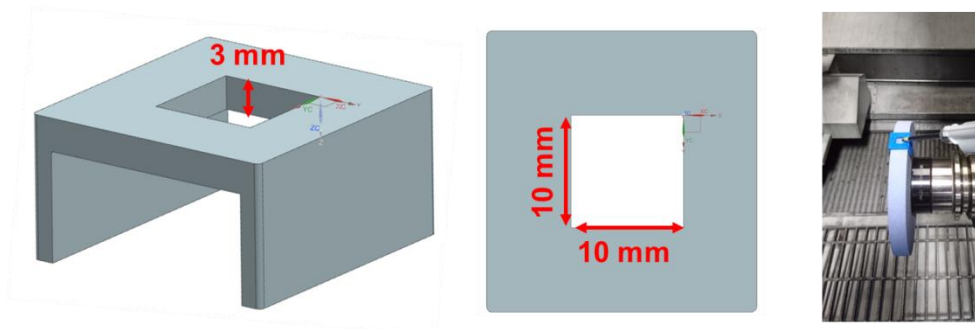
FIGURE 3.14 - DIMENSIONS AND APPLICATION OF THE 3D PRINTED REPLICATE JIGS ONTO THE ABRASIVE WHEELS [241]**.**

The Alicona system generates a distribution of measured heights over the scanned area. Any peak on the surface of a grinding wheel can be considered as the single tip of a cutting grit. According to Blunt et al. [4] 'a peak is defined as a point in the data array which is higher than its eight nearest neighbours' and this is used to define the number of peaks (or potential cutting points) on the surface of the abrasive wheel. Accurately determining micropeaks on the abrasive grits is very difficult, therefore only the highest peaks of individual grits were considered in this research. This enables the identification of whole-grain pull out and gives a better representation of the wheel surface topography. To examine only whole grain peaks, a reduction in the lateral spacing (reduction in horizontal resolution) of the scan sample measurements was required using the equation developed by Butler et al. [159] (Equation 3.2).

$$\frac{d_g}{4} \leq SS_{opt} \leq \frac{d_g}{3} \qquad\qquad \textbf{EQUATION 3.2}$$

SS_{opt} is the optimum sample spacing and d_g is the average grain size whereby an average grain size was found to be 220 μm for the conventional grits along the longest dimension after measurement of multiple grits on six different wheel surfaces. Using equation 3.2 the lateral spacing was reduced to 66 μm. This sample spacing was applied to the hybrid wheel as it contained similar sized conventional grits. It was also used with the elongated grit wheel for comparison however the large aspect ratio of the grits created some uncertainty as grit orientation would greatly influence the number of detected high points. Once the sample spacing of the 3D surface scan was reduced (see Figure 3.15) an in-house Matlab software program was developed and employed to identify peaks according to the definition by Blunt et al. [4]. The number of peaks was measured for each replicate sample, averaged and then reported as the number of peaks per unit area (peaks/mm²). Missing data points were discounted if they were identified as a peak.
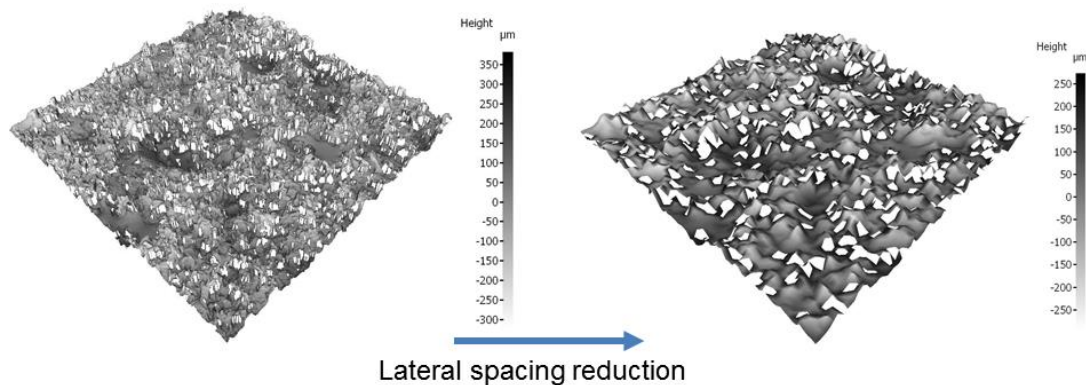
FIGURE 3.15 - REDUCTION IN THE SAMPLE SPACING FOR THE ALICONA SCAN IMAGE TO IDENTIFY PEAKS ON THE WHEEL.

A histogram of the distribution of heights on the surface was also generated using the captured information from the high resolution 3D surface scan. This was plotted as a cumulative frequency graph in which the negative region of the plot represents the valleys on the replicate (and therefore the peaks on the wheel) (Figure 3.16). The gradient of the slope in this region indicates the sharpness of the grits. A large gradient signifies blunt grits as a greater volume of the grit is visible. If the gradient is low then the grits on the surface are sharp and less of the grit is apparent (Figure 3.17). The gradient of the slope was measured to a 100 μm penetration depth into the surface of the wheel as this was approximately half the size of an abrasive grit and forms the sharp cutting region.
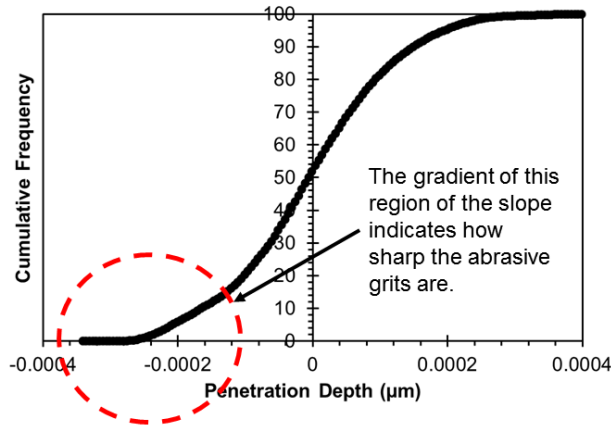
FIGURE 3.16 - CUMULATIVE FREQUENCY (OF % SCAN VOLUME) FOR ALL THE HEIGHTS MEASURED ON THE WHEEL REPLICATE. THE GRADIENT OF THE SLOPE IN THE HIGHLIGHTED REGION INDICATES THE SHARPNESS OF THE ABRASIVE GRITS.
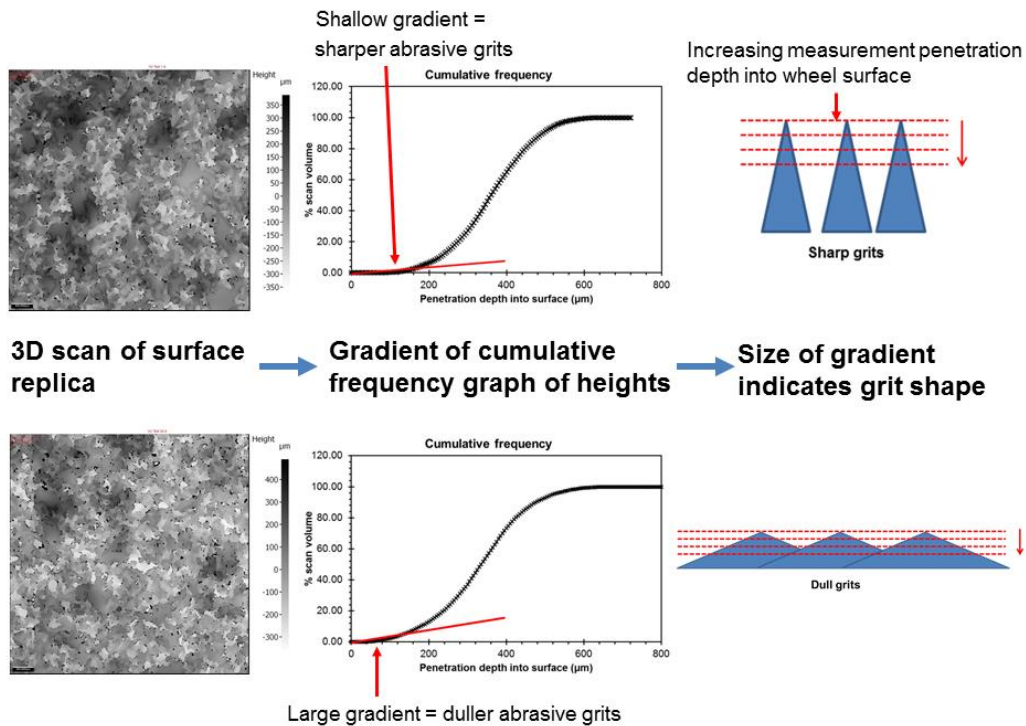
FIGURE 3.17 – GRIT SHAPE MEASUREMENT PROCESS.

The abrasive wheels were also placed under an optical microscope to investigate the fracture behaviour of the abrasive grits during dressing. The abrasive wheel was placed under a Zeiss Discovery V8 optical microscope after each dressing cut. A x10 magnification lens was used together with an incident light source perpendicular to the wheel surface (Figure 3.18A) at a constant brightness. Therefore the brightest spots on the resulting image are an indicator of flat regions on the wheel where the majority of the light is reflected back to the microscope (Figure 3.18B). Using

optical incident light has been shown to be an adequate method to determine flat regions on abrasive wheels as shown in literature [81], [242].
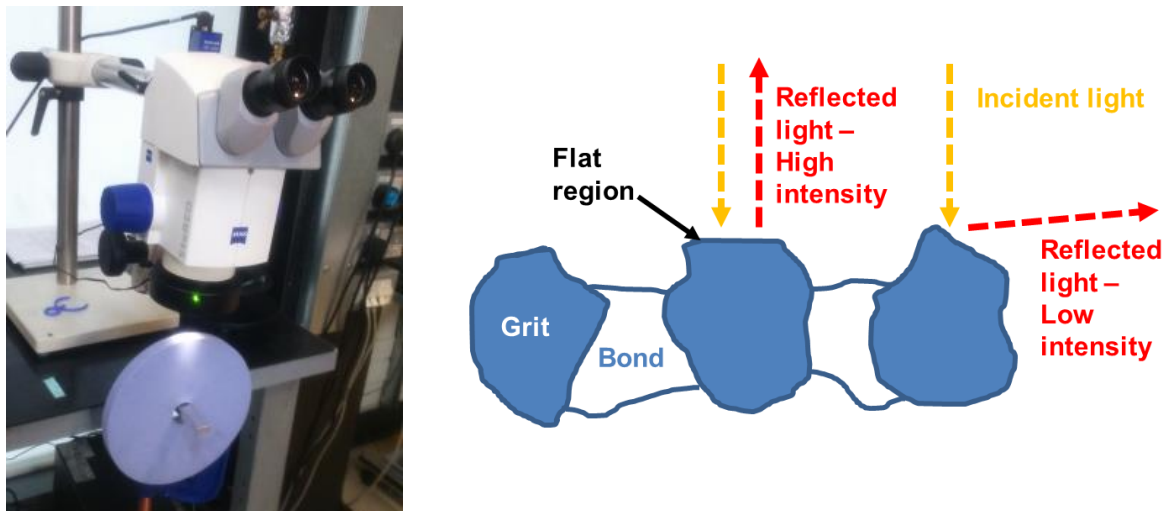
A. **B.**

FIGURE 3.18 – (A) CAPTURING OPTICAL IMAGES OF THE ABRASIVE WHEEL (B) THE PRINCIPLE OF BRIGHT SPOTS ON THE OPTICAL WHEEL IMAGE.

For each abrasive wheel type (standard, hybrid and elongated) high magnification images (x25) were used to identify clear flat regions on the abrasive grits. Six different grit flats for each wheel type were identified visually and using the Matlab Image Viewer app the average pixel value for a square region around the flat fractured grit was calculated (see Figure 3.19). The overall average across the six images was then evaluated to give a pixel intensity threshold above which the region can be deemed a fracture or wear flat. Greyscale images were used for the analysis so that the only variation in the image was pixel intensity.
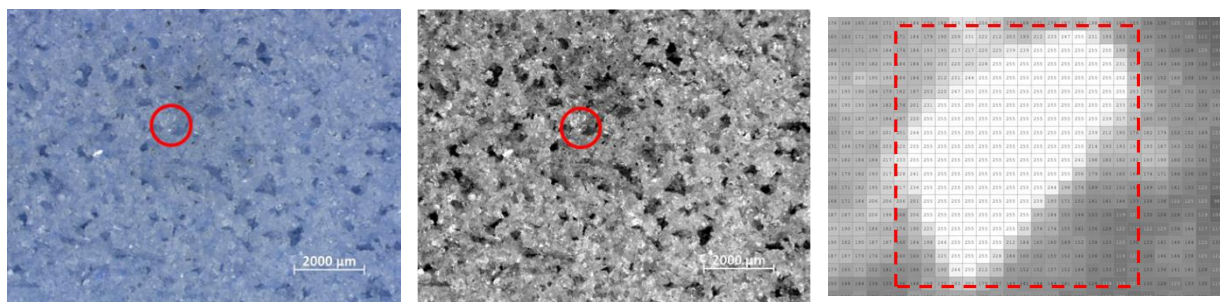
A. **B.** **C.**

FIGURE 3.19 – DETERMINING THE THRESHOLD INTENSITY OF FRACTURE FLATS (A) IDENTIFICATION OF A FRACTURE FLAT (B) CONVERSION OF THE IMAGE TO GREYSCALE (C) CALCULATION OF THE THRESHOLD INTENSITY IN MATLAB.
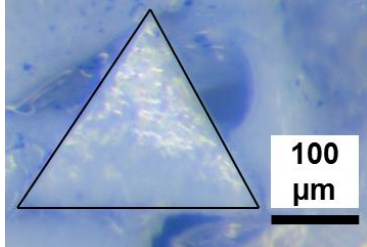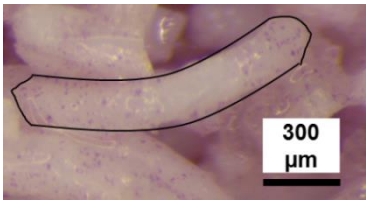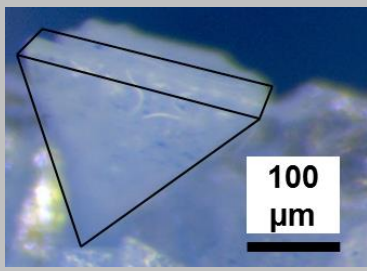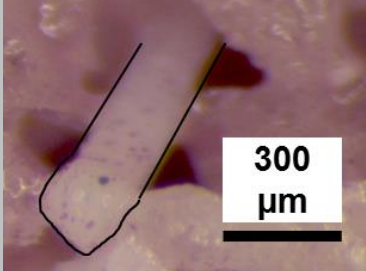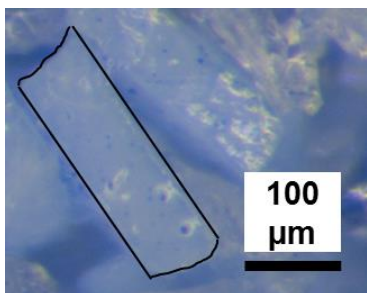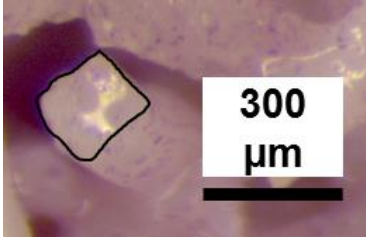
For the standard wheel type the threshold intensity was found to be 227, for the hybrid wheel 242 and for the elongated grit wheel 225, with the difference in threshold value likely a result of the

different colouration of the wheels. A further Matlab program was written to find the total number of pixels in each x10 magnification wheel image with an intensity value equal-to or above the threshold intensity when converted to greyscale. This was calculated as a percentage of pixels of the entire image. Three optical images at different points on the wheel were taken after every dressing pass. The percentage of pixels on fracture flats was calculated and then the average of the three images were used as the final percentage of fracture flats for each test. Further explanation of the threshold calculation technique is given in Appendix Div.

The variation in abrasive grit orientation on the wheels was also measured. The standard grit wheel used conventional grit shapes which are considered approximately spherical (Section 2.3.2) and so measuring their orientation is extremely difficult. For the engineered wheel types (triangular grits of the hybrid wheel, spaghetti grits in the elongated grit wheel) however, their unique shape and high aspect ratios (ratio of the longest dimension to the smallest dimension for an individual grit) means that the grit orientation could be very influential on the grinding wheel topography and dressing behaviour.

A single high magnification image (x25) of the wheel topography was taken after each dressing cut. The images were divided into nine evenly spaced squares and the analysis performed in just the central square due to the volume of analysis to be performed (Figure 3.20). The number of engineered grits in the central square were counted manually and each grit categorised according to their orientation (Table 3.7). Only grits in focus (and therefore on the outer surface of the wheel) were counted and those grits touching or intersecting the line of the central box were also included. The investigation was only performed on the wheels containing engineered grit shapes. The conventional wheels were assumed to have a uniform grit orientation due to the spherical shape of the abrasive grits. Therefore for any comparative analysis, the frequency of grits in the central square for the conventional wheels was divided three-ways (the number of orientation categories, Table 3.7) to assume an even distribution of grit orientations.

TABLE 3.7 - THE THREE DIFFERENT ORIENTATION CATEGORIES FOR THE ENGINEERED GRITS ON THE HYBRID AND ELONGATED GRIT WHEELS.

Hybrid wheel – triangular engineered grits		Elongated grit wheel – spaghetti engineered grits	
Example image	Orientation (°)	Example image	Orientation (°)
	0 - 20 (flat)		0 - 20 (flat)
	20 – 70 (tilted)		20 – 70 (tilted)
	70 – 90 (edge)		70 – 90 (end)
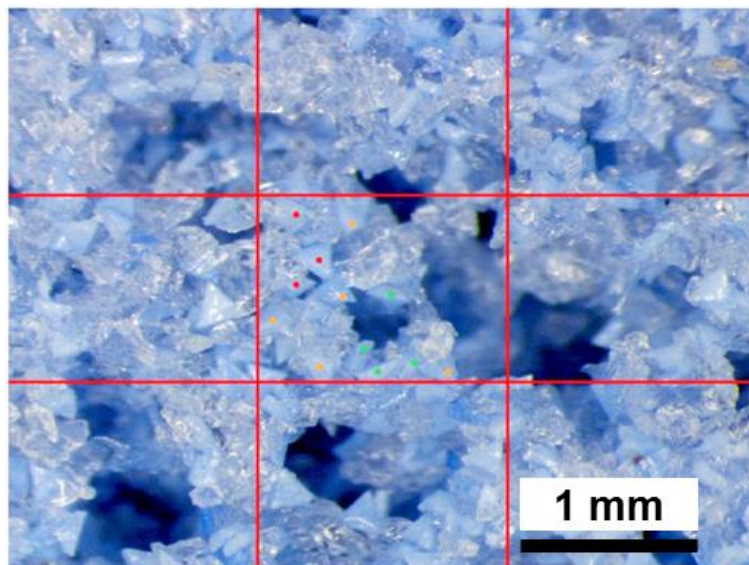
FIGURE 3.20 – AN EXAMPLE OF IMAGE DIVISION AND ENGINEERED GRIT ORIENTATION CATEGORISATION (COLOURED SPOTS).

3.2.3 SCANNING ELECTRON MICROSCOPY OF ABRASIVE WHEELS

To better capture the dressing mechanisms on the different grit shapes, sections of the wheels were obtained for direct SEM imaging. The three wheel types (conventional, hybrid and elongated) were examined under two different dressing extremes from aggressive (infeed rate 0.002 mm/rev, speed ratio 0.8) to gentle (infeed rate 0.0005 mm/rev, speed ratio -0.8) to capture the greatest variation in the wheel topography.

Due to volume restrictions of the vacuum chamber of the SEM, destructive preparation of the wheel samples was required. This also limited the number of different dressing conditions that could be tested. The wheels were broken by impact and approximately 10 mm x 10 mm x10 mm samples taken from the outer dressed surface (Figure 3.21). The non-conductive vitreous-bonded alumina wheels required gold coating to generate a conductive layer on the surface to capture an SEM micrograph. The wheel sections were mounted on small SEM stubs with silver paint before coating in an Emscope SC500 sputter coater unit for 3 minutes at 15 mA deposition current. The coated samples were allowed a minimum of 12 hours to fully dry.

A.   **B.**
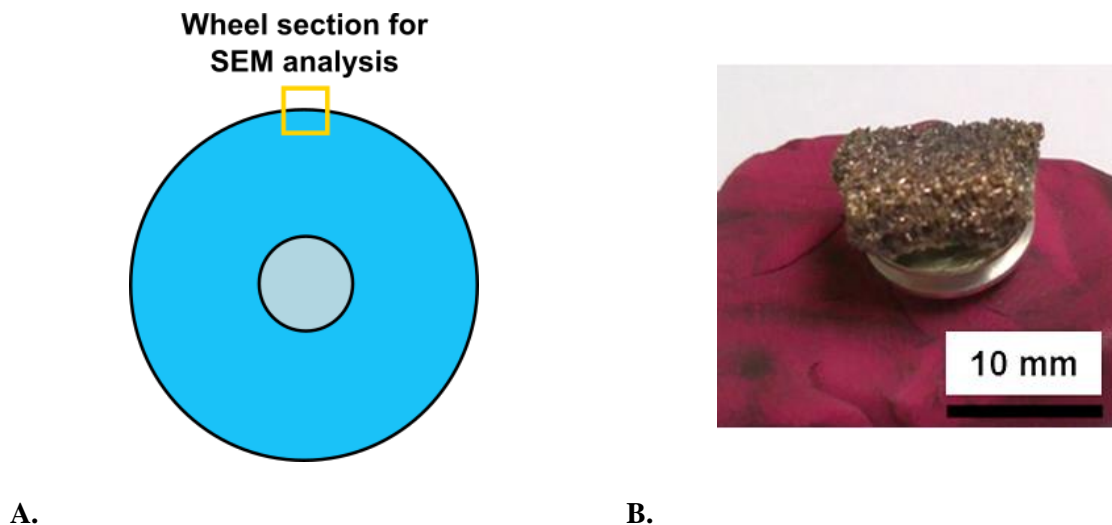
FIGURE 3.21 – (A) SCHEMATIC OF THE WHEEL SURFACE SECTION TAKEN FOR SEM ANALYSIS (B) EXAMPLE SAMPLE.

Imaging was performed in a FEG-SEM under a voltage of 20 kV, a spot size of 3.0 and working distance of 10 mm. All the samples were imaged at 80x magnification followed by higher magnifications to capture any notable features.

3.3 INFLUENCE OF GENERATED TOPOGRAPHY ON GRINDING PERFORMANCE

The following experimental continuous dressing grinding investigation was designed to understand the influence of dressing parameters on grinding behaviour of CMSX-4 Ni-base superalloy material, using the knowledge obtained from Section 3.2 to explain the phenomena. Continuous dressing grinding was performed in order to reduce grinding wheel wear effects and enable an improved analysis of the effects of the generated wheel topography only on grinding performance.

Figure 3.22 shows the experimental flow diagram wherein the entire trial was conducted using the wheels, material and equipment detailed in Section 3.1.
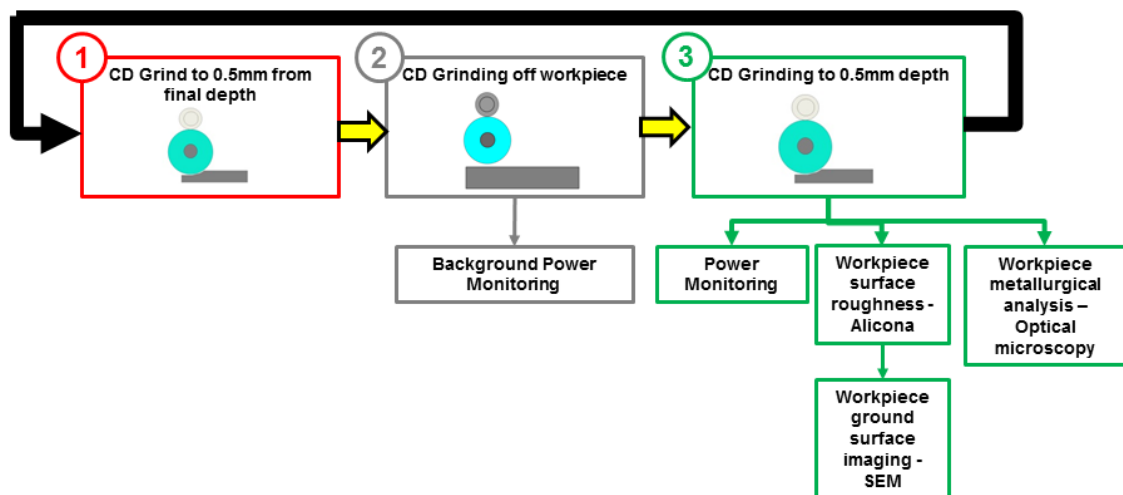
FIGURE 3.22 – EXPERIMENTAL STEP FLOW DIAGRAM FOR CD GRINDING TRIAL.

3.3.1 EXPERIMENTAL PLAN

The CMSX-4 slab (Section 3.1.4) was ground (0.3 mm a_e) initially to remove casting defects and create a flat surface start point. The most extreme dressing parameters and the central values were selected according to the results obtained from the trial in Section 3.2 and available materials for the grinding trials. These were dressing infeed rates of 0.0005 mm/rev and 0.002 mm/rev, and the speed ratios of -0.8, 0.4 and 0.8. The same dressing tool was used for this trial as in the previous experiment (3.2) and dressing grit wear monitored under an optical microscope. Semi-finishing grinding parameters were employed and kept constant throughout at 1200 mm/min feed rate, 50 m/s wheel surface speed and 0.5 mm depth of cut. Table 3.8 shows the test plan for the continuous dressing

parameters where every parameter variable was tested and repeated once. A total of 12 cuts per wheel type were performed using the entire width of the wheel (20 mm) with two cuts per dressing condition.

TABLE 3.8 - CD GRINDING TEST PLAN

Test ID no.	Infeed rate (mm/rev)	Speed ratio, q_d
C1	0.0005	0.8
C2	0.002	0.4
C3	0.002	0.8
C4	0.002	-0.8
C5	0.0005	0.8
C6	0.002	0.4
C7	0.002	0.8
C8	0.002	-0.8
C9	0.0005	0.4
C10	0.0005	-0.8
C11	0.0005	0.4
C12	0.0005	-0.8

Figure 3.23 shows schematics of the grinding tests on the CMSX-4 slabs. Each cut was performed in order to preserve ground surface for surface quality and metallurgical analysis.

A. **B.**
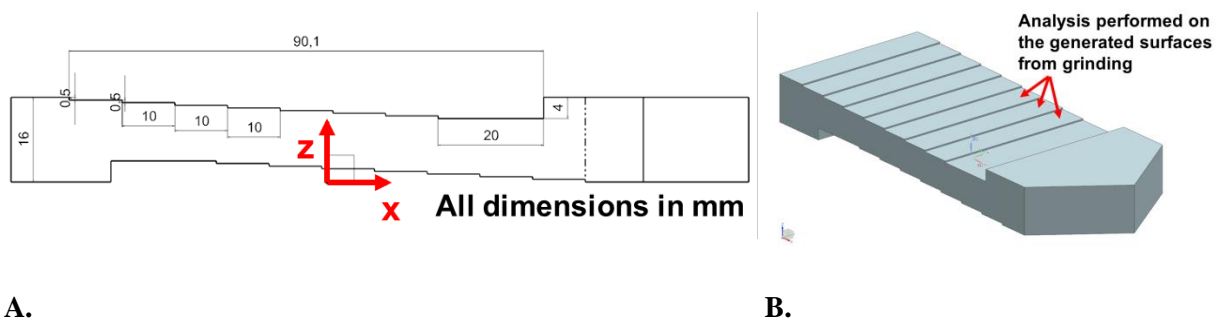
FIGURE 3.23 – (A) CROSS SECTION OF CD GRINDING PLAN ON CMSX-4 SLABS (B) 3D ISOMETRIC VIEW OF COMPONENT AFTER GRINDING.

After cleaning the slab a 20 mm width cut (cut 1) was performed to a cut depth of 0.5 mm and the power consumption recorded. Following this, the cut position was shifted 10 mm in the x direction (Figure 3.23A) and a cut executed to 0.5 mm depth from the surface (the same final depth as cut 1). This became the new datum surface and from this, cut 2 was performed to a depth of 0.5 mm. The cut position was then shifted in x by 10 mm again and a datum surface created at the same depth as cut 2. The entire process was then repeated until all the test cuts were completed, leaving a stepped final workpiece upon which surface analysis could be performed for each test cut.

3.3.2 IN-PROCESS MONITORING

CD grinding power consumption was measured using equipment described in Section 3.1.5. A dummy grinding pass with 1 mm offset from the workpiece was performed before each grinding test cut (same dressing parameters as the cut design) and power consumption of the grinding spindle was recorded to capture the consumption of the external factors (background), such as dressing and coolant, without removing workpiece material. A second grinding pass was then conducted with a 0.5 mm depth of cut into the workpiece and the spindle power was measured. The net difference between the background power and the material removal power was then calculated to give the power consumption from grinding only (Equation 3.3 and Figure 3.24).

$$P_{net} = P_{tot} - P_b \qquad \text{EQUATION 3.3}$$

Whereby P_{net} is the net power consumption from grinding only, P_{tot} is the total power consumption of the CD grinding process with material removal and P_b is background power.

A.   **B.**
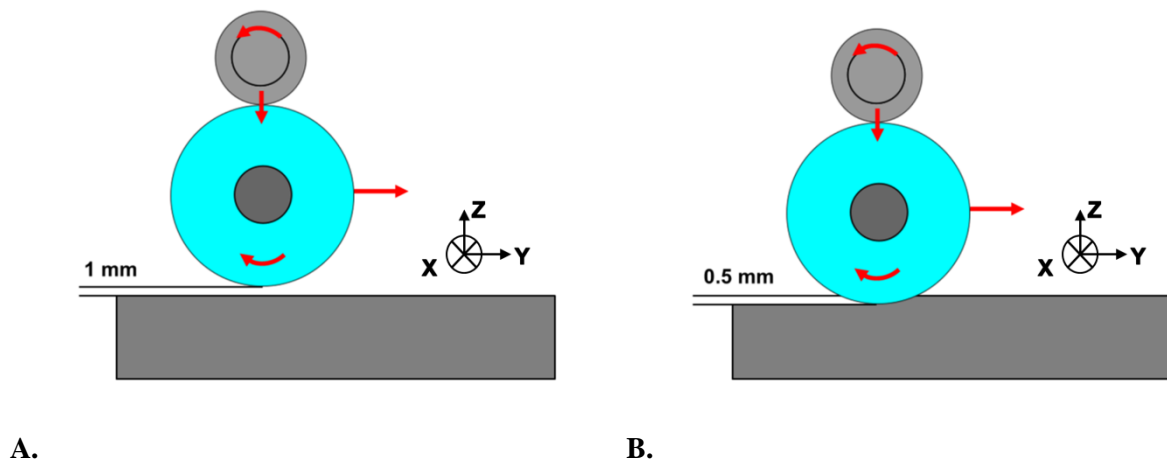
FIGURE 3.24 – SCHEMATIC OF THE CD GRINDING TRIAL UNDER SYNCHRONOUS SPEED RATIO (A) INITIAL BACKGROUND GRINDING PASS WITH 1MM OFFSET FROM WORKPIECE (B) SECOND GRINDING PASS WITH MATERIAL REMOVAL AT 0.5MM DEPTH OF CUT. *NOT TO SCALE!*

3.3.3 POST PROCESS MEASUREMENT

Figure 3.25 shows the schematic of the measurement plan using the technique described in Section 3.1.7.
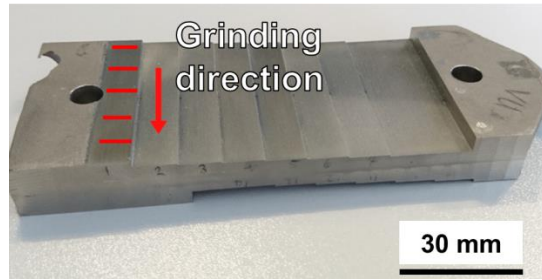
FIGURE 3.25 – SCHEMATIC OF THE ROUGHNESS CHARACTERISATION AFTER THE GRINDING TRIALS SHOWS THE LINES OF MEASUREMENT (RED LINES) AND THE GRINDING DIRECTION.

Further analysis was performed on the ground surface using a scanning electron microscope (SEM). The large depth of field and high resolution of the SEM enables analysis of the abrasive grit tracks on the ground workpiece surface to determine the dominant mechanism during the applied grinding conditions. Each ground cut was sectioned along the cut to generate samples of a suitable size for the SEM vacuum chamber. The centre of the entire grinding cut was identified and a 3 mm x 3 mm square area (large enough to capture the average appearance of the ground surface) scanned in a TM3030Plus Tabletop SEM to locate any notable features (such as deep scratches, redeposited material or embedded foreign material). Images at 200x (to capture result of multiple grits) and 600x (to clearly image surface features) magnification, with a beam voltage of 15 kV, were captured in a minimum of three different places in the imaged region. These parameters were selected based on a systematic imaging study that found these magnifications to have the best compromise between resolution and capturing as much of the surface as possible. Magnification of 1200x was also used for exceptional features of interest such as embedded abrasive grits in the surface. Figure 3.26 shows a schematic of the scanned area on the ground sample.
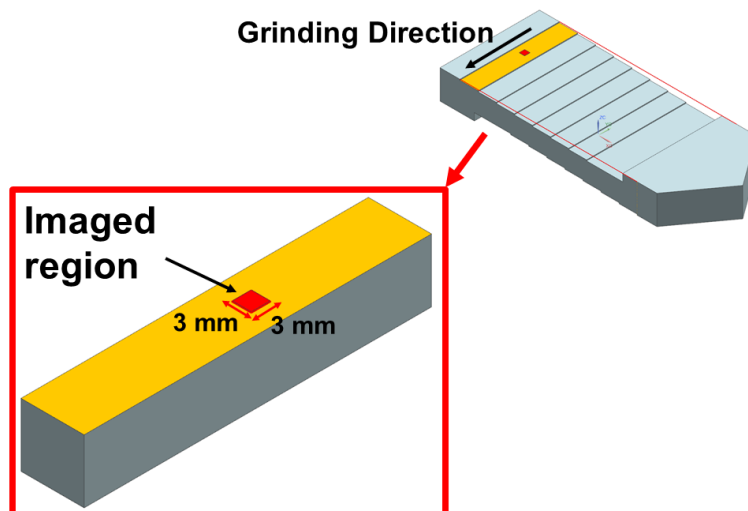
FIGURE 3.26 – SCHEMATIC OF THE SEM IMAGED AREA ON THE GROUND WORKPIECE WHERE GRINDING CONDITIONS ARE ASSUMED TO BE CONSISTENT.

Energy Dispersive X-ray (EDX) spectroscopy was used to determine chemical compositions of the embedded particle features detected on the ground surfaces particles using a 20 kV beam at a working distance of 10 mm and spot size of 3.0. This technique fires high energy electrons at the sample, exciting electrons to new energy levels in the atomic shell. As the electrons drop back down to lower energy levels they release the excess energy in the form of an X-ray. These X-rays are detected and depending on their energy can be used to determine the elements composing the sample.

Analysis of the metallurgical sub-surface of the workpieces was conducted by sectioning each workpiece in half by Wire Electrical Discharge Machining (WEDM). The slabs were then sectioned (as according to Figure 3.27), prepared and analysed to the method in Section 3.1.8
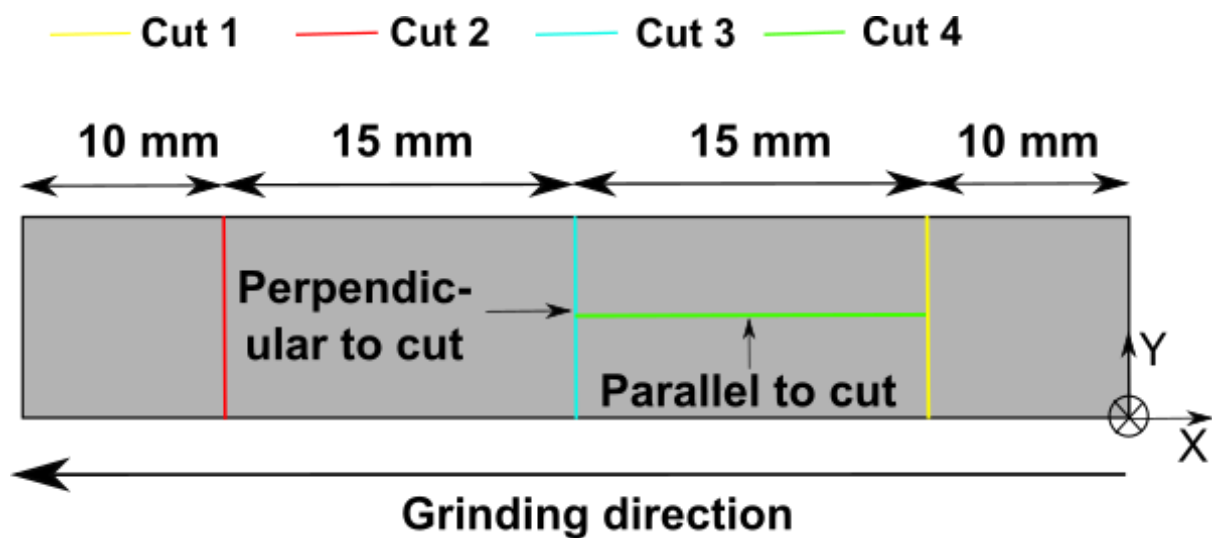
FIGURE 3.27 – SECTIONING SCHEMATIC FOR SUB-SURFACE ANALYSIS SAMPLES.

Two samples per grinding cut (longitudinal and transverse to the grinding direction, cut 4 and cut 2 respectively from Figure 3.27) were produced and analysed

3.4 BREAKDOWN OF GRINDING WHEEL TOPOGRAPHY

Figure 3.28 shows the flow diagram of the experimental procedure used to assess the wheel wear and identify wheel breakdown mechanisms in the studied abrasive wheels. A channel the full width of the wheel (20 mm) was ground into the workpiece slabs to a depth of 2.5 mm. This was immediately followed by a CD grinding pass (using the relevant dressing parameters for the test) to bring the final depth to 3 mm from the surface and generate a 'zero wear' surface. The wheel was then dressed according to the relevant dressing parameters to a radial depth of 0.3 mm. Repeated non-CD grinding passes were then performed on the workpiece (by half of the wheel width to capture wheel

wear) whilst grinding forces and power were recorded. This was performed for all three wheel types so a total of nine abrasive cuts were performed for each dressing condition and wheel type.
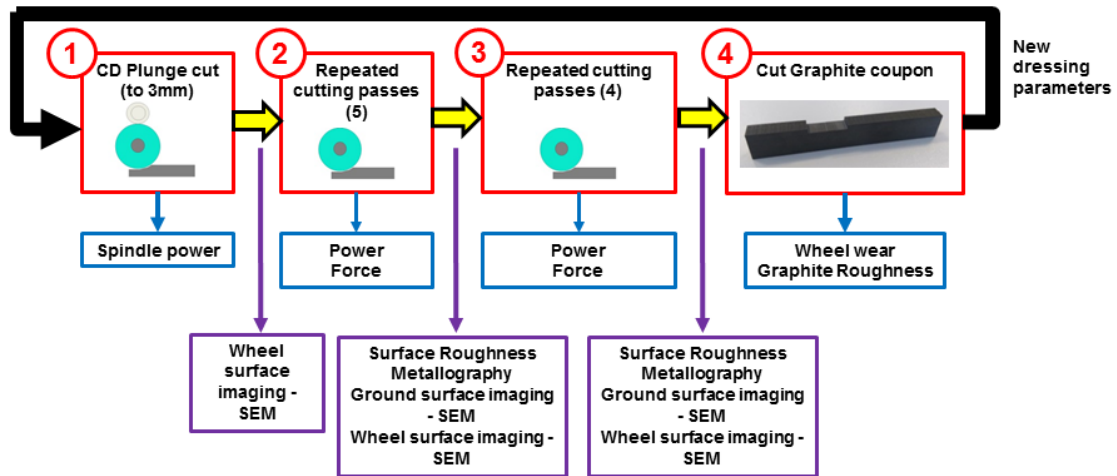
FIGURE 3.28 – EXPERIMENTAL FLOW DIAGRAM FOR WHEEL BREAKDOWN STUDY.

3.4.1 EXPERIMENTAL PLAN

Three different dressing conditions with the available grinding wheels were tested based upon the results from Section 3.3. The dressing conditions in which the lowest surface roughness was achieved at the lowest power consumption were used:

- 0.002 mm/rev infeed, -0.8 speed ratio

- 0.0005 mm/rev infeed, 0.8 speed ratio

Aggressive dressing conditions at high infeed (0.002 mm/rev) and high speed ratio (0.8) were also tested as these are typically used in industry and were shown in to generate a rough wheel topography in Sections 3.2 and 3.3. Table 3.9 shows the design of experiments using a full factorial design in which every dressing condition was tested for each of the abrasive wheel types. Fixed grinding parameters at 1200 mm/min feedrate, 50 m/s wheel surface speed and 0.5 mm depth of cut were used to maintain consistency with the previous trial and reduce the number of influencing variables.

TABLE 3.9 - CUTTING STRATEGY REPEATED FOR EACH WHEEL TYPE. GRINDING PARAMETERS WERE CONSTANT THROUGHOUT.

Surface no.	Total depth from surface (mm)	Total no. passes without dressing	Dressing infeed rate (mm/rev)	Dressing speed ratio
D1	3.0	0 (CD Grinding)	0.002	0.8
D2	2.5	5	0.002	0.8
D3	2.0	9	0.002	0.8
D4	3.0	0 (CD Grinding)	0.002	-0.8
D5	2.5	5	0.002	-0.8
D6	2.0	9	0.002	-0.8
D7	3.0	0 (CD Grinding)	0.0005	0.8
D8	2.5	5	0.0005	0.8
D9	2.0	9	0.0005	0.8

The cut position of the wheel was shifted by 10 mm each test so that half the wheel would cut material (10 mm wide cut) and half would rotate in free space. This allows more efficient use of the sample material as well as a measure of the degree of wear on the wheel.

Five repeat grinding passes were performed on the workpiece, for the sixth pass the wheel position was shifted 10mm again to cut on fresh material followed by three further repeat passes. A total of 9 non-CD grinding passes were made on the workpiece material for each dressing condition with ground surface preserved for the initial CD grind and after the 5th and 9th passes (Figure 3.29).
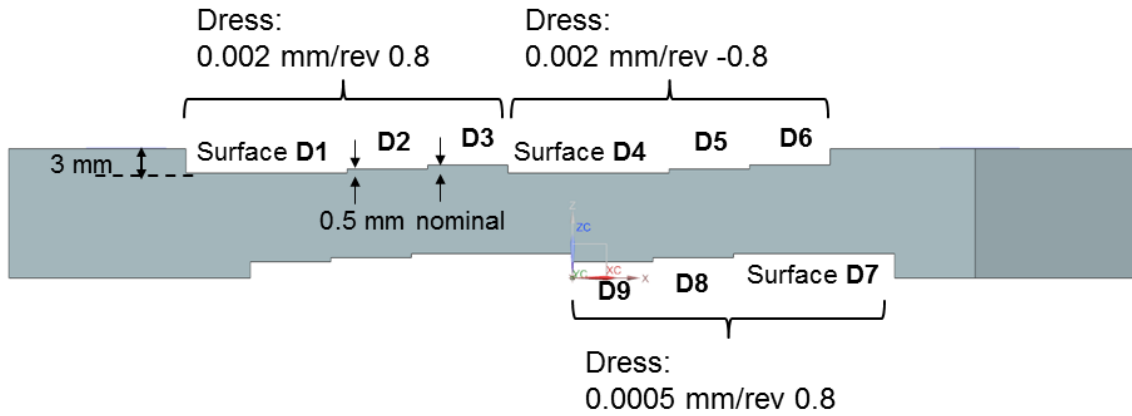
A.
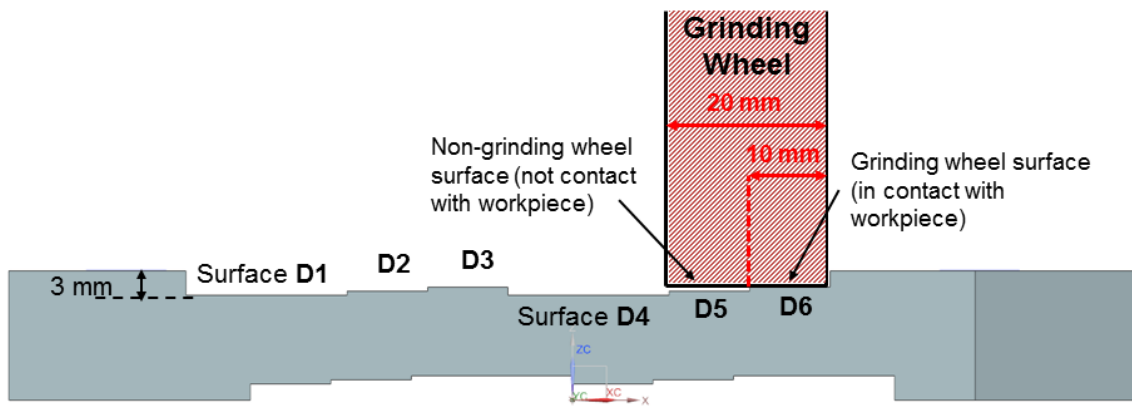
B.

FIGURE 3.29 – (A) SCHEMATIC OF THE GRINDING PLAN INDICATING THE 9 SURFACES PRESERVED AFTER MACHINING (B) SCHEMATIC OF THE GRINDING PLAN SHOWING HOW ONLY HALF THE WHEEL GROUND THE WORKPIECE.

After the ninth grinding pass, a graphite coupon was ground and the step measured to capture radial wheel wear. Surface roughness measurements and SEM images were taken on the preserved surfaces of the workpiece. Metallurgical analysis was also performed on the same samples as well.

The grinding experimental design described above was conducted for the three different wheel types using a single CMSX-4 cast slab workpiece for each wheel.

In order to assess the breakdown behaviour of the hybrid wheel and whether the process is dominated by the engineered triangular grits, the wheel detailed in Table 3.2 containing 100% triangular grits was also tested. The same strategy shown in Table 3.9 was used to capture the power consumption of the 100% engineered grit wheel under the three different dressing conditions. Grinding power and force measurements were taken for each pass using the method described in Sections 3.1.5 - 3.1.6.

3.4.2 POST PROCESS MEASUREMENT

As only half of the wheel was used to grind the workpiece material (Figure 3.29B), the worn part of the wheel was used to capture the degree of dimensional (radial) wear during the process. Graphite coupons were cut after the 9th grinding pass for each dressing condition and wheel type, using the same grinding parameters to cut the slabs, to preserve the wheel topography and maintain consistency. A small step generated on the coupon was measured to determine the level of wear (Figure 3.30A).

The size of the step on the graphite was measured using an Alicona InfiniteFocusSL variable height microscope with a magnification of x10. A vertical and lateral resolution of 0.2 μm and 4.0 μm respectively were used over a scan area of 20 mm x 3 mm (the entire width of the wheel) and the profile measured in three different locations along the width of the cut. The average line was calculated on both sides of the step (parallel lines) and the distance between them reported as the amount of wear on the abrasive wheel (Figure 3.30B). This was averaged for the three locations to give the overall wheel wear for each grinding test.

A.　　　　　　　　　　　　　　**B.**.
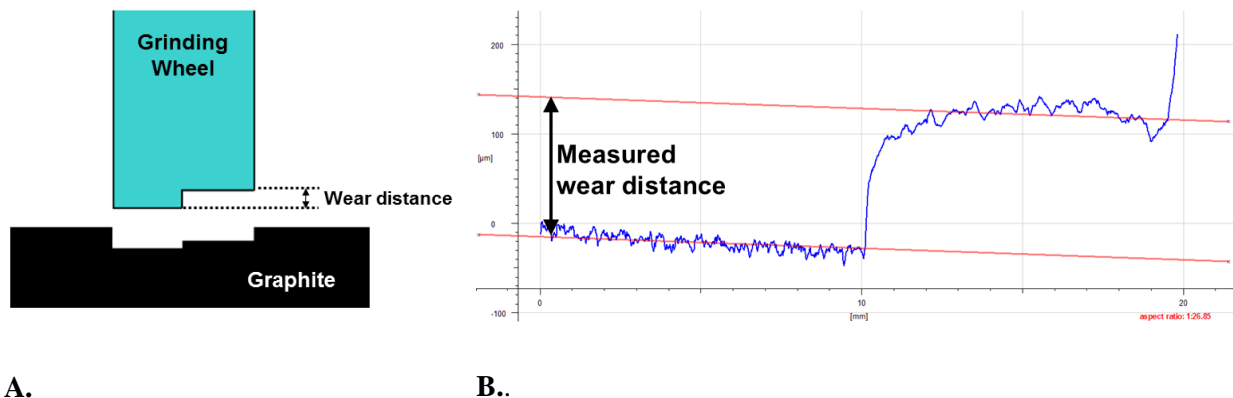
FIGURE 3.30 – (A) DIAGRAM SHOWING HOW WEAR IS CAPTURED ON THE GRAPHITE (B) MEASURED WHEEL WEAR ON ALICONA SYSTEM WITH THE RED LINES INDICATING THE AVERAGE HEIGHT OF EACH SURFACE.

The surface roughness of each preserved ground surface (CD pass, 5th pass and 9th pass) was measured using the technique described in Section 3.1.7. SEM imaging of the ground surfaces was also performed using the same imaging technique as in Section 3.3.3.

After all the DoE tests were completed all the wheels were dressed under the aggressive parameters (0.002 mm/rev infeed, 0.8 speed ratio). A stepped form was then created on each of the wheels with one third of the wheel width in the as-dressed condition, one third after 5 passes and one third after 9 passes (Figure 3.31). Sections of the wheel were then taken, gold coated and observed under an SEM using the technique as described in Section 3.3. This enabled visual comparison of the breakdown of the abrasive grits.
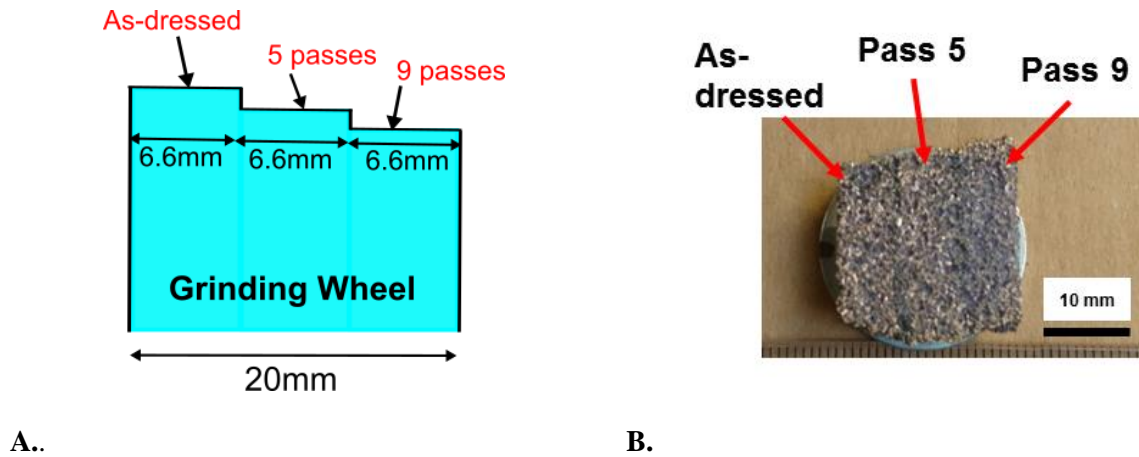
FIGURE 3.31 – (A) SCHEMATIC OF THE STEPPED WHEEL GROUND BY DIFFERENT AMOUNTS (B) MOUNTED AND GOLD COATED WHEEL SECTION FOR SEM ANALYSIS.

3.5 IMPACT OF GRINDING PARAMETERS ON TOPOGRAPHY BEHAVIOUR

A design of experiments was employed to capture how the wheel topography behaves under different grinding conditions and whether the influence of dressing and wear behaviour is similar as in the previous trial.

Figure 3.32 shows the experimental flow diagram for the study. In Sections 3.3 and 3.4, the grinding parameters were kept constant, so in this trial the grinding parameters were varied. A similar approach as in Section 3.4 was selected to perform the grinding cuts with each wheel being initially dressed followed by multiple non-CD grinding passes (with half of the wheel width to capture wear) and spindle power and grinding force measured in-cut.

Surface roughness of the workpiece after the final grinding pass was measured as well metallurgical analysis of the material conducted.
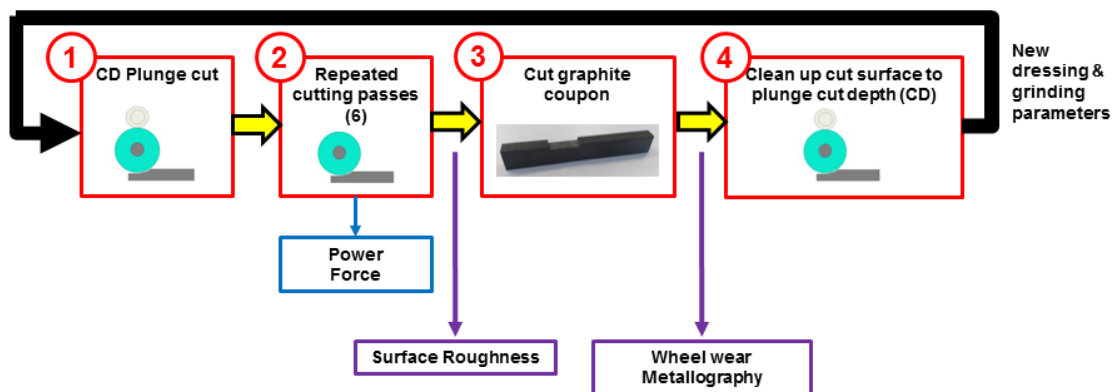
FIGURE 3.32 – EXPERIMENTAL FLOW DIAGRAM FOR GRINDING PARAMETERS TRIAL.

3.5.1 EXPERIMENTAL PLAN

Different combinations of grinding feed rates, depths of cut and wheel speeds were tested. The dressing conditions were also varied to alter the grinding wheel topography. The same dressing conditions as used in Section 3.4 were applied to maintain consistency. Three variations for each parameter were investigated as shown in Table 3.10.

TABLE 3.10 - THE THREE DIFFERENT LEVELS USED FOR EACH GRINDING PARAMETER.

Workpiece feed rate, v_f (mm/min)	Depth of Cut, a_e (mm)	Wheel surface speed, v_c (m/s)	Dressing Conditions (a_d, mm/rev / q_d)
1000	1	50.0	0.002 / 0.8
1500	0.5	40.0	0.002 / -0.8
2000	0.1	30.0	0.0005 / 0.8

A full factorial design of experiment, using the parameters in Table 3.10, provided the maximum amount of data (as every factor variable is combined with every other) however the volume of tests was too large (81 base runs with 1 replicate). Using Minitab statistical software, various DoE techniques were investigated that would provide a more targeted experimental design.

A response surface (Box-Behnken) design does not use an embedded factorial design and instead uses fractions of a 3^k (whereby k is the number of quantitative variables) design with additional centre points [243]. These designs are useful when the safe operating zone is known for the process and have fewer design points than another response surface technique (central-composite). The Box-Behnken design proved to have too many data points though (45 base runs with 1 replicate) and so this method was rejected.

The Taguchi method uses orthogonal arrays to estimate the effect of certain factors on the response mean [244]. It allows the assessment of each effect individually which is useful in this case when there are a number of controlled variables. When it was applied, the technique greatly reduced the number of test points (4 factors at 3 levels gave 9 experimental runs with 1 replicate). The Taguchi method was selected for this investigation as it enabled another replicate to be performed, improving result reliability, as well as its focus on identifying the parameters that cause most variation in a process.

Table 3.11 details the experimental plan wherein cuts 1- 9 show the initial Taguchi design with the whole plan repeated (10 -18) for statistical validity. The entire experimental design was performed for each abrasive wheel type. A total of six passes were conducted for each cutting condition as this was sufficient to capture wheel breakdown behaviour (based on previous results from Section 3.4)

whilst preserving the maximum amount of workpiece material. The ordering of the tests was randomised. An initial plunge cut was performed (as in Section 3.4) to provide enough clearance for half the wheel to grind only in a stepwise approach.

TABLE 3.11 - CUTTING STRATEGY FOR EACH WHEEL TYPE.

Cut ID no.	Feed rate (mm/min)	Depth of cut (mm)	Vc (m/s)	Specific material removal rate, Q' (mm³/ mm s)	Dressing strategy (infeed rate, mm/rev / speed ratio)	No. Passes
E1	1000	1.0	50	16.7	0.0005 / 0.8	6
E2	1500	1.0	40	25.0	0.002 / 0.8	6
E3	2000	1.0	30	33.3	0.002 / -0.8	6
E4	1000	0.5	40	8.3	0.002 / -0.8	6
E5	1500	0.5	30	12.5	0.0005 / 0.8	6
E6	2000	0.5	50	16.7	0.002 / 0.8	6
E7	1000	0.1	30	1.7	0.002 / 0.8	6
E8	1500	0.1	50	2.5	0.002 / -0.8	6
E9	2000	0.1	40	3.3	0.0005 / 0.8	6
E10	1000	1.0	50	16.7	0.0005 / 0.8	6
E11	1500	1.0	40	25.0	0.002 / 0.8	6
E12	2000	1.0	30	33.3	0.002 / -0.8	6
E13	1000	0.5	40	8.3	0.002 / -0.8	6
E14	1500	0.5	30	12.5	0.0005 / 0.8	6
E15	2000	0.5	50	16.7	0.002 / 0.8	6
E16	1000	0.1	30	1.7	0.002 / 0.8	6
E17	1500	0.1	50	2.5	0.002 / -0.8	6
E18	2000	0.1	40	3.3	0.0005 / 0.8	6

Due to the large amount of material required for this trial, after the sixth grinding pass the surface roughness of the material was captured and then ground over to make room for the next cuts. The schematic of the grinding plan is shown in Figure 3.33.
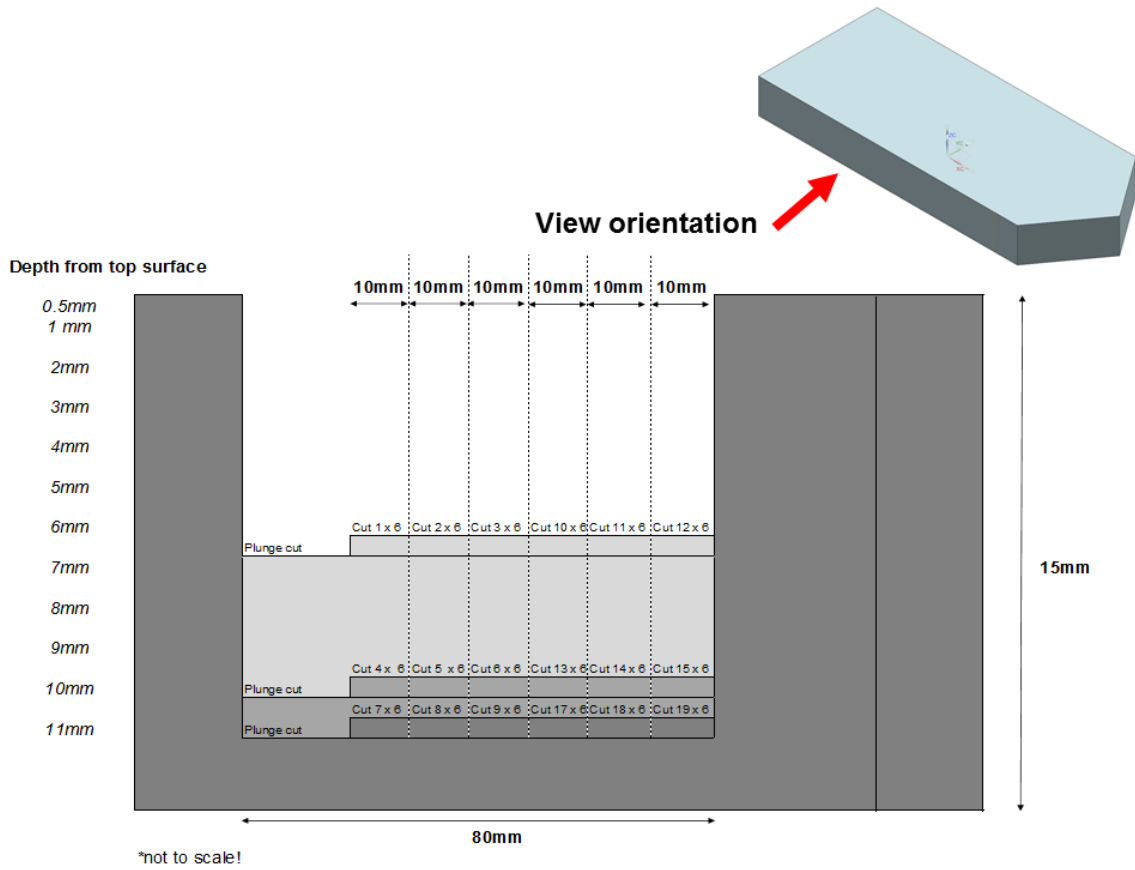
FIGURE 3.33 – SCHEMATIC CROSS SECTION OF THE WORKPIECE WITH THE CUTTING STRATEGY.

The results from the experimental plan in Table 3.11 were used to develop a statistical model for the studied behaviour. To validate this model, further follow up cuts were conducted using parameters beyond those in the experimental zone detailed above. Only single grinding passes in these conditions were performed due to limited workpiece material. The experimental plan for these validation cuts is shown in Table 3.12. Only one dressing strategy was used for these cuts for the sake of materials usage and the simplification of the experimental plan.

TABLE 3.12 - CUTTING STRATEGY FOR THE VALIDATION TRIALS WITH PARAMETERS OUTSIDE THE EXPERIMENTAL PARAMETER ZONE.

Cut no.	Feed rate (mm/min)	Depth of cut (mm)	Vc (m/s)	Specific material removal rate, Q' (mm³/ mm s)	Dressing strategy (infeed rate, mm/rev / speed ratio)	No. Passes
E19	800	0.05	25	0.7	0.002 / 0.8	1
E20	1200	1.0	50	20.0	0.002 / 0.8	1
E21	2100	1.5	35	52.5	0.002 / 0.8	1
E22	800	0.05	25	0.7	0.002 / 0.8	1
E23	1200	1.0	50	20.0	0.002 / 0.8	1
E24	2100	1.5	35	52.5	0.002 / 0.8	1
E25	800	0.05	25	0.7	0.002 / 0.8	1
E26	2100	1.5	35	52.5	0.002 / 0.8	1

For each grinding pass the power and force were captured using the method described in Sections 3.1.5 – 3.1.6.

3.5.2 POST PROCESS MEASUREMENT

Wheel wear was measured after the sixth, and final, grinding pass (Table 3.11) using the graphite coupon technique described in Section 3.4.3 (Figure 3.30).

Due to the limited volume of workpiece material available for the trials, none of the surfaces for cuts 1 – 18 were preserved. Each cut was ground over to make room for the next set of tests. In order to capture the surface roughness after the final grinding pass, the surface was dried with a clean rag and Struers Repliset T3 (Section 3.2) replicating material applied to the surface. This was allowed to cure for 10 minutes before being removed for surface roughness analysis as according to Section 3.1.7.

Five surfaces from the validation cuts (19, 20, 21, 24 & 26) were preserved for metallurgical analysis. This ensured the material was assessed in a wide range of grinding conditions. Sample preparation and assessment was performed according to the method in Section 3.1.8.

3.6 EXPERIMENTAL SUMMARY

The aim of work was to capture the influence of abrasive grit shape on the dressing and grinding performance of wheels when machining a Ni-base superalloy material. First the dressing power, topography sharpness and level of wear flats were measured under different dressing parameters (Section 3.2). SEM images were also taken of the different abrasive grit shapes at two dressing extremes.

CD grinding was then performed, using a range of dressing parameters, and the grinding power, surface roughness and workpiece sub-surface metallurgy analysed (Section 3.3). This was to reveal the impact of dressed topographies of different abrasive grit shapes on the grinding process. Conventional (non-CD) grinding with multiple passes followed this work with grinding power, force wheel wear and surface roughness measured to assess how the generated topography breaks down and how this affects grinding behaviour. SEM analysis of both the ground surfaces and the wheel topography were also captured to comprehend the wheel breakdown mechanisms (Section 3.4).

Finally an extensive series of grinding tests were conducted varying the grinding parameters, but with multiple passes, and grinding power, forces and surface roughness captured. This aimed to

provide an understanding of how cutting parameters can influence the grinding behaviour and breakdown of the generated wheel topographies. Wheel wear and metallurgical analyses were also performed (Section 3.5).

CHAPTER 4

RESULTS

4.0 RESULTS

The following Chapter presents all the results from the conducted experimental work. Error bars presented indicate the standard deviation of the data points.

4.1 DETERMINATION AND CONTROL OF GRINDING WHEEL TOPOGRAPHY

From the experiment discussed in Section 3.2, various output parameters (power, surface roughness etc.) were measured against the dressing parameters to understand their influence on the abrasive wheel topography and assess the impact of different grit morphologies.

4.1.1 POWER CONSUMPTION AND AVERAGE WHEEL ROUGHNESS

Figure 4.01A shows the net power consumption (Equation 3.1) during dressing of the three grinding wheel types. There is a minimum deviation between the wheel types at asynchronous (negative) speed ratios, however the gradient of the net dressing power increases greatly as the speed ratio becomes more positive. Figure 4.01B shows the net dressing power plotted against calculated interference angle (Equation 2.9) indicating that the power is much greater at the high infeed rates (solid line), across all wheels, compared to the low infeed rates (dotted line). It is clear from Figure 4.01 that the elongated grit wheel has the highest power consumption during dressing in both the high and low infeed rate conditions whereas the hybrid wheel displayed the lowest power in dressing. It is also of note that the power consumption dropped to a negative value when the dressing ratio was at unity. This is because the surface speed of the wheel and the dresser are equal. As power is measured on the grinding wheel spindle, then the dresser assists the turning of the wheel so the power is reduced. Figure 4.02 shows the power consumption for wheels containing 100% triangular engineered grits compared to hybrid wheels with only 30% triangular grits. It shows the same trend as in Figure 4.01A except the power in dressing was much less (32% average reduction across all dress parameters) compared to a hybrid wheel.
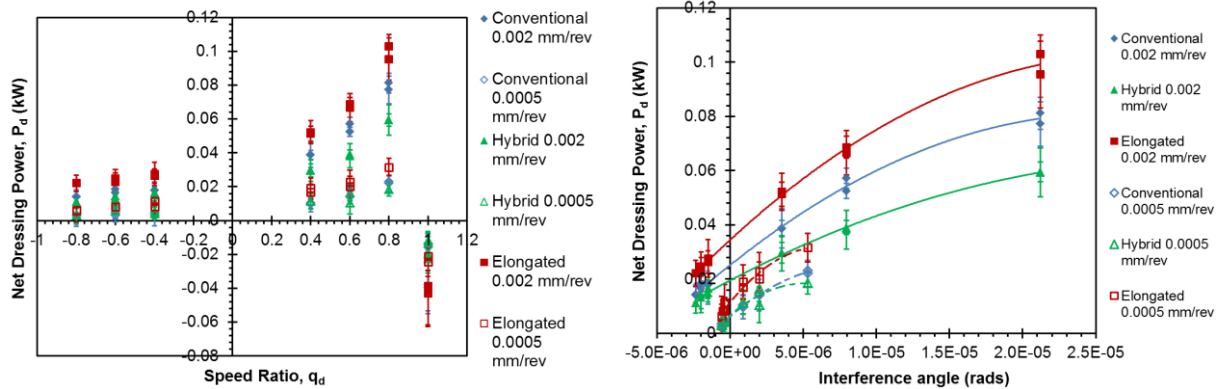
A.
                                    B.

FIGURE 4.01 – NET DRESSING POWER FOR THE 3 ABRASIVE WHEEL TYPES (A) AS A FUNCTION OF SPEED RATIO AND (B) AS A FUNCTION OF DRESSER DIAMOND INTERFERENCE ANGLE SHOWING HIGHER DRESSING POWER AT GREATER INTERFERENCE ANGLES.
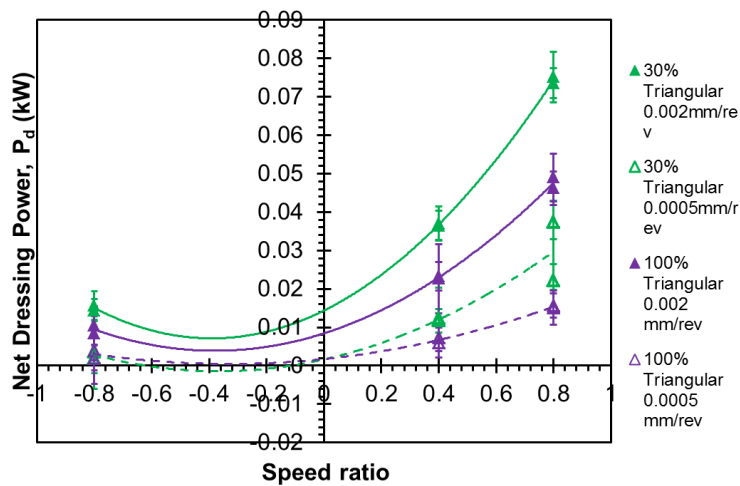
FIGURE 4.02 – HIGHER NET DRESSING POWER FOR HYBRID WHEEL (30% TRIANGULAR GRITS) OF GRIT SIZE #80 COMPARED TO 100% TRIANGULAR GRIT WHEEL OF GRIT SIZE #80 AGAINST NET DRESSING POWER.

The average roughness values of the abrasive wheels measured from the graphite coupons ground after dressing against the net dressing power are shown in Figure 4.03A (Section 3.2.3). Each point displayed is an average of five measurements. The solid lines in the graph show that the roughest wheel is generated at high dressing power conditions (high speed ratio) in high infeed rate conditions (solid line). The green curve indicates that the hybrid wheels proved to have the greatest variation in roughness over the smallest power range. Additionally, the highest roughness values were obtained when dressing with negative power consumptions as the dressing speed ratio is at unity ($q_d = 1.0$), therefore crushing of the grinding layer is the only dressing process. Figure 4.03B shows roughness of the graphite coupons plotted against calculated interference angle where it shows a similar trend as Figure 4.03A where the higher interface angles result in rougher wheel topography. The response is almost linear with the conventional wheel measuring the highest Ra value.
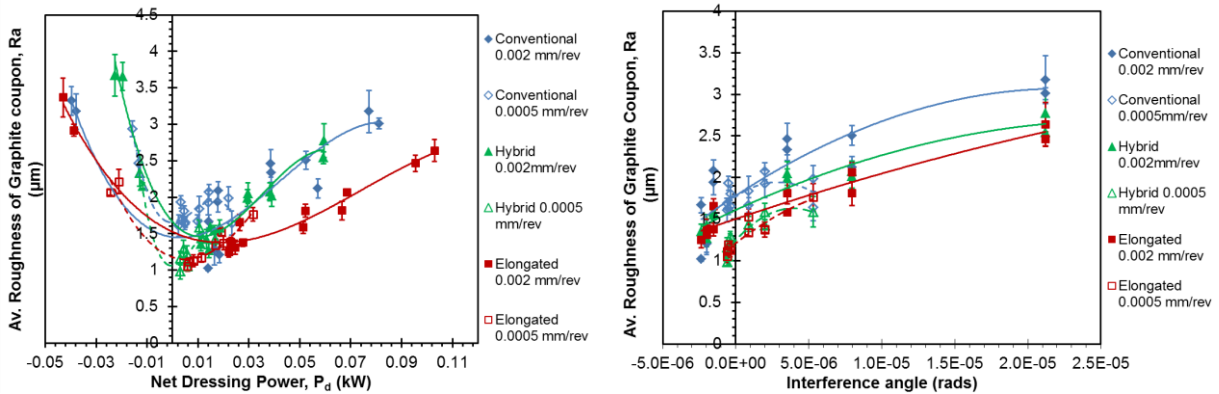
A.   B.

FIGURE 4.03 – (A) AVERAGE ROUGHNESS OF THE GRAPHITE COUPONS AGAINST DRESSING POWER (B) COUPON ROUGHNESS AS A FUNCTION OF CALCUALTED INTERFERENCE ANGLE.

Figure 4.04 shows the average roughness of the 100% triangular grit wheels compared with the hybrid wheels containing 30% triangular grits. Both wheels show a similar trend for roughness as a function of dressing power, suggesting that for a constant roughness, the dressing power is less for 100% triangular wheels. There is one clear point outside of the trend (as highlighted by the red circle at Ra 5.5 µm) but the power trend is followed for this cut, therefore suggesting no invalidity of the measurement, so this point is still included in the data set.
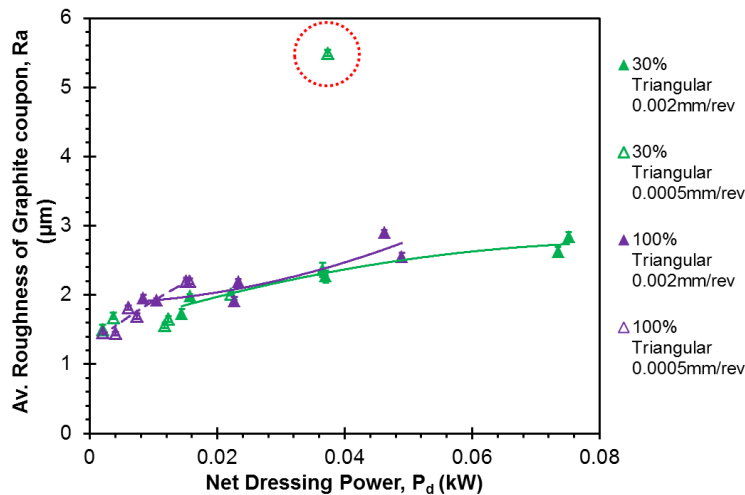
FIGURE 4.04 – AVERAGE ROUGHNESS OF GRAPHITE COUPON FOR HYBRID WHEEL (30% TRIANGULAR GRITS) OF GRIT SIZE #80 AND 100% TRIANGULAR GRIT WHEEL OF GRIT SIZE #80 WITH VERY SIMILAR TRENDS (OUTLYING POINT CIRCLED).

4.1.2 PEAK DENSITY AND GRIT SHAPE ANALYSIS

As discussed in Section 3.2.3, the peak density (number of high points per mm²) was determined using the replicating material on the periphery of the grinding wheel. The measurement

resolution was set to capture whole grit high points rather than micropeaks on individual abrasive grits. Figure 4.05 shows the peak density as a function of calculated interference angle.

The highest peak density as well as the largest degree of variation in peak density with interference angle is observed for the conventional wheel with a trend of reduced peak density as the interference angle increases. The curves associated with the hybrid and elongated grit wheels however, are almost flat with very little change in the peak density over the interference angle, particularly at high infeed rate. This could be due to reduced whole grain pull out. The hybrid wheel also demonstrated the lowest peak density of all the wheels. The comparison of curves with solid and broken lines indicate that the highest variation in the measured peak density occurs when low infeed values were selected independent of the type of the grinding wheel.
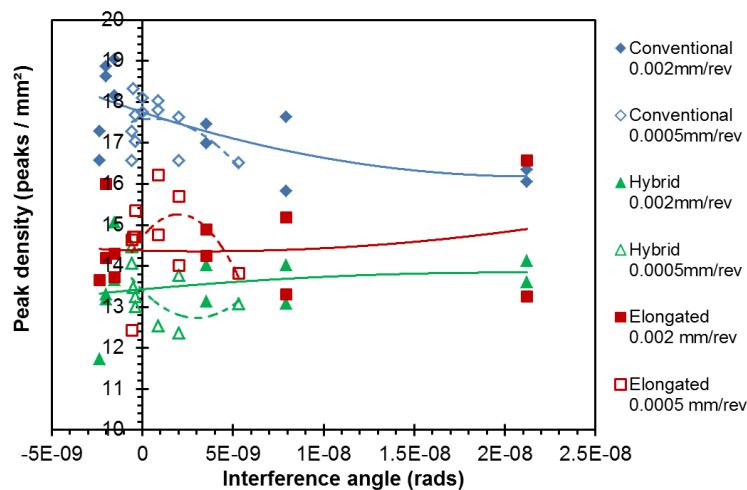
FIGURE 4.05 – PEAK DENSITY FOR THE THREE WHEEL TYPES WITH RESPECT TO THE CALCULATED DRESSING INTERFERENCE ANGLE.

An approximation of the sharpness of the abrasive grits was determined by measuring the gradient of a cumulative frequency graph of measured heights on the wheel surface replica (Section 3.2.2, Figure 3.16). This method indicates a sharper surface at lower gradient values. Figure 4.06A shows the cumulative gradient as a function of the graphite coupon roughness displaying the relationship between the grinding roughness and the wheel sharpness. For every wheel type, the negative trend of the solid lines indicates that the sharper the cutting points (low gradient), the rougher the wheel surface (graphite roughness) is. A similar trend is seen in the low infeed rate (dotted lines on Figure 4.06), however there is substantial scatter in the data at this dressing condition. Figure 4.06B shows the cumulative gradient against the measured peak density wherein for the high infeed rates at the higher gradients (i.e. dull grits) there are more cutting points on the wheel surface (higher peak density). Due to the significant variation in gradient at low infeed rate conditions, this trend is not as visible which could be due to duller peaks not being as well resolved by the technique as they do not protrude as far from the wheel surface. Trend lines were maintained for the low infeed in figure

4.06B, despite the variation, for consistency and comparison with figure 4.06A. All trend lines used a linear plot. Both figures appear to show that the hybrid wheel has the sharpest cutting points as this wheel measured the lowest cumulative gradient value compared to the other wheel types.

A.

B.
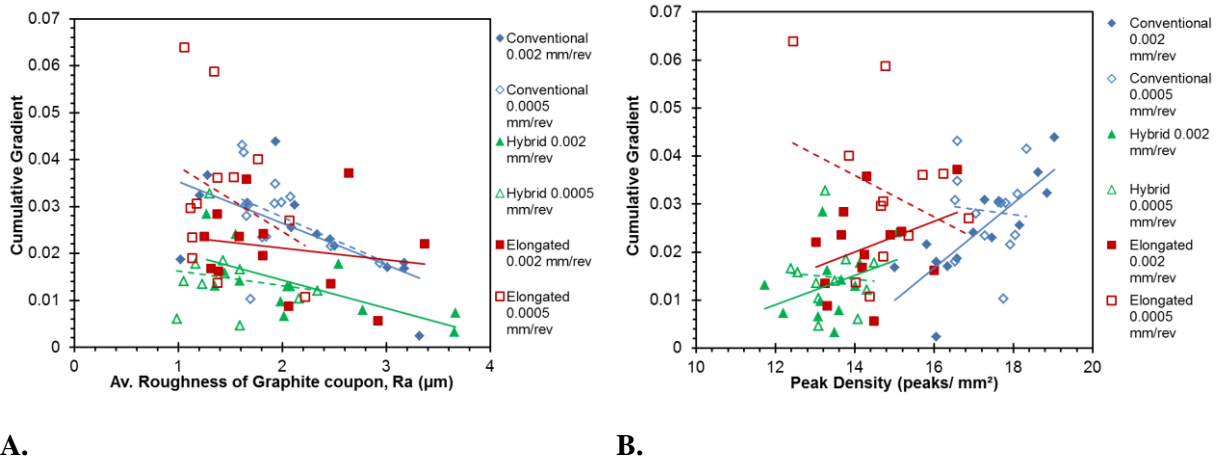
FIGURE 4.06 – (A) CUMULATIVE GRADIENT (GRIT SHARPNESS) AGAINST GRAPHITE COUPON ROUGHNESS (B) CUMULATIVE GRADIENT AGAINST PEAK DENSITY.

4.1.3 FRACTURE FLAT CHARACTERISATION AND TOPOGRAPHY IMAGE ANALYSIS

The identified fracture flats (as explained in Section 3.2.2) with respect to the dressing speed ratio are shown in Figure 4.07. There is little variation in the identified flat regions on the grits as a function of speed ratio, although it is clear that the elongated grits have the largest flat regions on the grits having highest percentage of 6% – 8%. The other wheel types had less flat regions with the hybrid wheel showing the lowest percentage of 1.6% - 1.8%. All wheel types showed no visible difference in fracture flat percentage between infeed rates, except for the conventional wheel which showed a small 0.2% difference.
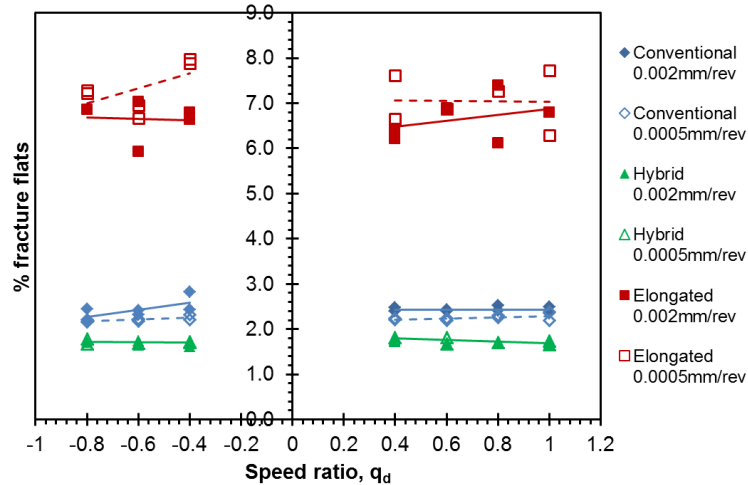
FIGURE 4.07 – THE PERCENTAGE OF FLAT REGIONS ON THE ABRASIVE GRITS WHICH WAS HIGHEST IN ELONGATED GRIT WHEELS.

The orientation distribution of the abrasive grits was determined from optical images of the grinding wheels surfaces, as described in Section 3.2.2 (Table 3.7) and is presented in Figure 4.08. The figure shows there are preferential orientations for the engineered grits with the elongated grits more likely to lie either flat with their longer side aligned tangential to the wheel edge or directly normal to the wheel surface along the radial direction.
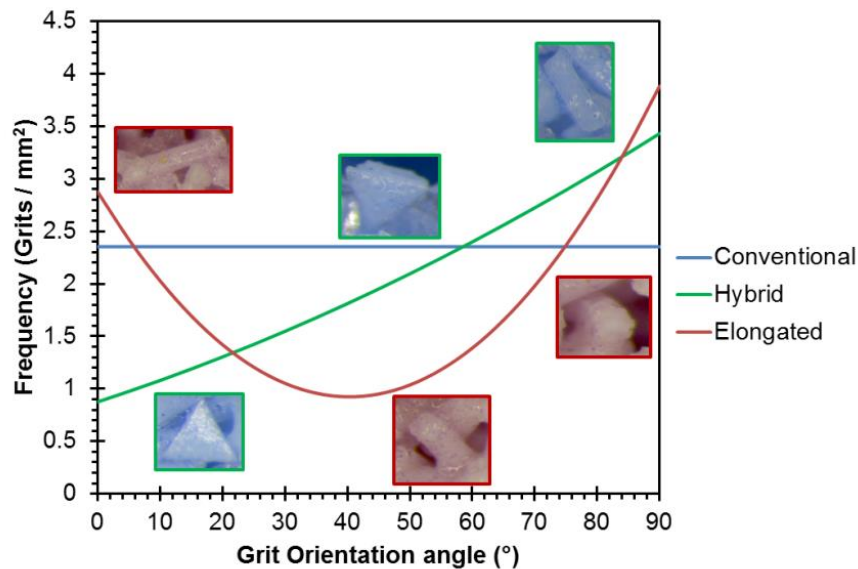
FIGURE 4.08 – ORIENTATION DISTRIBUTION OF ABRASIVE GRITS IN THREE DIFFERENT WHEEL TYPES.

The triangular engineered grits on the other hand, prefer to sit on their thin edge with them least likely to lie flat on the surface. The conventional grits were assumed to have an even distribution of orientations due to the grits being approximately spherical and very difficult to determine orientation.

SEM images of the wheels dressed under different extremes (infeed rate 0.002 mm/rev speed ratio 0.8 compared to infeed rate 0.0005 mm/rev speed ratio -0.8) are shown in Figures 4.9 – 4.15.

Figure 4.09 shows examples of macrocracks in the abrasive grits highlighted by the red arrows, observed under 0.002 mm/rev and q_d 0.8 dressing conditions (further evidence of this is seen in Appendix G). As the dressing condition changes to lower interference angle under 0.0005 mm/rev and q_d 0.8 dressing conditions more flat sections were identified, as indicated by arrows in Figure 4.10.
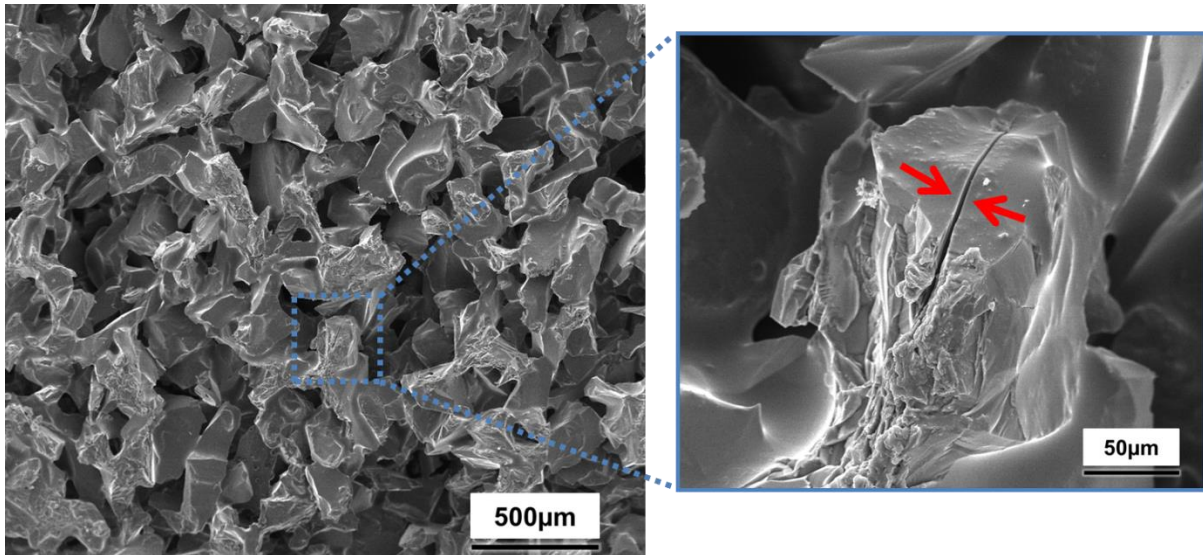
FIGURE 4.09 – LOW (X100) AND HIGH MAGNIFICATION MICROGRAPHS OF THE CONVENTIONAL WHEEL UNDER HIGH INTERFERENCE ANGLE DRESSING CONDITIONS (INFEED RATE 0.002 MM/REV, SPEED RATIO 0.8) WITH ARROWS IDENTIFYING MACROCRACKS.
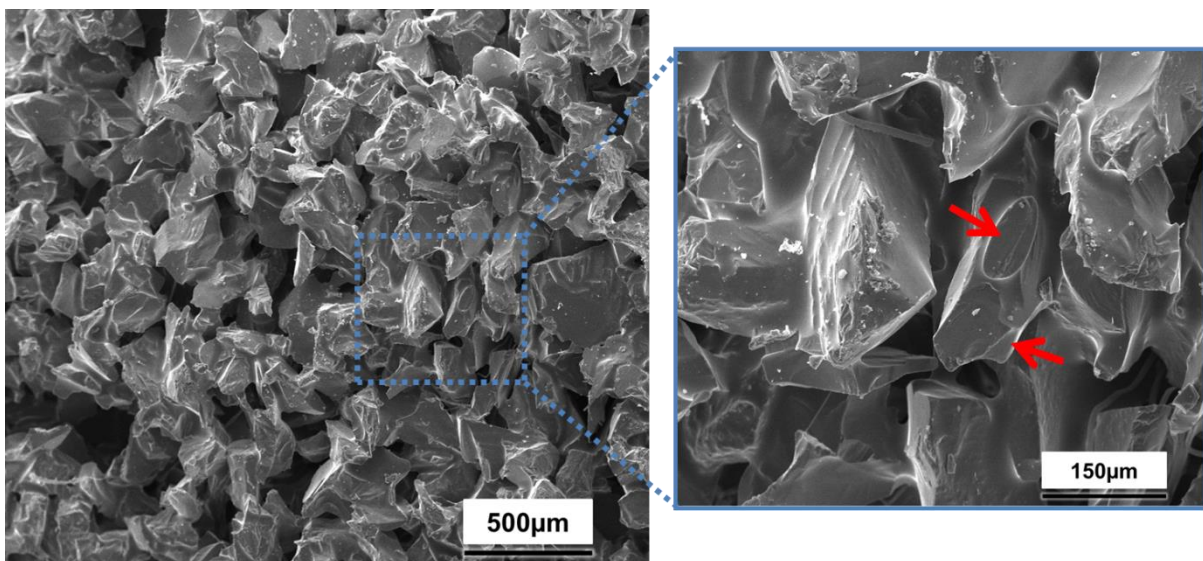
FIGURE 4.10 - LOW (X100) AND HIGH MAGNIFICATION MICROGRAPHS OF THE CONVENTIONAL WHEEL UNDER LOW INTERFERENCE ANGLE DRESSING CONDITIONS (INFEED RATE 0.0005 MM/REV, SPEED RATIO -0.8) WITH ARROWS IDENTIFYING FLAT REGIONS.

For the hybrid wheels however, at high interference angle dressing parameters several instances of microfracturing with sharp cutting points were detected on the engineered grits, as highlighted with arrows in Figure 4.11 (further evidence in Appendix G). Macrofractured engineered grits were also observed in this dress condition, such as that circled in Figure 4.12.
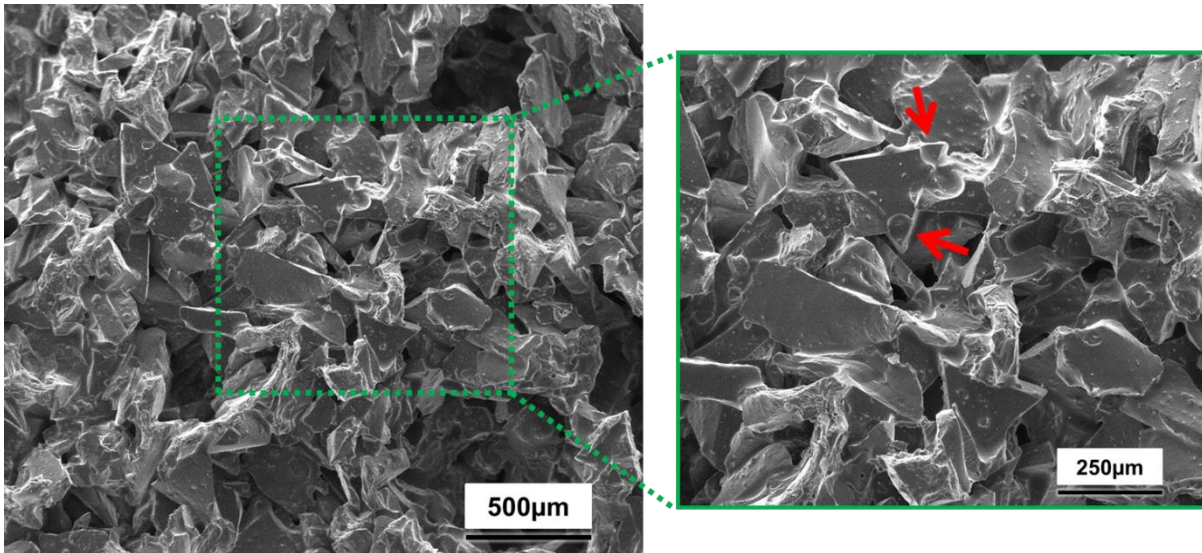
FIGURE 4.11 - LOW (X100) AND HIGH MAGNIFICATION MICROGRAPHS OF THE HYBRID WHEEL UNDER HIGH INTERFERENCE ANGLE DRESSING CONDITIONS (INFEED RATE 0.002 MM/REV, SPEED RATIO 0.8) WITH ARROWS IDENTIFYING MICRO FRACTURING.
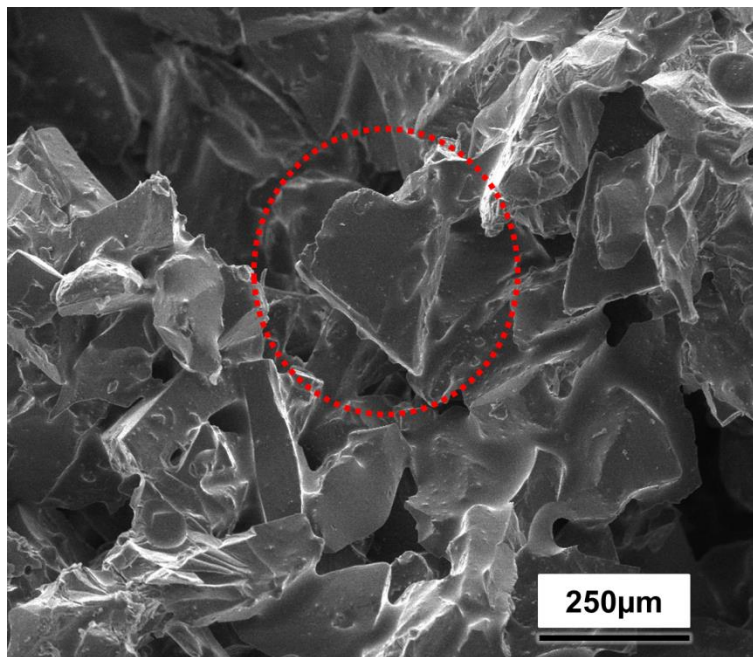
FIGURE 4.12 – HYBRID WHEEL UNDER INFEED 0.002 MM/REV SPEED RATIO 0.8 DRESSING CONDITIONS WITH TRIANGULAR GRIT MACROFRACTURE HIGHLIGHTED.

At low inference angles, the engineered grits tend to maintain their configurations as no fracture sites were identified in Figure 4.13 at the locations highlighted in Figures 4.11 – 4.12.
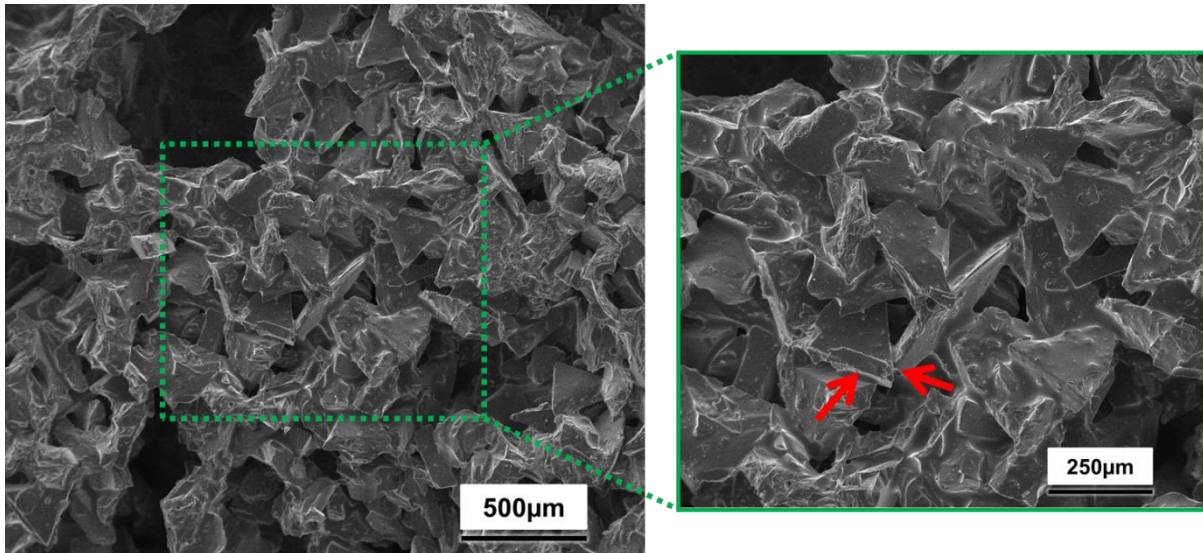
FIGURE 4.13 – LOW (X100) AND HIGH MAGNIFICATION MICROGRAPHS OF THE HYBRID WHEEL UNDER LOW INTERFERENCE ANGLE DRESSING CONDITIONS (INFEED RATE 0.0005 MM/REV, SPEED RATIO -0.8). ARROWS INDICATE WHERE FRACTURING WAS OBSERVED IN THE HIGH INFEED RATE CONDITIONS.

In Figure 4.14, the topography of the elongated grit wheel under 0.002 mm/rev and q_d 0.8 dressing conditions is shown. The top red arrow in the enlarged sub-figure indicates a sharp cutting point while fracture of the grits is also visible as identified by the two bottom red arrows.
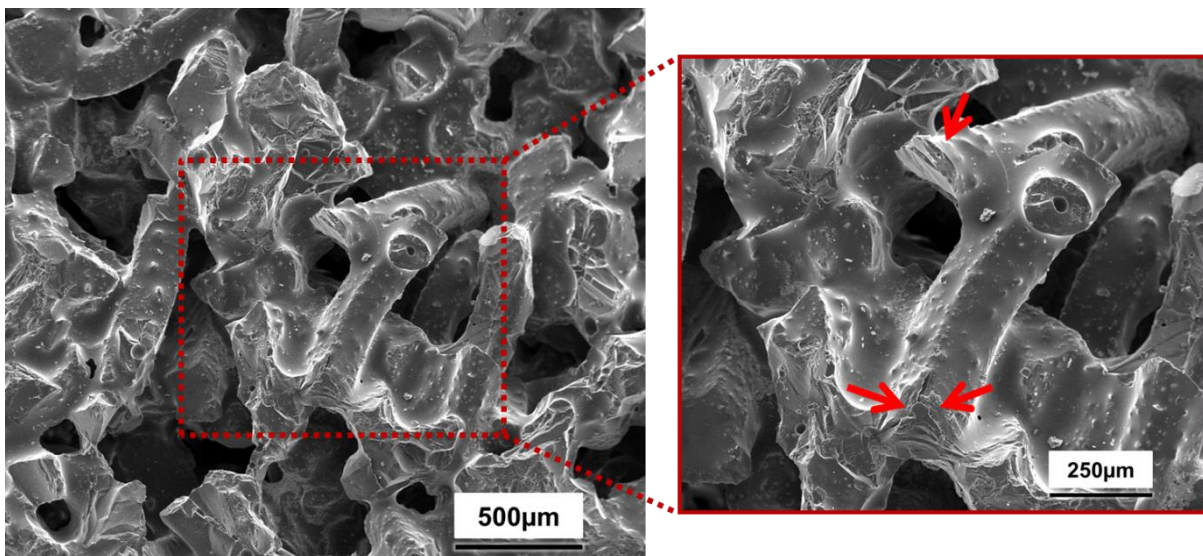
FIGURE 4.14 - LOW (X100) AND HIGH MAGNIFICATION MICROGRAPHS OF THE ELONGATED GRIT WHEEL UNDER HIGH INTERFERENCE ANGLE DRESSING CONDITIONS (INFEED RATE 0.002 MM/REV, SPEED RATIO 0.8). THE ARROWS INDENTIFY SHARP POINTS AND MACROCRACKS IN THE GRITS.

The elongated grit wheel in the low interference angle dressing condition is shown in Figure 4.15 with flat regions, identified by arrows, demonstrating grits orientated perpendicular to the central axis had been had been cleaved off (further evidence of this in Appendix G). Spherical features (circled on the low magnification image) were seen consistently over different samples and dressing conditions suggesting they are the result of air pockets during bond sintering.
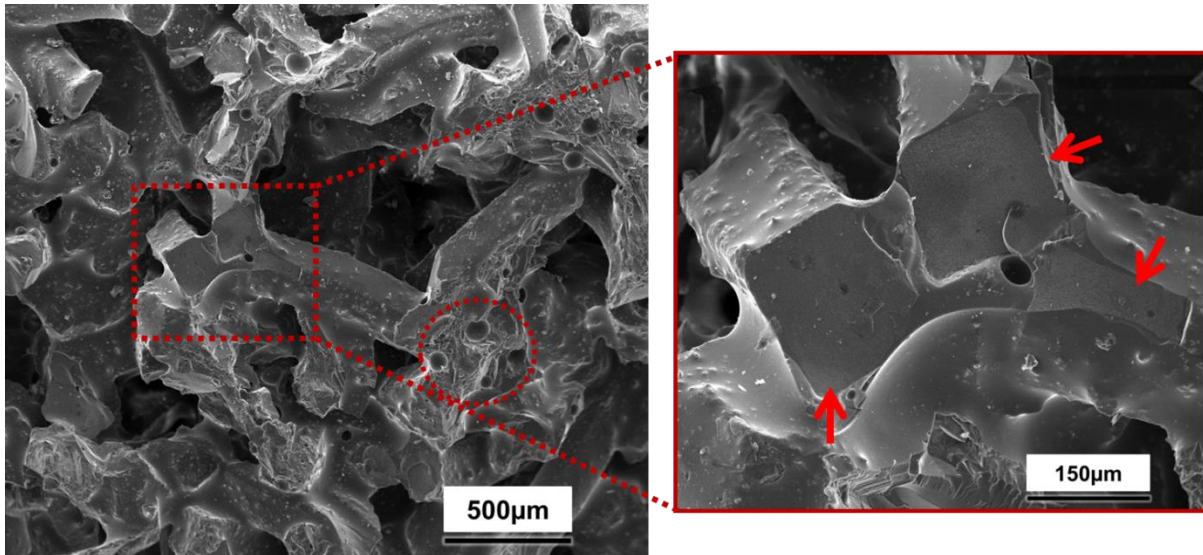
FIGURE 4.15 - LOW (X100) AND HIGH MAGNIFICATION IMAGES OF THE ELONGATED GRIT WHEEL UNDER SHALLOW INTERFERENCE ANGLE DRESSING CONDITIONS (INFEED RATE 0.0005 MM/REV, SPEED RATIO -0.8). ARROWS INDICATE CLEAVED GRITS AND AIR POCKETS ARE CIRCLED.

4.2 Influence of Generated Topography on Grinding Performance

As according to the experiment discussed in Section 3.3, a series of continuous dressing grinding cuts were performed on CMSX-4 Ni-base superalloy material under different dressing parameters to capture the grinding response whilst limiting the effect of wheel wear.

4.2.1 In-process Performance

Figure 4.16 shows the net power consumption (P_{net}) of the wheel spindle during CD grinding, calculated as the total power during material removal minus the power with coolant and continuous dressing but no engagement with the workpiece. The net power as a function of speed ratio with the high infeed rate (0.002 mm/rev) is shown in Figure 4.16A, indicated with a second-order, polynomial solid line (same for all graphs) and low infeed rate (0.0005 mm/rev) with a dotted line. For all of the tested wheels, a lower net power is required to grind the same volume of workpiece material at high infeed rate compared to the case when lower infeeds were used. For all wheels, the lowest net power was achieved at a high speed ratio (0.8) and high infeed rate. However, Figure 4.16B shows a greater variation in net power was observed at low infeed rate (dotted line) compared to the high infeed rate, despite the smaller interference angle range.
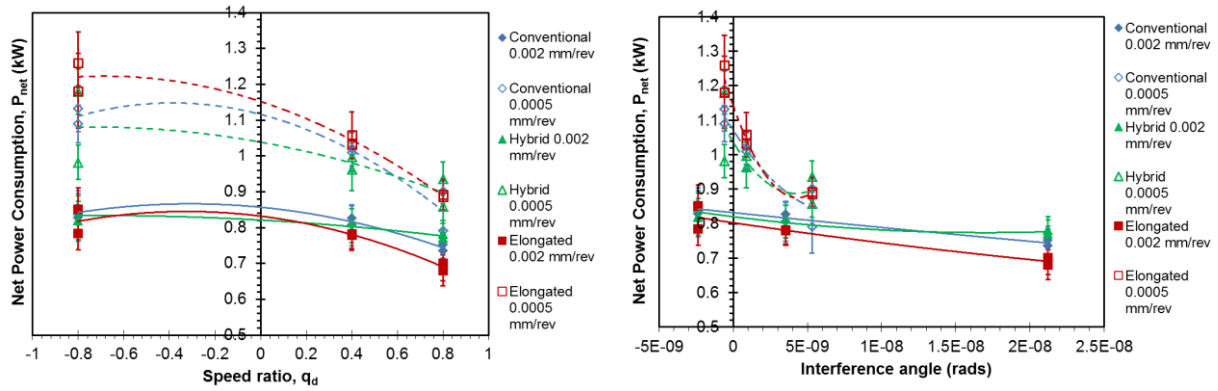
A.

B.

FIGURE 4.16 – (A) NET POWER CONSUMPTION AGAINST DRESSING SPEED RATIO (B) NET POWER CONSUMPTION REDUCTION AS CALCULATED INTERFERENCE ANGLE INCREASED.

The difference between the responses of the wheels in Figure 4.16A –B is small but is still significant as shown by a general linear model which was constructed for the grinding power based on infeed rate, speed ratio and wheel type. The alpha (significance) level was set to 5% and the wheel type produced a p-value of 0.7%, far below the set alpha level (Section 3.5.2).

4.2.2 SURFACE QUALITY ASSESSMENT (Ra, Rv)

Figure 4.17 shows the measured surface roughness of the workpiece plotted as a function of speed ratio (A) and the net power consumption (B). Across all wheels, the high infeed rate (solid lines) showed the highest surface roughness and over 60% more variation in surface roughness value compared to the equivalent low infeed rate. The elongated grits generate the roughest workpiece by far for both high and low infeed rates with an increasing roughness at higher synchronous speed ratios (Figure 4.17A).
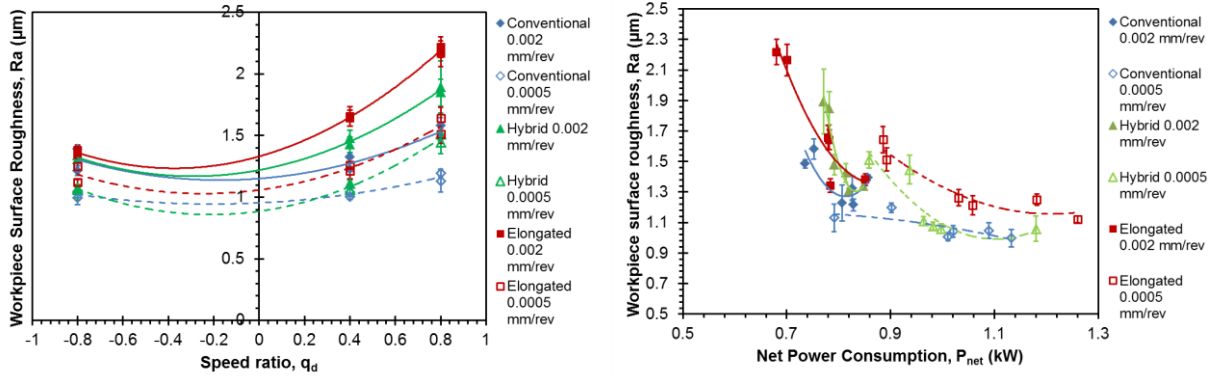
A. **B.**

FIGURE 4.17 – (A) WORKPIECE SURFACE ROUGHNESS AGAINST DRESSING SPEED RATIO (B) SURFACE ROUGHNESS OF THE WORKPIECE AGAINST MEASURED GRINDING POWER.

The hybrid wheels demonstrated the steepest gradient in the high infeed dressing condition compared to the other wheels (Figure 4.17B) indicating a large roughness variation for a small grinding power change. The conventional wheels however showed the lowest gradient (variation) and the lowest overall surface roughness.

The average maximum profile valley depth (Rv) measured on the workpiece for the three wheel types is an indication of the cut track depth formed by the abrasive grits. As Figure 4.18 displays a very similar trend to that seen in Figure 4.17A for the average roughness, this demonstrates that surface roughness is directly related to the cut track depth from the abrasive grits. Across all wheels, the largest profile valley depth was generated at high infeed rates and the elongated grit wheels had the highest Rv value (at q_d 0.8), generating the deepest valleys cut in the ground workpiece.
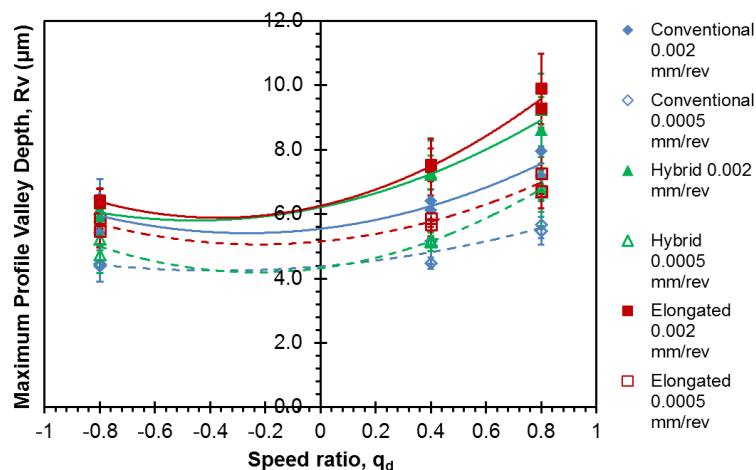
FIGURE 4.18 – AVERAGE MAXIMUM PROFILE VALLEY DEPTH AGAINST DRESSING SPEED RATIO WHICH WAS HIGHEST FOR ELONGATED GRIT WHEELS.

4.2.3 Image Analysis of Ground Surfaces

The ground surfaces were examined under an SEM to assess the shape of the grinding cut tracks. The micrographs are shown in association with the measured roughness values on the surface of the samples in Figures 4.19 – 4.20 where the deep cuts are indicated by arrows and smeared materials are highlighted by circles.

Visual assessment shows increased smearing and redeposited material on the surfaces from a high infeed rate dressed wheel (circled, Figure 4.19A, D & F and Figure 4.20A, B and D), for all wheel types, compared to the low infeed surfaces. Deeper grinding cut tracks are visible on the micrographs associated to high infeed rates (4.19A, B , D ,F and 4.20A, B and D) compared with those of the surfaces at low infeed rate (4.19C, E, G, H and 4.20C, E, F). The elongated grit wheel generated the deepest ground tracks (indicated by arrows in Figure 4.19A) compared with the other wheel types (Figure 4.19D & Figure 4.20B). The influence of speed ratio on the ground surfaces was not apparent as no consistent visual differences were seen between samples cut with different dressing speed ratios (at the same infeed rate).
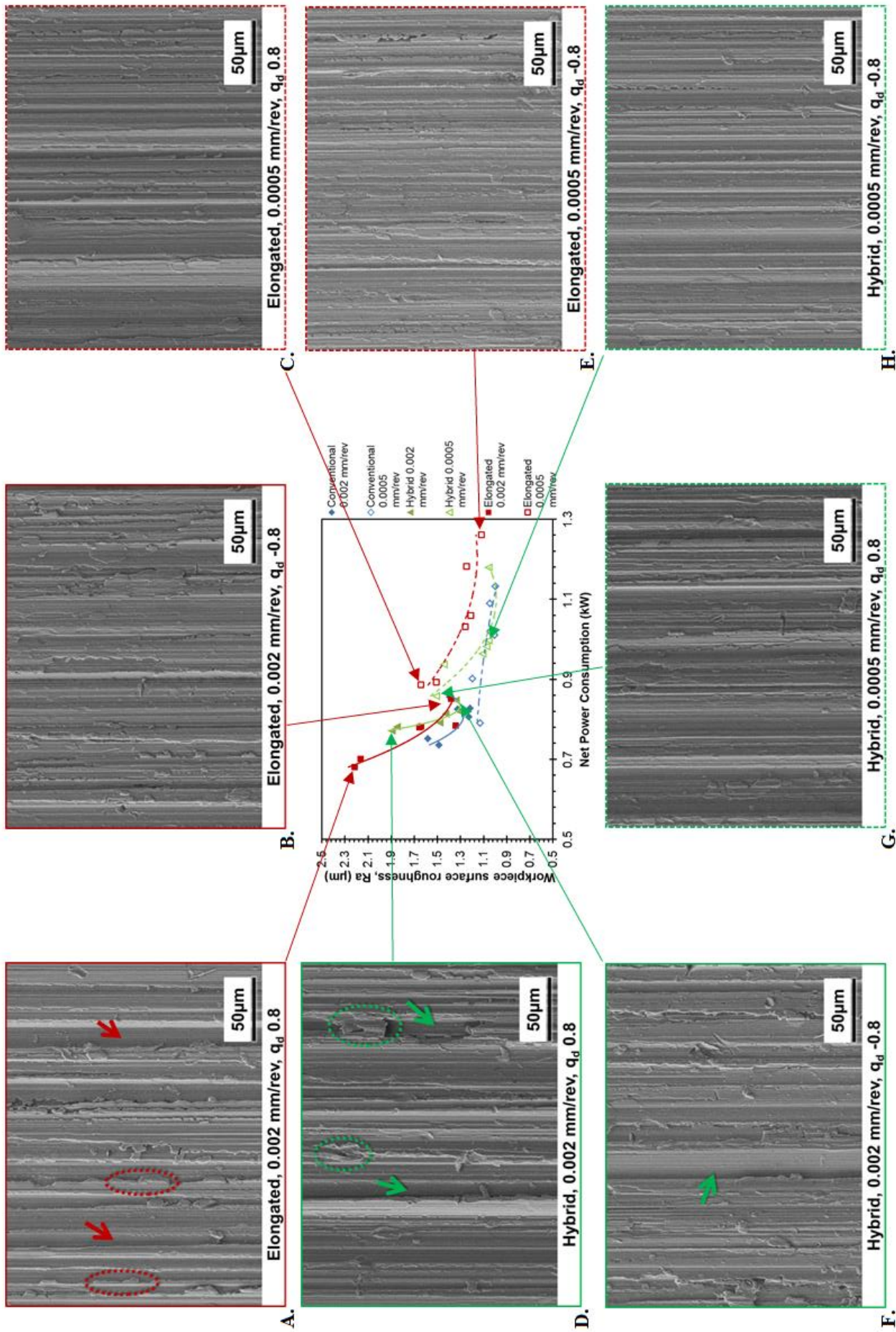
FIGURE 4.19 – SEM GROUND SURFACE MICROGRAPHS ASSOCIATING TO PARTICUALR MEASURED SURFACE ROUGHNESS VALUES (FIGURE 4.17B) FOR HYBRID AND ELONGATED GRIT WHEELS. DEEP CUT TRACKS ARE AND SMEARING ARE HIGHLIGHTED WITH LOW POWER GRINDS GENERATING THE MOST SURFACE FEATURES.
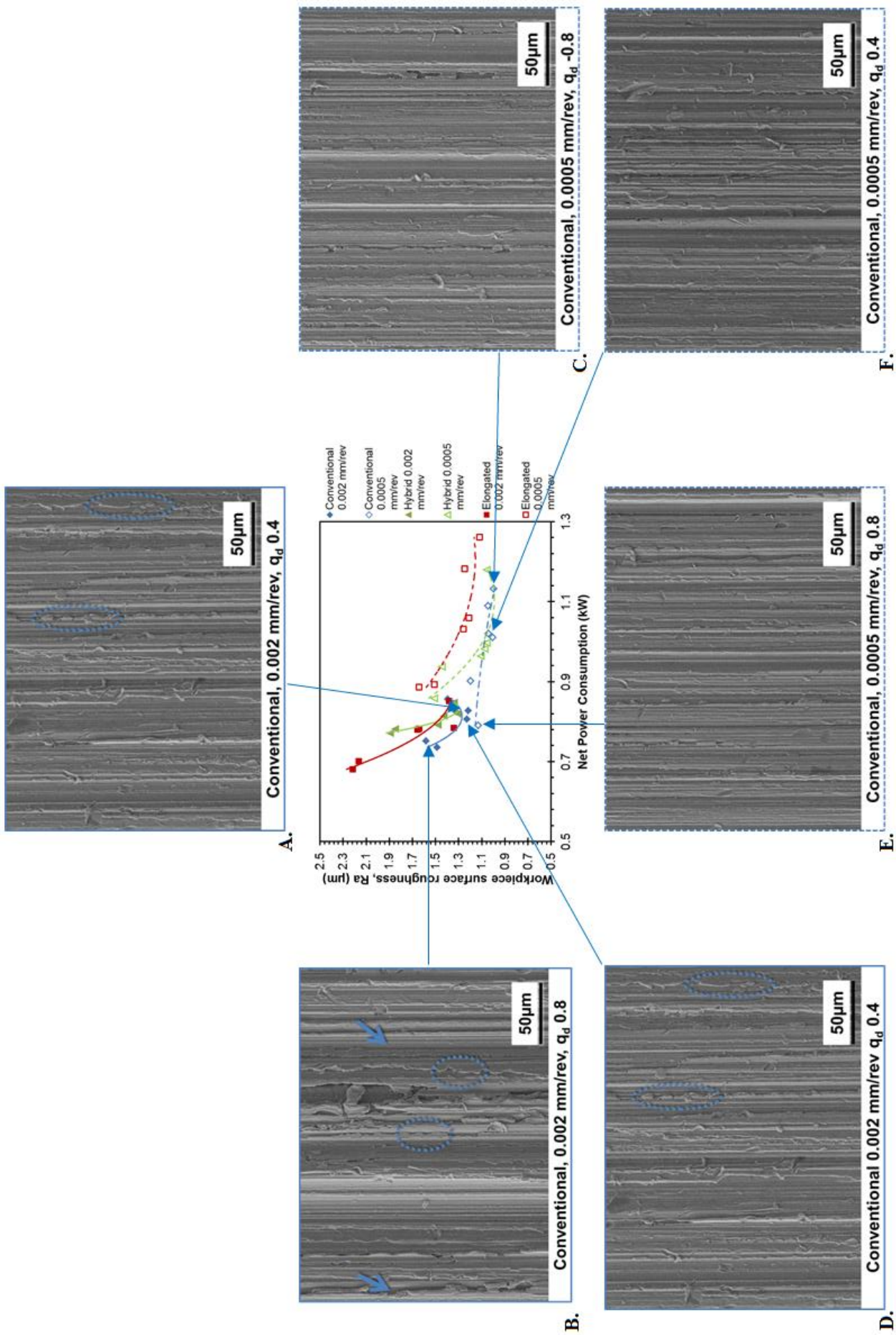
FIGURE 4.20 – SEM GROUND SURFACE MICROGRAPHS ASSOCIATING TO MEASURED SURFACE ROUGHNESS VALUES ON FIGURE 4.17B FOR THE CONVENTIONAL WHEELS WITH THE HIGHER INFEED RATE CREATING MORE SMEARING FEATURES AND DEEPER TRACKS.

Backscattered electron (BSE) imaging was used to identify embedded abrasive grits that had become lodged in the ground workpiece surface due to the high image contrast and the use of Energy Dispersive X-ray (EDX) spectroscopy. Alumina abrasive grits contain high levels of aluminium (Al) or oxygen (O) compared to the surrounding material rich in nickel (green spots). The EDX map in Figure 4.21, of a suspected embedded grit, shows a high concentration of aluminium (blue spots) and oxygen (yellow spots) in the dark region compared to the rest of the workpiece surface and so can be confirmed as an embedded abrasive grit. Features similar in appearance to that in Figure 4.21 can therefore be assumed to be embedded abrasive material in the workpiece. Examples of this feature for different wheel types are shown in Figures 4.22 – 4.24.
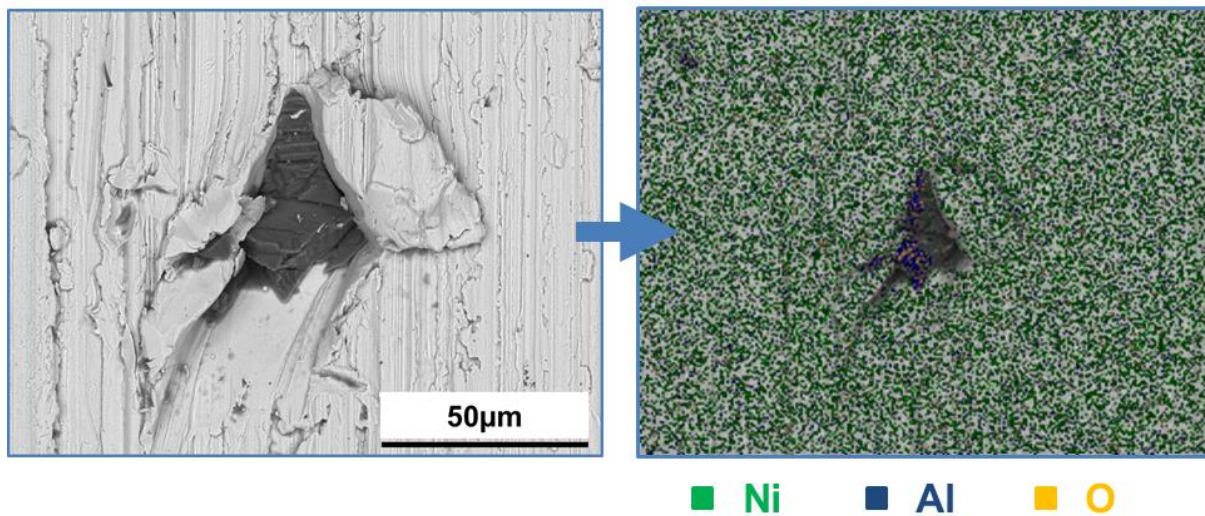
FIGURE 4.21 – EMBEDDED ABRASIVE GRIT IN THE GROUND SURFACE FROM THE CONVENTIONAL WHEEL. THE RIGHT-HAND IMAGE SHOWS THE EDX MAP WITH HIGH AL AND O CONCENTRATION IN THE GRIT.

A.   B.
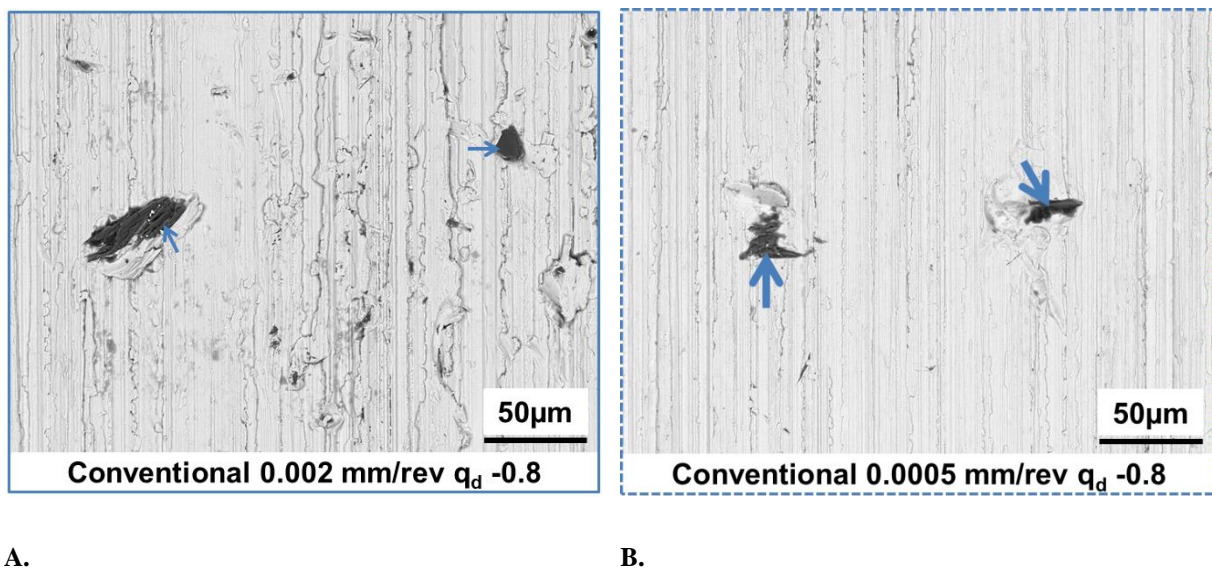
FIGURE 4.22 – BSE MICROGRAPH OF EMBEDDED GRITS FROM THE CONVENTIONAL WHEEL (A) UNDER HIGH DRESSING INFEED RATE (B) LOW DRESSING INFEED RATE SHOWING MULTIPLE INSTANCES OF SMALL GRITS.

A.   **B.**
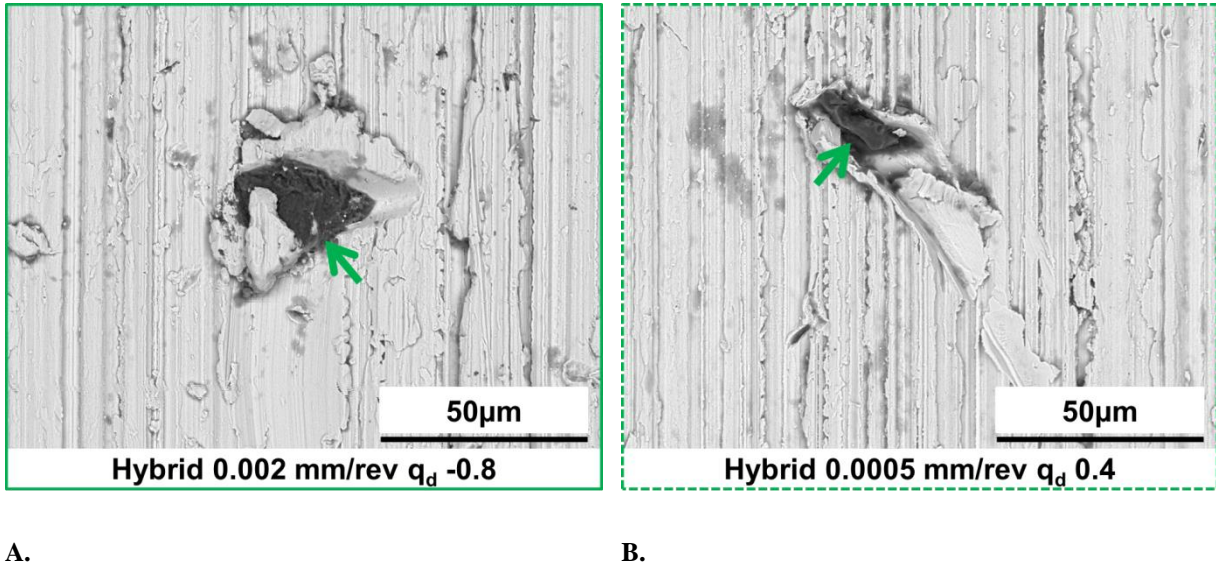
FIGURE 4.23 – EXAMPLES OF BSE MICROGRAPH OF EMBEDDED GRITS FROM THE HYBRID WHEEL UNDER (A) HIGH DRESSING INFEED RATE (B) LOW DRESSING INFEED RATE.

Examples of embedded grits were seen on all the conventional wheel samples but were only observed on 50% of the hybrid wheel samples, as highlighted by arrows in Figures 4.22 – 4.23. The identified embedded grits on the surfaces ground with conventional wheels were approximately 35% smaller (in the longest visible dimension) than those on the surfaces ground by hybrid wheels (Table 4.1).

Only one sample ground with the elongated grits had embedded grits (three grits identified) in the surface which was cut at 0.0005 mm/rev and q_d -0.8 dressing conditions (Figure 4.24).
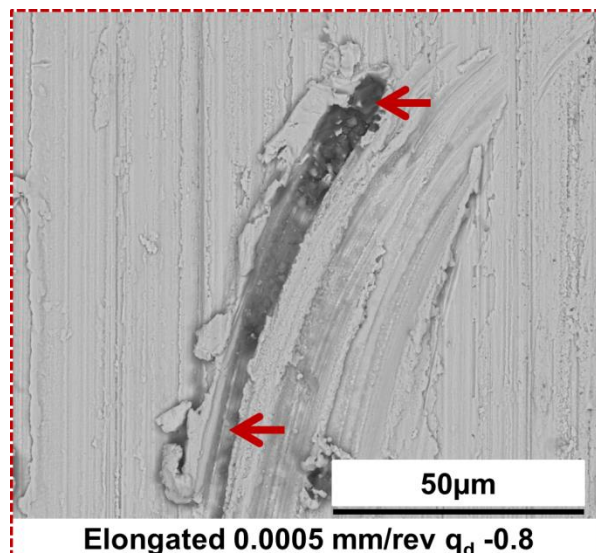
FIGURE 4.24 – BSE MICROGRAPH OF AN EMBEDDED GRIT FROM ELONGATED GRIT WHEEL. ARROWS INDICATE THE EMBEDDED GRIT AND THE TRACK CREATED.

Table 4.1 shows the number of embedded grits detected in the imaged area for the samples from the three different wheel types. The average grit size and standard deviation is also shown to indicate the variation in the embedded grit size. No significant trend was detected between the dressing parameter used and the density of embedded grits detected.

TABLE 4.1 – NUMBER OF EMBEDDED GRITS IDENTIFIED IN THE IMAGED AREA OF THE GROUND SURFACES WHICH WAS MUCH HIGHER FOR THE CONVENTIONAL WHEEL.

Wheel Type	Embedded grit density (no. grits in 27 mm² area total)	Av. Grit size (µm)	Av. Standard Deviation of embedded grit size
Conventional	40	18.44	7.91
Hybrid	11	24.77	12.23
Elongated	3	26.34	19.71

4.2.4 METALLURGICAL SURFACE ANALYSIS

Ground samples from each of the different dressing conditions (for all wheel types) were sectioned and analysed under optical microscopy to assess the metallurgical response of the CMSX-4 material to the various grinding wheel topographies. Assessment was conducted along the cutting direction as according to CME5043 and detailed in Section 3.2.

Some metallurgical features described in the CME standard (Appendix B) were detected on all of the samples investigated. White layer was observed on all the examined samples and its thickness was measured and the average calculated for each dressing condition (Figure 4.25). Elongated grit wheels showed the lowest average white layer thickness (Figure 4.25C – D) compared to the other wheel types as indicated by the central chart.

Redeposited material, which is caused by swarf entrapment in the wheel and deposition of machined material onto the ground surface, was also detected on all samples and the average thickness measured for each sample (Figure 4.26). The high infeed rate results in a thicker redeposited material on the surface as demonstrated in Figure 4.26A, C & F. The larger standard deviation (error bars) in some samples could be due to occasional large chips forming and being deposited on the workpiece surface, thus skewing the measured data.

4.0 Results

A. Conventional 0.0005 mm/rev q_d 0.8 – Optical Imaging
Av. White layer thickness 1.34µm
20µm

B. Conventional 0.0005 mm/rev q_d 0.8 – SEM Imaging
15µm

C. Elongated 0.0005 mm/rev q_d 0.8 – Optical Imaging
Av. White layer thickness 1.07µm
20µm

D. Hybrid 0.0005 mm/rev q_d 0.8 – SEM Imaging
15µm

E. Hybrid 0.0005 mm/rev q_d 0.8 – SEM Imaging
15µm

F. Hybrid 0.0005 mm/rev q_d 0.8 – Optical Imaging
Av. White layer thickness 1.43µm
20µm

White layer

Av. Feature Depth (µm)
Speed ratio, q_d

0.002 mm/rev Conventional
0.0005 mm/rev Conventional
0.002 mm/rev Hybrid
0.0005 mm/rev Hybrid
0.002 mm/rev Elongated
0.0005 mm/rev Elongated

FIGURE 4.25 – (A) – (F) OPTICAL AND SEM IMAGES OF THE GROUND MATERIAL CROSS SECTION EXAMINING WHITE LAYER THICKNESS. THE CENTRAL GRAPH DISPLAYS THE AVERAGE MEASURED WHITE LAYER THICKNESS WHICH WAS LOWEST FOR THE ELONGATED GRIT WHEELS.

©2019 Rolls-Royce
Not subject to Export Control
Private

146
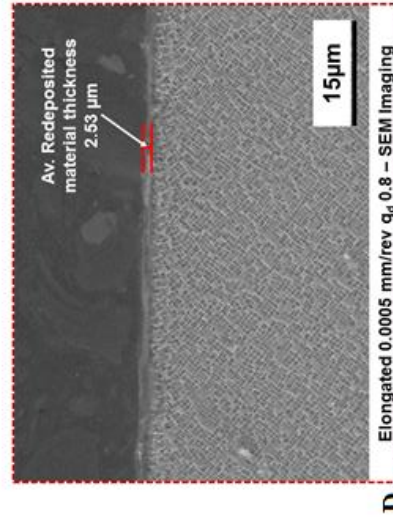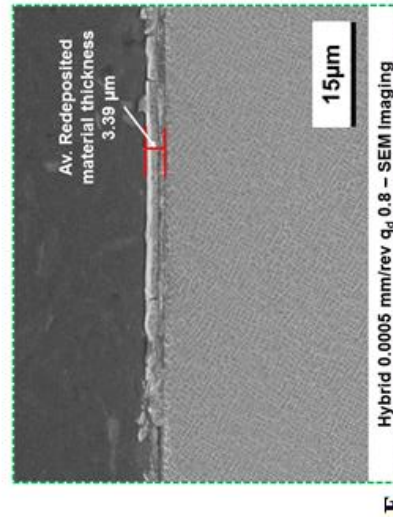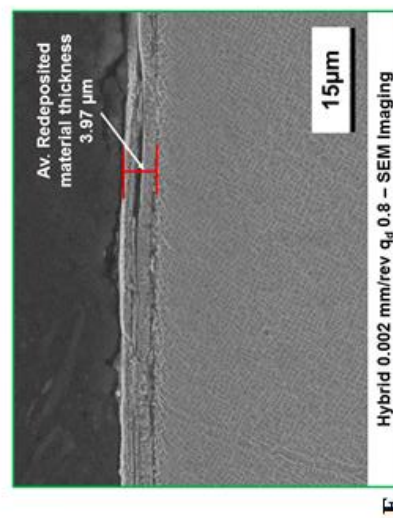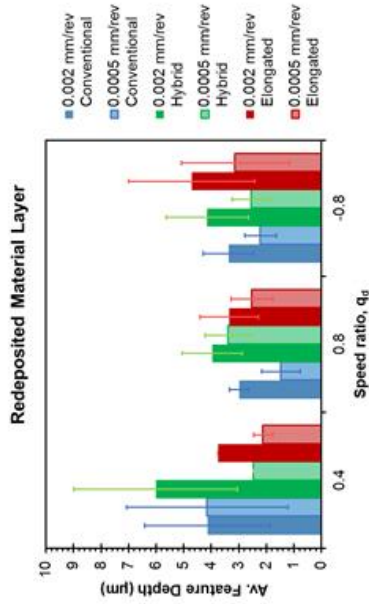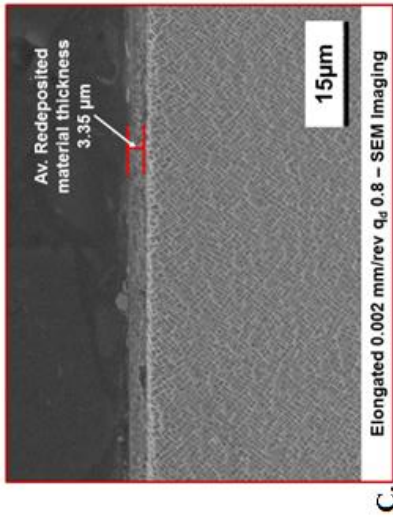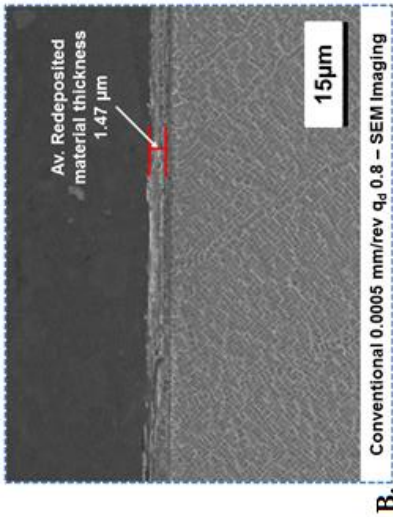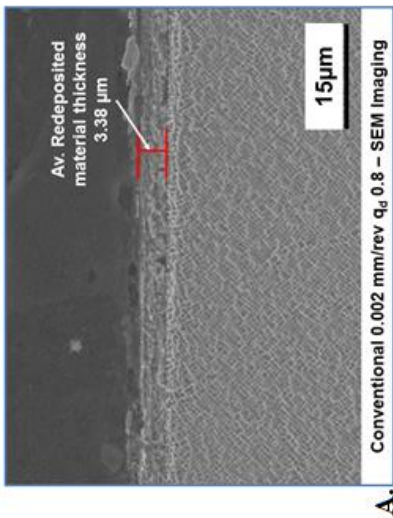
FIGURE 4.26 – (A) – (F) SEM IMAGES OF THE GROUND MATERIAL CROSS SECTION EXAMINING REDEPOSITED MATERIAL ON THE SURFACE. THE CENTRAL GRAPH DISPLAYS THE AVERAGE MEASURED REDEPOSITED MATERIAL THICKNESS. THICKER AVERAGE REDEPOSITED MATERIAL SEEN AT HIGHER DRESSING INFEED RATES.

A few 'plucking' features on the surface of the material sections were also detected under optical assessment of the samples. These occurred on all the samples for all wheel types and dressing conditions however there was no identifiable trend to the quantity and size of these features. Plucking is usually a result of tool wear or damage as well as swarf entrapment in the wheel and appears as a hole or pocket in the surface. Two examples are shown in Figure 4.27.
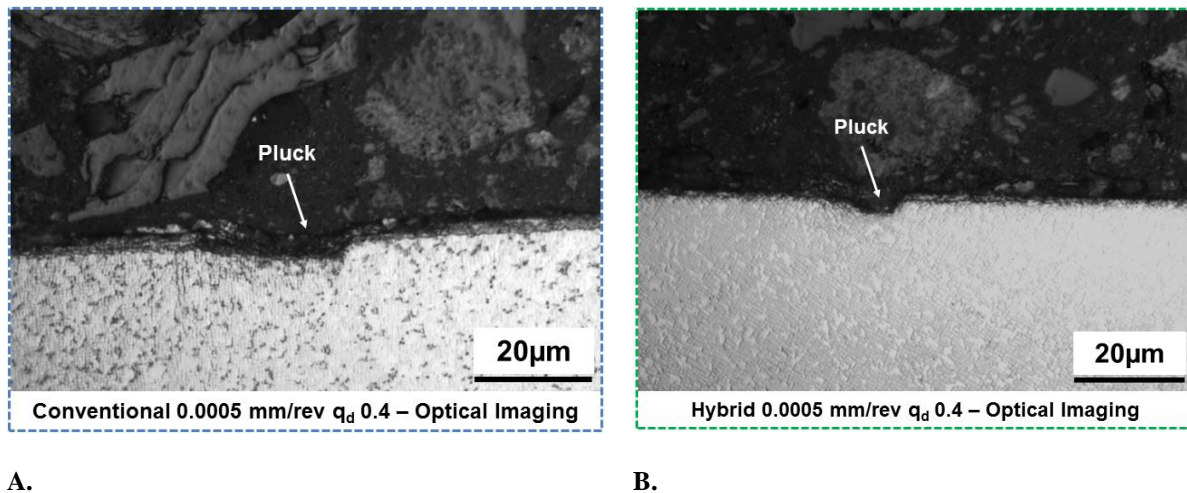
A.   **B.**

FIGURE 4.27 – OPTICAL IMAGES OF PLUCKING IN THE GROUND WORKPIECE MATERIAL (A) CONVENTIONAL WHEEL (B) HYBRID WHEEL.

4.3 BREAKDOWN OF GRINDING WHEEL TOPOGRAPHY

Following the results of Section 4.2 the dressing parameters with the lowest surface roughness and power consumption were carried forward to assess the breakdown of the generated topography on the different wheel types (Section 3.4). Multiple non-CD grinding passes were performed at the same grinding parameters and the change in grinding power and force captured. The wheel wear and surface roughness was measured at stages and SEM image analysis conducted on the ground workpieces and wheels to assess variation caused by the breakdown of the wheel topography.

4.3.1 GRINDING POWER ANALYSIS

Figure 4.28 shows the total power consumption of the grinding wheel spindle during grinding including coolant application for each grinding pass. The trend lines are third order polynomial as this produced the closest fit (based on R^2 value). There is a clear increase in the power consumption as the number of passes increase for all the wheels and dressing conditions with the elongated grit wheel demonstrating the steepest increase in power between passes $1 - 7$. Beyond pass 7, there is a small drop in the grinding power for the elongated grit wheels which is an indication of topography breakdown and new, sharp cutting points formed. A similar phenomenon occurred in the conventional

wheels after pass 6 with a significant power drop observed for the 0.002 mm/rev and q_d 0.8, and 0.0005 mm/rev and q_d 0.8 dressing conditions (Figure 4.28A & C). As seen in Section 4.2, the elongated grit wheels had the lowest power consumption for the first grinding pass where there is minimal topography wear. However, the hybrid wheels showed the lowest power consumption over the entire nine passes with the most consistent power response. The conventional wheels also demonstrated a large standard deviation (error bars) for the later grinding passes (pass 5 onwards) suggesting increased wheel breakdown causing high levels of power variation from the grinding spindle.

For all the wheel types and dress conditions, the power measured at pass 6 consistently did not fit the trend line of the other results. This point was when the cut position was shifted to a new location (Section 3.4.1) and is likely a result of variation in the workpiece casting reducing the actual depth of cut in the grind. All subsequent cuts however were to an accurate depth of cut.
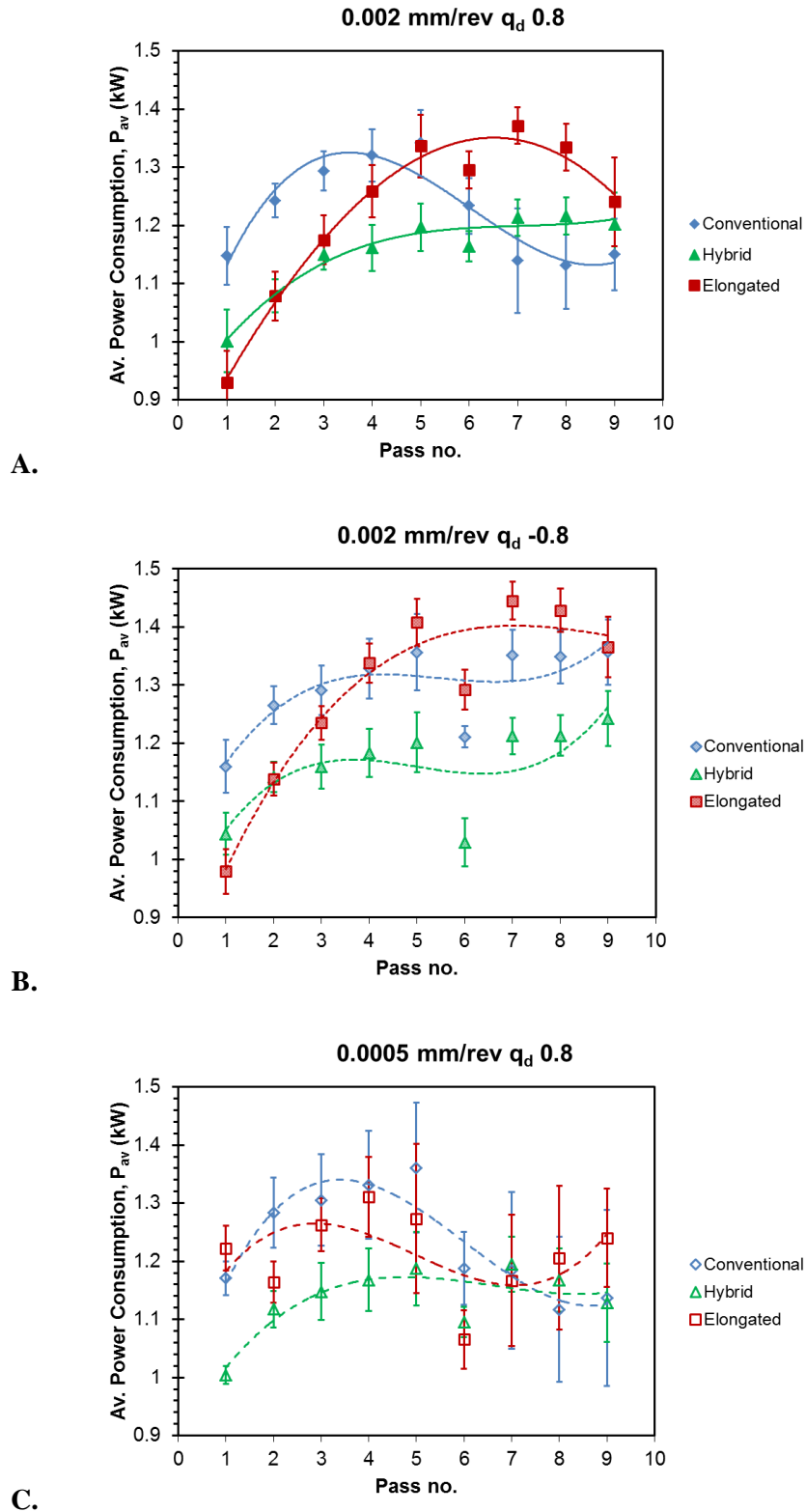
FIGURE 4.28 – POWER CONSUMPTION AS A FUNCTION OF GRINDING PASS NUMBER UNDER DIFFERENT INITIAL DRESSING CONDITIONS (A) 0.002 MM/REV AND Q_D 0.8 (B) 0.002 MM/REV AND Q_D -0.8 (C) 0.0005 MM/REV AND Q_D 0.8 ALL OF WHICH SHOW A RAPID INCREASE AFTER THE FIRST PASS.

Figure 4.29 shows the comparison of the grinding wheels behaviour using 30% and 100% triangular engineered grit by which the effects of the engineered grits on the wheel performance can

be assessed. The spindle power trend across nine passes for both wheel types is very similar with increasing power consumption between passes. The hybrid wheel showed some power reduction around pass 5 for the 0.0005 mm/rev and q_d 0.8 dressing condition. The average power consumed was less in the 100% triangular wheel, particularly at the 0.002 mm/rev and q_d 0.8 dressing condition. The selected infeed rates had a greater impact on the fully triangular grit wheel with larger power difference compared with the hybrid wheel.
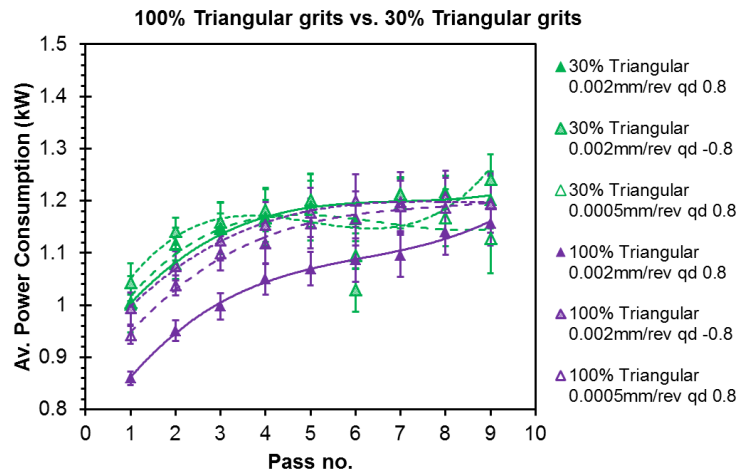
FIGURE 4.29 – POWER CONSUMPTION AS A FUNCTION OF GRINDING PASS FOR 100% TRIANGULAR GRIT WHEEL COMPARED TO 30% TRIANGUALR GRIT HYBRID WHEEL WHICH WAS GREATER AT DIFFERENT DRESSING CONDITIONS.

4.3.2 GRINDING FORCE ANALYSIS

Normal and tangential forces were recorded during wheel contact with the workpiece and are displayed in Figures 4.30A, C & E for each dressing condition. Each data point is an average from a sampling rate of 1000 Hz, therefore to determine the spread of the data as the cut progressed the corresponding standard deviations of the measured normal forces during cutting are presented in Figure 4.30B, D & F. As with the power consumption (Figure 4.28), there is a general pattern with a rapid increase in the normal force during early passes 1 – 6 where the normal force trend line is the steepest in the elongated grit wheel having a gradient of 81.4 vs 37.2 for conventional wheel pass 1 - 5 at 0.002 mm/rev and qd 0.8 dress. A dramatic drop was observed (>50 N) in the grinding force of the conventional wheel after pass 5/6 dressed in the 0.002 mm/rev and q_d 0.8, and 0.0005 mm/rev and q_d 0.8 conditions. As seen in Section 4.3.1, the elongate grit wheel had the lowest normal force for the first grinding pass (minimal wear) however, the hybrid wheels had the lowest force over the entire 9 passes. Tangential forces remained far more consistent with an approximate average difference of 15 – 20 N between the highest and lowest measured forces for all dressing conditions and wheel types. The standard deviation (Figure 4.30B & F) of normal force was seen to rapidly increase around pass 6

for the conventional and elongated grit wheels at the higher interference angle conditions. Comparatively, this remained consistently low for the hybrid grit structure wheel.

A.

B.

C.

D.

E.

F.
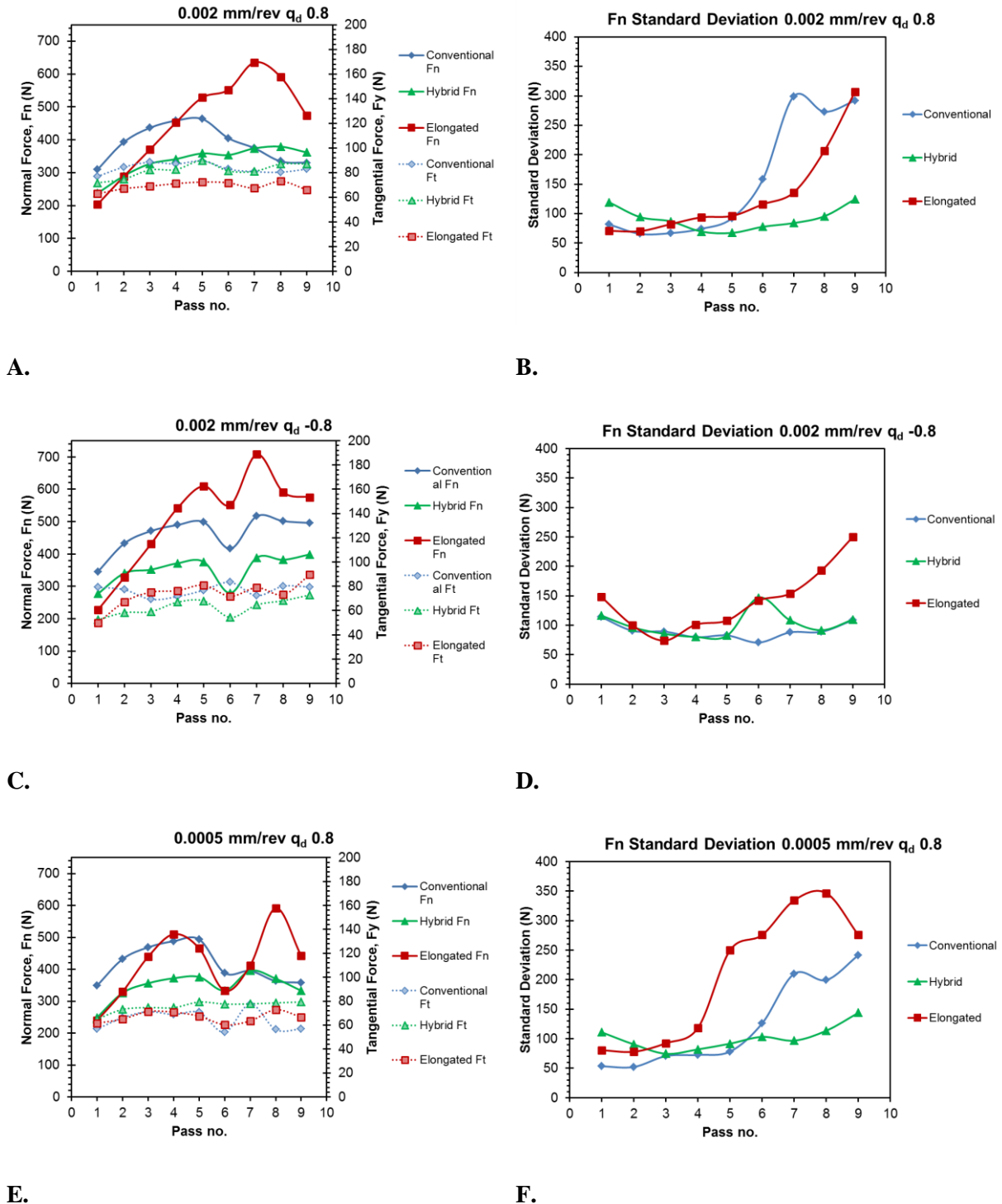
FIGURE 4.30 – AVERAGE NORMAL AND TANGENTIAL FORCES FOR EACH CUTTING PASS UNDER DIFFERENT DRESSING CONDITIONS AS WELL AS THE STANDARD DEVIATION OF THE MEASURED NORMAL FORCE (A) – (B) 0.002 MM/REV AND Q_D 0.8, (C) – (D) 0.002 MM/REV AND Q_D -0.8 (E) – (F) 0.0005 MM/REV AND Q_D 0.8.

4.3.3 GROUND SURFACE IMAGE ANALYSIS

Three ground surfaces were preserved for analysis in the CD ground condition, where the wheels stayed perfectly sharp, as well as after pass 5 and pass 9. As discussed in Section 3.3.3, a 3 mm² area was scanned under an SEM with displayed micrographs highlighting the general features observed on the surfaces to give a qualitative assessment of the ground workpiece surface. For the conventional wheels in the 0.002 mm/rev and q_d 0.8 dressing condition (Figure 4.31A-C) there are lots of deep tracks in the CD condition, highlighted by the arrows. By pass 5, there are more instances of overlapping workpiece material such as that circled in Figure 4.31B. At pass 9 both deep tracks (arrows) and embedded abrasive grits (circled) were visible at the surface. For the hybrid wheels (Figure 4.31D-F) there is little visual difference between the surfaces from CD to pass 9 with similar amounts of smearing (circled) and deeper tracks (arrows). As for the surfaces generated with the wheels with elongated grits (Figure 4.31G-F), by pass 9 there were more examples of redeposited workpiece material (small circle) and surface damage (large circle) compared to the CD surface.

A.

B.

C. Conventional, 0.002 mm/rev, q_d 0.8 – Pass 9

D. Hybrid, 0.002 mm/rev, q_d 0.8 – CD Pass

E. Hybrid, 0.002 mm/rev, q_d 0.8 – Pass 5

F. Hybrid, 0.002 mm/rev, q_d 0.8 – Pass 9

Elongated, 0.002 mm/rev, q_d 0.8 – CD Pass

Elongated, 0.002 mm/rev, q_d 0.8 – Pass 5

G.   **H.**

Elongated, 0.002 mm/rev, q_d 0.8 – Pass 9

I.
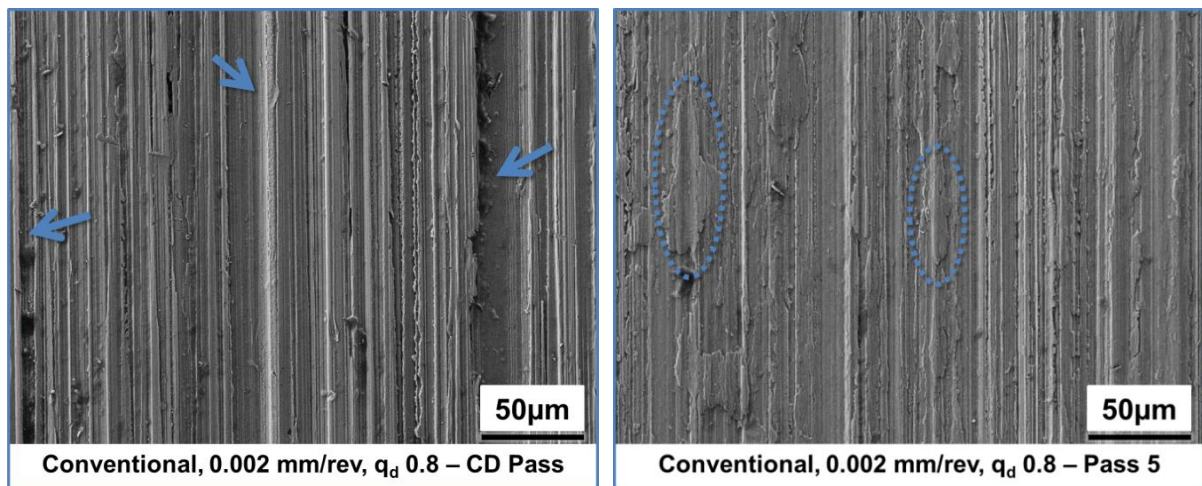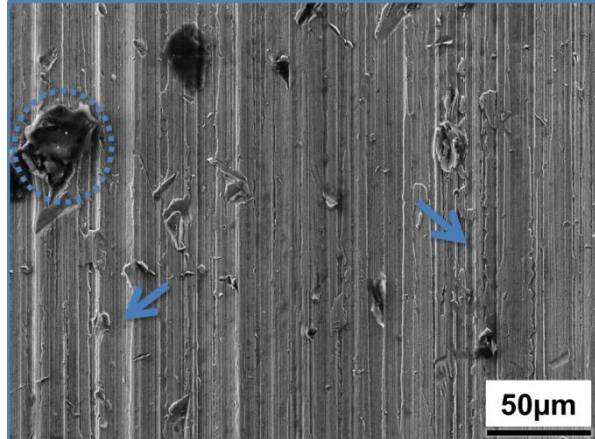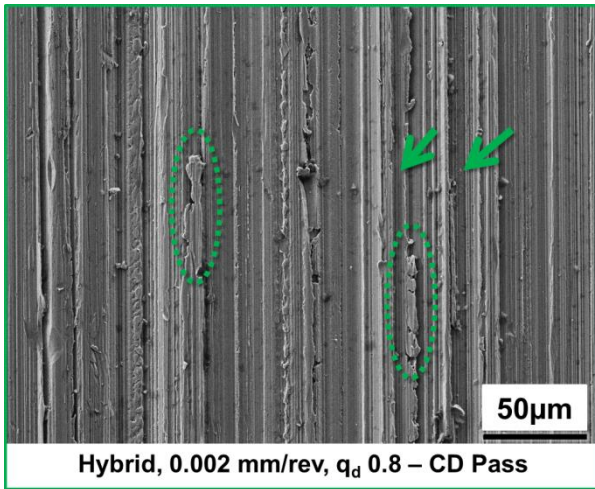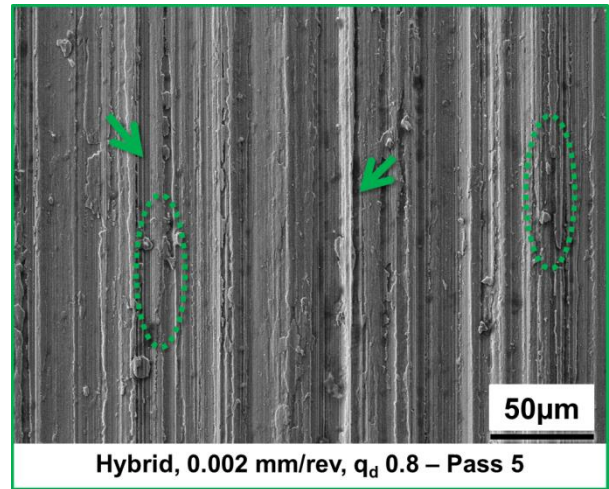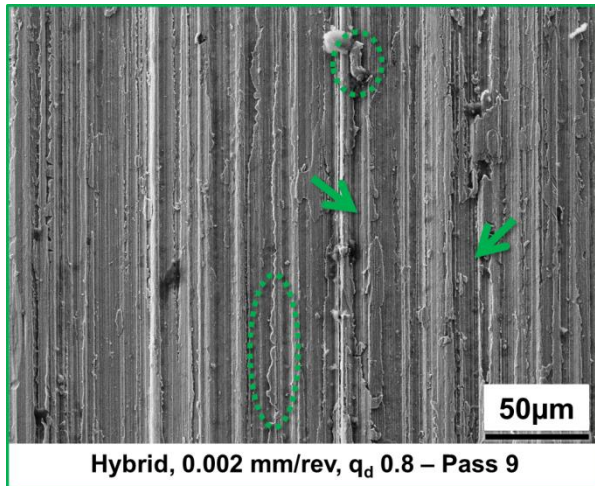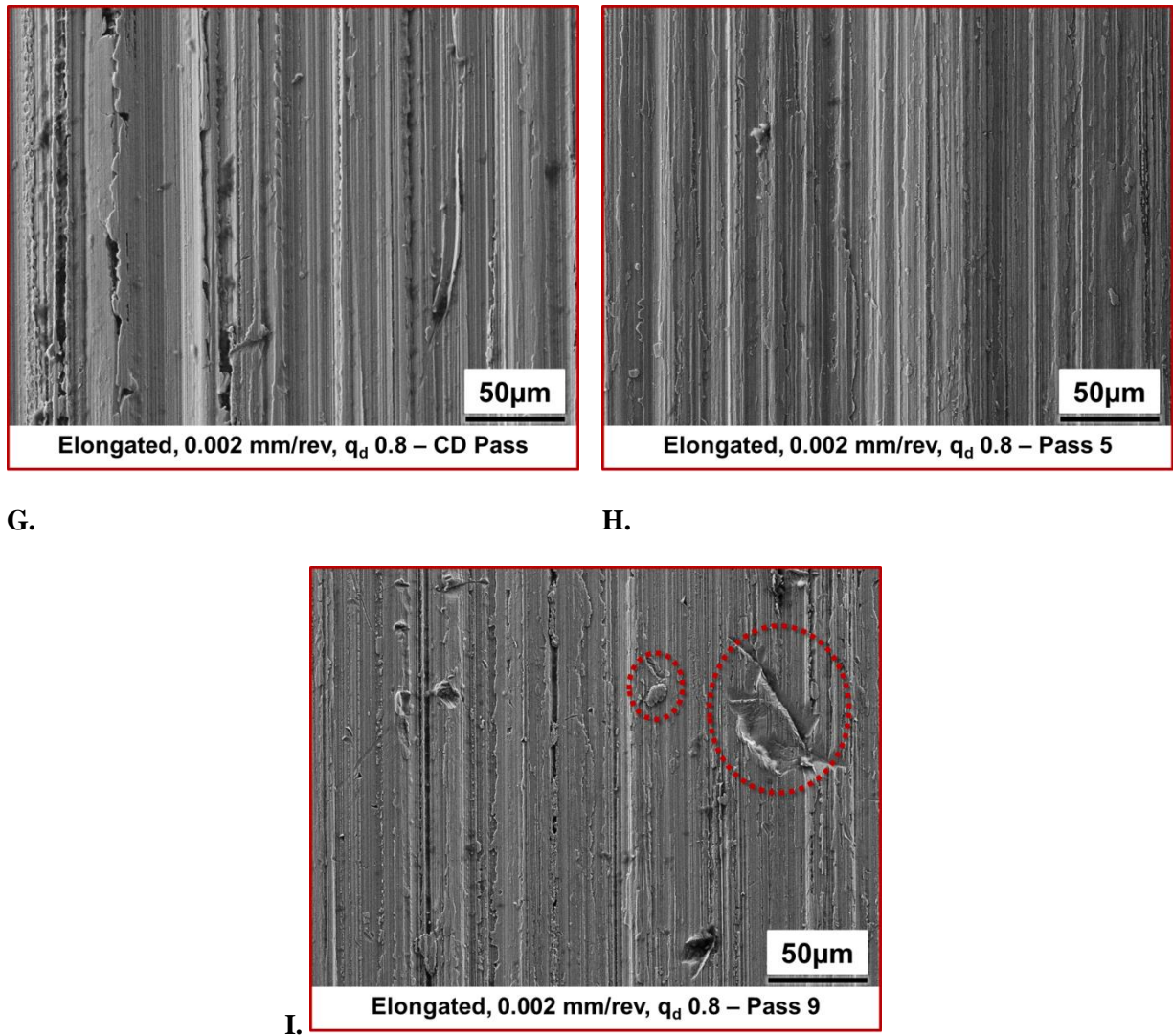
FIGURE 4.31 – SEM IMAGES OF GROUND SURFACES AFTER THE INITIAL CD GRINDING CUT, PASS 5 AND PASS 9. (A) – (C) CONVENTIONAL WITH GREATER EMBEDDED GRTIS AT PASS 9, (D) – (F) HYBRID SHOWING MORE CONSISTENT RESPONSE OVER 9 PASSES, (G) – (I) ELONGATED WITH MORE SURFACE FEATURES AT PASS 9.

The ground surface images for the 0.002 mm/rev and q_d -0.8 dressing condition are shown in Figure 4.32. For the conventional wheel (Figure 4.32A-C) the observations are similar to what is presented for the 0.002 mm/rev and q_d 0.8 dressing condition with deep tracks in the CD conditioned surface (arrows) and more overlapping material by pass 5 (circled). However, in pass 9 the tracks appear relatively shallow and no embedded grits were observed on the surface. A similar pattern seen on Figure 4.31 was found on the surfaces generated by the hybrid wheels (Figure 4.32D-F) although the overall level of smearing (circled) was reduced comparatively. As for the surfaces produced by the elongated grit wheel (Figure 4.32G-I) a trend of increased redeposited material (circled) from CD pass to pass 9 was seen.

Conventional, 0.002 mm/rev, q_d -0.8 – CD Pass

A.

Conventional, 0.002 mm/rev, q_d -0.8 – Pass 5

B.

Conventional, 0.002 mm/rev, q_d -0.8 – Pass 9

C.

Hybrid, 0.002 mm/rev, q_d -0.8 – CD Pass

D.

Hybrid, 0.002 mm/rev, q_d -0.8 – Pass 5

E.

F.

Hybrid, 0.002 mm/rev, q_d -0.8 – Pass 9

G.

Elongated, 0.002 mm/rev, q_d -0.8 – CD Pass

H.

Elongated, 0.002 mm/rev, q_d -0.8 – Pass 5

I.

Elongated, 0.002 mm/rev, q_d -0.8 – Pass 9
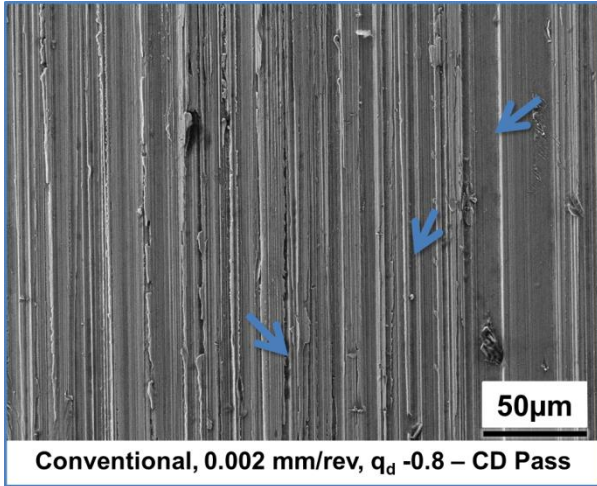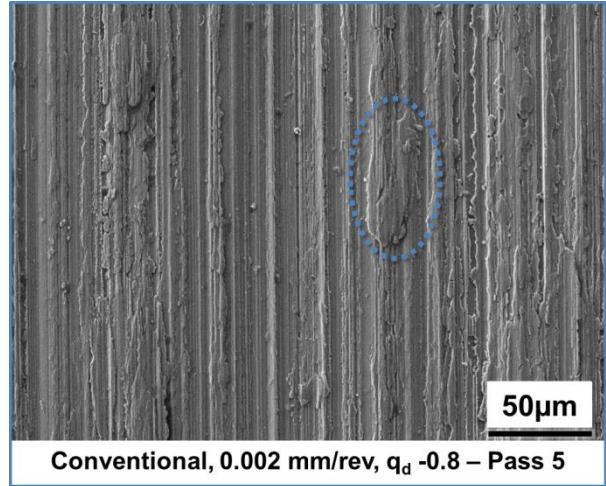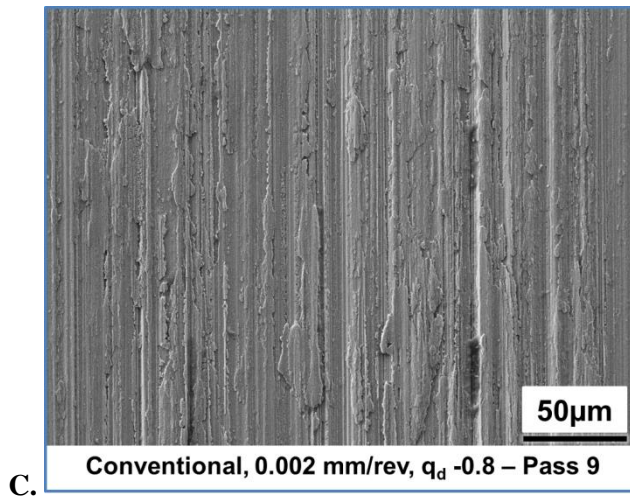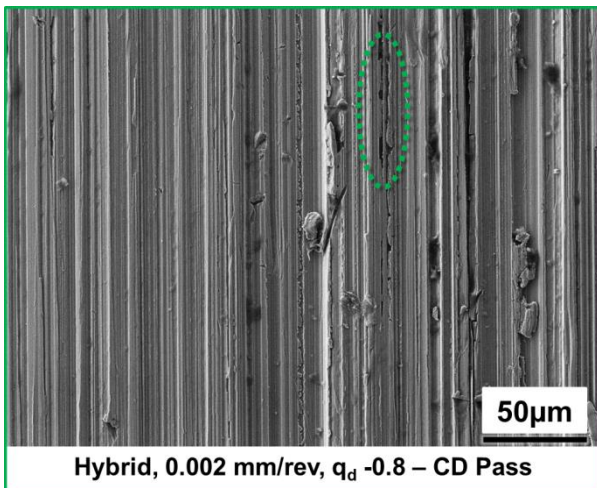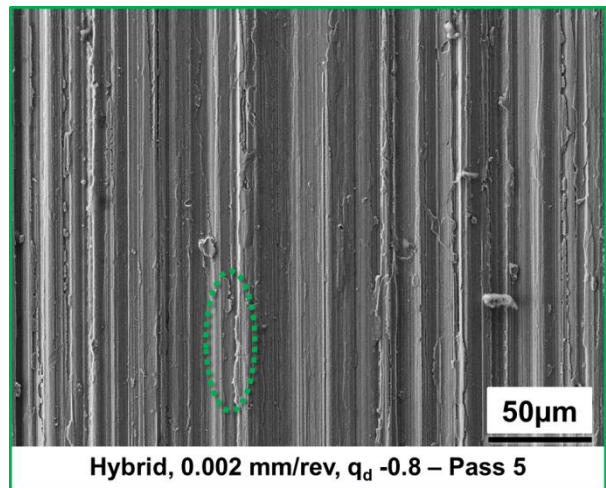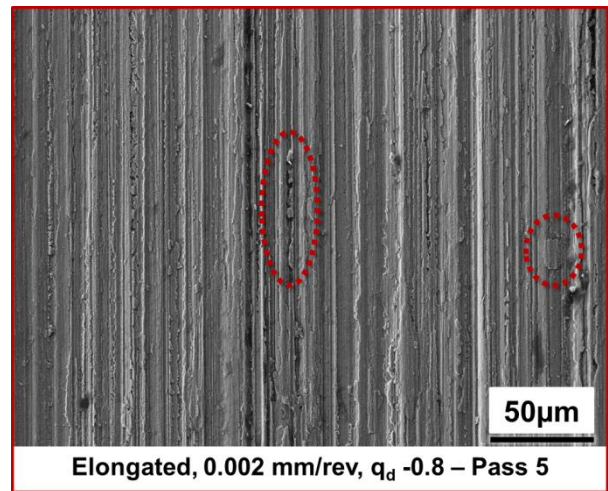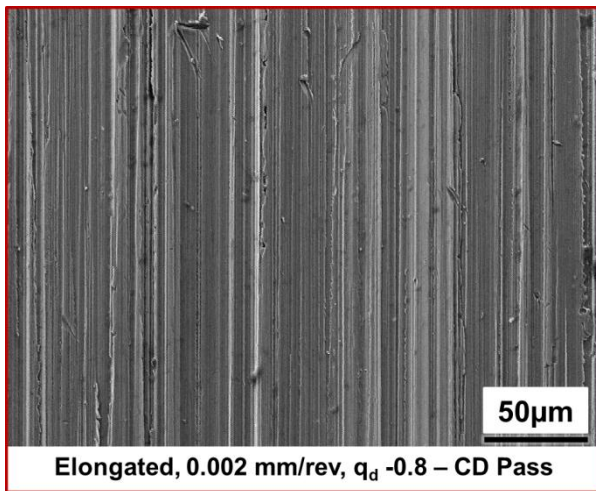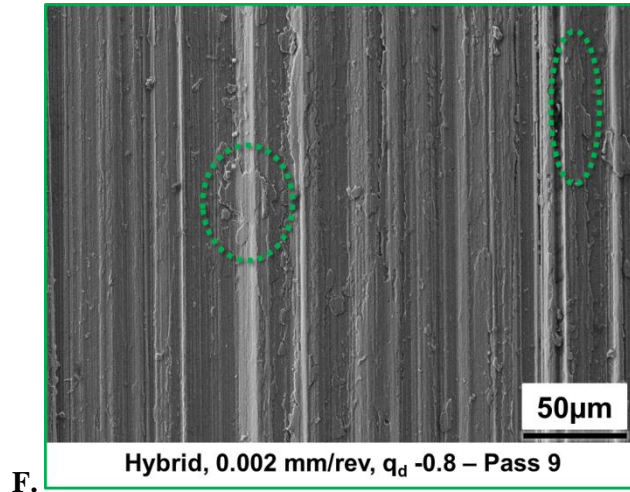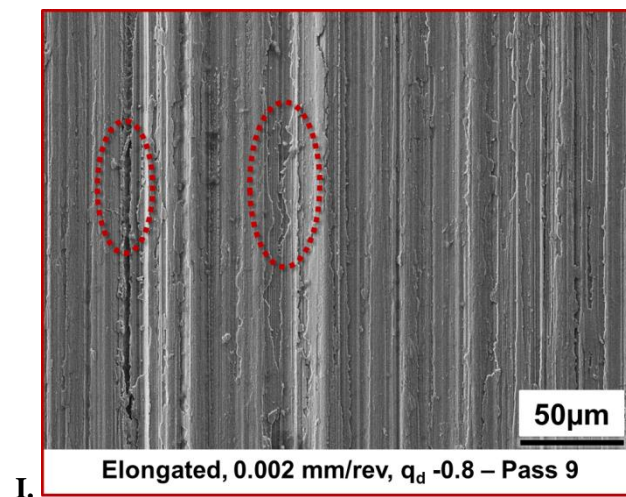
FIGURE 4.32 - SEM IMAGES OF GROUND SURFACES AFTER THE INITIAL CD GRINDING CUT, PASS 5 AND PASS 9. (A) – (C) CONVENTIONAL WITH SHALLOW TRACKS AT PASS 9, (D) – (F) HYBRID SHOWED REDUCED SMEARING, (G) – (I) ELONGATED IN THE 0.002 MM/REV Q_D -0.8 DRESSING CONDITION.WITH INCREASING REDEPOSITED MATERIAL.

Figure 4.33 shows SEM micrographs of ground surfaces using 0.0005 mm/rev and q_d 0.8 dressing condition. The surface ground by the conventional grit wheel (Figure 4.33A-C) exhibited increased levels of smearing (circled) and deeper tracks (arrows) at pass 9 compared to pass 5. The surfaces ground by the hybrid grit wheel (Figure 4.33D-F) again showed little visual difference between CD and pass 9, however, the level of smearing (circled) was reduced compared to the high interference angle dressing parameters (0.002 mm/rev and q_d 0.8). As in the 0.002 mm/rev and q_d -0.8 dressing condition, the elongated grit wheel (Figure 4.33G-I) surfaces showed an increasing level of deposited workpiece material on the surface of the relatively 'clean' CD ground surface to pass 9.

Conventional, 0.0005 mm/rev, q_d 0.8 – CD Pass

A.

Conventional, 0.0005 mm/rev, q_d 0.8 – Pass 5

B.

Conventional, 0.0005 mm/rev, q_d 0.8 – Pass 9

C.

Hybrid, 0.0005 mm/rev, q_d 0.8 – CD Pass

D.

Hybrid, 0.0005 mm/rev, q_d 0.8 – Pass 5

E.

Hybrid, 0.0005 mm/rev, q_d 0.8 – Pass 9

F.

Elongated, 0.0005 mm/rev, q_d 0.8 – CD Pass

G.

Elongated, 0.0005 mm/rev, q_d 0.8 – Pass 5
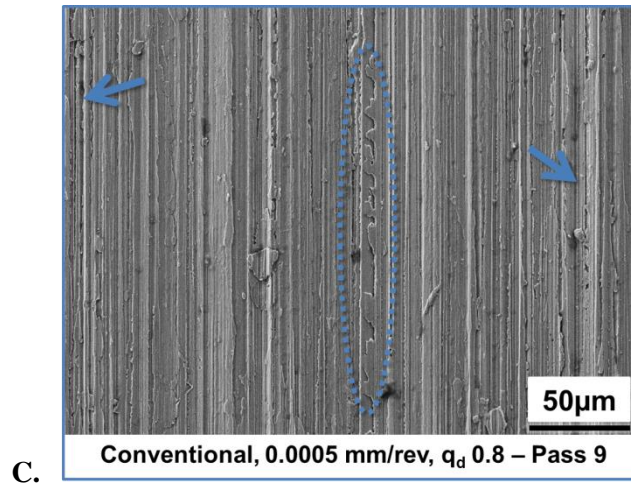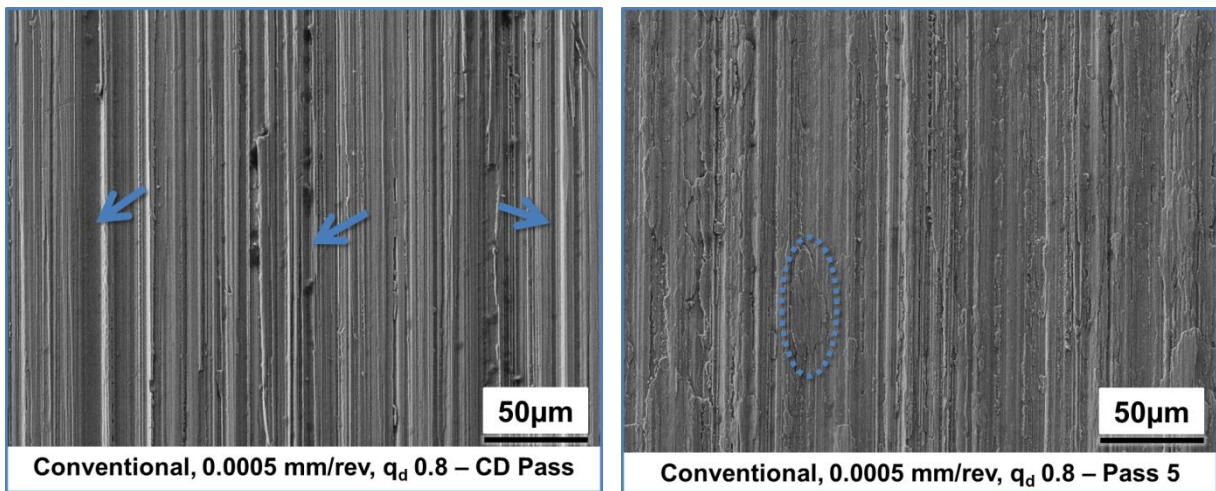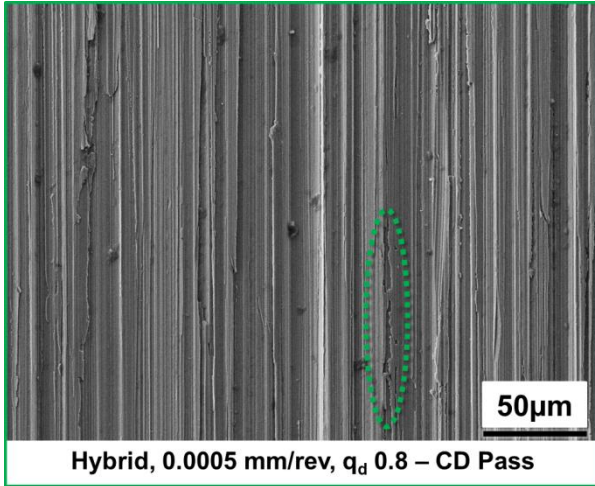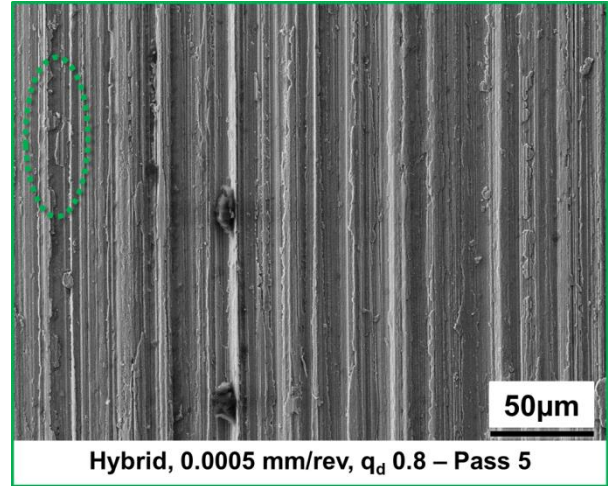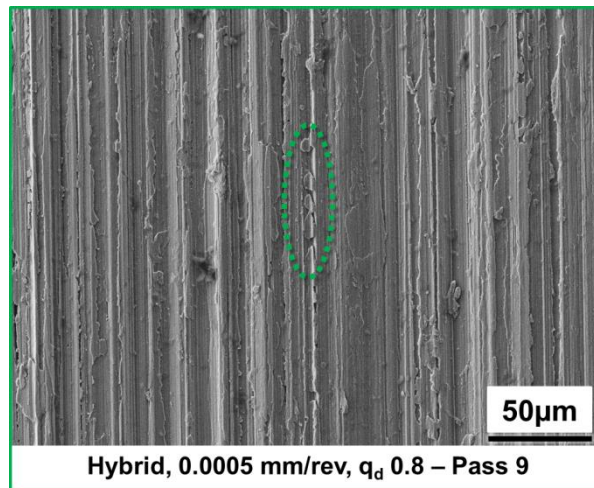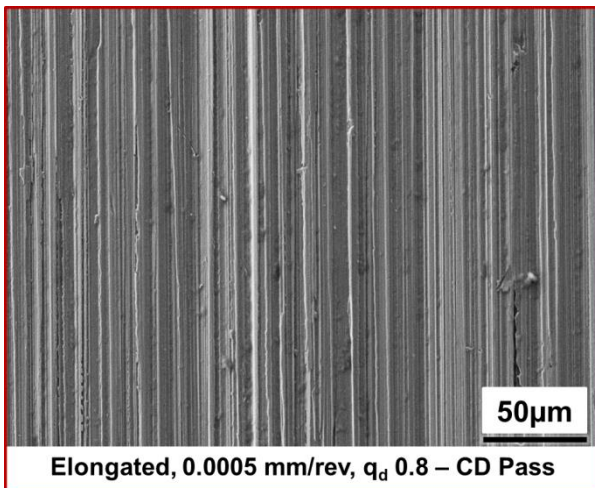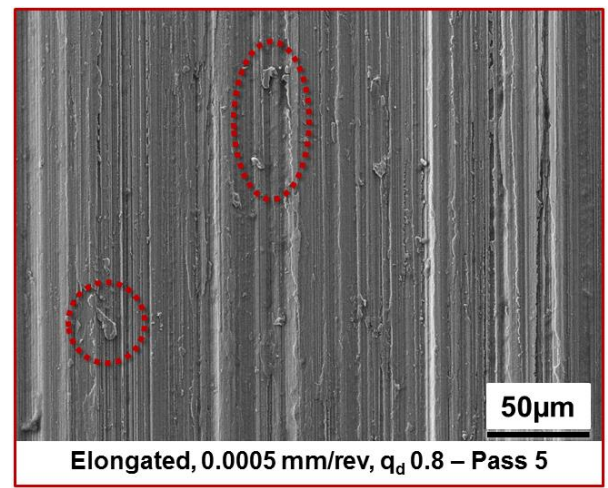
H.
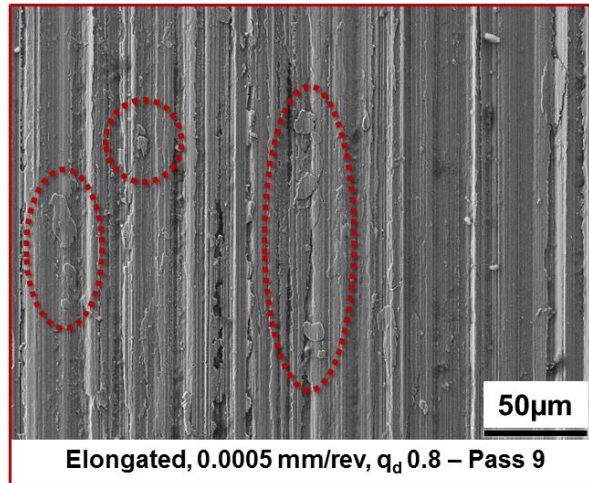
I.

FIGURE 4.33 - SEM IMAGES OF GROUND SURFACES AFTER THE INITIAL CD GRINDING CUT, PASS 5 AND PASS 9. (A) – (C) CONVENTIONAL WITH GREATER SMEARING AT PASS 9 COMPARED TO 5, (D) – (F) HYBRID WITH VERY CONSISTENT GROUND SURFACES , (G) – (I) ELONGATED IN THE 0.0005 MM/REV AND Q_D 0.8 DRESSING CONDITION WITH INCREASING REDEPOSITION.

4.3.4 WHEEL WEAR AND SURFACE ROUGHNESS ASSESSMENT

Figure 4.34 shows the radial wear of the abrasive wheels after nine grinding passes captured by grinding a step into graphite coupons (Section 3.4.3) with the worn wheel and measuring the size of the step using an Alicona variable height microscope (Section 3.4). It is clear that the hybrid grit wheel had the lowest level of radial wear compared to the others (>20% less wear). In both the conventional and hybrid wheels the lowest wheel wear was seen in the 0.002 mm/rev and q_d -0.8 dressing parameters, but the elongated grits wheel showed the greatest level of wear in this condition. Instead, the lowest wheel wear for the elongated grits wheel was seen at the low infeed rate condition (0.002 mm/rev and q_d 0.8).
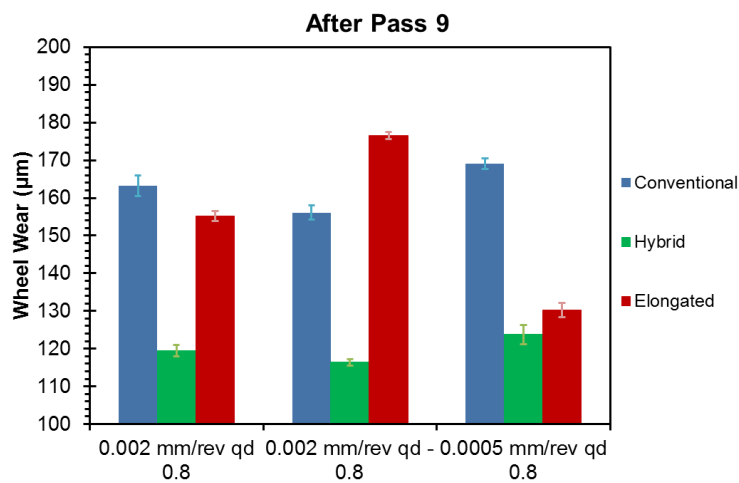
FIGURE 4.34 – ABRASIVE RADIAL WHEEL WEAR AFTER NINE GRINDING PASSES.

Surface roughness (Ra) was measured on the three preserved surfaces after the grinding cuts (initial CD pass, pass 5 and pass 9) and is shown in Figure 4.35. The conventional wheel surface roughness matches the behaviour seen in the ground surface images (Figure 4.31 – 4.33) with a decreasing roughness from the CD condition to pass 5 whereas for the higher interference angles (0.002 mm/rev and q_d 0.8, and 0.0005 mm/rev and q_d 0.8) the roughness increases again at pass 9. The hybrid wheel showed a higher roughness compared to the conventional one, over all the dressing conditions. The elongated grit wheels showed an increasing roughness trend however the Ra generated was much higher in the 0.002 mm/rev and q_d 0.8 dressing compared to the other parameters (as seen in Section 4.2).
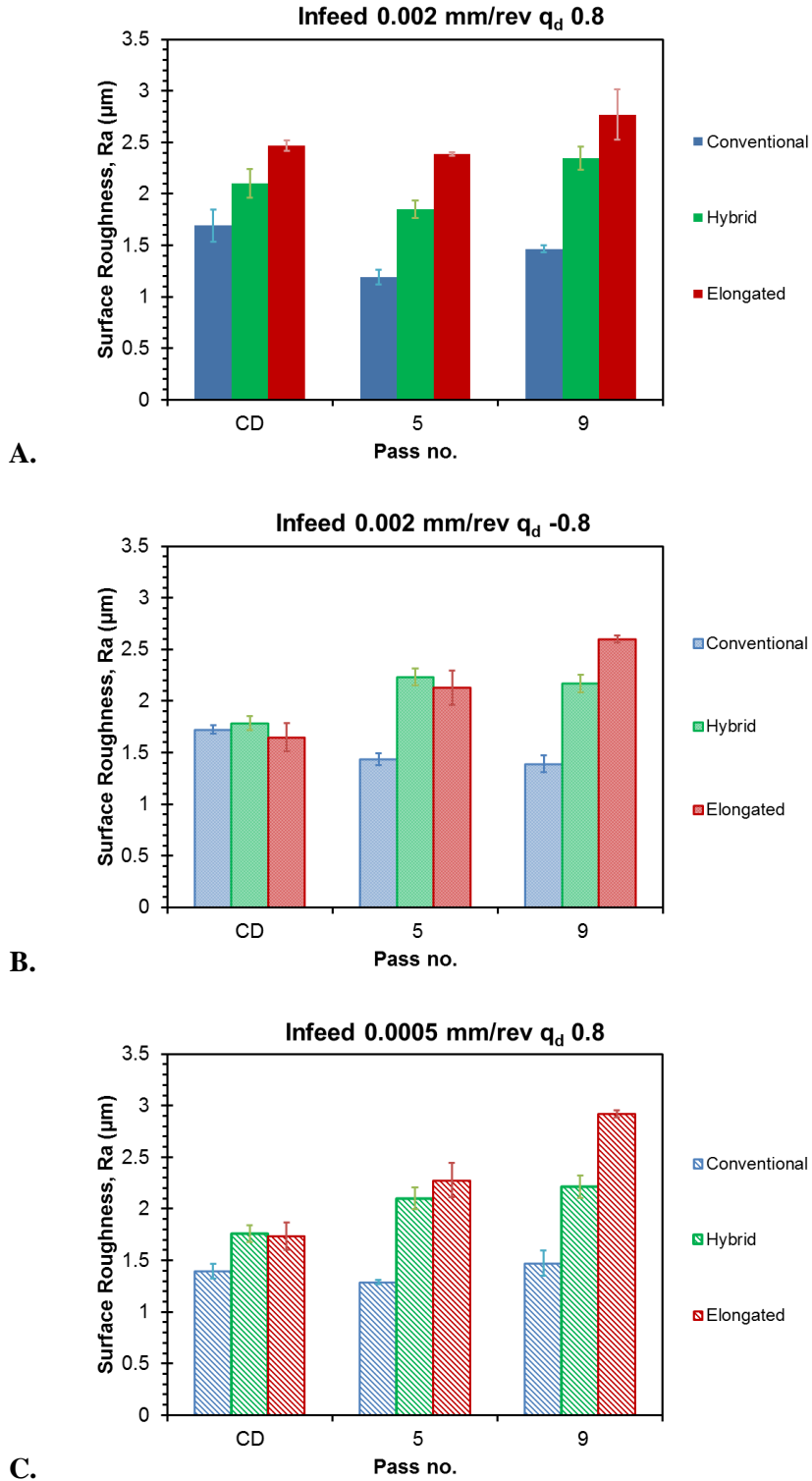
FIGURE 4.35 – SURFACE ROUGHNESS (RA) AFTER INITIAL CD PAS, PASS 5 AND PASS 9 FOR DRESSING CONDITION (A) 0.002 MM/REV AND Q$_D$ 0.8, (B) 0.002 MM/REV AND Q$_D$ -0.8, (C) 0.0005 MM/REV AND Q$_D$ 0.8.

4.3.5 Grinding Wheel Image Analysis

Each wheel type was dressed under 0.002 mm/rev infeed rate and 0.8 speed ratio and a stepped form created in the wheel by grinding it to different levels across the wheel width (as shown in Figure 3.31). These were sectioned and imaged under an SEM as described in Section 3.4. Figure 4.36 shows the micrographs of the grinding wheels after the selected dressing conditions and after pass 5 and 9 of the grinding process. The entire wheel samples were scanned and the images shown give examples of the features seen on the wheels. Macrofracture cracks were observed in the grits of the conventional and hybrid wheels immediately after dressing, as highlighted in the 'as dressed' column of Figure 4.36. For the elongated grit wheels, less cracking was seen but sharp cutting points were generated on the favourably orientated grits after dressing, as it is highlighted in Figure 4.36G.

4.0 Results

As Dressed	**Pass 5**	**Pass 9**

A.   B.   C.

D.   E.   F.

G.   H.   I.
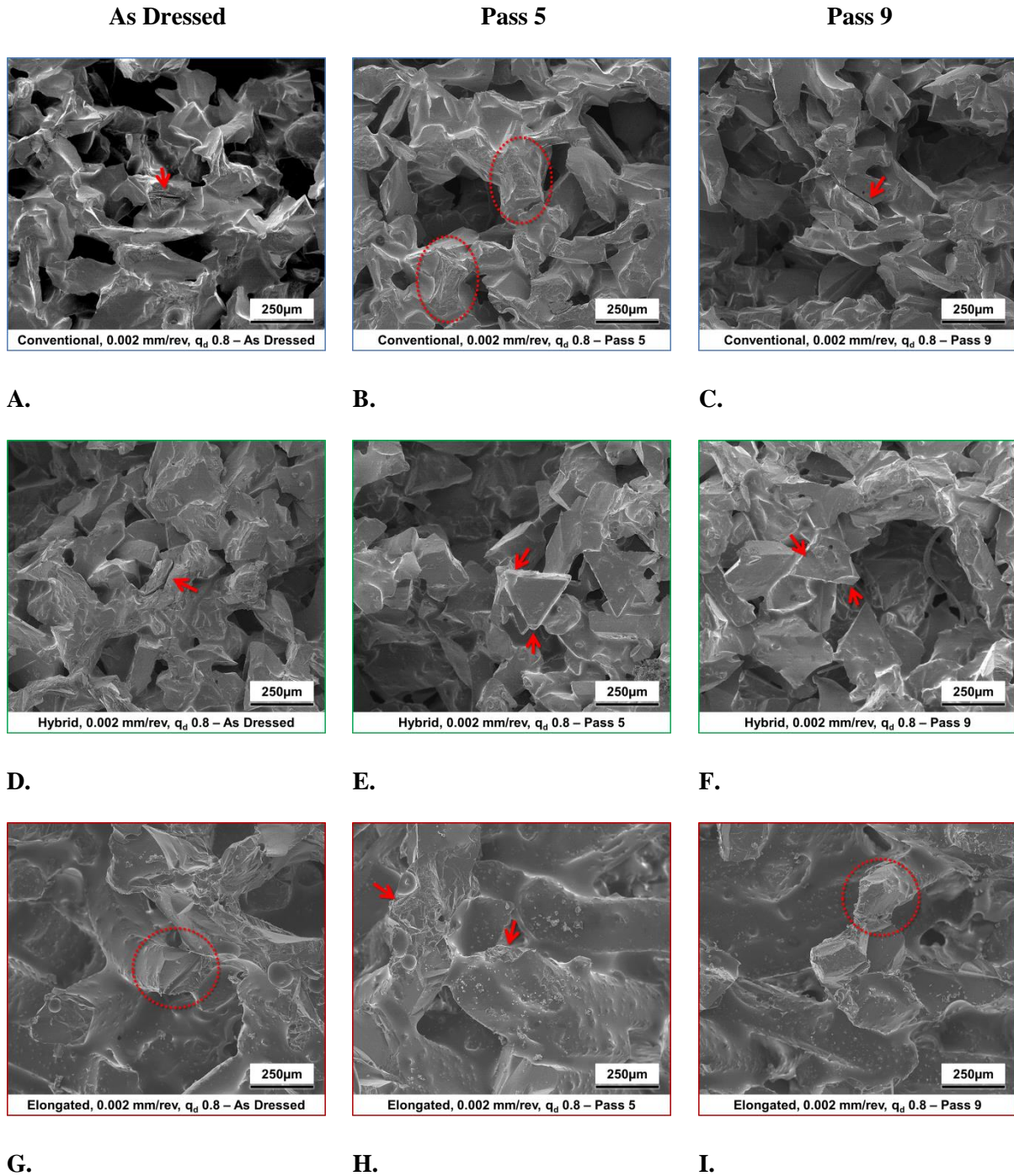
FIGURE 4.36 – SEM IMAGING OF GRINDING WHEEL TOPOGRAPHY IN THE AS DRESSED, AFTER 5 PASSES AND AFTER 9 PASSES FOR (A) – (C) CONVENTIONAL WITH DULLED GRITS IN PASS 5 AND CRACKS AT PASS 9, (D) – (F) HYBRID WITH MICROFRACTURING FOR ALL PASSES AND (G) – (I) ELONGATED GRIT WHEELS SHOWED SHARP CUTTING POINTS AT PASS 9 ON FAVOURABLY ORIETATED GRITS.

For all wheel types, by pass 5 extensive microfracture chipping of the grit tips is visible (highlighted, Figures 4.36B, E & H), particularly on the engineered grits of the hybrid wheel (Figure 4.36E), and no cracks were found. This behaviour continued to pass 9 for the hybrid wheel. For the conventional wheel however, cracking was seen again in the grits after 9 passes (arrow, Figure 4.36C). In the elongated grit wheel, some sharp points (circled, Figure 4.36I) as a result of

macrofracture were beginning to form on the favourably orientated grits again. Similar macrofracture behaviour is seen at pass 9 for the conventional wheel also (arrow, Figure 4.36C).

4.4 IMPACT OF GRINDING PARAMETERS ON TOPOGRAPHY PERFORMANCE

All previous trials have been conducted with fixed grinding parameters, therefore the behaviour of different topographies under varied grinding parameters must be understood. The different wheel types were tested under a Taguchi DoE to measure the influence of workpiece feed rate, depth of cut, wheel speed and dressing strategy on the grinding power, forces, wear and surface roughness. Metallurgical analysis was also performed on select samples to assess how the grinding parameters can impact the workpiece as well.

4.4.1 TOPOGRAPHY BREAKDOWN

Figure 4.37 shows the measured normal force (F_n) during grinding against specific material removal rate (Q') for each of the wheel types. Each data point indicates the measured, average F_n for a grinding cut (Table 3.11) with each grinding pass plotted separately. All trend lines were second order polynomials and red crosses show the results of validation trials for the general linear model explained in Section 3.5.1 (Table 3.12). In Figure 4.37A – B a red dashed line at Q' 25 mm^3 / mm s indicates substantial abrasive wheel breakdown point beyond which the normal forces and power consumption for passes 2 -6 were seen to be much lower than the first initial grinding cut. Therefore the grinding parameters were aggressive enough to trigger catastrophic bond fracture, causing extensive whole grain pull out and loss of wheel dimension. Hence the depth of cut is inaccurate (less than the nominal depth) and grinding forces decline. This breakdown response appeared to occur for both the conventional (Figure 4.37A) and hybrid (Figure 4.37B) wheels whereas the elongated grit showed increasing force beyond Q' 25 mm^3 / mm s suggesting no breakdown.
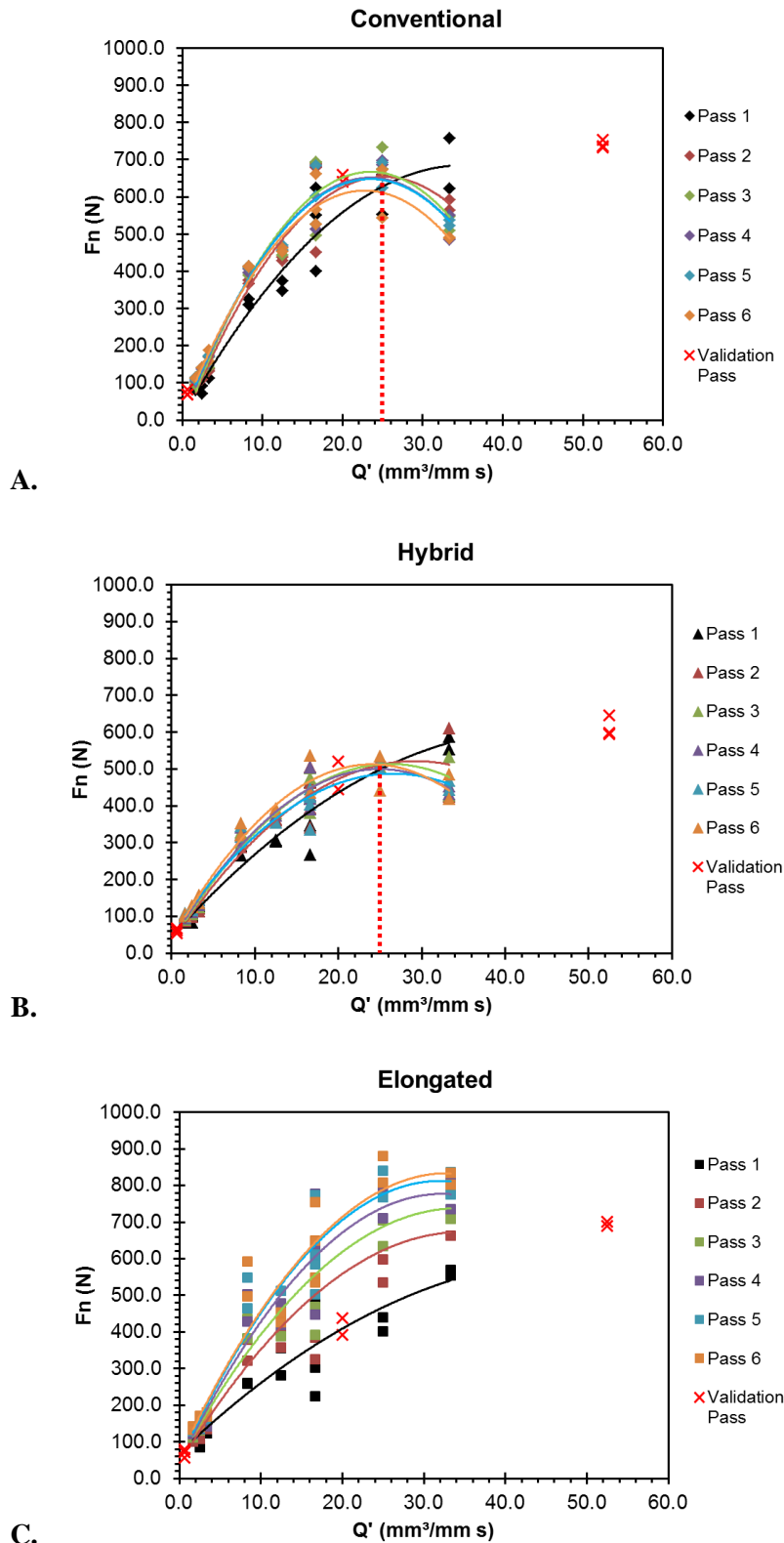
FIGURE 4.37 – NORMAL FORCE AS A FUNCTION OF MATERIAL REMOVAL RATE FOR (A) CONVENTIONAL, (B) HYBRID AND (C) ELONGATED GRIT WHEELS. THE DOTTED LINES INDICATE WHEEL BREAKDOWN AND THE RED CROSSES THE NORMAL FORCE FOR THE STATISTICAL MODEL VALIDATION.

This is further demonstrated by Figure 4.38 which shows wheel wear, measured on graphite coupons, as a function of Q' wherein the measured wheel wear is exponentially increasing for the conventional and hybrid grit wheels. This accelerates beyond a Q' of 25.0 mm^3 / mm s suggesting rapid bond breakdown in the wheel. For the elongated grit wheel however, the level of wheel wear remains relatively flat in the high Q' region.
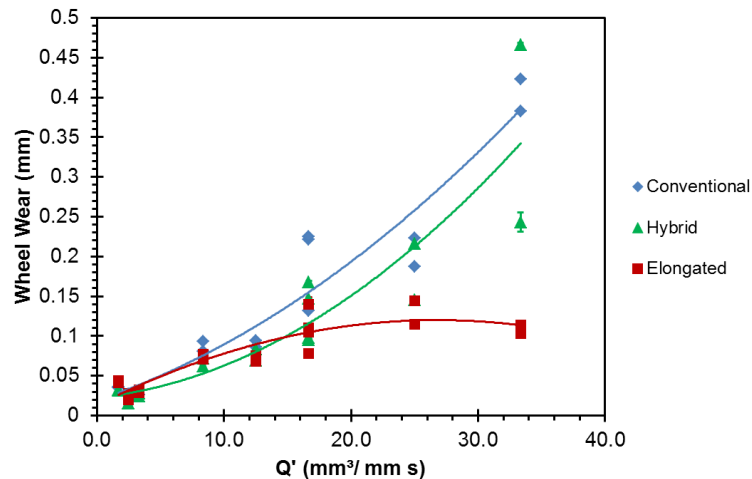
FIGURE 4.38 – INCREASING RADIAL WHEEL WEAR FOR EACH WHEEL TYPE AGAINST SPECIFIC MATERIAL REMOVAL RATE.

4.4.2 ANALYSIS OF VARIANCE

As mentioned in Section 3.5.1 a Taguchi factorial method was utilised for the experimental design due to the ability of the technique to reduce the number of experimental runs whilst enabling the testing of a wide range of parameters. This then became the basis of an Analysis of Variance (ANOVA) and a General Linear Model (GLM) to predict the behaviour of grinding normal force under different dressing conditions and material removal rates. The method was first developed in the 1980's by Prof. Taguchi to achieve three aims[245], [246]:

1. Design processes that are insensitive to uncontrollable environmental conditions.

2. Design products that are consistently on target.

3. Understand the source of variation of an output in a process.

It is this final aim that is particularly useful in this application as the purpose is to identify which parameters have the greatest influence on the measured variables in the grinding process.

The Taguchi method uses a Signal-to-Noise (S/N) ratio in order to measure the optimum parameters for a process, as well as ANOVA to identify the influential process parameters. For the S/N ratio, the signal (S) is the desirable value and the noise (N) is the undesirable value [247]. Therefore the higher the S/N ratio value, the more significant that parameter because it is less sensitive to uncontrollable environmental parameters (noise). The S/N ratio is calculated using equations which vary depending on the desired output of the measured parameter. This can be smaller-is-better (Equation 4.1) in which the aim is to minimise the measured variable, larger-is-better when it is to be maximised, and nominal-is-best [247].

$$\eta = -10\log\left[\left(\frac{1}{n}\left(y_1^2 + y_2^2\right)\right)\right] \qquad \text{EQUATION 4.1}$$

Whereby *y* is the observed data and *n* the number of observations.

ANOVA analysis compares the mean of the response output to different factor levels to determine the main effects and interactions [248], [249]. This can then be used to create a GLM to describe the relationship between the output variable and a number of continuous and categorical variables. An alpha level is determined (the risk of ruling that a difference exists between parameters when in reality, no difference is present) in order to find the p-value which indicates whether the null hypothesis (no significance in the difference between input parameters) can be rejected. A p-value below the alpha level suggests that the input parameters are significant. This technique was employed to predict the normal force during grinding from the data collected in the experiment (Section 3.5). Minitab software was used to calculate the S/N ratios for grinding force, surface roughness and wheel wear. The GLM predicting grinding forces is discussed in Section 5.4.3.

4.4.3 GRINDING FORCES

The signal-to-noise (S/N) ratio was assessed to capture the most influential parameters on the desired outcome of the experiment. The measured response was normal force and the factors for analysis were workpiece feed rate (mm/min), depth of cut (mm), wheel speed (m/s) and dressing strategy. The data was separated by wheel type and the data for passes 2 − 6 at Q' 33.3 mm^3 / mm s were removed for the conventional and hybrid wheels due to the catastrophic breakdown of these wheels which distorted their predicted behaviour at Q' < 25 mm^3 / mm s (Section 4.4.1).

The S/N ratio was calculated with 'smaller is better' (Equation 4.1) as minimised normal force is desired to reduce grinding friction and residual stresses in the material [1], [43]. Mean of S/N ratios are plotted in Figure 4.39 along with tables detailing the S/N ratio values. Dressing strategy 1 is 0.002 mm/rev and q_d 0.8, 2 is 0.002 mm/rev and q_d -0.8, and 3 is 0.0005 mm/rev and q_d 0.8.

Conventional Wheel

Signal-to-noise: Smaller is better

A.

Response Table for S/N Ratios – Conventional

B.
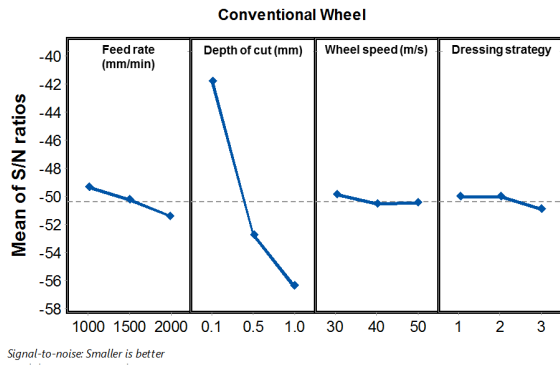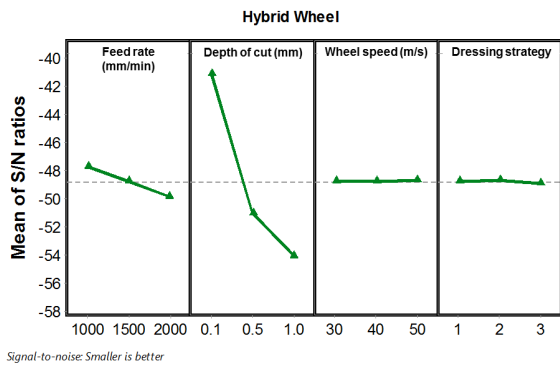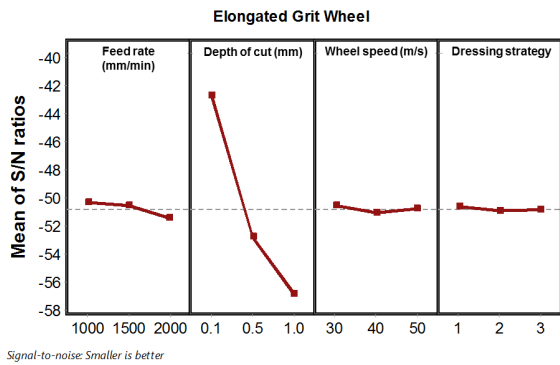
Level	Feed rate	Depth of Cut	Vc	Dressing Strategy
1	-49.37	-41.84	-49.93	-50.08
2	-50.27	-52.77	-50.6	-50.05
3	-51.44	-56.47	-50.54	-50.95
Delta	2.07	14.63	0.67	0.89
Rank	2	1	4	3

Hybrid Wheel

Signal-to-noise: Smaller is better

C.

Response Table for S/N Ratios - Hybrid

D.

Level	Feed rate	Depth of Cut	Vc	Dressing Strategy
1	-47.76	-41.20	-48.83	-48.77
2	-48.79	-51.10	-48.84	-48.71
3	-49.88	-54.13	-48.76	-48.95
Delta	2.12	12.94	0.08	0.24
Rank	2	1	4	3

Elongated Grit Wheel

Signal-to-noise: Smaller is better

E.

Response Table for S/N Ratios - Elongated

F.

Level	Feed rate	Depth of Cut	Vc	Dressing Strategy
1	-50.35	-42.73	-50.56	-50.66
2	-50.61	-52.83	-51.09	-50.92
3	-51.46	-56.86	-50.78	-50.85
Delta	1.11	14.13	0.53	0.26
Rank	2	1	3	4

FIGURE 4.39 – NORMAL FORCE MAIN EFFECTS PLOT OF S/N RATIO FOR (A)-(B) CONVENTIONAL, (C)-(D) HYBRID AND (E)-(F) ELONGATED GRIT WHEELS.

It is clear in (Figure 4.39A, C and E) that the depth of cut had the most variation in the S/N ratio mean, across all wheels, with the highest delta value and therefore highest rank. In the conventional and hybrid wheels, the dressing strategy was ranked third with the high infeed rate conditions (0.002 mm/rev) causing the generation of the highest S/N ratio. In the elongated grit wheel, the dressing strategy was ranked fourth with the lowest delta value (Figure 4.39F).

Using the same dataset from the analysis in Figure 4.39, an ANOVA test was performed to understand the level of contribution of each of the input factors on the grinding normal force. A GLM was created with workpiece feed rate, depth of cut, wheel speed and dressing strategy and input factors. No cross predictors were included in the model. Table 4.2 clearly indicates that depth of cut is

©2019 Rolls-Royce
Not subject to Export Control
Private

the most influential parameter on the normal force during grinding contributing over 84% across all the wheels. The influence of pass number is also significantly higher in the elongated grit wheel (6.56%) compared to the conventional and hybrid (0.57% and 0.84% respectively). The dressing strategy (0.53%) appeared to be the most influential for the hybrid wheels compared to the other wheel types, which appears to contradict the response seen in the previous investigation (Section 4.2). The dressing strategy also demonstrates more influence on the normal force compared to the wheel speed.

TABLE 4.2 - PERCENTAGE CONTRIBUTION OF GRINDING INPUT FACTORS TO NORMAL FORCE.

	% Contribution		
	Conventional	**Hybrid**	**Elongated**
Feed rate	0.77	0.09	0.55
Depth of Cut	94.09	90.17	84.79
Wheel speed	0.08	0.48	0.05
Dressing Strategy	0.08	0.53	0.16
Pass no.	0.57	0.84	6.56
Error	4.41	7.90	7.89

4.4.4 SPECIFIC ENERGY AND WHEEL WEAR

Specific energy is dependent on the tangential force in grinding and the actual depth of cut (Equation 2.3). The loss of dimensional form of the wheel affects the actual depth of cut so the level of wheel wear was measured after six grinding passes. The specific energy was then calculated as an average over six passes using the total wheel wear and total power consumption (as explained in Equation 2.3).

The data was categorised by wheel type and dressing condition and specific energy curves generated (such as Figure 5.03). The equations for these curves (see Appendix Hii, fitted with a power trend line) were used to predict the average specific energy for each of the wheels and topographies at three material removal rates, Q' 3.0, 9.0 and 18.0 mm^3 / mm s. The calculated specific energy is plotted on bar charts around the measured average specific energy curve in Figure 4.40.

The most variation in specific energy between the dressing conditions was seen in Figure 4.40A at the low material removal rate (Q' 3.0 mm^3 / mm s) with the 0.002 mm/rev and q_d 0.8 condition having the lowest grinding specific energy. At Q' 9.0 and 18.0 mm^3 / mm s (Figure 4.40B and C, respectively) the specific energy was more similar between the different dressing strategies. The elongated grit wheel had the lowest specific energy compared to the other wheels in all dressing conditions and material removal rates. At Q' 3.0 mm^3 / mm s the hybrid wheel had the largest specific energy however by Q' 18.0 mm^3 / mm s the conventional wheel became the most energy consuming

wheel. The 0.002 mm/rev and q_d -0.8 dressing condition caused the highest energy grinding at the Q' 3.0 and 9.0 mm^3 / mm s material removal rates. At Q' 18.0 mm^3 / mm s however, the difference between dressing conditions was very small (21.1 J/mm^3 at Q' 3.0 mm^3 / mm s compared to 2.3 J/mm^3 variation at Q' 18.0 mm^3 / mm s for the conventional wheel). This suggests dressing is less influential on the grinding behaviour at large volumes of material removal.
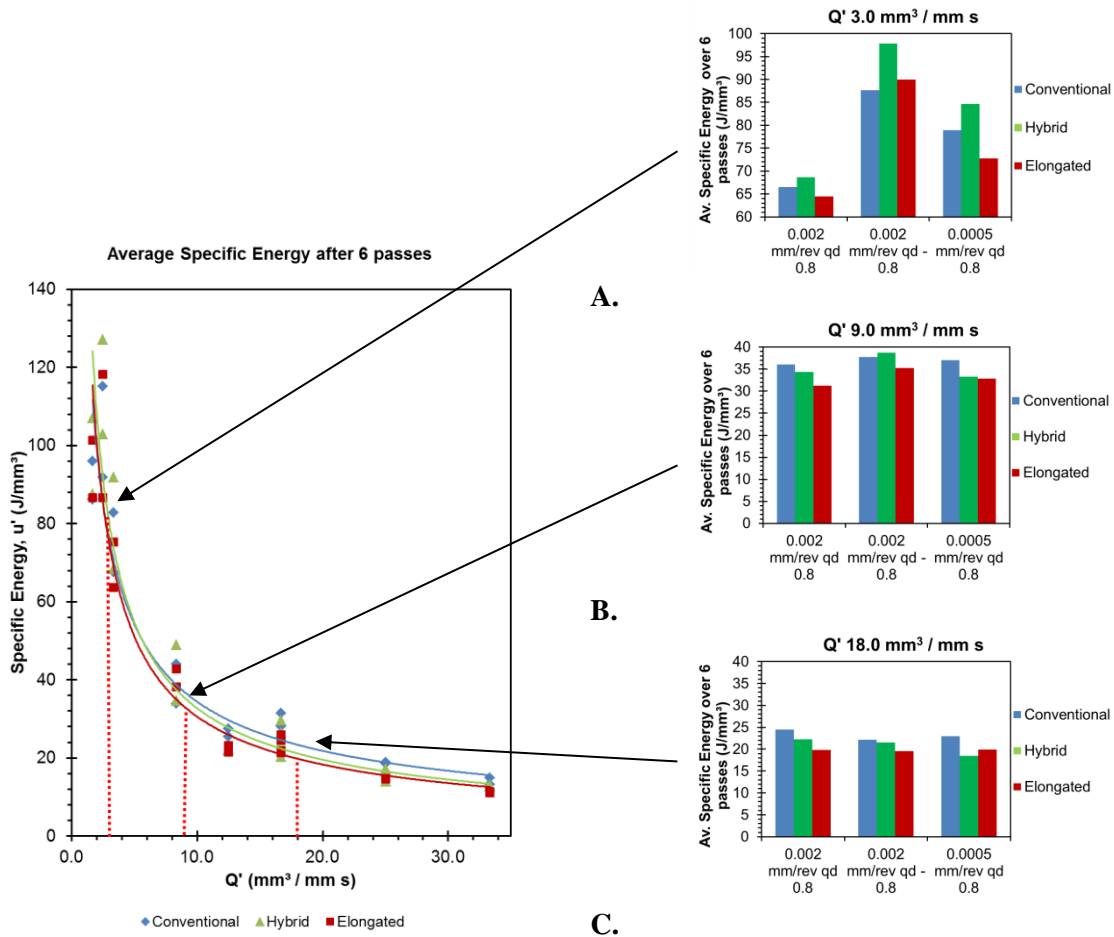
FIGURE 4.40 – PREDICTED AVERAGE SPECIFIC ENERGY OVER SIX GRINDING PASSES AT (A) Q' 3.0, (B) Q' 9.0 AND (C) Q' 18.0 MM^3 / MM S. THE RED, DOTTED LINES ON THE CURVE INDICATE THE LOCATION OF THE Q' VALUES ON THE SPECIFIC ENERGY CURVE.

Using the same average specific energy data a main effects plot was created comparing the wheel types across all grinding parameters and dressing conditions (Figure 4.41). This clearly indicates that the specific energy during grinding was reduced for the elongated grit wheel compared to the others.
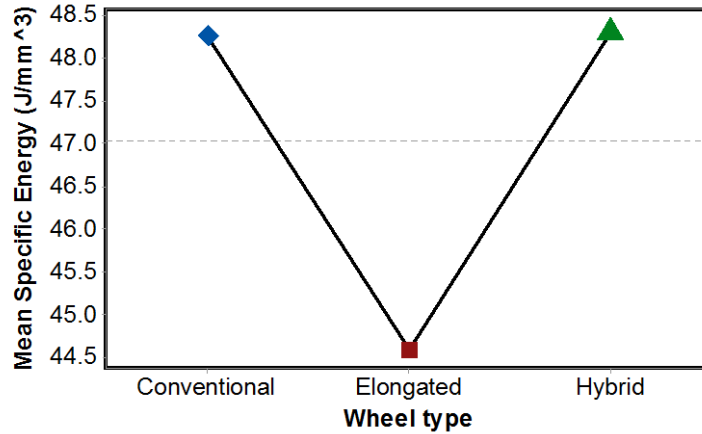
FIGURE 4.41 – MAIN EFFECTS PLOT OF AVERAGE SPECIFIC ENERGY BETWEEN EACH ABRASIVE WHEEL TYPE WHICH WAS LOWEST IN THE ELONGATED GRIT WHEELS.

Figure 4.42 shows the gradient of the linear relationship between the normal and tangential force, i.e. the friction coefficient, calculated for each wheel and dressing strategy. The data points for every pass were included in the gradient calculation. It is clear that the lowest friction was for the elongated grit wheels at the steep dressing interference angle (0.002 mm/rev and q_d 0.8). For the conventional and hybrid wheels the friction was greatest at the shallow interference angle condition (0.002 mm/rev and q_d -0.8) whereas it was greatest in the elongated grit wheels at the low infeed (0.0005 mm/rev).
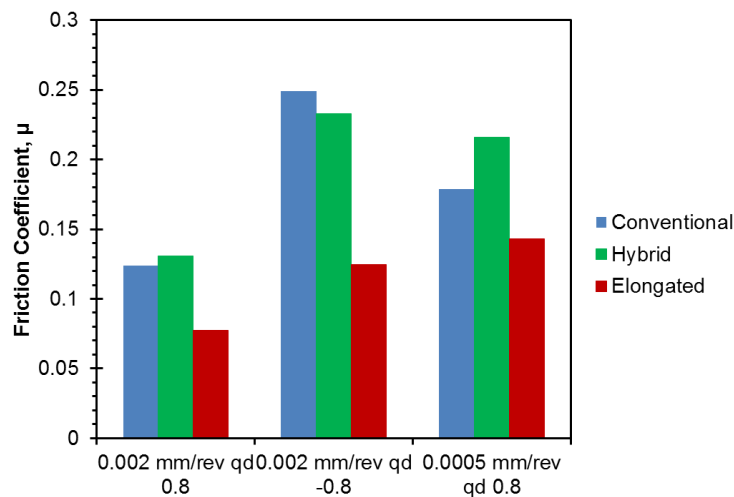
FIGURE 4.42 – FRICTION COEFFICIENT FOR EACH WHEELT TYPE AND DRESSING CONDITION. ACROSS ALL GRINDING PASSES.

Wheel wear was measured using the graphite coupon method discussed in Section 3.4.2. Figure 4.43 shows the S/N ratio calculated with 'smaller is better' for the abrasive wheel wear as minimal wear is desired to ensure the ground workpiece maintains dimensional accuracy. The data was separated by wheel type and the data points for passes 2- 6 removed in the Q' 33.3 mm^3 / mm s

grinding condition. Dressing strategy 1 is 0.002 mm/rev and q_d 0.8, 2 is 0.002 mm/rev and q_d -0.8, and 3 is 0.0005 mm/rev and q_d 0.8.

A.
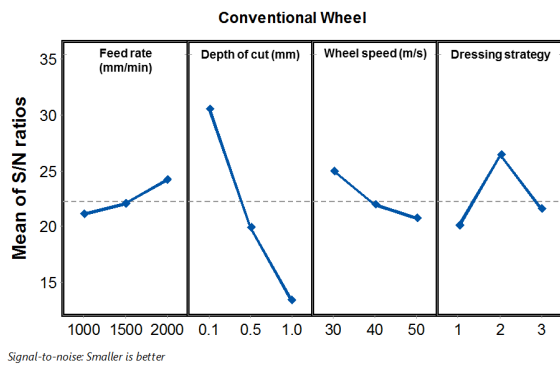
Response Table for S/N ratios - Conventional

Level	Feed rate	Depth of Cut	Vc	Dressing Strategy
1	21.10	30.49	24.96	20.12
2	22.07	19.89	21.91	26.41
3	24.20	13.38	20.75	21.57
Delta	3.10	17.12	4.21	6.29
Rank	4	1	3	2

B.

C.
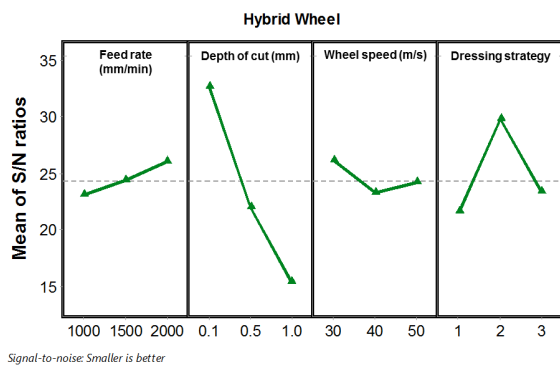
Response Table for S/N ratios - Hybrid

Level	Feed rate	Depth of Cut	Vc	Dressing Strategy
1	23.14	32.62	26.14	21.66
2	24.40	22.03	23.30	29.80
3	26.05	15.37	24.18	23.38
Delta	2.90	17.25	2.84	8.14
Rank	3	1	4	2

D.

E.
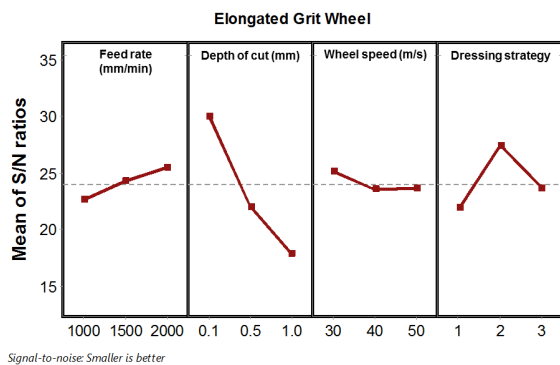
Response Table for S/N ratios - Elongated

Level	Feed rate	Depth of Cut	Vc	Dressing Strategy
1	22.68	30.02	23.19	21.93
2	24.3	22.04	23.54	24.75
3	23.42	18.33	23.66	23.72
Delta	1.63	11.7	0.47	2.82
Rank	3	1	4	2

F.

FIGURE 4.43 – WHEEL WEAR MEAN OF S/N RATIOS FOR (A)-(B) CONVENTIONAL, (C)-(D) HYBRID (E)-(F) ELONGATED GRIT WHEELS.

As with normal force, the depth of cut was ranked as the most influential parameter for reducing the grinding wheel wear in Figure 4.43. However, across all wheel types, the dressing strategy was the second most significant variable. The tables in Figure 4.43 (B, D and F) also suggest that the lowest wear can be achieved at the lowest dressing interference angle (level 2) as this had the highest S/N ratio values.

A GLM was created for wheel wear to understand the percentage influence of different parameters on the wear response after six grinding passes. The input factors for the model were workpiece feed rate, depth of cut, wheel speed and dressing strategy with no cross predictors included in the model. Table 4.3 shows the percentage contribution with depth of cut again being by far the most impactful parameter.

TABLE 4.3 – PERCENTAGE CONTRIBUTION OF INPUT PARAMETERS TO VARIATION IN GLM OF ABRASIVE WHEEL WEAR.

	% Contribution		
	Conventional	Hybrid	Elongated
Feed rate	5.46	2.10	0.15
Depth of Cut	90.57	89.88	88.94
Wheel speed	0.60	0.17	0.41
Dressing Strategy	2.42	2.30	4.29
Error	0.96	5.55	6.21

A main effects plot for wheel wear comparing the different wheel types, excluding all other factors, is shown in Figure 4.44. As with Figure 4.41 for normal force, the elongated grit wheel saw the lowest wheel wear.
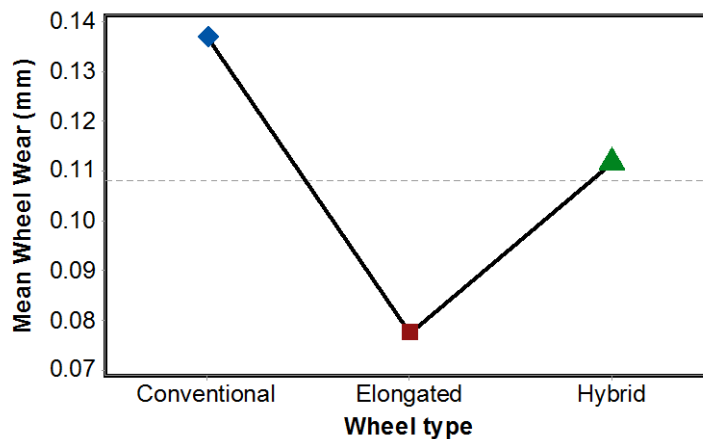
FIGURE 4.44 – MAIN EFFECTS PLOT FOR WHEEL WEAR FOR EACH ABRASIVE WHEEL TYPE.

4.4.5 SURFACE ROUGHNESS

The surface roughness measured after pass 6 on surface replicas is shown in Figure 4.45 for each of the wheel types against the equivalent chip thickness (calculated in Appendix A) which was used as a representation of grinding parameters by giving a simple approximate chip size. Actual chip thickness will show some variation between abrasive grit shapes and orientations. There is a clear trend in Figure 4.45 that as the equivalent chip thickness increases, the surface roughness (Ra) of the workpiece also increases linearly. The conventional wheel had the lowest roughness of all the wheels

at all chip thicknesses. The hybrid and elongated were noticeably higher with the hybrid generating the highest surface roughness workpiece at higher chip sizes.
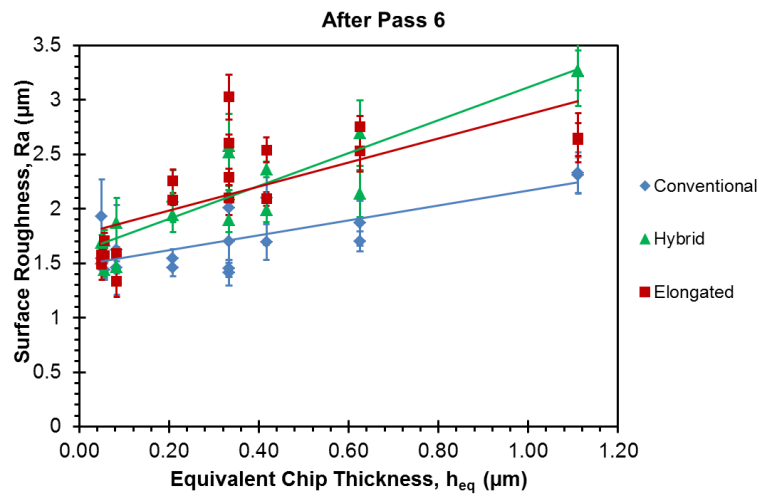
FIGURE 4.45 – SURFACE ROUGHNESS AGAINST THEORETICAL CHIP THICKNESS FOR THE THREE DIFFERENT WHEEL TYPES.

S/N ratios were calculated for the surface roughness data (Figure 4.46) using 'smaller is better' method as a rough surface can degrade the mechanical performance of the component [26] so a low roughness is preferable. As in Section 4.4.4 for wheel wear, the data points for passes 2- 6 were removed at Q' 33.3 mm^3 / mm s for the conventional and hybrid wheels.
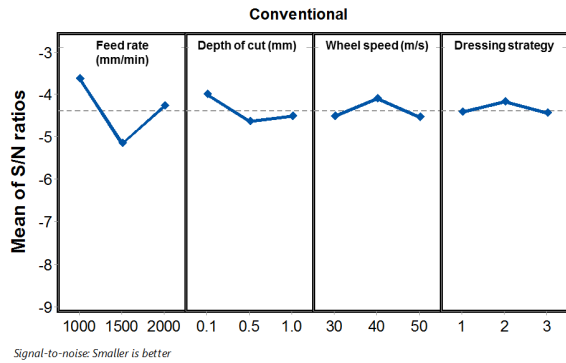
A.

B.

Response Table for S/N Ratios - Conventional

Level	Feed rate	Depth of Cut	Vc	Dressing Strategy
1	-3.65	-4.02	-4.53	-4.43
2	-5.17	-4.65	-4.11	-4.19
3	-4.28	-4.51	-4.54	-4.46
Delta	1.52	0.63	0.43	0.27
Rank	1	2	3	4

C.

D.
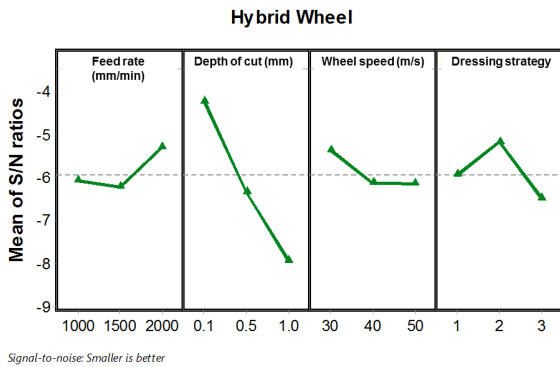
Response Table for S/N Ratios - Hybrid

Level	Feed rate	Depth of Cut	Vc	Dressing Strategy
1	-6.08	-4.22	-5.37	-5.93
2	-6.23	-6.34	-6.13	-5.17
3	-5.30	-7.92	-6.14	-6.48
Delta	0.93	3.70	0.76	1.31
Rank	3	1	4	2

E.

F.
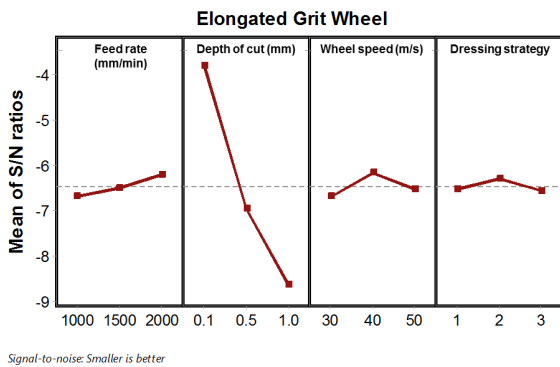
Response Table for S/N Ratio - Elongated

Level	Feed rate	Depth of Cut	Vc	Dressing Strategy
1	-6.674	-3.779	-6.691	-6.525
2	-6.498	-6.963	-6.165	-6.292
3	-6.202	-8.632	-6.519	-6.557
Delta	0.472	4.853	0.526	0.265
Rank	3	1	2	4

FIGURE 4.46 – S/N RATIO ANALYSES OF SURFACE ROUGHNESS FOR (A) CONVENTIONAL, (B) HYBRID AND (C) ELONGATED GRIT WHEEL TYPES SHOWING THE SIGNIFICANCE OF GRINDING PARAMETERS, PARTICULARLY DEPTH OF CUT.

Figure 4.46 indicates that for the hybrid and elongated grit wheels, the depth of cut was the most influential parameter on reducing surface roughness. The S/N ratio tables (Figure 4.46B, D and F) also suggest that the low dressing interference angle (0.002 mm/rev and q_d -0.8) generates the lowest roughness workpiece surface. The main effects plot for the surface roughness by abrasive wheel type is shown in Figure 4.47 wherein the entire dataset was included and clearly demonstrates that the lowest surface roughness was achieved with conventional wheels, overall.
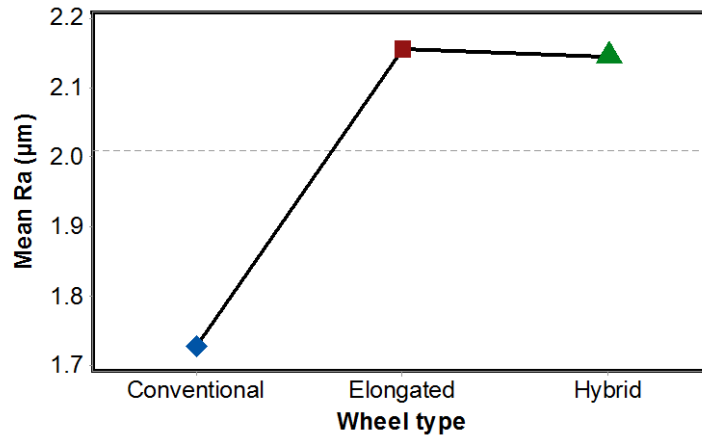
FIGURE 4.47 – MEAN EFFECTS PLOT OF SURFACE ROUGHNESS FOR THE THREE DIFFERENT ABRASIVE WHEEL TYPES WHICH WAS BEST IN THE CONVENTIONAL WHEEL.

4.4.6 METALLURGICAL ANALYSIS

To assess the surface integrity impact of the different wheel types under different grinding conditions, the validation cuts (Table 3.12) were sectioned and analysed as discussed in Section 3.5. The dressing conditions were kept constant (0.002 mm/rev and q_d 0.8) due to material limitations and to allow direct comparison between wheels. Two samples at Q' 0.7 and 52.5 mm^3 / mm s were analysed for each wheel along with a single sample at Q' 20 mm^3 / mm s.

Figure 4.48 displays optical images of white layer present on the samples. The label indicates the average thickness of the layer for that particular sample. As highlighted above, the increasing white layer thickness from Q' 0.7 mm^3 / mm s (Figure 4.49A – C) to Q' 52.5 mm^3 / mm s (Figure 4.49G – I) is clear with a large, fine crystal layer visible in G – H.
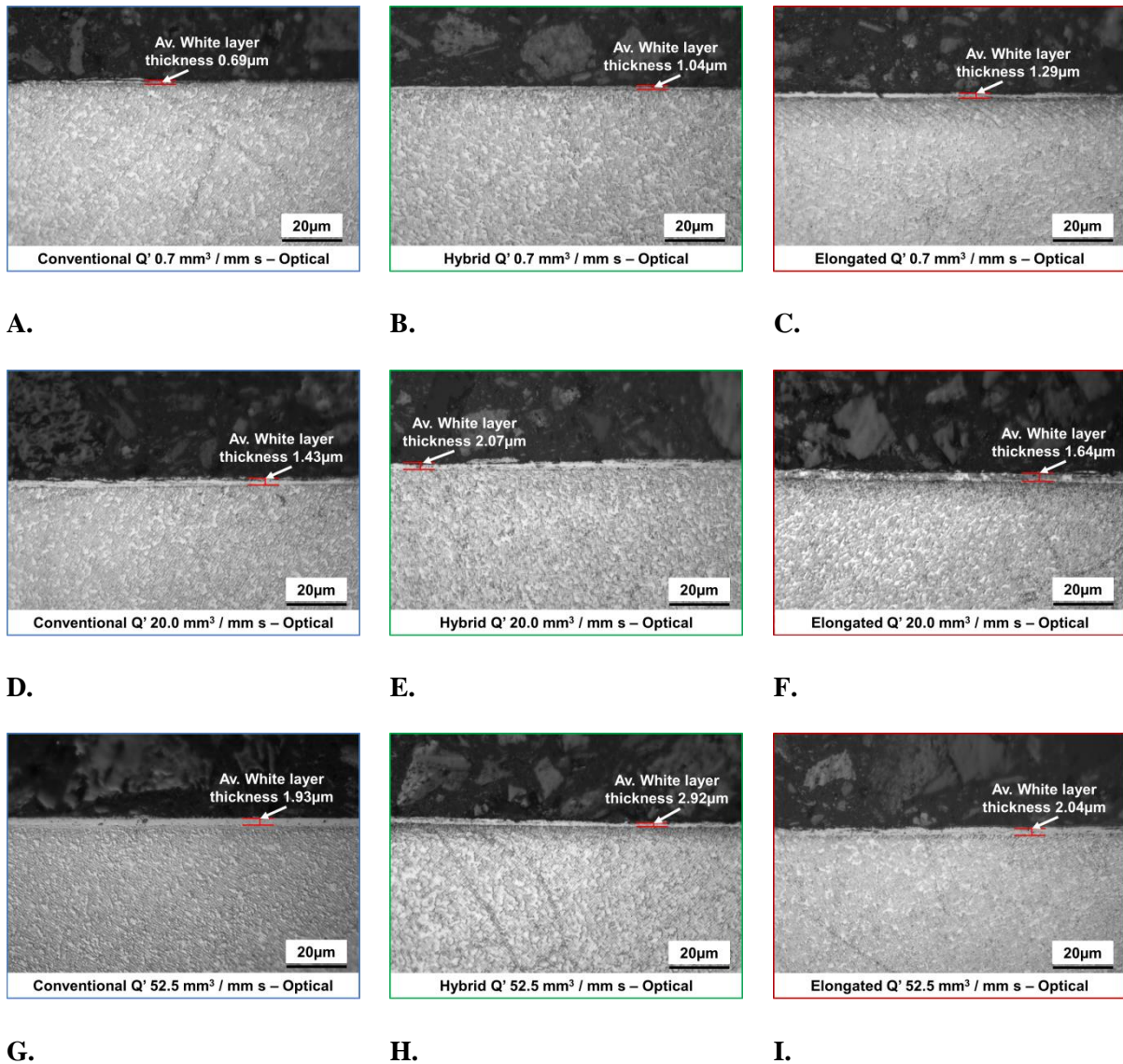
FIGURE 4.48 – COMPARISON OF WHITE LAYER FORMATION BETWEEN CONVENTIONAL (A, D, G), HYBRID (B, E, H) AND ELONGATED (C, F, I) WHEELS AT Q' 0.7 (A) – (C), 20.0 (D) – (F) AND 52.5 MM³ / MM S (G) – (I) WHICH SHOWED AN INCREASING THICKNESS TREND FOR ALL WHEEL TYPES.

As in Section 4.2, examples of white layer and redeposited material were seen on all of the samples. The average thicknesses of these features are shown in Figure 4.49. The white layer (Figure 4.48A) was shown to have the lowest average thickness in the conventional wheel ground samples whilst the elongated grits generated the thickest white layer in the finish grinding condition (Q' 0.7 mm³ / mm s). For all wheel types the average thickness of white layer increased as the material removal rate increased. A similar trend is seen in the redeposited material (Figure 4.48B) however, it is less apparent whether there is a difference in layer thickness between the wheel types.
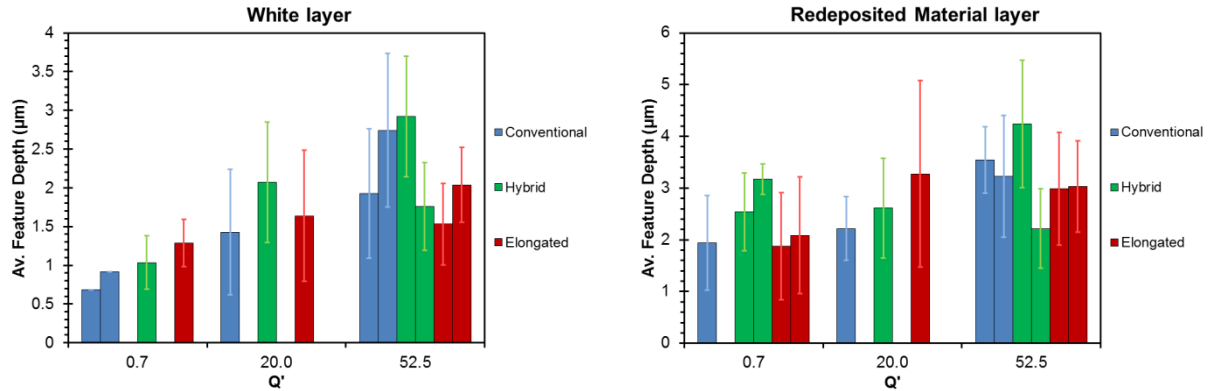
A.   **B.**

FIGURE 4.49 – AVERAGE DEPTH OF (A) WHITE LAYER AND (B) REDEPOSITED MATERIAL ON THE VALIDATION SAMPLES FOR EACH WHEEL TYPE.

4.5 RESULTS SUMMARY

The previous Sections displayed the experimental results of the thesis. From the data presented in Section 4.1, the following observations can be made of the wheel topography under different dressing conditions:

1. At high infeed rates and synchronous speed ratios the power consumption during dressing is highest leading to high dressing forces and the roughest wheel topography.
2. The infeed rate is the most influential dressing parameter with the most topography variation seen at high infeed rates.
3. For conventional wheels, grits consisting of few crystals and a relatively uniform grit shape encourages bond fracture (whole grain pull out) and macrofracture during aggressive dressing. This generates a coarse wheel topography with sharp and well-spaced cutting points.
4. For hybrid wheels, the triangular engineered grits dominate the dressing process due to their small crystal structure of the grits causes microfracturing, reducing the power during dressing. SEM imaging indicates an increase in both macro and microfracturing of the abrasive grits as the dressing process increases in aggression.
5. The dressing behaviour of elongated grits is highly dependent on the orientation of the grits. Outward facing grits are more favourable for cutting and will fracture sharper at higher interference angles. At low angles the grits cleave into much duller cutting points. The high grit volume of the elongated grits increases the dressing energy for the wheels.

CD grinding cuts in Section 4.2 assessed the impact of generated topographies from dressing on the grinding behaviour and the following observations can be made:

1. For all wheels, a higher dressing infeed rate and speed ratio creates a sharp wheel topography which cuts deeper tracks into the workpiece, reducing the grinding power (less rubbing and ploughing) and increasing the volume of material sideflow around the grits.

2. At low dressing infeed rates, small changes in topography (due to speed ratio) become more significant and the grinding specific energy is higher.

3. Elongated grit wheels contain the largest aspect ratio grits so sharp cutting points penetrate deeper into the workpiece so cutting is increased and surface roughness is high. This results in the thinnest average thickness of white layer (metallurgical damage).

4. A conventional grit wheel surface is more uniform and grit penetration is reduced so a less rough workpiece surface is formed. Lots of embedded grits in ground surface suggest difference in fracture behaviour compared to the engineered grits, such as the hybrid wheel which saw less embedded grits related to a reduced conventional grit content in the wheel.

Following Section 4.2, non-CD grinding cuts were conducted to analyse how the different abrasive topographies breakdown after multiple grinding passes (Section 4.3):

1. For all abrasive wheel types, rapid dulling of the cutting grits occurs initially as both grinding power and normal force increase from passes 1 to 5. This is due to attritious wear of the abrasive grits, revealed through SEM images of the wheel topography.

2. Dressing wheels with conventional grits under steep interference angles (0.002 mm/rev and q_d 0.8) causes structural damage to the abrasive grits in the grinding layer of the wheel. This is sufficient for macrofracture of the grits around pass 6/7 generating new, sharp cutting points which reduce the grinding power. This also leads to increased wheel wear and a rougher surface after 9 passes (as well as increased smearing).

3. Hybrid wheels demonstrate a steady microfracturing behaviour in the triangular, engineered grits which dominates the grinding mechanism leading to reduced grinding power and forces as well as the lowest level of wear of all wheel types. Sharp cutting points generated from the microfracture leads to a higher surface roughness however.

4. Elongated grit wheels show the lowest forces of all the wheels for the first pass but display very rapid dulling after the initial cut. Eventually forces build sufficiently for macrofracture of the grits after pass 7. Deep surface penetration of favourably orientated grits creates a high surface roughness.

Finally, the grinding parameters were varied to analyse the response of the different topographies and the following summary of the data can be made (Section 4.4):

1. Catastrophic breakdown of the conventional and hybrid grinding wheels was seen at Q' 33.3 mm^3 / mm s with extensive bond fracture causing a rapid decline in the grinding force after the first pass. The elongated grit wheel demonstrated the best wear response at high material removal rates (Q' >25.0 mm^3 / mm s).

2. Depth of cut is by far the most influential parameter on grinding forces (>84% contribution), wheel wear (>88%) and surface roughness (>75%) for all wheels as it directly influences the chip thickness.

3. Dressing strategy is the third most influential parameter (behind depth of cut and feed rate) on grinding normal force for the conventional and hybrid wheels. It is least impactful for the elongated grit wheels due to the random orientation of the engineered grits controlling the dressing effect.

4. Dressing parameters are most influential at low material removal rates as most specific energy variation was seen in this condition. Wear effects are minimised in this condition so the dressed topography is not lost through macrofracture / whole grain pullout.

5. Wheel wear lowest in hybrid wheel at Q' <15 mm^3 / mm s. Beyond this and elongated grit wheel most dimensionally accurate. Best wear behaviour achieved at low interference angle dressing (0.002 mm/rev and q_d -0.8) for all wheels as least damage in the grinding layer.

6. Best surface roughness (Ra) achieved at low material removal rates and low interference angle dressing for all wheels.

CHAPTER 5

DISCUSSION

5.0 DISCUSSION

The following chapter discusses the results reported in Chapter 4.0 and explains the response seen in the experiment. This is supported by evidence from literature and then summarised in Chapter 6.0 Conclusion.

5.1 DETERMINATION AND CONTROL OF GRINDING WHEEL TOPOGRAPHY

5.1.1 DRESSING POWER CONSUMPTION

Figure 5.01 shows the evolution of interference angle with speed ratio wherein the interference angle increases rapidly at high infeed rate and by speed ratio q_d 0.4, leading to a greater impact speeds between the dresser diamond and the wheel generating high dressing forces (Force = mass x acceleration). This increased impact force tends to consume a higher power during the dressing process, as it is already shown by Saad et al. [137], and explains the dressing power trend in Figure 4.01A which was consistent for all wheel types. Additionally at large interference angles, the approach of the dresser diamonds is very steep so the collision forces affect a larger volume of the grinding wheel and resistance to diamond movement is high (Figure 5.01). This is shown by FEM work by Linke [152] in which the dressing forces can impact multiple grit layers on the wheel. At shallow interference angles, the dresser diamonds skim the surface so the interaction volume is reduced. Therefore at high interference angles the energy required to remove material in dressing is much greater. Interference angle is dramatically changed in the higher infeed rates and speed ratios which leads to a significant change in the dressing power (Figure 4.01B).
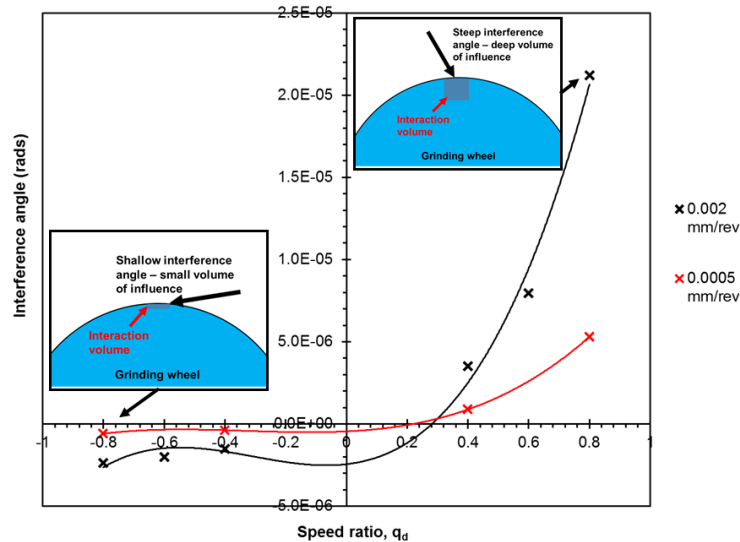
FIGURE 5.01 – CALCULATED INTERFERENCE ANGLE FOR TWO INFEED RATES USING EQUATION 2.9 WITH DIAGRAMS DEMONSTRATING THE CHANGE IN INTERACTION VOLUME.

A clear drop in dressing power was observed for all the tested wheels when the speed ratio of unity was used (Figure 4.01A). In this condition, the surface speed of the dresser and the abrasive wheel are equal so the dresser assists the turning of the grinding wheel reducing the measured power at the grinding spindle.

For Figure 4.2 the difference in dressing power consumption of 30% and 100% triangular engineered grit wheels can be linked to the difference in dressing response between the triangular and conventional grits showing that the sintered grits tend to fracture more easily during the dressing process (as a result of the small crystal structure). SEM micrographs of the wheel (Figures 4.11 - 4.13) show microfracturing occurring on the corners of the triangular grits, so less energy is required to fracture the grits and the dressing power is reduced. With higher proportions of conventional grits less low energy microfracturing can occur and so the dressing power increases. Sintered Cubitron grits (Section 2.3.2) are known to microfracture during grinding, as shown by Badger [102], which produces a lower grinding power. It is a reasonable assumption therefore that dressing power would be reduced also and the fracturing is concentrated on the triangle corners where the grit is most vunerable.

The wheel consisting of elongated abrasive grits showed the highest power consumption during dressing (Figure 4.01). The elongated grits had an aspect ratio of approximately 5 times larger than the other abrasive grit types, therefore there is a much larger volume of material to fracture (longer, larger grits). There is also significant variation in the orientation of the grits (Figure 4.08) with a high likelihood of them either lying tangential to the wheel (flat) or perpendicular (facing outwards). These different orientations will cause the grits to fracture at very different forces. Those lying tangential to

the wheel will have much more material support from the rest of the wheel than those facing outwards, so will fracture at a higher force. This is demonstrated in Figure 4.14 as at high dressing forces (steep inference angle) sharp points and cracks are seen on grits at very different angles (highlighted). In Figure 4.15 however, dressing forces are low and no cracks were observed and only outward facing grits had been cleaved into flat regions.

5.1.2 AVERAGE WHEEL ROUGHNESS

For all the wheel types tested, the highest average wheel roughness (measured roughness of the graphite coupon) was under the high infeed rate conditions (Figure 4.03). In this condition the dresser feeds faster into the wheel resulting in increased crushing of the abrasive grits and steeper interference angles so the dressing normal forces increase [6]. As a result, the level of fracturing of the grits and bond is higher which increases the likelihood of generating sharp cutting points on the topography. Sharp cutting points have a less negative rake angle [181] so grits penetrate more easily and deeper in the workpiece material increasing the volume of the material being cut and generating a rougher surface [6]. The trend of increased workpiece roughness at higher dressing interference angles (Figure 4.03B) is also seen in literature [137], [148].

For the conventional wheel, Figure 4.09 captured clear cracks in the grits after dressing at high infeed rate (0.002 mm/rev) and speed ratio (0.8) demonstrating macrofracturing behaviour which produces cutting points with small negative rake angles. At low interference angles (infeed rate 0.0005 mm/rev and q_d -0.8), dressing forces and therefore fracture is reduced thus a wheel topography with duller cutting points is formed, as highlighted in Figure 4.10. Hence the average roughness of the wheel is less (Figure 4.03) as the grits do not penetrate as deep into the graphite coupon.

The observed roughness range of the hybrid wheel compared to the 100% triangular grit wheel in Figure 4.04 was very similar, suggesting that the sintered grits dominate the cutting process as the same topography roughness can be achieved at a lower dressing power. Figure 4.06A shows that these grits generate sharp cutting points, likely a result of their shape and microfracturing behaviour. However, it is known that certain cutting point geometries are preferable for chip formation [44], [181] and there is an orientation variation (Figure 4.08) of the triangular grits. Hence these engineered grits do not always lie on their edge in a favourable orientation for cutting, which impacts the average roughness of the wheel topography. Work by Badger [250] on grinding discs demonstrates this response as the same triangular grits showed a higher surface roughness compared to conventional when all the grits were favourably aligned.

For the elongated grit wheels, grit orientation can also explain the roughness variation seen in Figure 4.03 on the graphite coupon as this wheel had the lowest average roughness variation of all the wheels. If sharp cutting points are formed only on the favourably orientated, outward facing grits then the dressing will be less influential on the sharpness of the wheel topography. Due to the high aspect ratio of the elongated grits, orientation will have a larger impact than that seen in the hybrid wheel. The variation that is seen is due to the high dressing power in steep interference angle conditions being sufficient to cause fracturing on some tangential lying grits (Figure 4.14).

5.1.3 PEAK DENSITY AND FLAT REGIONS

Higher energy collisions at a steeper angle increases the dressing force therefore a greater degree of bond fracture and loss of cutting points occurs in the conventional wheels, as shown in Figure 4.05 with a clear reduction in whole grain peak density as the interference angle increased. This response has also been reported by Malkin and Guo [1] and Linke [152] in aggressive dressing (steep interference angle) conditions. It also leads to macro fracturing of the grits generating wheel topography with sharp cutting points with large spacing between them (Figure 4.06B showing sharp points). Interestingly, the peak density for the low infeed condition is not greater than for the high infeed (Figure 4.05), although the density range is smaller. This indicates that bond fracturing, leading to whole grain pull out, is more dependent on the speed ratio wherein at higher speed ratios, the impact velocities between the dresser diamond and the abrasive wheel are higher leading to an increased dressing force and subsequent bond fracture. Grit fracture however is more dependent on dressing infeed rate as Figure 4.07 saw a 0.2 % greater surface area of flat regions (fracture flats indicating micro and macro fracture [122], [123]) on the conventional abrasive grits dressed at 0.002 mm/min compared to the low infeed rate. At higher infeed rates, the dressing forces are higher so more fracturing occurs which inevitably creates lots of both sharp cutting points and flat regions. No change was seen across the speed ratio range however the average error for the fracture flats in this investigation was ±0.13 % which is close to the 0.2 % difference seen between the dressing infeed rates. Therefore more future tests would be required to improve the reliability of the data.

The behaviour is different for the engineered grit wheels as Figure 4.05 shows very little change in the whole-grain peak density when the dressing interference angle is altered, for both the hybrid and elongated grit wheels at high infeed rate, implying that bond fracture is low and consistent. The microfracture of the triangular grits during dressing reduces the dressing power (Figure 4.01B) so the forces are not sufficient for extensive bond fracture. For the elongated grits, the large aspect ratio and orientation variation means achieving sufficient forces to remove a whole grit at once would be extremely difficult and the number of active grits on the topography can vary significantly. This is

further demonstrated in Figure 4.07 as the elongated grit wheels had 4% more flat regions than the other wheel types, caused by the high number of tangentially lying grits (Figure 4.08). These are difficult to fracture as they are well supported and reduce the roughness of the wheel (Figure 4.03). Figure 5.02 demonstrates the high level of grits lying flat on the surface.

A.   **B.**   **C.**
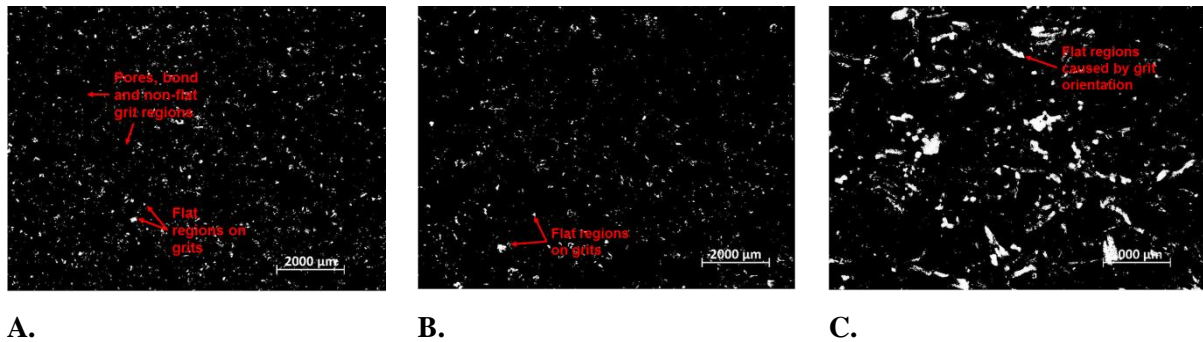
FIGURE 5.02 – FLAT REGIONS ON THE 3 ABRASIVE WHEEL TYPES (A) CONVENTIONAL (B) HYBRID (C) ELONGATED WITH THE LATTER SHOWING THE HIGHEST LEVEL DUE TO GRIT ORIENTATION FROM HIGH ASPECT RATIO.

5.2 INFLUENCE OF GENERATED TOPOGRAPHY ON GRINDING PERFORMANCE

5.2.1 POWER CONSUMPTION

Figure 4.16A clearly indicated that, for all wheels, a high infeed rate generates a coarser wheel topography (as seen in Sections 4.1 and 5.1) wherein the cutting points on the grits are sharper, therefore the level of cutting is increased and there is less rubbing and ploughing of the workpiece material. Hence less power is consumed (for all speed ratios) as the grinding energy is transferred to the chips [41], [59]. High infeed rate (0.002 mm/rev) and synchronous speed ratio (q_d 0.8) produced the lowest power grinding conditions.

The data in Figure 4.16B implies that the speed ratio becomes more significant at lower infeed rates, for all wheel types, as the gradient of the dotted curves are much steeper than the high infeed rate (solid lines). The level of bond and macro fracture is reduced at low infeed rate (as discussed in Section 5.1), therefore the abrasive grits on the wheel are not as sharp resulting in a reduced chip size [32] as it is shown in Figure 4.18 where reduced tracks depth are visible (lower Rv value). At small chip sizes, and therefore material removal rates, the specific energy of grinding is high and any change in chip size will cause a significant change in specific energy, as shown in literature, such as Figure 5.03 for material removal rate of less than 2 mm^2/s (units according to the graph). Hence variation in the speed ratio at low infeed rate causes a small change in grit sharpness and therefore chip size provoking a significant difference in the grinding energy (or power).
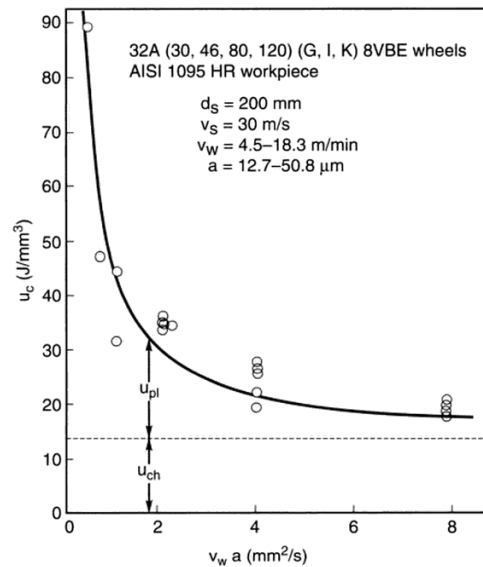
FIGURE 5.03 – SPECIFIC ENERGY (U_C) AS A FUNCTION OF MATERIAL REMOVAL RATE WITH CHIP FORMATION ENERGY (U_{CH}) AND PLOUGHING ENERGY (U_{PL}) INDICATED [1].

Interestingly, the hybrid wheels showed the least variation in power over the speed ratio for both dressing infeed rate conditions. As discussed in Section 5.1, the engineered, triangular grits dominate the dressing process and little change is seen in the number of cutting points as the interference angle in dressing changes. Hence any power difference seen is likely a result of increased microfracturing of the engineered grits forming sharper cutting points.

As all wheels were continuously dressed during cutting they can be considered sharp and chip formation to be dominant in the grinding energy partition [62]. The elongated grit wheel achieved the lowest power consumption in grinding of all the wheels of 0.68 kW net power (Figure 4.16A) due to the large aspect ratio of the elongated grits (5 times) and the sharp fracturing of favourably orientated grits. The chip size per active grit is large compared to the other wheels therefore the grinding power (and thus energy) is reduced so the chip formation energy (u_{ch}) is reduced (Equations 2.2 and 2.3). Maximum valley depths were greatest for the elongated grit wheel in Figure 4.18 and deep grinding tracks are visible on the ground surface micrographs of Figure 4.19A compared to the grinding tracks in Figure 4.20B cut by the conventional wheel, demonstrating the chip size difference.

5.2.2 SURFACE ROUGHNESS

As with grinding power, surface roughness is highest at high dressing infeed rate (0.002 mm/rev) and synchronous speed ratio (q_d 0.8) (Figure 4.17A). This was consistent across all wheels and aligns with data gathered by Baseri [144] and Malkin and Murray [148] who saw an increase in workpiece roughness as the speed ratio increased in the synchronous region (Figure 2.28B). At high

infeed rates and speed ratios, the interference angle in dressing is steeper creating sharper wheel topography cutting points which penetrate further into the workpiece, causing greater deviation of the surface from the 'average' line. Also, the surface roughness variation was less at the low infeed rate condition as a result of duller cutting edges and less transformation of the wheel topography over a range of speed ratios, as shown in Section 4.1.

According to Figure 4.17A-B, the elongated grit wheel generated the roughest workpiece surface (average Ra 2.18 µm vs. hybrid average Ra 1.87 µm, conventional average Ra 1.53 µm at dressing 0.002 mm/rev and q_d 0.8). The elongated grit wheel contains large abrasive grits (due to high aspect ratio) which penetrate deeper into the workpiece surface forming larger chips for each cutting point, reducing the grinding power and increasing the surface roughness [1]. Figure 4.18 furthers this understanding showing deeper maximum valleys (average Rv 9.58 µm) for the elongated grit wheel.

The trend demonstrated in Figure 4.17B matched well with literature [67] that as the power consumed in grinding increases, the roughness (Ra) of the workpiece declines as the level of rubbing and ploughing of the surface increases [1]. For the conventional wheels, at low infeed rate microfracture is the dominant dressing mechanism and the chip size is small due to lots of dull cutting points on the wheel surface (Section 4.1). Hence the gradient of the response in Figure 4.17B was low at the 0.0005 mm/min infeed rate. At the higher infeed rate, there is a transformation in the dressing mechanism as bond and macrofracture dominate creating well-spaced, sharp cutting points. This is implied by the steep gradient for the 0.002 mm/min infeed rate compared to the low infeed rate in Figure 4.17B. Figure 5.04 demonstrates this dressing mechanism change further by plotting the measured peak density for the corresponding dressing parameters against the workpiece surface roughness in Section 4.2 for the conventional wheel. At high infeed rate, peak density is reduced and the workpiece roughness increases. At low infeed rate, there are more cutting points (less bond fracture in dressing) the roughness does not vary greatly over the peak density range.
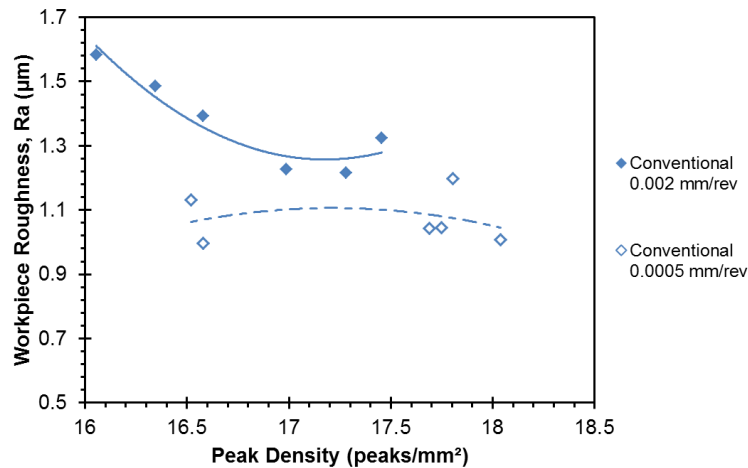
FIGURE 5.04 – PEAK DENSITY MEASURED IN SECTION 4.1 AGAINST WORKPIECE SURFACE ROUGHNESS FROM SECTION 4.2 FOR CONVENTIONAL ABRASIVE WHEELS WITH MORE VARIATION SEEN IN THE HIGH INFEED RATE.

The hybrid wheel showed the greatest change in surface roughness over a small power range compared to the other abrasive grit types in Figure 4.17B. The hybrid wheel contains engineered, triangular grits which have been shown to dominate the dressing response through microfracturing as the dressing parameters become more aggressive (higher infeed rate, greater speed ratio, Figure 4.11 - 12). Therefore, the number of cutting points does not vary as significantly as the conventional grit wheel due to the fact that whole grain pull out is reduced (Figure 4.05). As the grinding energy is dependent on the number of active cutting points in the process [1], [43] (Equation 2.1), the power will not change dramatically for the hybrid wheel. The substantial microfracturing on the triangular grits at steep interference angles though creates very sharp grits, which cut deep tracks on the workpiece and generate a rough surface. This is shown in Figure 4.18 as the measured Rv values for the hybrid wheel were almost as large as those for the elongated grit wheel.

5.2.3 SURFACE QUALITY

The level of smearing and plastic flow of the material is visibly greater at the 0.002 mm/rev infeed rate using all the tested wheels (Figure 4.19A, B, D, F and Figure 4.20A, B, D). This could be caused by sharper grits from the high infeed rate pushing deeper into the material inducing excessive side flow (Figure 5.05) of workpiece material around the abrasive grit which is smeared over the surface. Similar behaviour is discussed by Zeng et al. [228] with increases in depth of cut of a few microns. At high infeed rates, there is increased fracturing of the abrasive grits so the likelihood of generating flat regions on the grits is increased also (Section 5.1). Flats on the abrasive are known to promote plastic deformation [32] contributing to the visual response. Also, speed ratio is more significant at high infeed rate as the dressing force variation over the speed ratio range is greater (Figure 4.01), causing a larger change in the topography fracturing behaviour and thus a greater

difference was seen between the surface images at different speed ratios at the high infeed rate (Figure 4.19 - 4.20). At low infeed rate, microfracturing is the dominant dressing mechanism (Section 5.2.2) so topography changes are very subtle causing a small chip size change. This has little influence on the surface visually but is significant for grinding power and roughness.
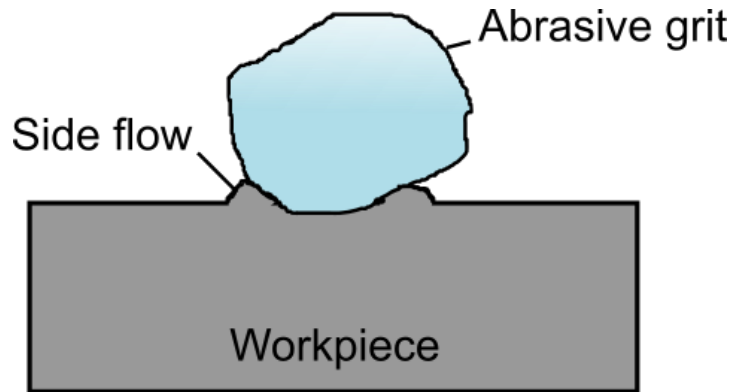
FIGURE 5.05 – DIAGRAM DEMONSTRATING SIDE FLOW AROUND AN ABRASIVE GRIT.

All the grits in the conventional wheel are approximately spherical meaning that the penetration and cutting depth is very consistent. This prevents single, deep tracks forming (e.g. arrowed on Figure 4.19A) which are a more common feature in the wheels with grits of large aspect ratio. Therefore the surfaces generated by the conventional wheels was found to have the lowest measured roughness as demonstrated in Figures 4.17 – 18 in the ground surface images with far less smearing and deep cut tracks. Figure 5.06 shows further ground surface images with deep grinding tracks highlighted in Figure 5.06B – C with arrows cut by engineered grit wheels.
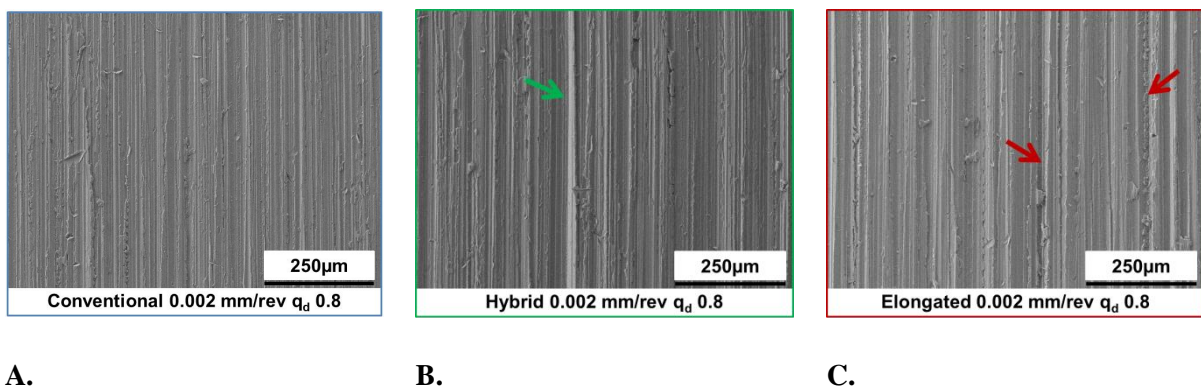
A.   B.   C.

FIGURE 5.06 – NI-BASE SUPERALLOY WORKPIECE GROUND SURFACE AT X200 MAGNIFICATION FOR (A) CONVENTIONAL, (B) HYBRID AND (C) ELONGATED GRIT WHEELS SHOWING THE DEEPER GRIT TRACKS CUT BY THE ENGINEERED GRIT WHEELS.

EDX spectroscopy (Figure 4.21) identified several embedded grits in the ground surface. The conventional wheel had almost four times higher embedded grit density compared to the hybrid wheel and over ten times against the elongated (Table 4.1). As the abrasive grits penetrate into the workpiece material, the forces on each grit build, as does the plastic flow of material around them

[26]. As the grit embeds in the workpiece surface during the ploughing stage of cutting (Figure 1.6), the plastic deformation of the workpiece increases until either the material is sheared or the grit fractures. If penetration is sufficient grits can be held in the surface by the plastically deformed material. Evidence of this deformed material around the grits is visible in Figures 4.22 – 23. For the sintered grits (triangular and elongated) however, their small crystal structure means as the forces increase, when they exceed the fracture toughness of the grit, microfracturing occurs. Hence inefficient contact points on the wheel are lost and not embedded in the surface.

The hybrid wheel contained a combination of electrofused and sintered grits, suggesting that the reduction in embedded grits from this wheel is a result of there being less (about 30%) conventional grits in the wheel. The sintered grits are known to have a sub-micron crystal size [6] yet all the embedded grits seen were of the order of 20 μm in size. The elongated grit wheel only contained sintered grits and therefore had very few embedded grits in the surface except for the very gentle dressing conditions (0.0005 mm/rev and q_d -0.8) in which the cutting points are dull and specific grinding energy is high which could cause extensive plastic deformation of the workpiece (Figure 4.19E). These were all also only found on one elongated sample so repeat experiments could be performed to confirm whether these were an anomaly.

5.2.4 METALLURGICAL ANALYSIS

White layer was a major surface feature observed in all of the analysed ground surfaces. It is reported that amorphous white layer formation is closely related to grinding temperature and local melting when the abrasive grits contact the workpiece [224], [236]. This is especially common in superalloy materials which is very sensitive to thermal damage [43].

The wheels with elongated grits generated on average a thinner white layer compared with the other wheels types in almost all dressing conditions except 0.0005 mm/rev and q_d -0.8 (Figure 4.25). The large aspect ratio of the grits means the favourably orientated grits (perpendicular to the central axis) form very sharp cutting points which can penetrated deep into the workpiece surface (as discussed in Section 5.2.3) and create a larger chip size from the less negative rake angles of the cutting points. Hence less grinding power is used in rubbing and ploughing thus reducing the friction and thermal input to the surface and therefore the grinding energy (and power) and thus temperature. Section 5.1 suggested that the orientation variation of the elongated grit limits the influence of dressing and interestingly, no clear trend was seen in white layer thickness for the different dressing conditions for the elongated grit wheel. This could show the orientation variation behaviour and that the alignment of the grits is the controlling factor for grinding temperature with these grits.

For the conventional and hybrid wheel types, the high infeed rate had a consistently higher level of white layer in Figure 4.25 compared to the low infeed rate. In conventional wheels, high infeed rate has a greater level of flat regions (Figure 4.07) due to increased fracture. Godino et al. [98] has shown that flat regions can lead to a temperature rise as a result of high forces and plastic deformation. The same work also suggested that sintered grits have a chemical reaction with the workpiece which cause higher temperatures and possibly explain the hybrid wheel behaviour. This reaction was countered in the elongated grit wheel due to the high sharpness. Guo et al. [62] saw white layer formation at high levels of flat regions on the wheel

Redeposited material was detected on all of the observed samples for each wheel type and dressing condition (Section 4.2.4). In Figure 4.26 consistently across all wheels the level of redeposited material is higher in the high infeed rate condition compared to the low. At high infeed, a sharper wheel topography is generated causing increased levels of chip formation in grinding. More chips, then more swarf is trapped in the wheel pores and the likelihood of it being released and redeposited on the wheel surface is large.

It must be noted that the spread of the measured white layer (± 0.4 µm average spread about the mean) and redeposited material was wide for all wheel types and the observed workpiece cross sections are only a snapshot of the entire ground sample. Therefore more workpiece sections should be imaged to make well supported conclusions.

5.3 THE BREAKDOWN OF GRINDING WHEEL TOPOGRAPHY

5.3.1 GENERAL OBSERVATIONS

The first continuous dressing pass generated a sharp wheel topography which dominates the grinding process but become blunt over time reducing the chip thickness. As stated by Chen et al. [124], sharp edges can break down very quickly after initial grinding as a result of microcracks formed on the grits giving the sharp cutting points a very low mechanical strength. Hence the energy partition in rubbing and ploughing increases, leading to an increase in force and power. This can be observed in the force and power evolution curves (Figures 4.28 – 30) as the measured values increase by time and from pass to pass and matches a similar force increase behaviour observed by Ghosh et al. [44]. A similar response was seen for all the wheels, but the elongated grit wheels proved to have the lowest normal force of all the grits in every dressing condition in the first grinding pass. This matches the behaviour in Section 4.2, as the elongated grits are larger so the chip size per grit is increased (as suggested by the higher Rv values in Figure 4.18) so the specific energy during grinding is reduced and so power consumption is less (Section 5.2.1).

5.3.2 GRINDING BEHAVIOUR OF CONVENTIONAL GRITS

In the conventional wheels for high interference angle conditions (0.002 mm/rev and q_d 0.8, and 0.0005 mm/rev and q_d 0.8 dressing conditions) there is deeper damage into the grinding wheel (Figure 5.01) as the dressing process shatters the grinding layer and weakens the abrasive grits [32], [152]. Therefore as grinding forces build from pass to pass, the weakened grits from the dressing conditions eventually lead to macro fracture. This is evidenced in Figure 4.28 and 4.30 in which there is a sudden drop in grinding power and force after pass 5. This response is not due to wheel diameter loss (from bond fracture) causing a reduction in grinding depth of cut as it was only measured to be 7 µm more in the 0.002 mm/rev and q_d 0.8 dressing condition compared to the 0.002 mm/rev and q_d -0.8 (Figure 4.34). This is only 4.4% of the total wheel wear and would not cause such a substantial drop in total grinding power. This behaviour is further demonstrated in Figure 4.36 with cracks visible in the grits at pass 9 for the corresponding dressing parameters.

For the low interference angle, the sub-surface damage in the grits is reduced and so the threshold fracture force of the grits is higher meaning that microfracturing and dulling of the grits continues. The standard deviation of normal force (calculated as shown in Figure 5.07) of the measured force for each pass (Figure 4.30B, D & F) is low after pass 6 (Figure 4.30D), demonstrating a continuation of the dulling, microfracturing behaviour of the grits. For the high interference angle conditions it rapidly increases after pass 5 suggesting macrofracturing of the abrasive grits as it alters the number of cutting points on the wheel and results in vast fluctuation of the grinding force.
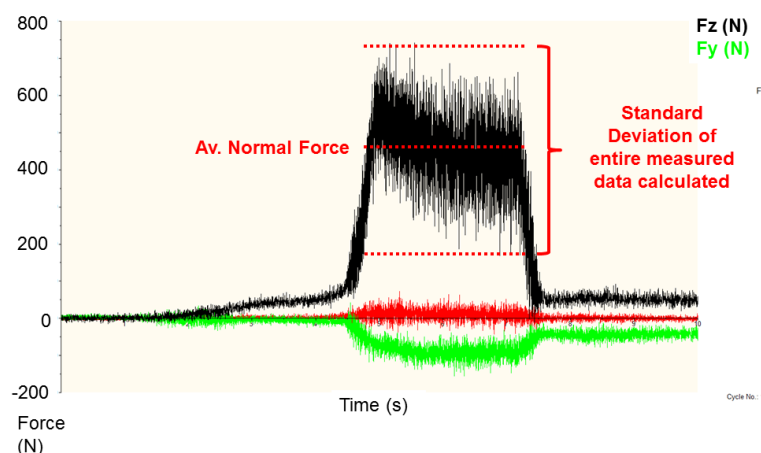
FIGURE 5.07 – EXAMPLE OF HOW THE STANDARD DEVIATION OF EACH DATA SET WAS CALCULATED WHICH INDICATES THE FORCE VARIATION WHILST THE WHEEL IS IN CONTACT WITH THE WORKPIECE.

These findings are also supported by the workpiece surface analysis as the measured surface roughness (Figures 4.31A – 4.33A) was highest at the CD grinding condition, when the wheel is sharpest for all dressing parameters. The roughness declined at pass 5 as a result of the cutting points

dulling as the forces build and shallower cut tracks are visible in Figure 4.31B – 4.33B compared to the CD ground surface. Duller cutting points leads to reduced grit penetration. At high interference angle, the threshold forces are sufficient (due to sub surface damage from dressing), to cause macrofracture by pass 9 and new sharp cutting points to be formed. Surface roughness increased in the 0.002 mm/rev and q_d 0.8, and 0.0005 mm/rev and q_d 0.8 dressing conditions and deeper grinding tracks and an indication of embedded grits (discussed Section 5.2) in the surface (Figure 4.31C - circled). In the 0.002 mm/rev and q_d -0.8 dress condition however, the grit tracks look very similar to pass 5 with extensive material overlap. The surface roughness of the material does not change much either with a decline of 0.06 µm which further shows that these grits have not been damaged deep into the grinding layer, so their threshold fracture force is higher. Hence they continue to dull.

5.3.3 GRINDING BEHAVIOUR OF HYBRID WHEELS

The hybrid wheel shows a rapid initial increase in the measured power pass-to-pass (Figure 4.28) but at approximately pass 3, the gradient of power increase declines and becomes almost linear. This suggests that the wheel enters a self-sharpening region in which the topography generates new cutting points as active points begin to dull, so keeping the power response almost constant. This response is likely a result of the microfracturing behaviour discussed in Section 5.2 on the engineered, triangular grits as increased levels of microfracturing (highlighted Figure 4.36) were seen on the engineered grits from as dressed to pass 9. Therefore new, sharp cutting points are generated, offsetting the dulling on the conventional grits of the hybrid wheel. This is further supported by the low normal force increase between passes in Figure 4.30 (gradient of force rise of 29.36 compared to 37.24 and 81.36 for the conventional and elongated grit wheels respectively in passes 1 – 5, see Figure 5.08) which shows that grits are remaining sharp and able to penetrate into the workpiece [32]. The standard deviation (Figure 4.30B, D and F) in all dressing conditions stays low for the hybrid wheels compared to conventional and elongated grit wheels indicating a steady microfracture wear mechanism which dominates the response of the conventional grits. These triangular grits remain much sharper than the conventional and thus perform the majority of the cutting action in grinding. This result also matches with the fused vs. sol-gel alumina wheel comparison study by Selvakumaran et al. [100] which saw a reduction in grinding forces over multiple grinding passes. The authors argue that the sol-gel grits, due to their sub-micron crystal size, have high fracture toughness and microfracture characteristics so they maintain their sharpness. However this work was at much smaller depths of cut (10 µm) and all the grits had a random (not engineered) shape.

Further evidence of the dominance of triangular grits in the cutting mechanism is shown in Figure 4.29 as 100% triangular grit wheel and hybrid wheel displayed a very similar trend. The 100%

triangular grit wheel showed a lower power response for all dressing conditions however due to the higher engineered grit content providing more frequent, sharp cutting points so rubbing and ploughing energy contributed by dull conventional grits is reduced.
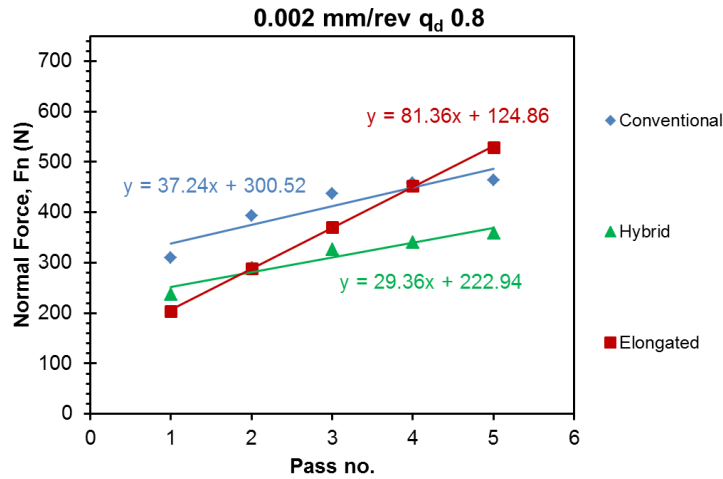
FIGURE 5.08 – GRADIENT OF THE NORMAL FORCE IN THE 0.002 MM/REV AND Q_D 0.8 DRESSING CONDITION FOR THE FIRST 5 PASSES WHICH WAS GREATEST FOR THE ELONGATED GRIT WHEEL.

Over 20% less wheel wear, across all dressing strategies (Figure 4.34), was seen for the hybrid wheel compared to the other wheel types providing further evidence for microfracture as the volume of abrasive grit lost is greatly reduced. As only small chips of abrasive material are lost to maintain cutting point sharpness, it means the hybrid wheel had a high G-ratio compared to the other wheels (2.99 G-ratio vs. 2.20 for the conventional wheel and 2.36 for the elongated grit wheel). Low interference angles reduced the wear further as, like in conventional wheels, the impact depth of the dressing is minimal so less damage is inflicted below the grinding layer and into the grits. Hence macrofracture threshold remains high and wheel material is preserved. This is shown by 0.002 mm/rev and q_d -0.8 condition causing the least amount of radial wheel loss (116.4 µm).

From visual analysis of the ground surfaces generated by the hybrid wheel it is difficult to detect a difference in the workpiece from CD to passes 5 and 9. In Figure 4.31D - F (0.002 mm/rev and q_d 0.8) there are very similar levels of smearing and redeposited material at all points suggesting that the breakdown mechanism in the wheel is consistent throughout. This pattern continues for 0.002 mm/rev and q_d -0.8 (Figure 4.31D – F) and 0.0005 mm/rev and q_d 0.8 (Figure 4.31D – F) dressing conditions however the level of smearing appears to be reduced compared to the highest interference angle condition. This is expected as the cutting points are well distributed and sharpest in this dressing condition (Section 5.1) so the grits will penetrate deeper into the workpiece causing increased amounts of material sideflow.

The surface roughness data (Figure 4.35) indicates a general increase in the surface roughness of the workpiece from the CD ground surface to pass 9. This provides further support to the self-sharpening behaviour of the engineered grits generating new sharp cutting points increasing the deviation of the surface from the 'mean line'. This matches the response discussed by Hou and Komandori [32] who reported grits breaking out of the surface during grinding, generating a rougher workpiece surface.

5.3.4 GRINDING BEHAVIOUR OF ELONGATED GRIT WHEELS

As shown in Section 4.2, for the wheels with elongated grits the aggressive 0.002 mm/rev and q_d 0.8 dressing condition had the lowest power consumption for pass 1 (0.93 kW) as the steep interference angle generates very sharp cutting points on favourably orientated grits (perpendicular to the central axis of the grinding spindle). However both the grinding power and the normal force show a very rapid increase from passes 1 to pass 7. Rapid dulling of the favourably orientated cutting points due to extensive dulling (Figure 4.36H) causes a reduced chip thickness. This coupled with the rubbing action from the unfavourably orientated grits leads to reduced chip formation during grinding and thus substantial increase in grinding power and force.

Alternatively, the rapid dulling behaviour could be related to deposition wear in which workpiece material is deposited in the pores, ahead of cutting points in the wheel as discussed by Marinescu [43]. The sharp cutting points cause lots of plastic deformation and cutting of the workpiece material which builds around the points during grinding until cutting is no longer possible at the affected grits. Figure 5.09C shows examples of deposited workpiece material around grits in the elongated grit wheel with far more chips visible than the other wheel types (Figure 5.09A – B). It is likely that the rapid force and power increase in the elongated grit wheel is a combination of both microfracture dulling the cutting points, and deposited workpiece material embedded in the wheel pores.

A.   **B.**   **C.**
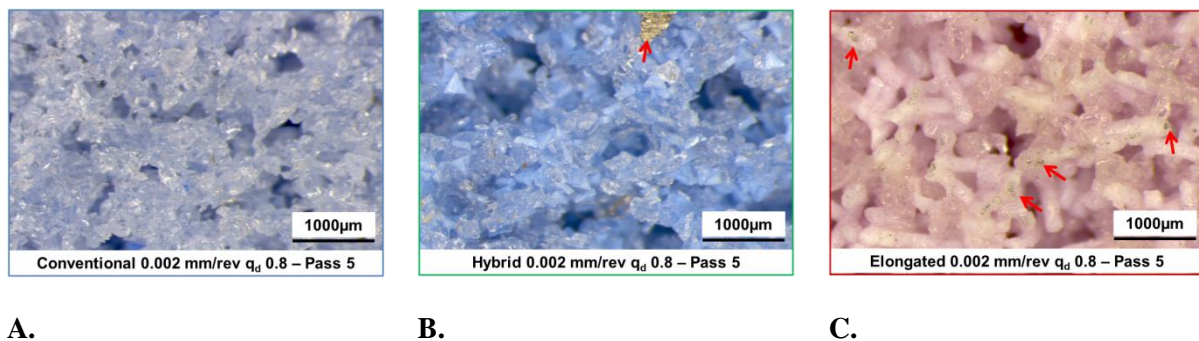
FIGURE 5.09 – OPTICAL IMAGES AT X25 MAGNIFICATION OF DEPOSITED WORKPIECE MATERIAL IN (A) CONVENTIONAL, (B) HYBRID AND (C) ELONGATED GRIT WHEELS WITH HIGHEST LEVELS SEEN AROUND THE ELONGATED GRITS.

For all dressing conditions the normal force was seen to drop by pass 9 with a peak force occurring around pass 7. This signals that as the grits continue to dull, the forces build until the stress on the grit is sufficient to cause macrofracture of the grit, revealing a new, sharp cutting point which reduces the grinding force. Evidence for this is shown in Figure 4.36C as sharp, macrofractured grits are visible on the favourably orientated grits in the SEM images.

As with the hybrid wheels, the surface roughness of the workpieces increased from CD condition to pass 9. In the 0.002 mm/rev and q_d -0.8, and 0.0005 mm/rev and q_d 0.8 dressing conditions, the surface roughness increased from the CD pass to pass 5, despite the dulling of the cutting points. This could be due to high levels of deposited material (from the wheel pores as described in Figure 5.09) on the workpiece surface (Figure 4.32H and 4.33H) generated due to the dominance of cutting at high interference angle dressing conditions.

Interestingly, the highest level of wheel wear resulted from the lowest interference angle dressing strategy (0.002 mm/rev and q_d -0.8, Figure 4.34). This is the opposite behaviour to that seen in the conventional and hybrid wheels. This dressing condition has been shown to produce blunt grinding wheel topographies (Section 5.1) and so grinding forces and power are higher. The normal forces during grinding were highest for this dressing condition compared to the others (peaking at 707.8 N at pass 7, Figure 4.30C) which could cause significant damage to the abrasive grits and bond. This leads to greater grit macrofracture and so a greater loss in the wheel diameter.

5.4 IMPACT OF GRINDING PARAMETERS ON TOPOGRAPHY PERFORMANCE

5.4.1 TOPOGRAPHY BREAKDOWN

In Figure 4.37 the normal force for each pass is shown and up to Q' 25.0 mm^3 / mm s there is increasing force between passes. For the conventional and hybrid wheels (Figure 4.37A – B), beyond Q' 25.0 mm^3 / mm s (dotted line) the force is seen to drop after the first grinding pass (at Q' 33.3 mm^3 / mm s). This is due to high grinding forces exceeding the failure strength of the bond causing catastrophic breakdown of the wheel with extensive bond fracturing and whole-grain pullout, as seen by Baul et al. [162]. Although this can have self-sharpening effects on the topography by revealing new cutting points, it also leads to extensive wheel wear and loss of dimensional accuracy (incorrect depth of cut) as stated by Jackson [125]. The elongated grit wheel however demonstrated increasing normal force between passes after Q' 25.0 mm^3 / mm s (Figure 5.10 at Q' 33.3 mm^3 / mm s),

indicating that the wheel was still performing in the attritious/ grit macrofracture wear zone and not experiencing catastrophic bond fracture.
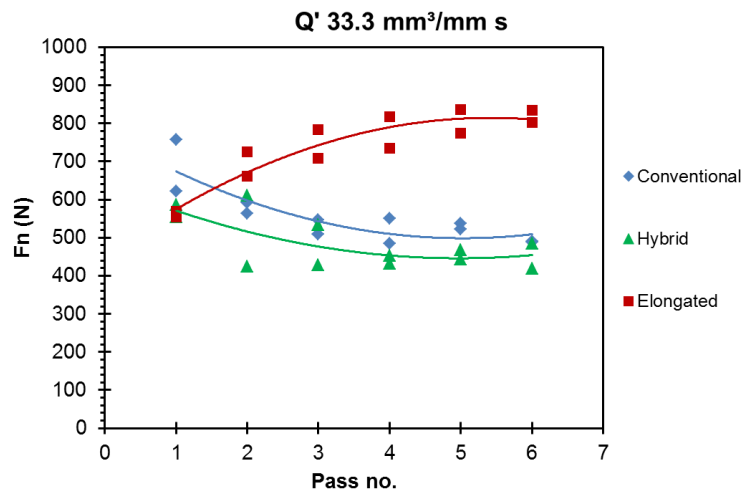
FIGURE 5.10 – CATASTROPHIC BREAKDOWN OF COVENTIONAL AND HYBRID WHEELS AT Q' 33.3 MM³ / MM S (>25.0). ELONGATED GRIT WHEEL MAINTAINS ATTRITIOUS WEAR BEHAVIOUR. CUTS E3 & E12 FROM TABLE 3.11.

The catastrophic bond breakdown of the conventional and hybrid wheels is further demonstrated by the measured wheel wear (Figure 4.38) with an average of 96% increase in wear between Q' 25.0 mm^3 / mm s and Q' 33.3 mm^3 / mm s. Rapid wear is a clear indication of whole-grain pullout, as much larger volumes of abrasive material are lost during grinding than in grit fracture. This matches work by Stetiu [121] who saw larger grinding wheel debris when the wheel wear was high, indicating fracture of the bond material. The elongated grit wheel on the other hand saw an average wear increase of 16% at the same conditions.

The difference in wear behaviour between the wheel types is due to a combination of mechanisms (Figure 5.11). Matching the response seen in Section 4.3, the hybrid wheel has the lowest wheel wear at Q' <15.0 mm^3 / mm s in Figure 4.38. At this stage, microfracture of the triangular grits dominates the process (Figure 5.11) and the volume of lost abrasive in the material is low. In the conventional wheel, the fused grits with large crystal size leads to increased macrofracture of the grits and a higher level of wheel wear. As discussed in Section 5.3, the elongated grit wheels show both dulling of the cutting points and macrofracture. As material removal rate increases beyond Q' 15.0 mm^3 / mm s, the grinding forces increase sufficiently for macrofracturing and bond fracture of the triangular, engineered grits in the hybrid wheel leading to dramatic wheel wear. In the elongated grit wheel however, the high aspect ratio leads to lots of grits overlapping and lying in different directions (Figure 4.08). This provides mechanical support for the grits on the surface as well as making whole-grain pullout difficult. Hence micro and macrofracture continues in the wheel and wear remains low at high material removal rates as the forces are not sufficient for substantial fracture.

It must also be noted that the wheels tested were from three different wheel suppliers. Therefore although the wheel code indicates they should have the same bond hardness there is likely to be some variation between the wheels.
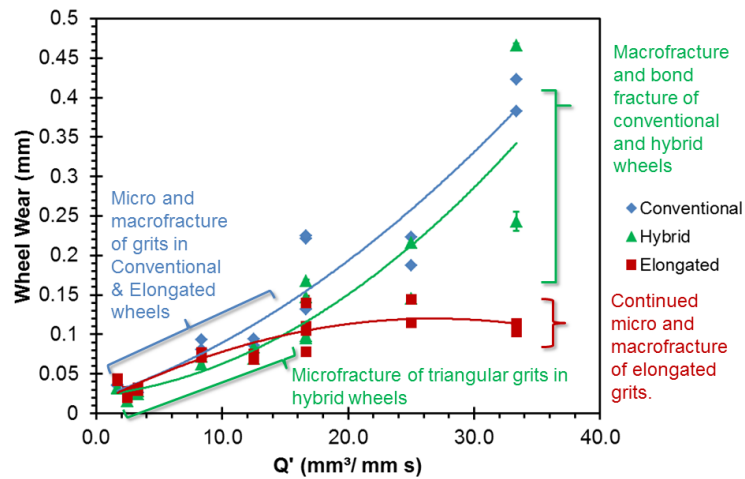
FIGURE 5.11 – RADIAL WHEEL WEAR DIAGRAM FROM FIGURE 4.38 WITH LABELLED WEAR MECHANISMS BASED ON THE RESULTS OBSERVED.

5.4.2 ANALYSIS OF VARIANCE – NORMAL FORCE

Clearly, depth of cut is the most influential parameter on the grinding normal force for all wheel types with a rank of 1 for all wheel types (Figure 4.39B, D & F) and a contribution of over 84% from this parameter in the ANOVA (Table 4.2). This is expected as chip size is highly dependent on depth of cut (Equation 2.1) and it greatly influences the level of ploughing force during grinding [64]. At higher depths of cut, the grits must penetrate deeper into the surface of the workpiece and so the normal force increases [57], [58].

The dressing strategy is the third most influential parameter on reducing normal force, as shown in Figure 4.39B & D, for the conventional and hybrid wheels whereas for the elongated grit wheels it is the least impactful (rank 4). This correlates well with previous results (Sections 5.1 – 5.2) which expressed that the high aspect ratio, at a random distribution, of the elongated grits restricted the impact of dressing on the wheel topography. Only grits facing perpendicular to the central axis are favourable for cutting and these only form sharp cutting points at high dressing interference angles (Figure 4.14).

The grinding pass number was also included in the ANOVA model (Table 4.2) and had a much higher contribution to the normal force for the elongated grit wheel (6.56%) compared to the conventional and hybrid wheels (0.57% and 0.84% respectively). Again, this correlates with data from Section 4.3 as the elongated grit wheels showed a very rapid dulling behaviour between passes as the

favourable grits for cutting dull through microfracturing. The other wheels however showed a comparatively steady increase in force between passes. The hybrid wheel sees microfracturing of triangular grits forming sharp cutting points and the conventional wheel has a lower threshold force for macrofracture to occur and new sharp cutting points to be revealed.

5.4.3 GENERAL LINEAR MODEL – NORMAL FORCE

To capture and predict the force response of the process to various input grinding parameters a GLM was created. This model could then be used to predict the pass-to-pass behaviour of the different wheel types and examine the breakdown of different topographies under various grinding conditions.

As in the previous section (Section 4.4.2) the data for the conventional and hybrid wheels in passes $2 - 6$ in the Q' 33.3 mm^3 / mm s condition were removed as catastrophic wheel breakdown occurred at this point. All the data was separated by wheel type and a separate model generated for each. The factors were the dressing strategy and the model co-variates workpiece feed rate, depth of cut, wheel speed and pass number. Crossed factors and co-variates were used in the model as well as second-order interactions between them in order to increase the accuracy of the model.

A regression equation for each dressing condition, for each wheel (9 regression equations total, Appendix Hi), were generated and compared against the validation points detailed in Table 3.12. These are shown in Figure 5.12. For Figure 5.12A the model shows a good fit at Q' 0.7 mm^3 / mm s lying between the three validation measurement data points at the corresponding material removal rate. At Q' 20.0 mm^3 / mm s the predicted data point lies 43 N (6.8%) away from the nearest measured validation point. By the high material removal rate (Q' 52.5 mm^3 / mm s) the difference between the model prediction and the measured validation points is larger (17% deviation), and the prediction trend inversed, however this is not of concern as the model predicts forces at Q' values less than 25.0 mm^3 / mm s. For the hybrid wheel (Figure 5.12B) the fit demonstrated is even better with the predicted values being well within the range of measured values at both Q' 0.7 and 20.0 mm^3 / mm s. There is some deviation at Q' 52.5 mm^3 / mm s however this is very small (4.8%). The elongated grit wheel (Figure 5.12C) model showed inverse behaviour to the conventional wheel with improved model fit at higher material removal rates (Q' 20.0 and 52.5 mm^3 / mm s).

A.

B.

C.
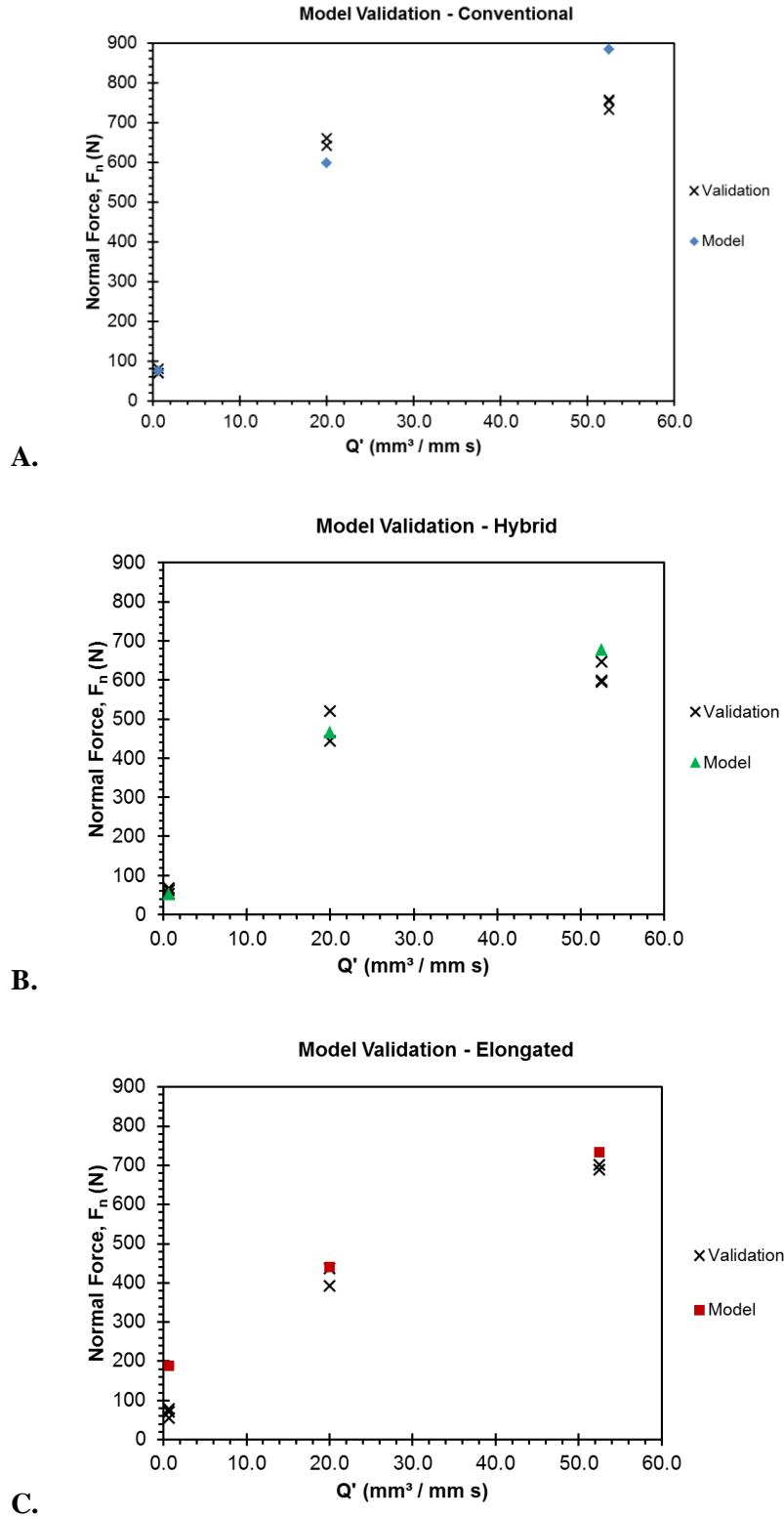
FIGURE 5.12 – COMPARISON BETWEEN THE GLM PREDICTED POINTS AND EXPERIMENTALLY MEASURED VALIDATION POINTS FOR (A) CONVENTIONAL, (B) HYBRID AND (C) ELONGATED GRIT WHEELS. ALL WHEELS SHOWED A GOOD FIT WITH THE EXPERIMENTAL DATA WITH VARIATION OF LESS THAN 17% IN THE CONVENTIONAL WHEEL.

A summary of each regression model is shown in Figure 5.13. The *S* value describes the average of how far the measured values fall from the model values, the lower this value is the better

prediction of the model. The *R-sq* values indicates how well the model fits the data whilst *R-sq(pred)* explains how accurately the model can predict the behaviour in the form of a percentage[251]. Cross predictors and second order terms were also included in the model to improve the accuracy of the prediction.

Model Summary - Conventional

S	R-sq	R-sq (adj)	R-sq (pred)
26.09	98.98%	98.62%	97.19%

A.

Model Summary - Hybrid

S	R-sq	R-sq (adj)	R-sq (pred)
23.61	98.32%	97.77%	96.11%

B.

Model Summary - Elongated

S	R-sq	R-sq (adj)	R-sq (pred)
42.80	97.62%	96.93%	95.73%

C.

FIGURE 5.13 – GLM MODEL SUMMARIES FOR (A) CONVENTIONAL, (B) HYBRID AND (C) ELONGATED GRIT WHEELS.

An R-sq (pred) value over 95% in Figure 5.13 indicates the GLM predicts the normal force accurately for all wheels, especially in the Q' 20 mm^3 / mm s region (Figure 5.12). The hybrid wheel model showed the best prediction across the Q' range with the lowest *S* value of 23.61. In comparison, the conventional and elongated grit wheels showed more significant deviation at Q' 52.5 mm^3 / mm s and Q' 0.7 mm^3 / mm s respectively with the elongated grit wheel having the highest *S* value (42.80).

Further validation of the models was performed against the measured data from the trial in Section 4.3 (Appendix Hi) to assess the prediction accuracy for multiple grinding passes. This revealed a close fit for the shape of the force response pass-to-pass (similar force gradient) however there was approximately 26% deviation in the actual predicted values. Therefore the GLM models described here should be used to describe the impact of wear trends on the wheels between passes, rather than for an accurate prediction of normal force value.

Using the models described above, the normal force response for passes 1 – 6 for the three wheel types and three dressing conditions were predicted. Three different Q' values were set at an even distribution within the testing range of the trial described in Table 3.10 at 3.0, 9.0 and 18.0. Table 4.2 indicated that the depth of cut is the most influential parameter on normal force, hence feed rate and wheel speed were kept constant at 1200 mm/min and 40 m/s, respectively, and the depth of cut set at three levels of 0.15 mm, 0.45 mm and 0.9 mm. The results are shown in Figure 5.14 on the specific energy curve for the data after 6 grinding passes as this shows the dominant chip formation process (cutting or rubbing/ploughing) which assists in explaining the phenomena.

Figure 5.14 shows that across all the material removal rates and dressing conditions, the steepest increase in normal force was in the elongated abrasive wheels. The hybrid wheels however indicated the lowest normal force increase pass-to-pass. It is notable that at low material removal rates (Q' 3.0 mm^3 / mm s, Figure 5.14B - D) the difference between the predicted normal force for

conventional and hybrid wheels is small (average <15 N). At higher Q' values (Q' 18 mm^3 / mm s, Figure 5.14H – J), this difference is much greater (>130 N average). The conventional and hybrid wheel also showed the greatest increase in normal force at the mid-range material removal rate (Q' 9.0 mm^3 / mm s, Figure 5.14E – G). The force increase was much reduced at the high material removal rate (Q' 18.0 mm^3 / mm s, Figure 5.14H – J).
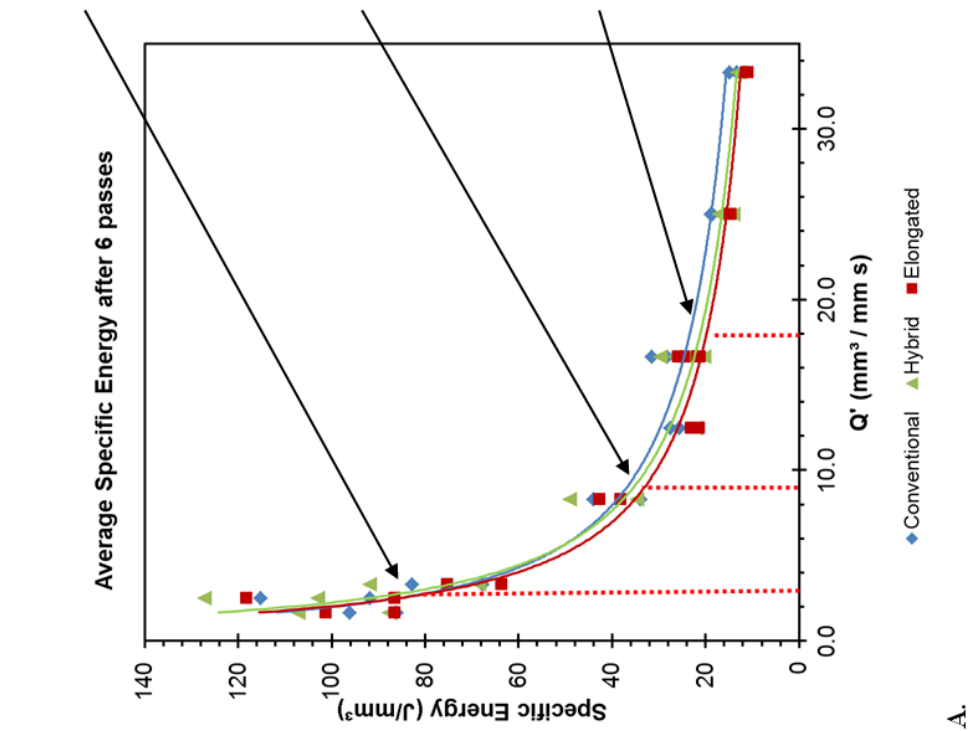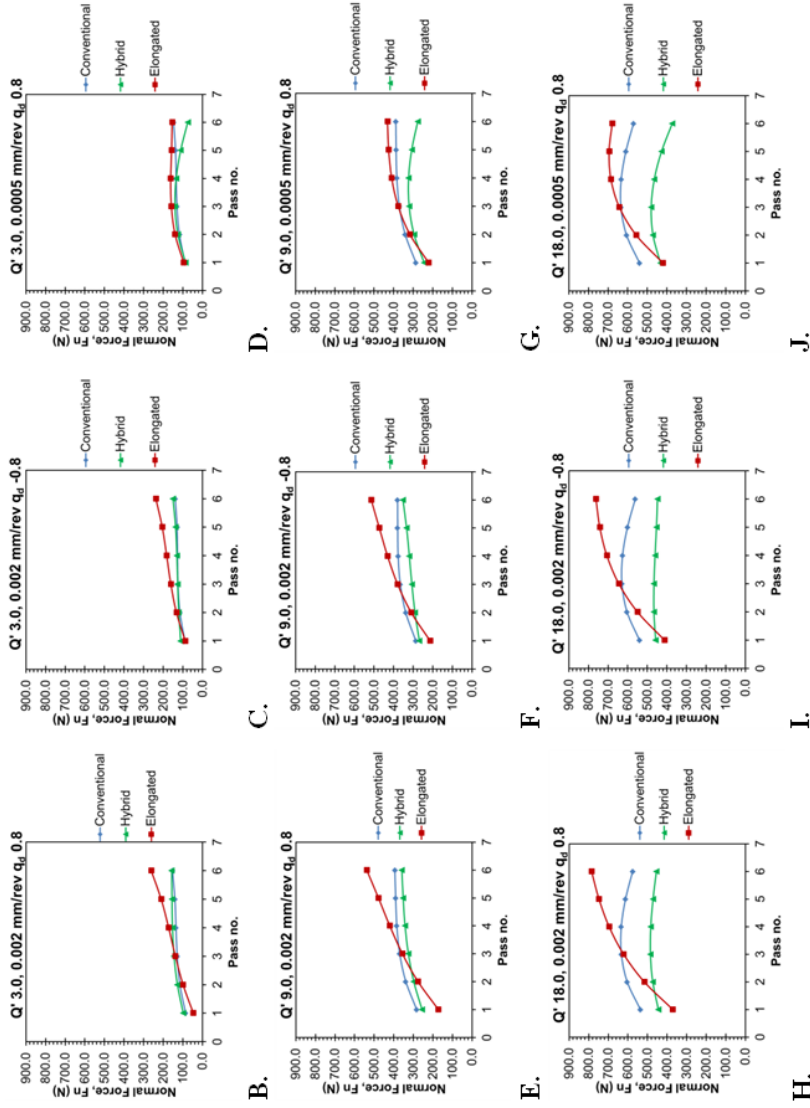
FIGURE 5.14 – (A) MEASURED AVERAGE SPECIFIC ENERGY AFTER 6 PASSES VWITH DOTTED LINES INDICATING THE SET Q' LEVELS FOR THE GLM. (B) – (D) NORMAL FORCE MODEL PREDICTION AT 0.002 MM/REV AND Q_D 0.8 (E) – (G) MODEL PREDICTION AT 0.002 MM/REV AND Q_D -0.8 (H) – (I) MODEL PREDICTION AT 0.0005 MM/REV AND Q_D 0.8. ALL Q' VALUES HAVE UNITS OF MM^3 / MM S.

It is observed in Figure 5.14 that at all Q' values the elongated grits showed the most rapid increase in normal force from pass-to-pass, for all dressing strategies. This matched well with the trend shown in Section 4.3 (Figure 4.30). The gradient of the normal force for these grits was greatest at the highest Q' (18.0 mm^3 / mm s) and at dressing condition 0.002 mm/rev and q_d 0.8 (Figure 5.15). Under this aggressive dressing parameter, the topography consists of sharp, well distributed cutting points (Section 5.1) so the initial, first grinding pass has a low normal force. This increases rapidly however as the steep interference angle and high crushing effects from dressing cause damage in the abrasive grits meaning fracture is easy and the cutting points dull quickly. At a high Q', the grinding forces are higher, as shown by Kwak et al. [67], encouraging more rapid progress of attritious wear so the sharpness of the grits is lost quicker than at lower material removal rates (so rapid normal force increase, as shown in Figure 5.14).

For the conventional and hybrid wheels however, the highest rate of dulling (steepest gradient of normal force), was in the mid-range Q' (9.0 mm^3 / mm s) for all dressing conditions (Figure 5.15B). In this range the forces are sufficient for rapid attritious wear compared to the low Q' condition (3.0 mm^3 / mm s) but do not build sufficiently to cause macrofracture as seen in Section 4.3. At the higher Q' (18.0 mm^3 / mm s), forces on the grits are greater so macrofracturing of the grits occurs sooner generating new sharp cutting points and limiting the rise in grinding forces and power.

A.

B.

C.
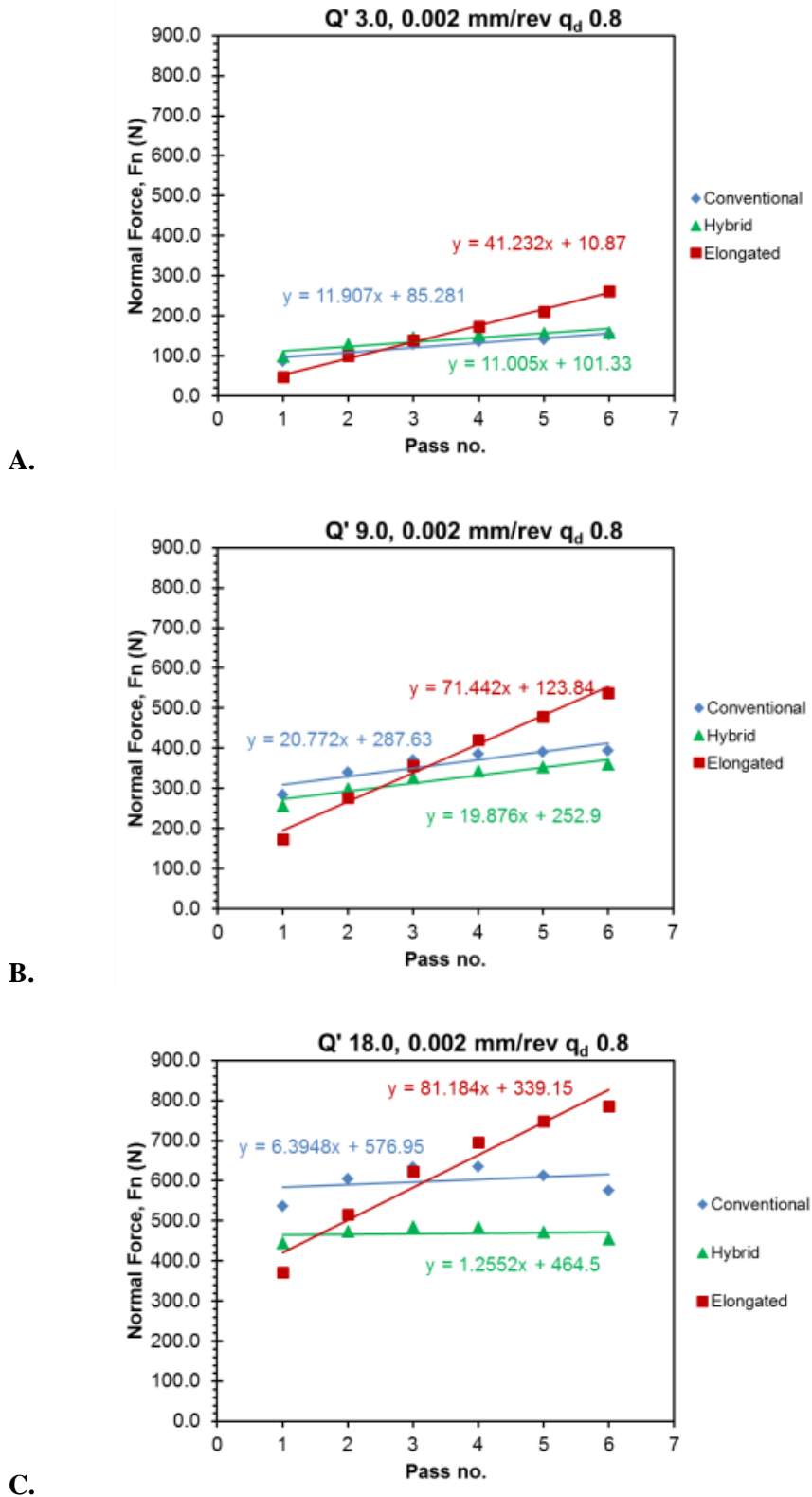
FIGURE 5.15 – PREDICTED NORMAL FORCE USING GLM FOR 0.002 MM/REV AND Q_D 0.8 DRESSING CONDITION AT (A) Q' 3.0, (B) Q' 9.0 AND (C) Q' 18.0 MM^3 / MM S WITH SLOPE GRADIENTS SHOWN.

It is suggested by Figure 5.15 that as the material removal rate gets higher, the dominance of the engineered grits in the hybrid wheel increases. At low Q' (3.0 mm^3 / mm s), the predicted force is very similar for the conventional and hybrid wheels (average difference of <15 N), the forces are low so fracturing of the grits is reduced so cutting is performed by both conventional and triangular grits. As the grinding parameters become more aggressive the difference between the wheels (40 – 65 N average difference at Q' 9.0 mm^3 / mm s and 130 – 160 N average at Q' 18.0 mm^3 / mm s) increases, the forces increase sufficiently to cause the triangular grits microfracture keeping the topography sharp and the normal forces low. In the conventional wheel however the large crystal structure means fracture is difficult, so the grits continue to dull and the forces are increased.

At high material removal rates (Q' 18.0 mm^3 / mm s), the normal force trend is very flat for the hybrid wheel (Figure 5.14H – J), suggesting that it is self-sharpening during grinding. Rather than catastrophic breakdown of the wheel seen at Q' 33 mm^3 / mm s (Figure 4.37B) the grits are continually micro and macrofracturing (in the mechanism described in Section 5.2), thus generating fresh, sharp cutting points which can penetrated the workpiece easily and keep the forces low. Due to the triangular shape of the engineered grits in the wheel, sharp points are formed easily and dominate the material removal process.

5.4.4 ANALYSIS OF WHEEL TYPE ON GRINDING SPECIFIC ENERGY

The topography generated from dressing has a greater influence over more grinding passes at low material removal rates as in Figure 5.14 the most variation in specific energy, between dressing conditions, is seen at the lowest Q' (3.0 mm^3 / mm s) for all abrasive wheel types. At this stage the chip thickness is small, therefore the grinding forces are reduced (Figure 4.37) so the wear effects on the abrasive are minimised (which are also influenced by wheel bond strength and porosity etc.[1], [252]). With less wear, the initial topography of a wheel at pass 1 is maintained for more passes. Therefore the most effective grinding topography is at 0.002 mm/rev and q_d 0.8 at low material removal rates, as further demonstrated by the friction coefficient being lowest in this condition for all wheels (Figure 4.42). The sharp topography means increased cutting and less rubbing. Most variation occurred in the conventional wheels supporting the behaviour seen in the topography (Section 5.1) that the uniform grit shape leads to better control on topography by the dresser.

At Q' 3.0 mm^3 / mm s the elongated grit wheel showed the lowest specific energy due to very sharp cutting points on the favourably orientated (perpendicular to central axis) grits. These penetrate deeper into the workpiece and the grinding power is reduced (Figure 4.16). This explanation fits also for the pattern shown in the main effects plot (Figure 4.41) in which the elongated grit wheel has by far the lowest mean specific energy (44.6 J/mm³) compared to the conventional (48.3 J/mm³) and

hybrid (48.3 J/mm³) wheels. The large aspect ratio and sharp cutting points reduce the grinding power whilst less wheel wear leads to a higher material removal rate and thus lower specific energy (Equation 2.3).

The hybrid wheel had the least variation in average specific energy of all the wheels at Q' 3.0 mm^3 / mm s. This matches with conclusions in Section 5.2 in which the hybrid wheel had the least variation in grinding power over the dressing range (Figure 4.16). This was due to the engineered grits in the wheel limiting the influence of dressing on wheel topography. Further support for this argument is shown in Figure 4.42 as the friction coefficient showed the lowest fluctuation for the hybrid wheel against all the others suggesting a more consistent topography.

At Q' 9.0 mm^3 / mm s (Figure 4.40B) much less difference is visible between the dressing conditions due to the increased influence of abrasive wear in the process. Dressing condition 0.002 mm/rev and q_d 0.8 still showed the lowest grinding energy in all wheels as the high interference angle generates sharp cutting points. It is notable that at the higher interference angle dressing parameters (0.002 mm/rev and q_d 0.8, and 0.0005 mm/rev and q_d 0.8), the hybrid wheel has a lower mean specific energy than the conventional (elongated still the lowest energy). This is related to the wear behaviour, which was seen to be much higher for the conventional wheel in Section 4.3. The microfracturing mechanism of the triangular grits in the hybrid wheel ensure that dulling wear is minimised. Hence the specific grinding energy is reduced.

By Q' 18.0 mm^3 / mm s dressing is least influential as there is the least variation between dressing conditions as the grinding forces are higher and the dressed topography breaks down rapidly as the wheel dulls or self-sharpens. The conventional wheel has the highest specific energy as it has the greatest number of cutting points on the surface (Figure 4.05) and the most wheel wear of all the wheels (Figure 4.38). The hybrid wheel showed the lowest specific energy of all the wheels in the 0.0005 mm/rev and q_d 0.8 dressing condition which differs from the response seen in Sections 4.2 and 4.3. This could be due to the reduced dressing forces from the lower infeed rate, so less damage in the grinding layer on the dominant engineered grits so they remain sharp for longer. As the grinding forces are greater at higher Q', the sharp 0.002 mm/rev and q_d 0.8 topography breaks down quickly as a result of large sub-surface damage and the effect of dressing is lost.

5.4.5 THE EFFECTS OF GRIT MORPHOLOGY ON WHEEL WEAR

The contribution Table 4.3 showed that the depth of cut is the most influential parameter on wheel wear (>88% for all wheels). The higher the depth of cut, the deeper the grits must penetrate into the workpiece surface, therefore the normal forces are larger and the wheel wear increased. Dressing

strategy was ranked as the second most influential parameter on wheel wear (Figure 4.43). Interestingly, the elongated grit wheels have the highest percentage contribution of the dressing strategy (4.29% compared to 2.42% and 2.30% for the conventional and hybrid wheels respectively). This could be a result of the damage caused by the dressing strategy, weakening the large extruded grits. The contribution of dressing in the conventional and hybrid wheels however is very similar (0.12% difference). In Section 4.3.4, the microfracture behaviour of the hybrid wheel meant reduced wear compared to the other wheels and this is seen in Figure 4.38 at Q' less than 14.0 mm^3 / mm s. However grinding at higher removal rates has revealed improved wear performance in the elongated grit wheel likely a result of its high aspect ratio shape making break down difficult because of grit overlap preventing whole grit pull out. In the hybrid, the triangular grits are smaller and do not provide the same level of support so at sufficiently high grinding forces, catastrophic breakdown can occur.

For all wheels dressing using parameters 0.002 mm/rev and q_d -0.8 had the highest S/N ratio, indicating that this is the optimum condition to reduce wheel wear (smaller is better analysis). Under these dressing parameters, the interference angle during dressing is very shallow so the wheel topography is blunt and less damage is inflicted deep into the grinding layer of the abrasive wheel which could encourage bond fracture and loss of grits.

5.4.6 SURFACE ROUGHNESS

It is shown in Figure 4.45 that the surface roughness after pass 6 increases by an increase in the theoretical chip thickness. This is similar to work by Zeng et al. [228] in which increased surface roughness is seen at higher depths of cut leading to deeper penetration of the abrasive grits and thus greater deviation from the mean line of the surface. It is known that the cutting point spacing, and grit protrusion both influence the size of the grooves cut into the workpiece, and therefore the surface roughness [32]. As the conventional wheel has the most uniform wheel topography because of the electrofused, approximately spherical grits, as well as the highest peak density on the topography (Figure 4.05) then a low surface roughness would be expected (Figure 5.16).
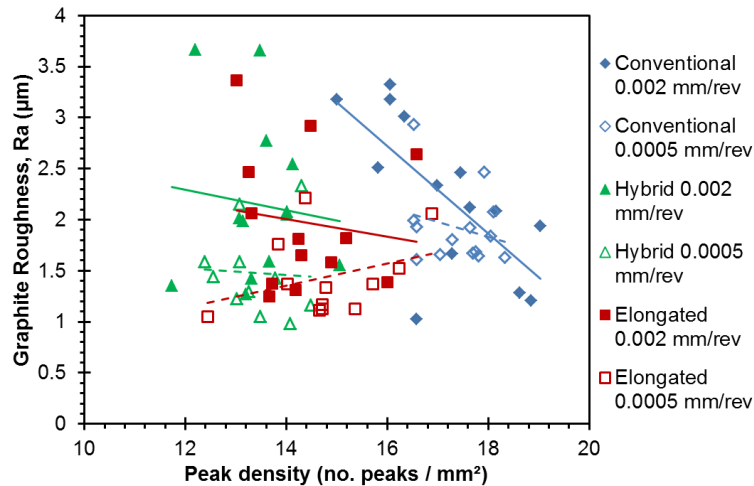
FIGURE 5.16 – GRAPHITE ROUGHNESS AS A FUNCTION OF PEAK DENSITY USING SECTION 4.2 DATA SET. DEMONSTRATES INFLUENCE OF CUTTING POINT VARIATION ON WHEEL ROUGHNESS.

Regarding process parameters, the S/N ratios in Figure 4.46 show an interesting response with the depth of cut most influential (rank 1) for the hybrid and elongated grit wheel but feed rate is most impactful on roughness in the conventional wheel. This is likely due to the high level of variation in the data. ANOVA analysis of the data showed error of 80.61% for the conventional wheel compared to 18% and 10% for the hybrid and elongated grit wheels respectively. The ratios did indicate that the optimum dressing strategy for reduced surface roughness is 0.002 mm/rev and q_d -0.8 for all wheels. At shallow interference angle the cutting points on the topography are dull and so the grinding tracks are reduced and the surface experiences much less variation.

It is notable that the measured surface roughness on the workpieces at very low chip thicknesses ($<1 \times 10^{-6}$ mm) is much higher than expected for an #80 grit wheel (1.3 µm measured Ra compared to expected <0.8µm as according to Rolls-Royce quality standard CME). This could be due to a number of factors including the surface being measured after 6 grinding passes, therefore wear has occurred on the cutting points of grits and the surface will be of a reduced quality. However, at very low chip thicknesses the level of wear will be small on the wheel topography and would form dull cutting points. As such the grinding tracks would be reduced and a lower surface roughness on the workpiece. Another likely explanation is vibration present in the experimental set up. Also wear to the dresser diamonds would reduce their effectiveness on the abrasive grits, although dresser quality was monitored visually throughout the work (Appendix Di) with no change detected. Bhaduri et al. [175] has shown that vibration can increase the level of smearing and surface roughness on a workpiece and the vibration can be transferred onto the surface of the workpiece [6]. In this trial, the workpiece was clamped to the top of a force dynamometer using steel clamps (Figure 3.27). However the workpiece was held vertically and there was no support beneath the superalloy slab, therefore

vibration could have occurred here. Further evidence of this was seen on the ground surfaces (Figure 5.17) with regular vibration marks visible on the surface.
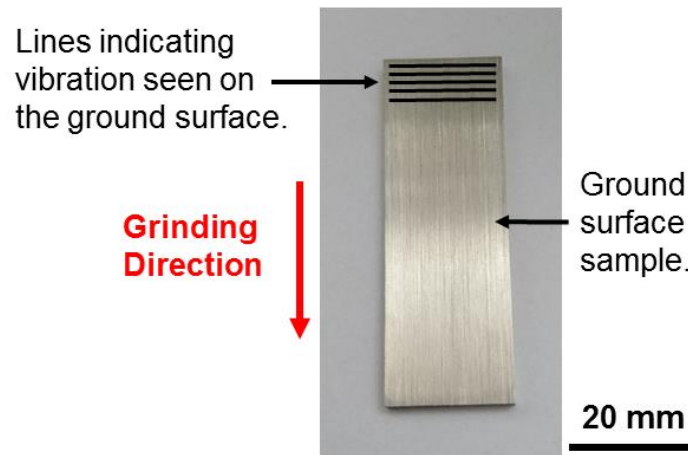
FIGURE 5.17 – DIAGRAM OF THE VIBRATION MARKS SEEN ON ONE OF THE GROUND SURFACE SAMPLES.

Despite the large roughness values, the set up was consistent throughout the entire trial and the expected roughness trend is still observed (Figure 4.45). Therefore this data is suitable for comparison between wheels but not for predicting exact roughness values.

5.4.7 METALLURGICAL ANALYSIS

As only a total of five samples were studied for each wheel type, for a short length of the cut (approximately 10 cm), more samples may be required in order to detect a trend. The sample size is too small to capture consistent metallurgical response. However, instances of both white layer and redeposited material were seen on the samples for all wheels. A noticeable increase in the average feature thickness from Q' 0.7 mm^3 / mm s to 52.5 mm^3 / mm s can be seen in Figure 4.48A - B. This is expected for the redeposited material layer because as the chip thickness increases, greater amounts of cutting of the workpiece generates more chips which can get redeposited on the ground surface [Rolls-Royce CME5043 Section 2]. High levels of clogged workpiece material, seen particularly in the hybrid and elongated grit wheels (Figure 5.09), are released by the wheel and deposited on the surface of the Ni-superalloy workpiece. However there was no obvious trend visible between the conventional, hybrid and elongated grit wheel types in the level of redeposited material. This suggests that it is the material removal rate that most influences the thickness of redeposited material.

A similar pattern was seen with the white layer as increasing average thickness was measured from Q' 0.7 to 52.5 mm^3 / mm s for all wheels. It is known that white layer can result from either high surface mechanical deformation, or high surface temperature (as shown by Guo et al. [62]). At high

material removal rates (Q' 52.5 mm^3 / mm s) the grinding forces, and thus grinding energy, is large (Figure 5.12). This generates high temperatures during grinding compared to low removal rates as demonstrated by Liu et al. [93] (Figure 2.39). These high temperatures, encourages material softening and allows increased mechanical deformation of the surface and thus a thicker white layer is formed [221]. This is further supported by the images in Figure 5.18 in which some material deformation in the surface can be seen at high Q'. At low Q' (0.7 mm^3 / mm s), the contact length of the wheel on the workpiece, and the power consumption during grinding is reduced. Hence a thinner white layer is detected.
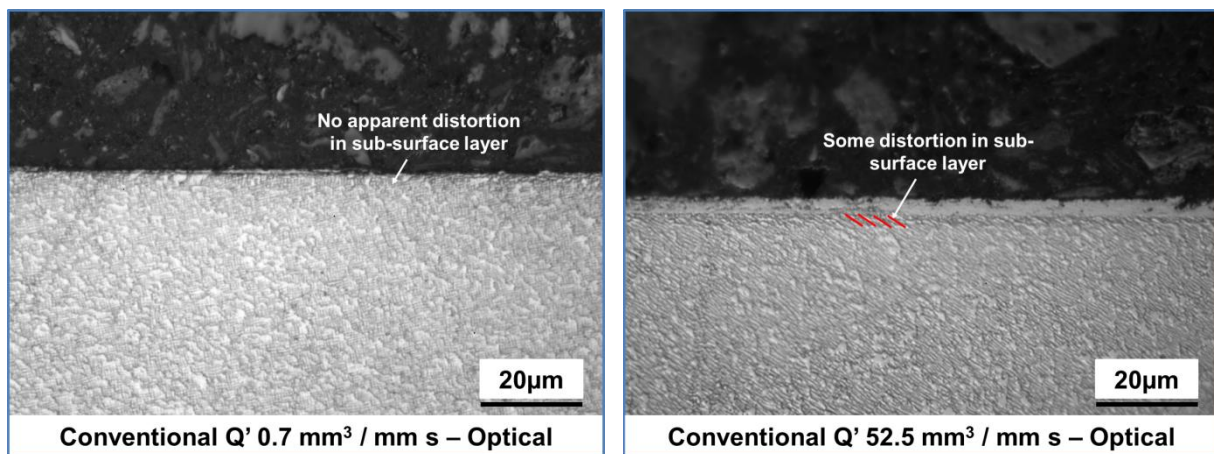
A.   **B.**

FIGURE 5.18 – METALLOGRAPHIC IMAGES OF GROUND SURFACE CROSS SECTIONS (A) AT Q' 0.7 MM^3 / MM S WITH NO SUB-SURFACE DISTORTION AND (B) Q' 52.5 MM^3 / MM S WITH VISIBLE SUB-SURFACE DISTORTION.

The conventional wheel generated the lowest average thickness of white layer of all the wheels in the finish grinding condition (Q' 0.7 mm^3 / mm s), Figure 4.49, which aligns with the surface roughness response which was lowest for this wheel (Figure 4.45). This matches with Xu et al. [224] who measured a lower grinding surface temperature generated a lower surface roughness which is explained as many shallow overlapping cuts. The more uniform topography of the conventional wheel creates lots of cutting points at a similar protrusion distance from the wheel. These create small chips, reducing surface temperature and maintain a low surface roughness. Due to the orientation variation of the engineered grits in the hybrid and elongated wheel, at low depths of cut, the sharp cutting points are more irregular on the wheel surface and protrude further generating a rougher surface roughness on the workpiece. The unfavourably orientated grits though do not penetrate deep enough into the workpiece to cause shearing (and cutting) and instead encourage increased rubbing leading to temperature generation and white layer. However the grinding normal forces were highest for the conventional wheel compared to the others, indicating duller cutting points. Work by Guo et al. [62] saw the appearance of white layer when the flat regions on the abrasive grits was high therefore

further comparison work between grit shapes on the metallurgical response at low material removal rates is required.

The elongated grit wheel showed the lowest average thickness of white layer at the highest material removal rate (Q' 52.5 mm^3 / mm s). The average specific energy as well as the friction coefficient was the lowest when grinding using this wheel in the 0.002 mm/rev and q_d 0.8 dressing condition (Figure 4.40). The favourably orientated, large elongated grits penetrate deeper into the workpiece leading to a dominance of cutting over rubbing and ploughing as well as transferring more of the heat into the chips. Penetration of the chips is greater so the rubbing effect of the unfavourably orientated grits is reduced.

It is important to note that all the samples analysed would fail the Rolls-Royce CME5043 material standard as no white layer must be detected. The reason for failure is likely related to the 'finishing' depths of cut used in this study being relatively high as the aerospace industry will typically perform finishing passes at < 50µm depths of cut. Also, as mentioned in Section 5.4.6, vibration was an issue in the trial due to the clamping method on the workpiece being different to that used in industry because of the workpiece form. This would lead to a higher surface roughness and increased sub-surface damage.

CHAPTER 6

CONCLUSIONS

6.0 CONCLUSIONS

The following Section collates the discussion of the data in Section 5.0 and summarises the key observations.

6.1 SCIENTIFIC OBSERVATIONS

6.1.1 GENERAL OBSERVATIONS

There are a number of consistent conclusions that can be drawn for all the abrasive wheels investigated:

1. Synchronous dressing at high infeed rates and speed ratios creates steep interference angles of the dresser diamonds on the abrasive wheels. This impacts a greater volume of the wheel and dressing power is a maximum. Asynchronous dressing at a low infeed rate creates a shallow interference angle and a low dressing power.

2. Infeed rate is the most influential dressing parameter on wheel topography and grinding response.

3. Attritious wear occurs on all abrasive grit shapes and rapid dulling is noticeable after a first grinding pass.

4. In grinding, depth of cut is the most significant parameter on grinding forces, wear and workpiece roughness.

5. Engineered grit shapes directly influence the dressing/ grinding mechanisms and grit orientation is critical.

6.1.2 CONVENTIONAL GRITS

The following conclusions can be drawn for the conventional grain abrasive wheels:

1. High dressing interference angle generates a rough wheel topography with sharp, widely-spaced cutting points due to extensive macro and bond fracture. This causes damage deeper into the grinding layer of the abrasive wheel which leads to increased wheel wear after multiple grinding passes.

2. There is a transformation of dressing mechanism from macro fracturing of grits at high dressing infeed rates (0.002 mm/rev) to microfracturing at low infeed rates (0.0005 mm/rev).

3. Due to a more uniform, spherical grit shape (compared to the triangular and elongated) the conventional wheels generated the lowest surface roughness of the abrasives tested (1.22 µm average Ra compared to 1.38 µm and 1.53 µm for the other abrasives).

4. Catastrophic wear of the wheel (due to bond fracture) was seen at Q' 33.3 (average 400 µm in radial wear after 9 grinding passes).

5. Dulling of the wheel is most significant in semi-finishing conditions (around Q' 9.0) as the grinding forces are high enough for microfracture but not macro.

6.1.3 HYBRID GRIT WHEELS

The following conclusions can be drawn for the hybrid abrasive wheels containing 70% conventional and 30% triangular grains:

1. The triangular, engineered grit shapes dominate the dressing process of the wheel due to their microfracturing behaviour. The level of both macro and microfracturing increases as the interference angle in dressing increases also. The higher the engineered grit content, the lower the dressing power due to the easy microfracture of the grits.

2. The triangular, engineered grits in the hybrid wheel dominate the grinding process due to their microfracturing behaviour (small crystal size) which limits normal forces and wheel wear between grinding passes as the topography remains sharp. These wheels demonstrated the best self-sharpening behaviour.

3. Catastrophic wheel breakdown (from bond fracture) occurs at Q' >33.3 (average 350 µm in radial wear after 9 grinding passes).

4. The hybrid wheel showed the best wear response of all the wheels tested at Q' <15. Above this removal rate, macrofracture led to higher wheel breakdown compared to the elongated wheel.

5. The influence of the triangular grains is more significant at higher material removal rates due to higher grinding forces encouraging increased fracturing of the triangular, engineered grains. The irregular shape of the engineered grits lead to a rougher surface finish compared to the conventional wheel (minimum of 13% higher surface roughness).

6.1.4 ELONGATED GRIT WHEELS

The following conclusions can be drawn for the abrasive wheels containing elongated abrasive grits:

1. The high aspect ratio of the elongated abrasive grits restricts the influence of dressing parameters on the topography of the wheel. At shallow interference angles (speed ratio less than 0.4, and/or infeed rate 0.0005 mm/rev) then only the favourably orientated (perpendicular to the spindle) fracture.

2. This wheel had the highest dressing energy of all the wheels investigated due to the high material volume of the grits (approximately 40% higher across all dressing conditions).

3. Grit orientation dominates the grinding process with those aligned perpendicular to the central axis cutting the workpiece. This generated the highest workpiece surface roughness (Ra 2.19 µm) as result of deep grit penetration into the workpiece.

4. Lowest first grinding pass normal forces and power however very rapid dulling of the cutting points (from attritious wear) leads to very high grinding forces.

5. No catastrophic breakdown of the wheels occurred over the removal rate range tested, meaning low wheel wear at high Q' values (>15). High grit aspect ratio ensures whole-grain pull out is difficult.

6.2 INDUSTRIAL IMPACT

This EngD work was sponsored by Rolls-Royce plc. and a number of useful conclusions can be drawn from the data for application in an industrial VIPER grinding environment.

1. High infeed rates and synchronous speed ratios should be used for dressing when performing rough grinding for any wheel type. This creates a sharp topography suitable for large chips and material removal.

2. Asynchronous speed ratios should be used for initially dressing the wheel to a basic shape to preserve dresser lifetime. This reduces the dressing power and therefore the forces on the diamond dressing roll, decreasing the likelihood of dresser diamonds being dulled and/or pulled out of the roll surface.

3. The hybrid wheel demonstrated the least wheel wear at Q'< 18.0 and force increase between passes was the lowest of all the wheel types. Therefore this wheel would require less frequent dressing and would maintain a grinding form best. It also has reduced dressing power causing less dresser wear (cost saving). Combined with the relatively low individual wheel price (hybrid £29.89[1], conventional £24.15, elongated £54.58), it could provide a better cost benefit compared to the other wheels for roughing (wheel wear x wheel cost calculations below, lowest value desired):

> At Q' 10.0 (section 4.3.4): Conventional wheel cost efficiency 3.9 mm £, Hybrid wheel cost efficiency 3.6 mm £, Elongated grit wheel cost efficiency 8.5 mm £.

4. At very high material removal rates (Q' > 25.0) the elongated grit wheel would be most suitable as catastrophic bond breakdown occurs on the other wheel types.

5. The more uniform grit shape of the conventional wheel produces the lowest surface finish of all the wheel types, at all grinding parameters. It also generated the least white layer in the samples indicating this is the best wheel for finishing grinding cuts.

6. Data in Section 4.0 will contribute towards a VIPER grinding neural network model to improve the prediction of the process when designing manufacturing processes.

---

[1] All wheel prices from supplier quotes 2018.

CHAPTER 7

FUTURE WORK

7.0 FUTURE WORK

This EngD thesis concentrated on the impact of dressing and grinding parameters on the response of wheels with different abrasive grit shapes when grinding Ni-base superalloy. However further work is required to validate the results and gain full understanding of the VIPER grinding process.

The work presented in this thesis compares the nature of different abrasive grit shapes by considering the overall wheel performance. There is scope to compare these shapes at the individual-grit level by conducting single-grit grinding experiments and finite element modelling to understand their chip formation mechanisms. This EngD indicates that grit orientation of engineered grits is very influential on grinding and modelling of individual grits would provide further evidence whether this conclusion is accurate. This investigation would also enable measurement of actual chip sizes from different grit shapes for improved grinding mechanism comparison. Finite element analysis of the triangular and elongated grits at the three different orientation classes discussed in Section 4.1.3 would give data on chip formation forces and chip size. This could then be supported by experimental grinding trials with single grits (at different orientations) mounted on a rotating wheel and used to grind Ni-base superalloy samples with force measurements and SEM analysis performed on the ground channel of the workpiece.

This EngD thesis only investigates three wheel types and no coverage is made in this work regarding different wheel parameters such as bond strength, porosity or grit size. Although their influence on conventional wheels in creep feed grinding is relatively well researched [88], [117], [253], [254], the impact of these on the behaviour of engineered grit shapes is not. Hence a dressing study (Section 3.2) and a grinding breakdown investigation (Section 3.4) should be performed to give a complete picture of the entire process. Grit size may influence the fracture behaviour of the engineered grits and assessing different bond strengths will reveal the significance of the bonding on grinding performance compared to the abrasive grit shape. Three levels of grit size (#60, #80 and #120), bond strength (G, H and I) and porosity (10, 12 and 15) could be tested which would provide to understand behaviour trends. This work would also provide extensive data for a knowledge database which could be used by industry to select the correct wheels for a component.

Finally, much industrial grinding (particularly aerospace) dresses a form into abrasive wheels which is then formed on the workpiece. An investigation into the breakdown of the wheels studied in this thesis with forms on the wheel would provide more information on the suitability of the wheels for application. A complex form could cause a concentration of forces which will influence the grinding response of differently shaped grits. Therefore a grinding trial with the same wheels, each

dressed with a common industrial form (such as a turbine blade firtree) should be conducted, and multiple grinding passes made and the breakdown of the feature form measured. The graphite block technique described throughout the thesis could be used to capture form radius on an Alicona microscope whilst metallurgical analysis and surface imaging will study the effect on the workpiece.

REFERENCES

[1]   S. Malkin and C. Guo, *Grinding Technology: Theory and Application of Machining with Abrasives*, 2nd ed. New York: Industrial Press Inc., 2008.

[2]   F. Klocke, S. L. Soo, B. Karpuschewski, J. a. Webster, D. Novovic, A. Elfizy, D. a. Axinte, and S. Tönissen, "Abrasive machining of advanced aerospace alloys and composites," *CIRP Ann. - Manuf. Technol.*, vol. 64, no. 2, pp. 581–604, 2015.

[3]   E. Brinksmeier and F. Werner, "Monitoring of Grinding Wheel Wear," *CIRP Ann. - Manuf. Technol.*, vol. 41, no. 1, pp. 373–376, 1992.

[4]   L. A. Blunt and S. Ebdon, "The Application of Three-Dimensional Surface Measurement Techniques to Characterizing Grinding Wheel Topography," *Int. J. Mach. Tools …*, vol. 36, no. 1, pp. 1207–1226, 1996.

[5]   J. L. Jiang, P. Q. Ge, W. B. Bi, L. Zhang, D. X. Wang, and Y. Zhang, "2D/3D ground surface topography modeling considering dressing and wear effects in grinding process," *Int. J. Mach. Tools Manuf.*, vol. 74, pp. 29–40, 2013.

[6]   W. Rowe, *Principles of modern grinding technology*, 1st ed. Oxford: William Andrew, 2009.

[7]   D. A. Stephenson and J. S. Agapiou, *Metal Cutting: Theory & Practice*, 2nd ed. Boca Raton, 2006.

[8]   W. Rowe and S. Black, "Grinding temperatures and energy partitioning," *… R. …*, vol. 453, no. 1960, pp. 1083–1104, 1997.

[9]   P. F. Ostwald and J. Munoz, *Manufacturing Processes and Systems*, 9th ed. New York; Chichester: John Wiley & Sons, 1997.

[10]   E. P. Degarmo, J. T. Black, and R. A. Kosher, *Materials and Processes in Manufacturing*, 9th ed. New York; Chichester: John Wiley & Sons, 2003.

[11]   Z. B. Hou and R. Komanduri, "On the mechanics of the grinding process, Part II—thermal analysis of fine grinding," *Int. J. Mach. Tools Manuf.*, vol. 44, no. 2–3, pp. 247–270, Feb. 2004.

[12]   I. S. Jawahir, E. Brinksmeier, R. M'Saoubi, D. K. Aspinwall, J. C. Outeiro, D. Meyer, D. Umbrello, and a. D. Jayal, "Surface integrity in material removal processes: Recent advances," *CIRP Ann. - Manuf. Technol.*, vol. 60, no. 2, pp. 603–626, Jan. 2011.

[13]   M. C. Shaw and A. Vyas, "Heat-Affected Zones in Grinding Steel," *CIRP Ann. - Manuf. Technol.*, vol. 43, no. 1, pp. 279–282, 1994.

[14]   J. F. G. Oliveira, E. J. Silva, C. Guo, and F. Hashimoto, "Industrial challenges in grinding," *CIRP Ann. - Manuf. Technol.*, vol. 58, no. 2, pp. 663–680, Jan. 2009.

[15]   J. Webster and M. Tricard, "Innovations in abrasive products for precision grinding," *CIRP Ann. Technol.*, no. 1, 2004.

[16]   Y. Changyong, X. Jiuhua, D. Wenfeng, C. Zhenzhen, and F. Yucan, "Dimension accuracy and surface integrity of creep feed ground titanium alloy with monolayer brazed CBN shaped wheels," *Chinese J. Aeronaut.*, vol. 23, no. 5, pp. 585–590, 2010.

[17]   A. S. Lavine and S. Malkin, "The role of cooling in creep feed grinding," *Int. J. Adv. Manuf. Technol.*, vol. 5, no. 2, pp. 97–111, 1990.

[18]   R. Alberdi, J. A. Sanchez, I. Pombo, N. Ortega, B. Izquierdo, S. Plaza, and D. Barrenetxea, "Strategies for optimal use of fluids in grinding," *Int. J. Mach. Tools Manuf.*, vol. 51, no. 6, pp. 491–499, 2011.

[19]   K. Ramesh, S. Yeo, Z. Zhong, and K. Sim, "Coolant shoe development for high efficiency grinding," *J. Mater. Process. …*, vol. 114, pp. 240–245, 2001.

[20]   E. Brinksmeier and E. Minke, "High-performance surface grinding–the influence of coolant on the abrasive process," *CIRP Ann. Technol.*, vol. 42, no. 2, pp. 367–370, 1993.

[21]   C. P. R. Hill, J. R. Watkins, and C. Ray, "Method and Apparatus for Grinding," EU Patent EP 0924028B1, 2004.

[22]   D. K. Aspinwall, S. L. Soo, D. T. Curtis, and A. L. Mantle, "Profiled superabrasive grinding wheels for the machining of a nickel based superalloy," *CIRP Ann. - Manuf. Technol.*, vol. 56,

no. 1, pp. 335–338, 2007.

[23] D. T. Curtis, S. L. Soo, D. K. Aspinwall, and C. Sage, "Electrochemical superabrasive machining of a nickel-based aeroengine alloy using mounted grinding points," *CIRP Ann. - Manuf. Technol.*, vol. 58, no. 1, pp. 173–176, 2009.

[24] H. Tönshoff, J. Peters, I. Inasaki, and T. Paul, "Modelling and simulation of grinding processes," *CIRP Ann. …*, vol. 41, no. 1, pp. 677–688, 1992.

[25] I. Inasaki, H. K. Tönshoff, and T. D. Howes, "Abrasive Machining in the Future," *CIRP Ann. - Manuf. Technol.*, vol. 42, no. 2, pp. 723–732, 1993.

[26] D. Ulutan and T. Ozel, "Machining induced surface integrity in titanium and nickel alloys: A review," *Int. J. Mach. Tools Manuf.*, vol. 51, no. 3, pp. 250–280, Mar. 2011.

[27] I. . Choudhury and M. . El-Baradie, "Machinability of nickel-base super alloys: a general review," *J. Mater. Process. Technol.*, vol. 77, no. 1–3, pp. 278–284, May 1998.

[28] M. Alauddin, M. A El Baradie, and M. S. J. Hashmi, "End-milling machinability of Inconel 718," *Arch. Proc. Inst. Mech. Eng. Part B J. Eng. Manuf. 1989-1996 (vols 203-210)*, vol. 210, no. 12, pp. 11–23, Jun. 1996.

[29] S. Beale, "Precision engineering for future propulsion and power systems: a perspective from Rolls-Royce.," *Philos. Trans. R. Soc. A Math. Phys. Eng. Sci.*, vol. 370, no. 1973, pp. 4130–53, 2012.

[30] R. Gadow, F. Kern, and H. Ulutas, "Mechanical properties of ceramic matrix composites with siloxane matrix and liquid phase coated carbon fiber reinforcement," *J. Eur. Ceram. Soc.*, vol. 25, no. 2–3 SPEC. ISS., pp. 221–225, 2005.

[31] S. Kannappan and S. Malkin, "Effects of Grain Size and Operating Parameters on the Mechanics of Grinding," *J. Eng. Ind.*, vol. 94, no. 3, pp. 833–842, 1972.

[32] I. Marinescu, W. B. Rowe, B. Dimitrov, and I. Inasaki, *Tribology of Abrasive Machining Processes*, 1st ed. Norwich: William Andrew, 2004.

[33] S. Malkin and R. Anderson, "Thermal Aspects of Grinding: Part 1—Energy Partition," *J. Eng. Ind.*, vol. 96, no. 4, pp. 1177–1183, 1974.

[34] X. U. N. Chen and W. B. Rowe, "Analysis and Simulation of the Grinding Process Part II: Mechanics of Grinding," *Int. J. Mach. Tools …*, vol. 36, no. 8, pp. 883–896, 1996.

[35] R. Komanduri, "Some aspects of machining with negative rake tools simulating grinding," *Int. J. Mach. tool Des. …*, vol. 11, pp. 223–233, 1971.

[36] R. Komanduri, N. Chandresekaran, and L. M. Raff, "Some aspects of machining with negative-rake tools simulating grinding: A molecular dynamics simulation approach," *Philos. Mag.*, vol. 79, no. 7, 1999.

[37] M. Moneim, A. Nasser, and A. Mahboud, "A fundamental study of cutting employing orthogonal negative rake tools," *Wear*, vol. 85, pp. 171–180, 1983.

[38] N. Fang, "Tool-chip friction in machining with a large negative rake angle tool," *Wear*, vol. 258, no. 5–6, pp. 890–897, Feb. 2005.

[39] Y. Ohbuchi and T. Obikawa, "Finite Element Modeling of Chip Formation in the Domain of Negative Rake Angle Cutting," *J. Eng. Mater. Technol.*, vol. 125, no. 3, p. 324, 2003.

[40] Y. Ohbuchi and T. Matsuo, "Force and chip formation in single-grit orthogonal cutting with shaped cBN and diamond grains," *CIRP Ann. Technol.*, vol. 40, pp. 7–10, 1991.

[41] M. Shaw, "Energy Conversion in Cutting and Grinding*," *CIRP Ann. Technol.*, vol. 45, pp. 101–104, 1996.

[42] K. Nakayama, J. Takagi, and T. Abe, "Grinding wheel with helical grooves - an attempt to improve the grinding performance," *Manuf Technol, Gen Assem CIRP, 27th*, vol. 26, no. 1, pp. 133–138, 1977.

[43] I. Marinescu, M. Hitchiner, E. Uhlmann, W. B. Rowe, and I. Inasaki, *Handbook of Machining with Grinding Wheels*, 2nd ed. Taylor & Francis Group, 2016.

[44] S. Ghosh, a. B. Chattopadhyay, and S. Paul, "Modelling of specific energy requirement during high-efficiency deep grinding," *Int. J. Mach. Tools Manuf.*, vol. 48, no. 11, pp. 1242–1253, Sep. 2008.

[45] Z. B. Hou and R. Komanduri, "On the mechanics of the grinding process – Part I. Stochastic nature of the grinding process," *Int. J. Mach. Tools Manuf.*, vol. 43, no. 15, pp. 1579–1593,

Dec. 2003.

[46] W. R. Backer, E. R. Marshall, and M. C. Shaw, "The size effect in Metal cutting," *Trans. Asme*, vol. 74, no. 1, 1952.

[47] M. Shaw, "The size effect in metal cutting," *Sadhana*, vol. 28, no. October, pp. 875–896, 2003.

[48] D. Dinesh, S. Swaminathan, S. Chandresekar, and T. N. Farris, "An instrinsic size effect in machining due to the strain gradient," *Proc. ASME IMECE*, pp. 197–204, 2001.

[49] S. S. Joshi and S. N. Melkote, "An Explanation for the Size-Effect in Machining Using Strain Gradient Plasticity," *J. Manuf. Sci. Eng.*, vol. 126, no. 4, p. 679, 2004.

[50] N. a. Stelmashenko, M. G. Walls, L. M. Brown, and Y. V. Milman, "Microindentations on W and Mo oriented single crystals: An STM study," *Acta Metall. Mater.*, vol. 41, no. 10, pp. 2855–2865, Oct. 1993.

[51] W. Nix and H. Gao, "Indentation size effects in crystalline materials: a law for strain gradient plasticity," *J. Mech. Phys. Solids*, vol. 46, no. 3, 1998.

[52] W. W. Gerberich, N. I. Tymiak, J. C. Grunlan, M. F. Horstemeyer, and M. I. Baskes, "Interpretations of Indentation Size Effects," *J. Appl. Mech.*, vol. 69, no. 4, p. 433, 2002.

[53] W. B. Rowe and X. Chen, "Characterization of the size effect in grinding and the sliced bread analogy," *Int. J. Prod. Res.*, vol. 35, no. 3, pp. 887–889, 1997.

[54] T. Matsuo, S. Toyoura, E. Oshima, and Y. Ohbuchi, "Effect of Grain Shape on Cutting Force in Superabrasive Single-Grit Tests," *CIRP Ann. - Manuf. Technol.*, vol. 38, no. 1, pp. 323–326, Jan. 1989.

[55] D. Graham and R. M. Baul, "An Investigation into the Mode of Metal Removal in the Grinding Process," *Wear*, vol. 19, no. 3, pp. 301–314, 1972.

[56] Y. Kita, M. Ido, and S. Hata, "The mechanism of metal removal by an abrasive tool," *Wear*, vol. 47, pp. 185–193, 1978.

[57] D. Anderson, A. Warkentin, and R. Bauer, "Experimental and numerical investigations of single abrasive-grain cutting," *Int. J. Mach. Tools Manuf.*, vol. 51, no. 12, pp. 898–910, 2011.

[58] J. Tang, J. Du, and Y. Chen, "Modeling and experimental study of grinding forces in surface grinding," *J. Mater. Process. Technol.*, vol. 209, no. 6, pp. 2847–2854, 2009.

[59] K. Brach, D. Pai, E. Ratterman, and M. C. Shaw, "Grinding forces and energy," *J. Eng. Ind.*, vol. 110, no. 87, pp. 25–31, 1988.

[60] C. Yao, T. Wang, W. Xiao, X. Huang, and J. Ren, "Experimental study on grinding force and grinding temperature of Aermet 100 steel in surface grinding," *J. Mater. Process. Technol.*, vol. 214, no. 11, pp. 2191–2199, 2014.

[61] D. A. Doman, A. Warkentin, and R. Bauer, "Finite element modeling approaches in grinding," *Int. J. Mach. Tools Manuf.*, vol. 49, no. 2, pp. 109–116, Feb. 2009.

[62] C. Guo, Z. Shi, H. Attia, and D. Mcintosh, "Power and wheel wear for grinding nickel alloy with plated CBN wheels," *CIRP Ann. - Manuf. Technol.*, vol. 56, no. 1, pp. 343–346, 2007.

[63] R. S. Hahn, "On the Mechanics of the Grinding Process Under Plunge Cut Conditions," *J. Eng. Ind.*, vol. 88, no. 1, pp. 72–79, 1966.

[64] U. S. Patnaik Durgumahanti, V. Singh, and P. Venkateswara Rao, "A New Model for Grinding Force Prediction and Analysis," *Int. J. Mach. Tools Manuf.*, vol. 50, no. 3, pp. 231–240, 2010.

[65] G. Q. Cai, B. F. Feng, T. Jin, and Y. D. Gong, "Study on the friction coefficient in grinding," *J. Mater. Process. Technol.*, vol. 129, no. 1–3, pp. 25–29, 2002.

[66] G. Subhash and W. Zhang, "Investigation of the overall friction coefficient in single-pass scratch test," *Wear*, vol. 252, pp. 123–134, 2002.

[67] J. S. Kwak, S. B. Sim, and Y. D. Jeong, "An analysis of grinding power and surface roughness in external cylindrical grinding of hardened SCM440 steel using the response surface method," *Int. J. Mach. Tools Manuf.*, vol. 46, no. 3–4, pp. 304–312, 2006.

[68] X. Chen, W. B. Rowe, D. R. Allanson, and B. Mills, "A Grinding Power Model for Selection of Dressing and Grinding Conditions," *J. Manuf. Sci. Eng.*, vol. 121, no. 4, p. 632, 1999.

[69] E. Brinksmeier, J. C. Aurich, E. Govekar, C. Heinzel, H.-W. Hoffmeister, F. Klocke, J. Peters, R. Rentsch, D. J. Stephenson, E. Uhlmann, K. Weinert, and M. Wittmann, "Advances in Modeling and Simulation of Grinding Processes," *CIRP Ann. - Manuf. Technol.*, vol. 55, no. 2,

pp. 667–696, Jan. 2006.

[70] G. S. Reichenbach, "The Role of Chip Thickness in Grinding," *Trans. Asme1*, vol. 78, no. 8, p. 23, 1956.

[71] M. C. Shaw, "Interpretation of Grinding Data," Carnegie-Mellow University, 1971.

[72] G. Warnecke and U. Zitt, "Kinematic Simulation for Analyzing and Predicting High-Performance Grinding Processes," *CIRP Ann. - Manuf. Technol.*, vol. 47, pp. 265–270, 1998.

[73] R. L. Hecker, I. M. Ramoneda, and S. Y. Liang, "Analysis of Wheel Topography and Grit Force for Grinding Process Modeling," *J. Manuf. Process.*, vol. 5, no. 1, pp. 13–23, 2003.

[74] R. L. Hecker, S. Y. Liang, X. J. Wu, P. Xia, and D. G. W. Jin, "Grinding force and power modeling based on chip thickness analysis," *Int. J. Adv. Manuf. Technol.*, vol. 33, pp. 449–459, 2007.

[75] H. C. Chang and J. J. J. Wang, "A stochastic grinding force model considering random grit distribution," *Int. J. Mach. Tools Manuf.*, vol. 48, no. 12–13, pp. 1335–1344, 2008.

[76] R. Snoeys, J. Peters, and A. Decneut, "The significance of chip thickness in grinding," *Ann. CIRP*, vol. 23, no. 2, pp. 227–237, 1974.

[77] L. Lichun, F. Jizai, and J. Peklenik, "A Study of Grinding Force Mathematical Model," *CIRP Ann. - Manuf. Technol.*, vol. 29, no. 1, pp. 245–249, 1980.

[78] M. Younis, M. M. Sadek, and T. El-Wardani, "A New Approach to Development of a Grinding Force Model," *J. Eng. Ind.*, vol. 109, no. 4, p. 306, 1987.

[79] T. G. Bifano and S. C. Fawcettt, "Specific grinding energy as an in-process control variable for ductile-regime grinding," *Precis. Eng.*, vol. 13, no. 4, pp. 256–262, 1991.

[80] V. Singh, P. Venkateswara Rao, and S. Ghosh, "Development of specific grinding energy model," *Int. J. Mach. Tools Manuf.*, vol. 60, pp. 1–13, 2012.

[81] T. W. Hwang, C. J. Evans, and S. Malkin, "High Speed Grinding of Silicon Nitride With Electroplated Diamond Wheels, Part 2: Wheel Topography and Grinding Mechanisms," *J. Manuf. Sci. Eng.*, vol. 122, no. 1, p. 42, 2000.

[82] R. S. Hahn, "The relation between grinding conditions and thermal damage in the workpiece," *Trans. Asme*, vol. 78, pp. 807–812, 1956.

[83] P. G. Werner, M. A. Younis, and R. Schlingersiepen, "Creep feed - an effective method to reduce work surface temperatures in high efficiency grinding processes," in *Proceedings of the 8th North American Manufacturing Research Conference*, 1980, p. 132.

[84] S. Malkin and C. Guo, "Thermal Analysis of Grinding," *CIRP Ann. - Manuf. Technol.*, vol. 56, no. 2, pp. 760–782, Jan. 2007.

[85] C. Guo and S. Malkin, "Analytical and Experimental Investigation of Burnout in Creep-Feed Grinding," *CIRP Ann. - Manuf. Technol.*, vol. 43, no. 1, pp. 283–286, 1994.

[86] K. Wegener, F. Bleicher, P. Krajnik, H. Hoffmeister, and C. Brecher, "Recent developments in grinding machines," *CIRP Ann. - Manuf. Technol.*, vol. 66, no. 2, pp. 779–802, 2017.

[87] H. Tönshoff, T. Friemuth, and J. Becker, "Process monitoring in grinding," *CIRP Ann. …*, 2002.

[88] J. Kopac and P. Krajnik, "High-performance grinding—A review," *J. Mater. Process. Technol.*, vol. 175, no. 1–3, pp. 278–284, Jun. 2006.

[89] J. Takagi and M. Liu, "Fracture Characteristics of Grain Cutting Edges of CBN Wheel in Truing Operation," *J. Mater. Process. Technol.*, vol. 0136, no. 62, pp. 367–402, 1996.

[90] A. Azizi, S. M. Rezaei, and A. Rahimi, "Study on the rotary cup dressing of CBN grinding wheel and the grinding performance," *Int. J. Adv. Manuf. Technol.*, vol. 47, no. 9–12, pp. 1053–1063, 2010.

[91] F. Klocke, a. Baus, and T. Beck, "Coolant Induced Forces in CBN High Speed Grinding with Shoe Nozzles," *CIRP Ann. - Manuf. Technol.*, vol. 49, no. 1, pp. 241–244, Jan. 2000.

[92] R. P. Upadhyaya and J. H. Fiecoat, "Factors affecting grinding performance with electroplated CBN wheels," *CIRP Ann. - Manuf. Technol.*, vol. 56, no. 1, pp. 339–342, 2007.

[93] Q. Liu, X. Chen, and N. Gindy, "Assessment of Al2O3 and superabrasive wheels in nickel-based alloy grinding," *Int. J. Adv. Manuf. Technol.*, vol. 33, no. 9–10, pp. 940–951, 2007.

[94] Z. Shi, A. Elfizy, B. St-Pierre, and H. Attia, "Experimental Study on Grinding of a Nickel-Based Alloy Using Vitrified CBN Wheels," *Adv. Mater. Res.*, vol. 325, pp. 134–139, 2011.

[95]   R. Hood, P. Cooper, D. K. Aspinwall, S. L. Soo, and D. S. Lee, "Creep feed grinding of gamma-TiAl using single layer electroplated diamond superabrasive wheels," *CIRP J. Manuf. Sci. Technol.*, vol. 11, pp. 36–44, 2015.

[96]   M. J. Jackson, B. Mills, and M. P. Hitchiner, "Controlled wear of vitrified abrasive materials for precision grinding applications," *Sadhana*, vol. 28, no. 5, pp. 897–914, 2003.

[97]   J. N. Brecker, "The Fracture Strength of Abrasive Grains," *J. Eng. Ind.*, no. November 1974, pp. 1253–1257, 1974.

[98]   L. Godino, I. Pombo, J. A. Sanchez, and J. Alvarez, "On the development and evolution of wear flats in microcrystalline sintered alumina grinding wheels," *J. Manuf. Process.*, vol. 32, pp. 494–505, 2018.

[99]   U. Madopothula and V. Lakshmanan, "Time dependent behavior of alumina grains manufactured by two different routes while grinding of AISI 52100 steels," *Arch. Civ. Mech. Eng.*, vol. 17, no. 2, pp. 400–409, 2016.

[100]   D. Selvakumaran, N. Arunachalam, L. Vijayaraghavan, and A. S. . Balan, "Performance Comparison of Duplex Sol-gel Stainless with White Alumina Abrasives for Grinding of Super Steel (SDSS)," *Procedia Manuf.*, vol. 26, pp. 1448–1458, 2018.

[101]   A. Krell, P. Blank, E. Wagner, and G. Bartels, "Advances in the Grinding Efficiency of Sintered Alumina Abrasives," *J. Am. Ceram. Soc.*, vol. 79, no. 3, pp. 763–769, 1996.

[102]   J. a. Badger, "Microfracturing Ceramic Abrasive in Grinding," *ASME 2012 Int. ...*, no. 3, pp. 1–9, 2012.

[103]   H. Frantisek, B. Martin, D. Milan, and R. Jan, "Application of New Abrasives and their Quality Parameters," *Solid State Phenom.*, vol. 261, pp. 181–188, 2017.

[104]   E. García, D. Méresse, I. Pombo, S. Harmand, and J. Antonio, "Identification of heat partition in grinding related to process parameters , using the inverse heat fl ux conduction model," *Appl. Therm. Eng.*, vol. 66, no. 1–2, pp. 122–130, 2014.

[105]   C. Nizankowski, G. Struzikiewicz, and A. Matras, "Simulation Roughness of the Steel Rollers' Surface Layer with Cubitron II Grinding Wheels by the Quickpoint Technique," *J. Mach. Eng.*, vol. 17, no. 4, pp. 54–68, 2017.

[106]   D. Setti, S. Ghosh, and P. V. Rao, "A method for prediction of active grits count in surface grinding," *Wear*, vol. 382–383, no. March, pp. 71–77, 2017.

[107]   H. N. Li, T. B. Yu, Z. X. Wang, L. Da Zhu, and W. S. Wang, "Detailed modeling of cutting forces in grinding process considering variable stages of grain-workpiece micro interactions," *Int. J. Mech. Sci.*, vol. 126, no. May 2016, pp. 319–339, 2017.

[108]   Y. Namba, H. Kobayashi, H. Suzuki, K. Yamashita, and N. Taniguchi, "Ultraprecision Surface Grinding of Chemical Vapor Deposited Silicon Carbide for X-Ray Mirrors Using Resinoid-Bonded Diamond Wheels," *CIRP Ann. - Manuf. Technol.*, vol. 48, no. 1, pp. 277–280, 1999.

[109]   I. Inasaki and K. Nakayama, "High-Efficiency Grinding of Advanced Ceramics," *CIRP Ann. - Manuf. Technol.*, vol. 35, no. 1, pp. 211–214, 1986.

[110]   J. P. Davim, *Machining: Fundamentals and Recent Advances*, 1st ed. Springer Science & Business Media, 2008.

[111]   R. K. . Shiue, S. T. . Buljan, and T. W. . Eagar, "Abrasion resistant active braze alloys for metal single layer technology," *Sci. Technol. Weld. Join.*, vol. 2, no. 2, pp. 71–78, 1997.

[112]   J. Yang, D. Y. Kim, and H. Y. Kim, "Effect of glass composition on the strength of vitreous bonded c-BN grinding wheels," *Ceram. Int.*, vol. 19, no. 2, pp. 87–92, 1993.

[113]   H. J. Kim, S. S. Ryu, S. Kim, and H. T. Kim, "Mechanical properties of new vitrified bonds for cBN grinding wheel," *Int. J. Precis. Eng. Manuf.*, vol. 10, no. 3, pp. 13–17, 2009.

[114]   K. H. Lin, S. F. Peng, and S. T. Lin, "Sintering parameters and wear performances of vitrified bond diamond grinding wheels," *Int. J. Refract. Met. Hard Mater.*, vol. 25, no. 1, pp. 25–31, 2007.

[115]   J. F. G. de Oliveira and D. A. Dornfeld, "Dimensional Characterization of Grinding Wheel Surface through Acoustic Emission," *CIRP Ann. - Manuf. Technol.*, vol. 43, no. 1, pp. 291–294, 1994.

[116]   D. P. Saini, "Wheel hardness and local elastic deflections in grinding," *Int. J. Mach. Tools Manuf.*, vol. 30, no. 4, pp. 637–649, 1990.

[117] D. Herman and J. Krzos, "Influence of vitrified bond structure on radial wear of cBN grinding wheels," *J. Mater. Process. Technol.*, vol. 209, no. 14, pp. 5377–5386, 2009.

[118] F. Engineer, S. Malkin, and C. Guo, "Experimental Measurement of Fluid Flow Through the Grinding Zone," *J. Eng. Ind.*, vol. 114, no. 1, pp. 61–66, 1992.

[119] M. N. Morgan, A. R. Jackson, H. Wu, V. Baines-jones, A. Batako, and W. B. Rowe, "Optimisation of fluid application in grinding," *CIRP Ann. - Manuf. Technol.*, vol. 57, no. 1, pp. 363–366, 2008.

[120] X. Chen, W. B. Rowe, and R. Cai, "Precision grinding using CBN wheels," *Int. J. Mach. Tools Manuf.*, vol. 42, no. 5, pp. 585–593, 2002.

[121] G. Stetiu and G. K. Lal, "Wear of grinding wheels," *Wear*, vol. 30, no. 2, pp. 229–236, 1974.

[122] S. Malkin and N. H. Cook, "The Wear of Grinding Wheels Part 1- Attritious wear," *J. Eng. Ind.*, vol. 93, no. 4, pp. 1129–1133, 1971.

[123] P. L. Tso, "Study on the grinding of Inconel 718," *J. Mater. Process. Tech.*, vol. 55, no. 3–4, pp. 421–426, 1995.

[124] X. Chen, B. Rowe, B. Mills, and D. R. Allanson, "Analysis and Simulation of the Grinding Process Part IV: Effects of Wheel Wear," *Int. J. Mach. Tools Manuf.*, vol. 38, no. 1–2, pp. 41–49, 1998.

[125] M. J. Jackson, "Fracture dominated wear of sharp abrasive grains and grinding wheels," *Proc. Inst. Mech. Eng. Part J J. Eng. Tribol.*, vol. 218, no. 3, pp. 225–235, 2004.

[126] Sunarto and Y. Ichida, "Creep feed profile grinding of Ni-based superalloys with ultrafine-polycrystalline cBN abrasive grits," *Precis. Eng.*, vol. 25, no. 4, pp. 274–283, 2001.

[127] H. Yoshikawa and T. Sata, "Study on Wear of Grinding Wheels: 1—Bond Fracture in Grinding Wheels," *J. Eng. Ind.*, vol. 85, no. 1, pp. 39–42, 1963.

[128] T. C. Buttery, A. Statham, J. B. Percival, and M. S. Hamed, "Some effects of dressing on grinding performance," *Wear*, vol. 55, no. 2, pp. 195–219, 1979.

[129] J. Badger, "Manufacturing Technology Factors affecting wheel collapse in grinding," *CIRP Ann.*, vol. 58, pp. 307–310, 2009.

[130] 3M, *Handbook: Surface Grinding*. Meerbusch, Germany: 3M Abrasive Systems Division, 2015.

[131] Y. Novoselov, S. Bratan, and V. Bogutsky, "Analysis of Relation between Grinding Wheel Wear and Abrasive Grains Wear," *Procedia Eng.*, vol. 150, pp. 809–814, 2016.

[132] M. K. Krueger, S. C. Yoon, D. G. Milacron, R. J. P. Oak, and R. National, "New Technology in Metalworking Fluids and Grinding Wheels Achieves Tenfold Improvement in Grinding Performance," 2000.

[133] W. L. Cooper and A. S. Lavine, "Grinding Process Size Effect and Kinematics Numerical Analysis," *J. Manuf. Sci. Eng.*, vol. 122, no. February 2000, pp. 59–69, 2001.

[134] Y. Ohbuchi and T. Obikawa, "Surface generation model in grinding with effect of grain shape and cutting speed," *JSME Int. J. Ser. C*, vol. 49, no. 1, pp. 114–120, 2006.

[135] Y. Liu, a. Warkentin, R. Bauer, and Y. Gong, "Investigation of different grain shapes and dressing to predict surface roughness in grinding using kinematic simulations," *Precis. Eng.*, vol. 37, no. 3, pp. 758–764, 2013.

[136] A. A. Torrance and J. A. Badger, "Relation between the traverse dressing of vitrified grinding wheels and their performance," *Int. J. Mach. Tools Manuf.*, vol. 40, no. 12, pp. 1787–1811, 2000.

[137] A. Saad, R. Bauer, and A. Warkentin, "Investigation of single-point dressing overlap ratio and diamond-roll dressing interference angle on surface roughness in grinding," *Trans. Can. Soc. Mech. Eng.*, vol. 34, no. 2, pp. 295–308, 2010.

[138] I. Pombo, X. Cearsolo, J. A. Sánchez, and I. Cabanes, "Experimental and numerical analysis of thermal phenomena in the wear of single point diamond dressing tools," *J. Manuf. Process.*, vol. 27, pp. 145–157, 2017.

[139] A. Kubo, A. M. M. S. Ullah, and J. Tamaki, "Computer-aided simulation of dressing using diamond rotary dresser and visualization of dressing process," *Adv. Mater. Res.*, vol. 1017, pp. 592–597, 2014.

[140] C. Guo, M. Campomanes, D. McIntosh, C. Becze, and S. Malkin, "Model-based monitoring

and control of continuous dress creep-feed form grinding," *CIRP Ann. - Manuf. Technol.*, vol. 53, no. 1, pp. 263–266, 2004.

[141] C. Guo, M. Campomanes, D. Mcintosh, C. Becze, and T. Green, "Optimization of Continuous Dress Creep-Feed Form Grinding Process," *CIRP Ann.*, vol. 52, no. 1, pp. 259–262, 2003.

[142] K. Wegener, H. W. Hoffmeister, B. Karpuschewski, F. Kuster, W. C. Hahmann, and M. Rabiey, "Conditioning and monitoring of grinding wheels," *CIRP Ann. - Manuf. Technol.*, vol. 60, no. 2, pp. 757–777, 2011.

[143] J. A. Kirk, "An Evaluation of Grinding Performance for Single and Polycrystal Grit Aluminium-Oxide Grinding Wheels," *J. Eng. Ind.*, no. February 1976, pp. 189–195, 1976.

[144] H. Baseri, "Simulated annealing based optimization of dressing conditions for increasing the grinding performance," *Int. J. Adv. Manuf. Technol.*, vol. 59, no. 5–8, pp. 531–538, 2012.

[145] S. Malkin and R. B. Anderson, "Active grains and dressing particles in grinding," in *Proc. Int. Grinding Conf., Pittsburgh.*, 1972.

[146] X. Chen and W. Rowe, "Analysis and simulation of the grinding process. Part I: generation of the grinding wheel surface," *Int. J. Mach. Tools …*, vol. 36, no. 8, pp. 871–882, 1996.

[147] S. Malkin and T. Murray, "Mechanics of Rotary Dressing of Grinding Wheels," *J. Eng. Ind.*, vol. 100, no. 1, pp. 95–102, 1978.

[148] T. Murray and S. Malkin, "Effects of Rotary Dressing on Grinding Wheel Performance," *J. Eng. Ind.*, vol. 100, no. 3, pp. 297–302, 1978.

[149] M. A. K. Chowdhury, A. Kubo, J. Tamaki, and A. M. M. S. Ullah, "Computer-aided Simulation of Rotary Diamond Dressing Based on Kinematic Analysis," *J. Adv. Mech. Des. Syst. Manuf.*, vol. 7, no. 4, pp. 506–520, 2013.

[150] H. Baseri, S. M. Rezaei, A. Rahimi, and M. Saadat, "Analysis of the Disc Dressing Effects on Grinding Performance—Part 1: Simulation of the Disc Dressed Wheel Surface," *Mach. Sci. Technol.*, vol. 12, no. 2, pp. 183–196, 2008.

[151] H. Baseri, S. M. Rezaei, A. Rahimi, and M. Saadat, "Analysis of the Disc Dressing Effects on Grinding Performance—Part 2: Effects of the Wheel Topographical Parameters on the Specific Energy and Workpiece Surface Roughness," *Mach. Sci. Technol.*, vol. 12, no. 2, pp. 183–196, 2008.

[152] B. Linke, "Dressing process model for vitrified bonded grinding wheels," *CIRP Ann. - Manuf. Technol.*, vol. 57, no. 1, pp. 345–348, 2008.

[153] F. Klocke and B. Linke, "Mechanisms in the generation of grinding wheel topography by dressing," *Prod. Eng.*, vol. 2, no. 2, pp. 157–163, 2008.

[154] X. Chen, "Strategy for the Selection of Grinding Wheel Dressing Conditions," Liverpool John Moores University, 1995.

[155] F. Klocke, J. Thiermann, and P. Mattfeld, "Influence of the dressing process on grinding wheel wear," *Prod. Eng.*, vol. 9, no. 5–6, pp. 563–568, 2015.

[156] A. Warkentin, R. Bauer, and S. Sultana, "Novel Instrumentation for Measuring the Effect of Dressing Conditions on Wheel Wear," in *IMAC-XXIII: Conference & Exposition on Structural Dynamics*, 2005.

[157] Z. Prusak, J. A. Webster, and I. D. Marinescu, "Influence of Dressing Parameters on Grinding Performance of CBN / Seeded Gel Hybrid Wheels in Cylindrical Grinding," *Int. J. Prod. Res.*, vol. 35, no. 10, pp. 2899–2915, 1997.

[158] A. T. Nguyen and D. L. Butler, "Correlation of grinding wheel topography and grinding performance: A study from a viewpoint of three-dimensional surface characterisation," *J. Mater. Process. Technol.*, vol. 208, no. 1–3, pp. 14–23, 2008.

[159] D. L. Butler, L. . Blunt, B. . See, J. . Webster, and K. . Stout, "The characterisation of grinding wheels using 3D surface measurement techniques," *J. Mater. Process. Technol.*, vol. 127, no. 2, pp. 234–237, 2002.

[160] E. J. Salisbury, K. V. Domala, K. S. Moon, M. H. Miller, and J. W. Sutherland, "A Three-Dimensional Model for the Surface Texture in Surface Grinding, Part 2: Grinding Wheel Surface Texture Model," *J. Manuf. Sci. Eng.*, vol. 123, no. 4, p. 582, 2001.

[161] A. Koziarski and A. Golabczak, "The Assessment of the Grinding Wheel Cutting Surface Condition after Dressing with the Single Point Diamond Dresser," *Int. J. Mach. Tool Des. Res*,

vol. 25, no. 4, pp. 313–325, 1985.

[162] R. M. Baul, D. Graham, and W. Scott, "Characterization of the working surface of abrasive wheels," *Tribology*, vol. 5, no. 4, pp. 169–176, 1972.

[163] X. Zhou and F. Xi, "Modeling and predicting surface roughness of the grinding process," *Int. J. Mach. Tools Manuf.*, vol. 42, no. 8, pp. 969–977, Jun. 2002.

[164] E. Brinksmeler and a. Glwerzew, "Chip Formation Mechanisms in Grinding at Low Speeds," *CIRP Ann. - Manuf. Technol.*, vol. 52, no. I, pp. 253–258, 2003.

[165] R. Cai and W. B. Rowe, "Assessment of vitrified CBN wheels for precision grinding," *Int. J. Mach. Tools Manuf.*, vol. 44, no. 12–13, pp. 1391–1402, 2004.

[166] R. Cai, "Assessment of vitrified CBN wheels for precision grinding," 2002.

[167] H. Baseri, "Modeling of grinding wheel sharpness by using neural network," *Proc. 11th Int. Conf. Comput. Syst. Technol. Work. PhD Students Comput. Int. Conf. Comput. Syst. Technol. - CompSysTech '10*, p. 205, 2010.

[168] R. St. Gelais, "Investigation into the Characterization and Generation of Grinding Wheel Sharpness in Diamond Roll Plunge Dressing," Worcester Polytechnic Institute, 2006.

[169] I. Inasaki, "Grinding Process Simulation Based on the Wheel Topography Measurement," *CIRP Ann. - Manuf. Technol.*, vol. 45, no. 1, pp. 347–350, 1996.

[170] C. Woodin, H. Malshe, and S. Melkote, "Effects of single point dressing on seeded gel grinding wheel surface topography," in *ASME 2014 International Manufacturing Science and Engineering Conference, MSEC 2014 Collocated with the JSME 2014 International Conference on Materials and Processing and the 42nd North American Manufacturing Research Conference*, 2014, vol. 2, pp. 1–10.

[171] L. Yan, Y. M. Rong, F. Jiang, and Z. X. Zhou, "Three-dimension surface characterization of grinding wheel using white light interferometer," *Int. J. Adv. Manuf. Technol.*, vol. 55, no. 1–4, pp. 133–141, 2011.

[172] K. J. Stout and L. Blunt, *Three Dimensional Surface Topography*. Elsevier, 2000.

[173] N. Arunachalam and B. Ramamoorthy, "Texture analysis for grinding wheel wear assessment using machine vision," *Proc. Inst. Mech. Eng. Part B J. Eng. Manuf.*, vol. 221, no. 3, pp. 419–430, 2007.

[174] E. Altıntaş and E. Güngör, "Alternative Surface Roughness Measurement Technique for Inaccessible Surfaces of Jet Engine Parts Using the Rubber Silicon Replica Method," *Metallogr. Microstruct. Anal.*, vol. 2, no. 5, pp. 337–342, 2013.

[175] D. Bhaduri, S. L. Soo, D. Novovic, D. K. Aspinwall, P. Harden, C. Waterhouse, S. Bohr, a. C. Mathieson, and M. Lucas, "Ultrasonic assisted creep feed grinding of Inconel 718," *Procedia CIRP*, vol. 6, pp. 615–620, 2013.

[176] A. Darafon, "Measuring and Modeling of Grinding Wheel Topography," Dalhousie University, Halifax Nova Scotia, 2013.

[177] L. Nilsson and R. Ohlsson, "Accuracy of replica materials when measuring engineering surfaces," *Int. J. Mach. Tools Manuf.*, vol. 41, no. 13–14, pp. 2139–2145, 2001.

[178] J. F. G. de Oliveira, R. T. Coelho, and C. K. Neto, "Development of an Optical Scanner To Study Wear on the Working Surface of Grinding Wheels," *Mach. Sci. Technol.*, vol. 3, no. 2, pp. 239–253, 1999.

[179] H. T. Young and D. J. Chen, "Online dressing of profile grinding wheels," *Int. J. Adv. Manuf. Technol.*, vol. 27, no. 9–10, pp. 883–888, 2006.

[180] H. Hamdi, M. Dursapt, and H. Zahouani, "Characterization of abrasive grain's behavior and wear mechanisms," *Wear*, vol. 254, no. 12, pp. 1294–1298, 2003.

[181] F. Klocke, C. Wrobel, M. Rasim, and P. Mattfeld, "Approach of Characterization of the Grinding Wheel Topography as a Contribution to the Energy Modelling of Grinding Processes," *Procedia CIRP*, vol. 46, pp. 631–635, 2016.

[182] Y. Xie and J. A. Williams, "The generation of worn surfaces by the repeated parallel grooves interaction of," *Wear*, vol. 164, pp. 864–872, 1993.

[183] M. Rasim, P. Mattfeld, and F. Klocke, "Analysis of the grain shape influence on the chip formation in grinding," *J. Mater. Process. Tech.*, vol. 226, pp. 60–68, 2015.

[184] I. Zarudi and L. C. Zhang, "A revisit to some wheel – workpiece interaction problems in

surface grinding," *Int. J. Mach. Tools Manuf.*, vol. 42, no. 2002, pp. 905–913, 2006.

[185] T. Warren Liao, "Feature extraction and selection from acoustic emission signals with an application in grinding wheel condition monitoring," *Eng. Appl. Artif. Intell.*, vol. 23, no. 1, pp. 74–84, 2010.

[186] T. W. Liao, F. Tang, J. Qu, and P. J. Blau, "Grinding wheel condition monitoring with boosted minimum distance classifiers," *Mech. Syst. Signal Process.*, vol. 22, no. 1, pp. 217–232, 2008.

[187] T. Warren Liao, C. F. Ting, J. Qu, and P. J. Blau, "A wavelet-based methodology for grinding wheel condition monitoring," *Int. J. Mach. Tools Manuf.*, vol. 47, no. 3–4, pp. 580–592, 2007.

[188] J. K. Tien, *Superalloys, Supercomposites and Superceramics*. Elsevier, 2012.

[189] E. O. Ezugwu, Z. M. Wang, and a. R. Machado, "The machinability of nickel-based alloys: a review," *J. Mater. Process. Technol.*, vol. 86, no. 1–3, pp. 1–16, Feb. 1999.

[190] K. P. L. Fullagar, R. W. Broomfield, M. Hulands, K. Harris, G. L. Erickson, and S. L. Sikkenga, "Aero Engine Test Experience With CMSX-4® Alloy Single-Crystal Turbine Blades," *J. Eng. Gas Turbines Power*, vol. 118, no. April 1996, p. 380, 1996.

[191] N. Matan, D. C. Cox, P. Carter, M. a. Rist, C. M. F. Rae, and R. C. Reed, "42-Creep of CMSX-4 superalloy single crystals: effects of misorientation and temperature," *Acta Mater.*, vol. 47, no. 5, pp. 1549–1563, 1999.

[192] V. Sass, U. Glatzel, and M. Feller-Kniepmeier, "Anisotropic creep properties of the nickel-base superalloy CMSX-4," *Acta Mater.*, vol. 44, no. 5, pp. 1967–1977, 1996.

[193] J. J. Moverare, S. Johansson, and R. C. Reed, "Deformation and damage mechanisms during thermal-mechanical fatigue of a single-crystal superalloy," *Acta Mater.*, vol. 57, no. 7, pp. 2266–2276, 2009.

[194] M. Okazaki and M. Sakaguchi, "Thermo-mechanical fatigue failure of a single crystal Ni-based superalloy," *Int. J. Fatigue*, vol. 30, pp. 318–323, 2008.

[195] B. Baufeld, M. Bartsch, and M. Heinzelmann, "Advanced thermal gradient mechanical fatigue testing of CMSX-4 with an oxidation protection coating," *Int. J. Fatigue*, vol. 30, pp. 219–225, 2008.

[196] M. Ott and H. Mughrabi, "Dependence of the high-temperature low-cycle fatigue behaviour of the monocrystalline nickel-base superalloys CMSX-4 and CMSX-6 on the γ/γ′-morphology," *Mater. Sci. Eng. A*, vol. 272, pp. 24–30, 1999.

[197] T. A. Egly, K. H. Lang, and D. Löhe, "Influence of phase shift and strain path on the thermomechanical fatigue behavior of CMSX-4 specimens," *Int. J. Fatigue*, vol. 30, pp. 249–256, 2008.

[198] A. Ma, D. Dye, and R. C. Reed, "A model for the creep deformation behaviour of single-crystal superalloy CMSX-4," *Acta Mater.*, vol. 56, pp. 1657–1670, 2008.

[199] R. C. Reed, N. Matan, D. C. Cox, M. a. Rist, and C. M. F. Rae, "Creep of CMSX-4 superalloy single crystals: effects of rafting at high temperature," *Acta Mater.*, vol. 47, no. 12, pp. 3367–3381, 1999.

[200] W. D. Callister Jr, *Materials Science and Engineering An Introduction*, 7th ed. New York: John Wiley & Sons, 2007.

[201] T. M. Pollock and S. Tin, "Nickel-Based Superalloys for Advanced Turbine Engines: Chemistry, Microstructure and Properties," *J. Propuls. Power*, vol. 22, no. 2, pp. 361–374, 2006.

[202] A. Sharman, R. Dewes, and D. Aspinwall, "Tool life when high speed ball nose end milling Inconel 718™," *J. Mater. Process. Technol.*, vol. 118, pp. 29–35, 2001.

[203] E. Arzt, "Size effects in materials due to microstructural and dimensional constraints: a comparative review," *Acta Mater.*, vol. 46, no. 16, pp. 5611–5626, Oct. 1998.

[204] D. A. Hughes and N. Hansen, "High angle boundaries formed by grain subdivision mechanisms," *Acta Mater.*, vol. 45, no. 9, pp. 3871–3886, 1997.

[205] S. A. Sajjadi and S. Nategh, "A high temperature deformation mechanism map for the high performance Ni-base superalloy GTD-111," *Mater. Sci. Eng. A*, vol. 307, no. 1–2, pp. 158–164, 2001.

[206] F. I. Versnyder and M. E. Shank, "The development of columnar grain and single crystal high temperature materials through directional solidification," *Mater. Sci. Eng.*, vol. 6, no. 4, pp.

213–247, 1970.

[207] S. Jones and C. Yuan, "Advances in shell moulding for investment casting," *J. Mater. Process. Technol.*, vol. 135, no. 2–3 SPEC., pp. 258–265, 2003.

[208] S. Pattnaik, D. B. Karunakar, and P. K. Jha, "Developments in investment casting process - A review," *J. Mater. Process. Technol.*, vol. 212, no. 11, pp. 2332–2348, 2012.

[209] M. W. H. Pollock T.M., "The breakdown of single crystal solidification in high refractory nickel base alloys," *Met. Mater. Trans. A*, vol. 27A, no. April, pp. 1081–1094, 1996.

[210] C. Beckermann, J. Gu, and W. Boettinger, "Development of a freckle predictor via rayleigh number method for single-crystal nickel-base superalloy castings," *Metall. Mater. Trans. A*, vol. 31, no. 10, pp. 2545–2557, 2000.

[211] L. Liu, T. Huang, M. Qu, G. Liu, J. Zhang, and H. Fu, "High thermal gradient directional solidification and its application in the processing of nickel-based superalloys," *J. Mater. Process. Technol.*, vol. 210, no. 1, pp. 159–165, 2010.

[212] S. F. Gao, L. Liu, N. Wang, X. B. Zhao, J. Zhang, and H. Z. Fu, "Grain Selection During Casting Ni-Base , Single-Crystal Superalloys with Spiral Grain Selector," *Metall. Mater. Trans. A*, vol. 43, no. 10, pp. 3767–3775, 2012.

[213] R. M. Niemi, "Integrity Prediction," *SME Tech. Pap.*, 1971.

[214] S. L. Soo, R. Hood, D. K. Aspinwall, W. E. Voice, and C. Sage, "Machinability and surface integrity of RR1000 nickel based superalloy," *CIRP Ann. - Manuf. Technol.*, vol. 60, pp. 89–92, 2011.

[215] E. O. Ezugwu and S. H. Tang, "Surface abuse when machining cast iron (G-17) and nickel-base superalloy (Inconel 718) with ceramic tools," *J. Mater. Process. Technol.*, vol. 55, no. 2, pp. 63–69, Nov. 1995.

[216] D. Dudzinski, a Devillez, a Moufki, D. Larrouquère, V. Zerrouki, and J. Vigneau, "A review of developments towards dry and high speed machining of Inconel 718 alloy," *Int. J. Mach. Tools Manuf.*, vol. 44, no. 4, pp. 439–456, Mar. 2004.

[217] R. S. Pawade, S. S. Joshi, and P. K. Brahmankar, "Effect of machining parameters and cutting edge geometry on surface integrity of high-speed turned Inconel 718," *Int. J. Mach. Tools Manuf.*, vol. 48, no. 1, pp. 15–28, Jan. 2008.

[218] J. Sun and Y. B. Guo, "A comprehensive experimental study on surface integrity by end milling Ti-6Al-4V," *J. Mater. Process. Technol.*, vol. 209, pp. 4036–4042, 2009.

[219] P. Chevrier, a. Tidu, B. Bolle, P. Cezard, and J. P. Tinnes, "Investigation of surface integrity in high speed end milling of a low alloyed steel," *Int. J. Mach. Tools Manuf.*, vol. 43, pp. 1135–1142, 2003.

[220] A. Devillez, G. Le Coz, S. Dominiak, and D. Dudzinski, "Dry machining of Inconel 718, workpiece surface integrity," *J. Mater. Process. Technol.*, vol. 211, no. 10, pp. 1590–1598, Oct. 2011.

[221] W. Österle and P. X. Li, "Mechanical and thermal response of a nickel-base superalloy upon grinding with high removal rates," *Mater. Sci. Eng. A*, vol. 238, no. 2, pp. 357–366, Nov. 1997.

[222] B. Zhang, W. Shen, Y. Liu, X. Tang, and Y. Wang, "Microstructures of surface white layer and internal white adiabatic shear band," *Wear*, vol. 211, no. 2, pp. 164–168, 1997.

[223] S. S. Bosheh and P. T. Mativenga, "White layer formation in hard turning of H13 tool steel at high cutting speeds using CBN tooling," *Int. J. Mach. Tools Manuf.*, vol. 46, no. 2, pp. 225–233, Feb. 2006.

[224] X. Xu, Y. Yu, and H. Xu, "Effect of grinding temperatures on the surface integrity of a nickel-based superalloy," *J. Mater. Process. Technol.*, vol. 129, no. 1–3, pp. 359–363, Oct. 2002.

[225] M. Chen, F. H. Sun, Y. M. Lee, and S. H. Yang, "Surface Quality Studies with Respect to Grinding Burn of New Typical Nickel-Based Superalloy," *Key Eng. Mater.*, vol. 259–260, pp. 233–238, 2004.

[226] Q. Huang and J. J. Xin, "Surface Intergity and Its Effects on the Fatigue Life on Nickel Based Superalloy GH33A," *Int. J. Fatigue*, vol. 13, no. 4, p. 4, 1991.

[227] C. Ming, L. Xiaotian, S. Fanghong, X. Yucheng, and X. Bingyuan, "Studies on the grinding characteristics of directionally solidified nickel-based superalloy," *J. Mater. Process. Technol.*,

vol. 116, no. 2–3, pp. 165–169, 2001.

[228] Q. Zeng, G. Liu, L. Liu, and Y. Qin, "Investigation into grindability of a superalloy and effects of grinding parameters on its surface integrity," *Proc. Inst. Mech. Eng. Part B J. Eng. Manuf.*, vol. 229, no. 2, pp. 238–250, 2015.

[229] R. M. Arunachalam, M. a. Mannan, and a. C. Spowage, "Surface integrity when machining age hardened Inconel 718 with coated carbide cutting tools," *Int. J. Mach. Tools Manuf.*, vol. 44, no. 14, pp. 1481–1491, Nov. 2004.

[230] C. F. Yao, Q. C. Jin, X. C. Huang, D. X. Wu, J. X. Ren, and D. H. Zhang, "Research on surface integrity of grinding Inconel 718," *Int. J. Adv. Manuf. Technol.*, vol. 65, no. 5–8, pp. 1019–1030, 2013.

[231] Z. Zhong, K. Ramesh, and S. H. Yeo, "Grinding of nickel-based super-alloys and advanced ceramics," *Mater. Manuf. Process.*, vol. 16, no. 2, pp. 195–207, 2001.

[232] S. Huddedar, P. Chitalkar, A. Chavan, and R. . Pawade, "Nickel Based Superalloy Inconel 718," *Journal of Applied Sciences*, vol. 12, no. 10. pp. 947–954, 2012.

[233] A. McDonald, A. M. O. Mohamed, A. Warkentin, and R. J. Bauer, "Kinematic simulation of the uncut chip thickness and surface finish using a reduced set of 3D grinding wheel measurements," *Precis. Eng.*, vol. 49, pp. 169–178, 2017.

[234] A. Darafon, A. Warkentin, and R. Bauer, "3D metal removal simulation to determine uncut chip thickness, contact length, and surface finish in grinding," *Int. J. Adv. Manuf. Technol.*, vol. 66, no. 9–12, pp. 1715–1724, 2013.

[235] S. Chakrabarti and S. Paul, "Numerical Modelling of Surface Topography in Superabrasive Grinding," *Int. J. Adv. Manuf. Technol.*, vol. 39, no. 1–2, pp. 29–38, 2008.

[236] W. Osterle, P. X. Li, and G. Nolze, "Influence of surface finishing on residual stress depth profiles of a coarse-grained nickel-base superalloy," *Mater. Sci. Eng. A*, vol. 262, no. 1, pp. 308–311, 1999.

[237] S. M. H-Gangaraj, G. H. Farrahi, and H. Ghadbeigi, "On The Temperature and Residual Stress Field During Grinding," in *Proceedings of the World Congress on Engineering*, 2010, vol. II.

[238] D. Wenfeng, X. Jiuhua, C. Zhenzhen, S. Honghua, and F. Yucan, "Grindability and Surface Integrity of Cast Nickel-based Superalloy in Creep Feed Grinding with Brazed CBN Abrasive Wheels," *Chinese J. Aeronaut.*, vol. 23, no. 4, pp. 501–510, 2010.

[239] Rolls-Royce, "CME5043 Section 2," no. 3, 2007.

[240] G. F. Van der Voort, *Metallography, principles and practice*. ASM International, 1984.

[241] J. Palmer, H. Ghadbeigi, D. Novovic, and D. Curtis, "An experimental study of the effects of dressing parameters on the topography of grinding wheels during roller dressing," *J. Manuf. Process.*, vol. 31, pp. 348–355, 2018.

[242] T. W. Hwang, C. J. Evans, and S. Malkin, "High Speed Grinding of Silicon Nitride With Electroplated Diamond Wheels, Part 1: Wear and Wheel Life," *J. Manuf. Sci. Eng.*, vol. 122, no. 1, p. 42, 2000.

[243] P. Mathews, *Design of Experiments with Minitab*. Milwaukee: ASQ Quality Press, 2005.

[244] J. Antony, *Design of Experiments for Engineers and Scientists*, 1st ed. Oxford: Butterworth-Heinemann, 2003.

[245] D. R. Cox and N. Reid, *The Theory of the Design of Experiments*, First. Chapman and Hall/CRC, 2000.

[246] D. Montgomery, *Design and Analysis of Experiments*, Third. Singapore: John Wiley & Sons, 1991.

[247] F. C. Hsu, T. Y. Tai, V. N. Vo, S. Y. Chen, and Y. H. Chen, "The machining characteristics of polycrystalline diamond (PCD) by micro-WEDM," *Procedia CIRP*, vol. 6, pp. 261–266, 2013.

[248] Minitab, "What is ANOVA?," *Minitab Inc.*, 2017. [Online]. Available: https://support.minitab.com/en-us/minitab/18/help-and-how-to/modeling-statistics/anova/supporting-topics/basics/what-is-anova/.

[249] W. D. Penny, K. J. Friston, J. T. Ashburner, S. J. Kiebel, and T. E. Nichols, *Statistical Parametric Mapping: The Analysis of Functional Brain Images*, First. London: Elsevier, 2007.

[250] J. Badger, "Evaluation of Triangular , Engineered-Shape Ceramic Abrasive in Cutting Discs," *Weld. J.*, no. April, pp. 107–115, 2014.

[251] Minitab, "Interpret the key results for Fit General Linear Model," 2018. [Online]. Available: https://support.minitab.com/en-us/minitab/18/help-and-how-to/modeling-statistics/anova/how-to/fit-general-linear-model/interpret-the-results/key-results/. [Accessed: 17-Aug-2018].

[252] M. J. Jackson and B. Mills, "Microscale wear of vitrified abrasive materials," *J. Mater. Sci.*, vol. 39, no. 6, pp. 2131–2143, 2004.

[253] C. Zhenzhen, X. Jiuhua, D. Wenfeng, and M. Changyu, "Grinding performance evaluation of porous composite-bonded CBN wheels for Inconel 718," *Chinese J. Aeronaut.*, vol. 27, no. 4, pp. 1022–1029, 2014.

[254] M. . Jackson and B. Mills, "Materials selection applied to vitrified alumina & CBN grinding wheels," *J. Mater. Process. Technol.*, vol. 108, no. 1, pp. 114–124, 2000.

[255] Alicona, "Focus Variation: The Technical Principle," 2019. [Online]. Available: https://www.alicona.com/focus-variation/.

APPENDICES
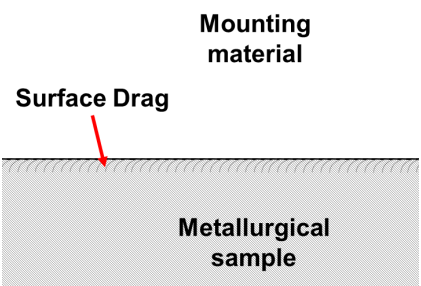
APPENDIX A (SECTION 2.2)

Equivalent chip thickness, h_{eq} :
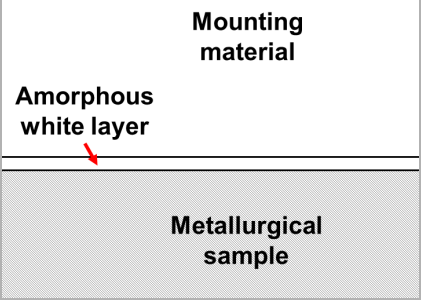
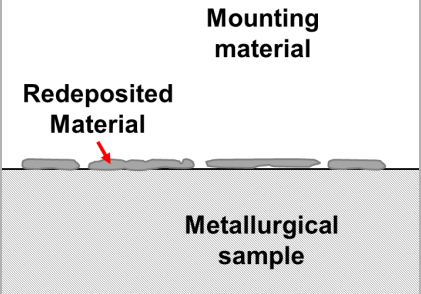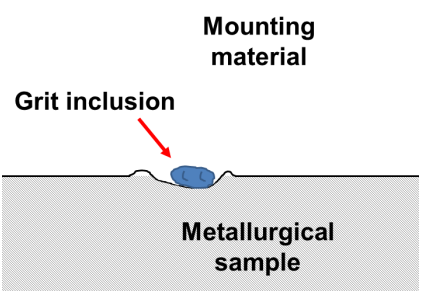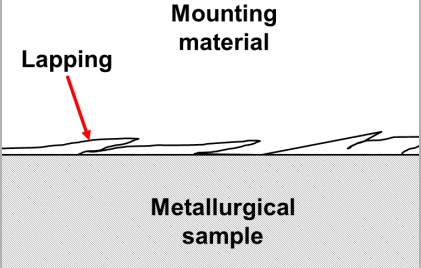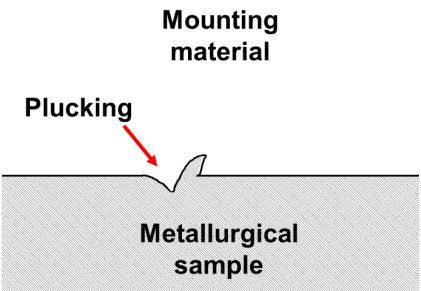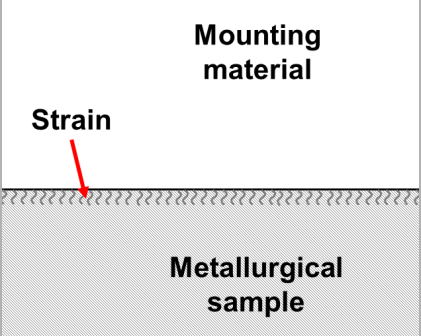$$h_{eq} = a_e . \frac{v_w}{v_c} \qquad \text{EQUATION A.1}$$

Whereby a_e is depth fo cut, v_w is feed rate and v_c is wheel speed.

APPENDIX B (SECTION 2.6)

Metallurgical analysis of cut ups shown in the thesis were compared against the Rolls-Royce Surface Condition Standards for Chip Forming Machining of Turbine Blades CME5043 Section 2 Issue 3[239]. This document details defines the acceptance levels of grinding defects in Ni-base superalloys and to determine whether a process is permissible for production. Interpreted diagrams of the relevant defects for this thesis and their definition from the CME5043 document are shown (Figure B.1), the tolerance bands and actual micrographs from are omitted for Intellectual Property.

TABLE B.1 – DIAGRAMS OF DEFECTS AND POTENTIAL CAUSES FROM GRINDING NI-BASE SUPERALLOYS AS ACCORDING CME5043 [239].

| Defect	Description and Definition
Mounting material **Amorphous white layer** **Metallurgical sample** **White Layer**	A region of material which is metallurgically different from the bulk parent material (may be seen as intermittent or discreet zones on the surface).
Mounting material **Surface Drag** **Metallurgical sample** **Surface Drag**	The surface layer may distorted and damaged in the direction of machining, as a consequence of cutting forces required to separate a chip of material from the component surface.

Diagram	Description
Redeposited material — Mounting material, Redeposited Material, Metallurgical sample	Swarf entrapment between the machined surface and the tool (grinding wheel) tip which may form a continuous layer over the machined surface. May be produced by release of loading of the grinding wheel or built up edge of the tool tip A distinct layer attached to the surface, of flowed material with evidence of heavily deformed structure.
Grit inclusion — Mounting material, Grit inclusion, Metallurgical sample	This appears as discreet particles randomly distributed on the surface. Material from a foreign object which has become joined to the parent material.
Lapping — Mounting material, Lapping, Metallurgical sample	Discrete region where plastic working of the material causes a fold in the surface.
Plucking — Mounting material, Plucking, Metallurgical sample	Small holes or pockets in the surface due to the mechanical removal of small particles of material (grains, particulate, phases) from the surface.
Strain (Work hardening) — Mounting material, Strain, Metallurgical sample	Evidence of strain bands in near surface grain structure, evidence of lattice strain either optically or by micro hardness changes. May be seen as undulation on the machined surface.

APPENDIX C (SECTION 3.1)

Three different replica materials were investigated to determine the optimum material to capture the topography of a vitreous bonded grinding wheel:

1. Struers Repliset T3 – Thixotropic, rapid curing silicon compound. Resolution of 0.1um and curing time of 10 minutes. Good for overhead/vertical surfaces.
2. Microset Forming Putty 121F – Two part synthetic rubber compound, each mixed together evenly and applied to surface. Resolution of 10um and curing time of 10 minutes.
3. Freeman Thermo-Stable sheet wax – Firm wax not typically used for replicant purposes. Melting point of 138°C and resolution unknown.

All three replicants were tested on a surface with a known form (roughness comparator). Each replica material was then applied to the comparator (Figure C.1) and measured individually under the Alicona. The measured roughness (Ra) and peak angle were then compared to identify the most appropriate material.
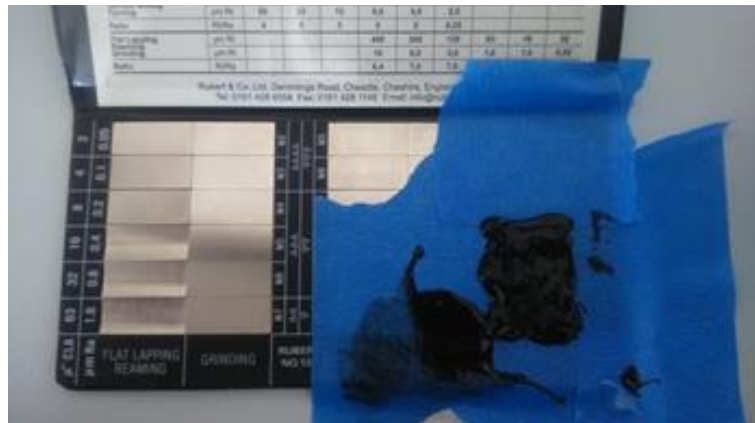
FIGURE C.1 – EXAMPLE OF THE APPLICATION OF THE STRUERS REPLISET ON THE ROUGHNESS COMPARATOR WITH A KNOWN ROUGHNESS.

Figure C.2 shows the error between the measured value on the replica materials and that measured directly on the roughness comparator. Repliset had the lowest error overall and so was selected as the most appropriate material to capture the topography of the abrasive wheels used in the thesis.
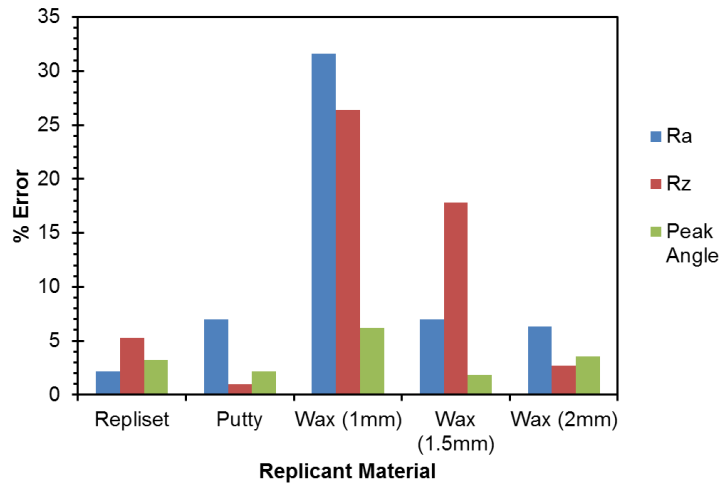
FIGURE C.2 – PERCENTAGE ERROR BETWEEN REPLICA MATERIAL AND ROUGHNESS COMPARATOR.

APPENDIX D (SECTION 3.2)

APPENDIX Di.

Figure D.1 shows examples of images captured of the dresser to monitor wear. Taken between the experiments discussed in the thesis, from the same location on the dresser, negligible wear was seen on the dresser therefore the impact of dresser wear on the data was assumed to be insignificant.
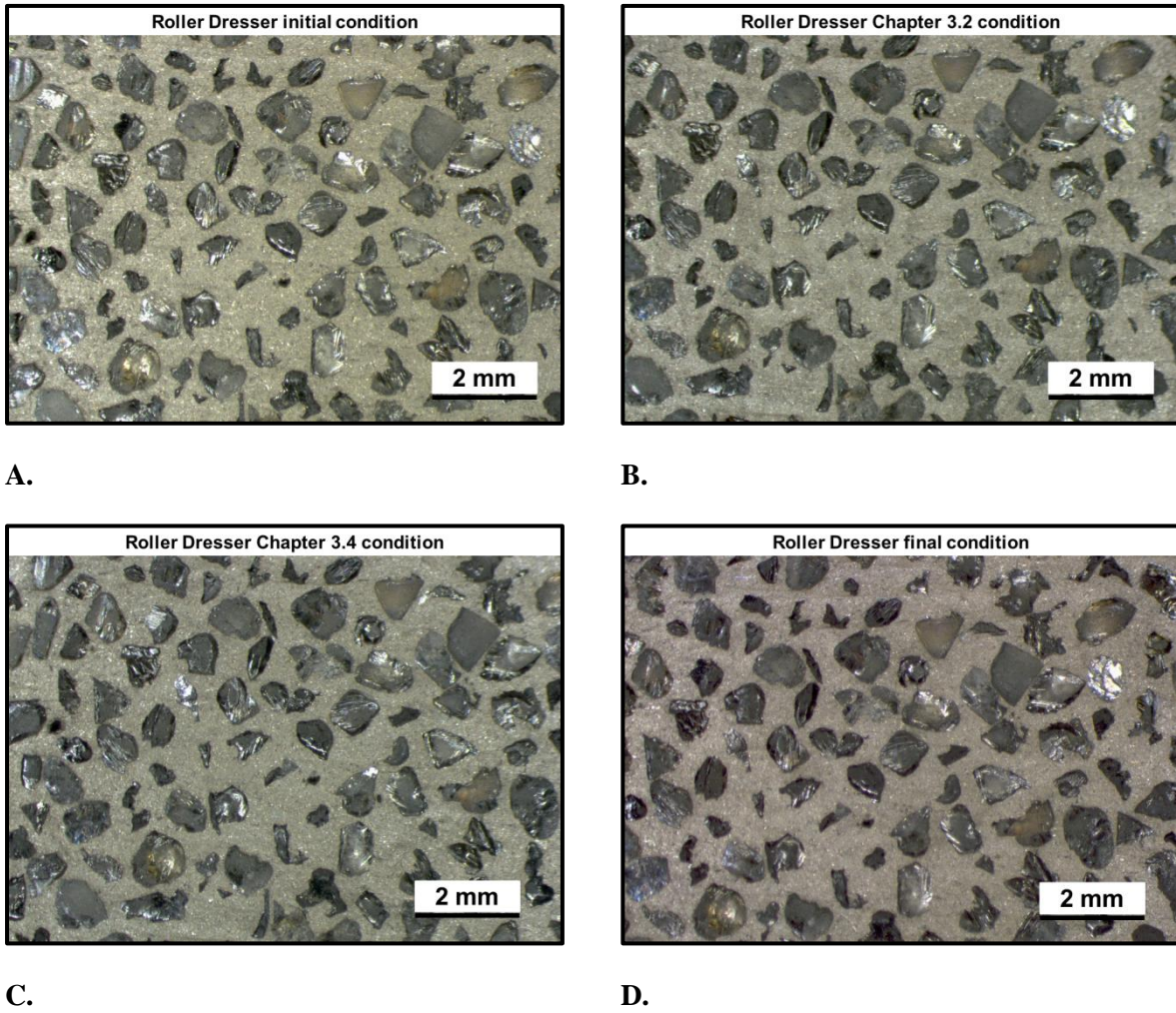
A.

B.

C.

D.

FIGURE D.1 – OPTICAL IMAGES OF THE ROLLER DRESSER USED IN THE EXPERIMENTS.

APPENDIX Dii

TABLE D.1 – GRAPHITE COUPON SPECIFICATION (GD4430).

Bulk Density	1.77
Hardness	54
Flexural Strength (kg cm^{-2})	400
Compressive strength (kg cm^{-2})	800
Tensile strength (kg cm^{-2})	250
Modulus of Elasticity (kg mm^{-2})	1000
Porosity (%)	17-18

APPENDIX Diii

TABLE D.2 – TECHNICAL SPECIFICATIONS FOR THE ALICONA INIFINITEFOCUSSL.

Working distance (mm)	17.5
Max. vertial resolution (nm)	100
Height step accuracy (%)	0.1
Min. measurable roughness (µm)	0.3
Min. measurable radius (µm)	5

The Alicona equipment uses focus-variation in order to gather measurements of the samples, a particularly useful method for samples with a large height range. A white light source is applied in the optical path of the lens and reflected off the sample. This scatter light is gathered by the lens and interpreted by the sensors in the system. Due to the height variation on the sample, only a small part of the image will be in sharp focus. Therefore the optic lens is moved vertically to capture the entire image in sharp focus. These moves are logged to determine the height at which different regions of the sample were in focus, which can thus be translated into a depth measurement of the sample. This enables the user to capture 3D texture scans of the sample as well as roughness data [255].

APPENDIX Div

Six images (x25) at different regions of the wheel were taken and a clear flattened grit determined. The image was turned to greyscale and a square region around the flat bounded as 1 pixel away from the most extreme points of the grit at a maximum intensity of 255 (Figure D.2).
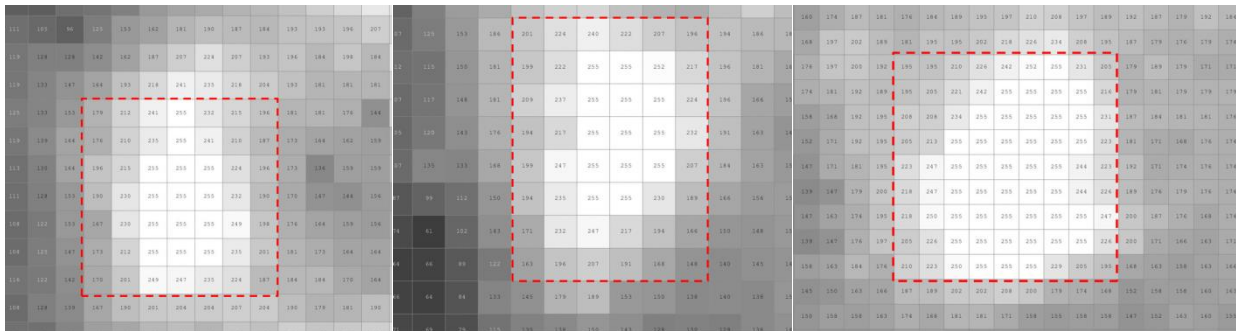
A.   **B.**   **C.**

FIGURE D.2 – EXAMPLES OF FLAT REGIONS IDENTIFIED ON ABRASIVE GRITS AND THE PIXEL RANGE USED TO CALCULATE THE THRESHOLD INSTENSITY.

The following average intensities for the identified flat regions on the six images (for each wheel) are shown along with the calculated average:

Conventional: $(223 + 228 + 228 + 221 + 239 + 224) / 6 = \mathbf{227.54}$

Hybrid: $(241 + 244 + 237 + 236 + 240 + 246) / 6 = \mathbf{241.15}$

Elongated: $(235 + 241 + 218 + 215 + 233 + 208) / 6 = \mathbf{225}$

APPENDIX E (SECTION 3.3)

Roughness measurement comparison between the Alicona InfiniteFocusSL optical system and the Mitutoyo SJ301 portable roughness probe.
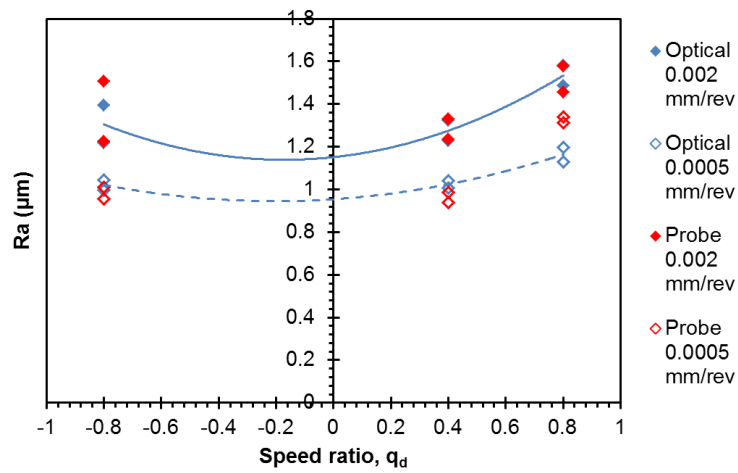

FIGURE E.1 – MEASUREMENT SYSTEM COMPARISON ON THE CD GROUND WORKPIECE BY THE CONVENTIONAL WHEELS.

Figure E.1 demonstrates that the measurement techniques give very similar results so the optical method can be considered an accurate method to capture surface data.

APPENDIX F (SECTION 3.4)

Technical specification of the Kistler Force Dynamometer used for force measurements (Figure F.1).
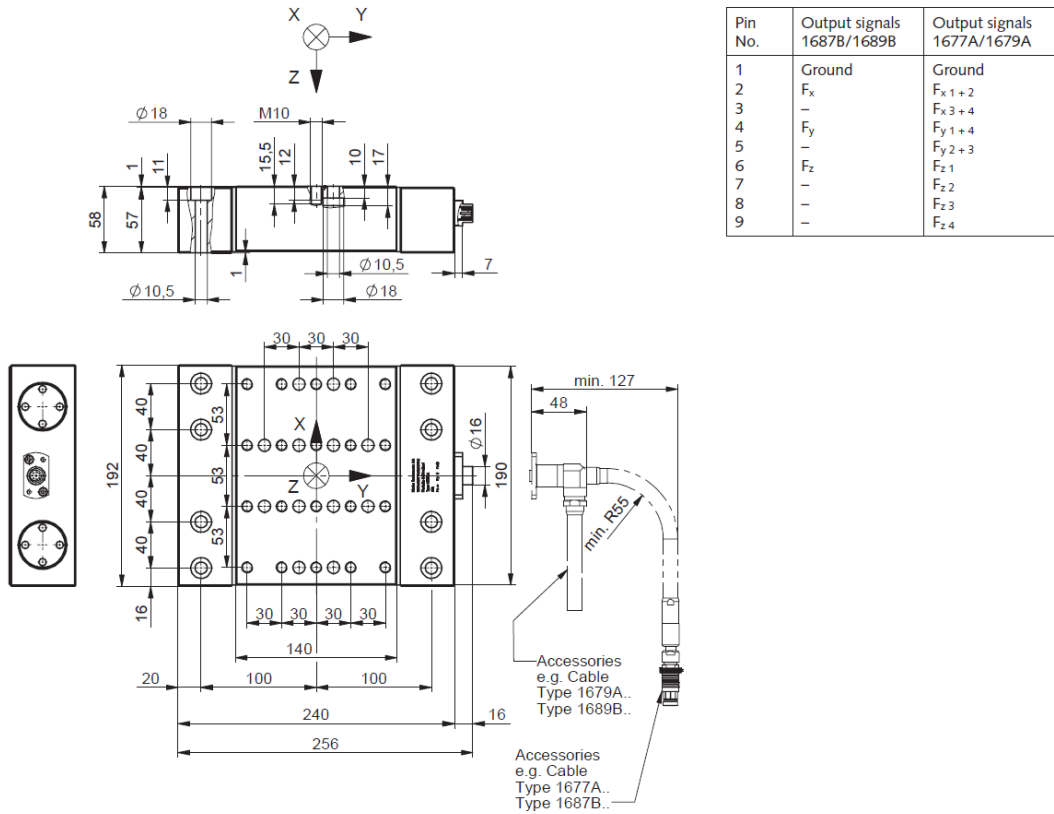

Pin No.	Output signals 1687B/1689B	Output signals 1677A/1679A
1	Ground	Ground
2	F_x	$F_{x\,1+2}$
3	–	$F_{x\,3+4}$
4	F_y	$F_{y\,1+4}$
5	–	$F_{y\,2+3}$
6	F_z	$F_{z\,1}$
7	–	$F_{z\,2}$
8	–	$F_{z\,3}$
9	–	$F_{z\,4}$

FIGURE F.1 – TECHNICAL DRAWING OF THE KISTLER FORCE DYNAMOMETER TYPE 9139AA.

APPENDIX G (SECTION 4.1)

Figure G.1 shows further evidence of macro cracking seen in conventional wheel grits when dressed at high interference angle (0.002 mm/rev, q_d 0.8). Figure G.2 shows further evidence of flat regions forming on the conventional wheels dressed under shallow interference angles (0.0005 mm/rev, q_d -0.8). Images were taken from the same respective wheel surfaces as those displayed in Section 4.1.3.
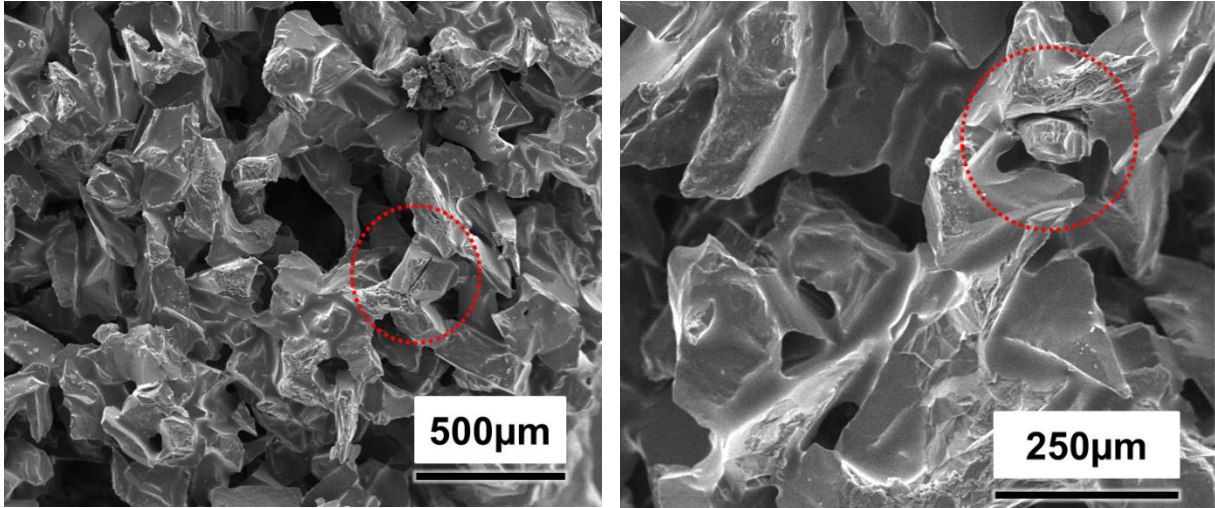
A.   **B.**

FIGURE G.1 – EVIDENCE OF MACROCRACKING OF ABRASIVE GRITS WHEN DRESSED AT 0.002 MM/REV, Q_D 0.8.
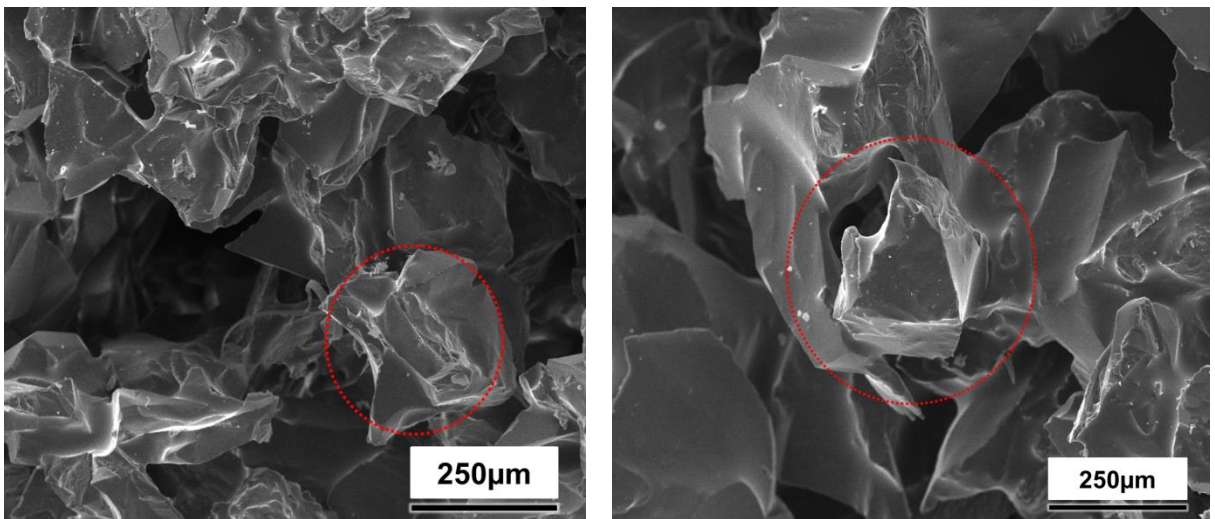
**A.**   **B.**

FIGURE G.2 – EVIDENCE OF FLAT REGIONS FORMING ON ABRASIVE GRITS WHEN DRESSING AT 0.0005 MM/REV, Q_D -0.8.

Figure G.3A shows further evidence of micro cracking on the triangular, engineered grits of the hybrid wheel when dressing at 0.002 mm/rev, q_d 0.8. Figure G.3B demonstrates the reduced micro cracking seen at the corners of the engineered grits when dressed at 0.0005 mm/rev, q_d -0.8.
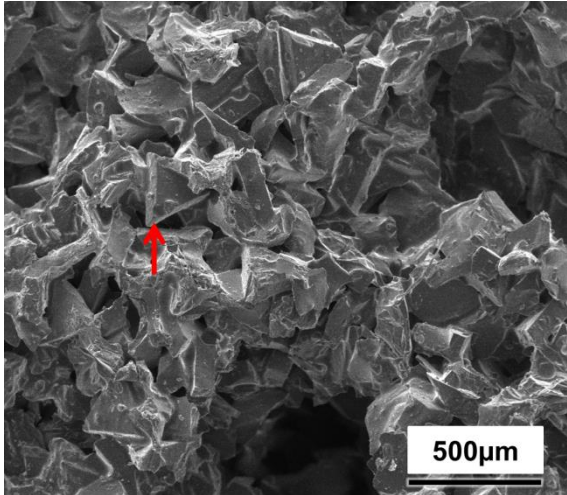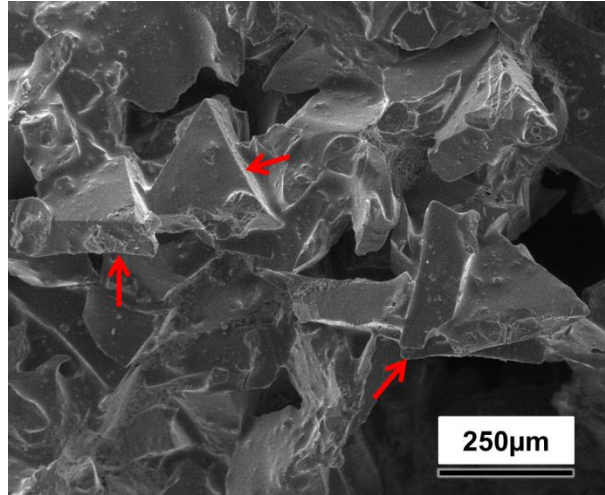
A.   **B.**

FIGURE G.3 – (A) EVIDENCE OF MICROCRACKING AT THE CORNERS OF THE TRIANGULAR GRITS IN HYBRID WHEELS DRESSED AT 0.002 MM/REV, Q_D 0.8 (B) REDUCED CRACKING SEEN WHEN DRESSED AT 0.0005 MM/REV, Q_D -0.8.

Figure G.4A demonstrates sharp cracking of the elongated grits of the elongated grit wheel when dressing at 0.002 mm/rev, q_d 0.8. Figure G.4B shows cleaved grits orientated perpendicular to the spindle axis when dressed at 0.0005 mm/rev, q_d -0.8.
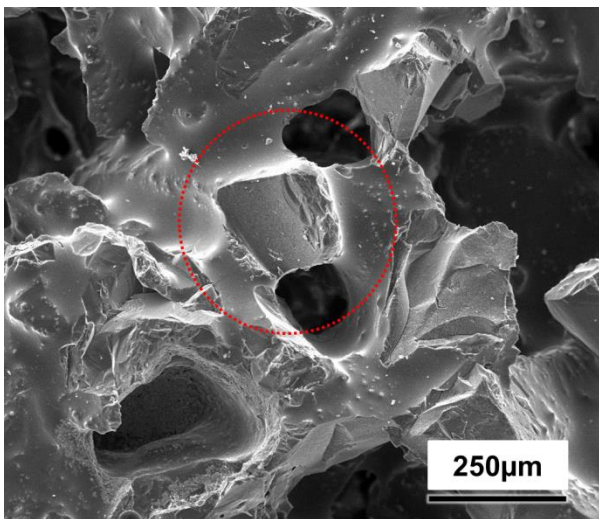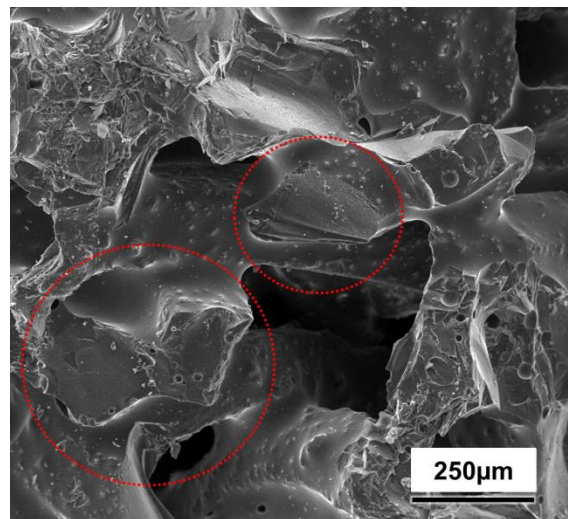
A.   **B.**

FIGURE G.4 – (A) A SHARP CUTTING POINT FORMED ON A FAVOURABLY ORIENTATED ELONGATED GRIT DRESSED AT 0.002 MM/REV, Q_D 0.8 (B) CLEAVED FLAT GRITS WHEN WHEEL DRESSED AT 0.0005 MM/REV, Q_D -0.8.

APPENDIX H (SECTION 4.4)

APPENDIX Hi.

The GLM regression equations for each dressing condition and wheel type are shown below whereby *Vw* is cut feed rate (mm/min), *Vc* is wheel surface speed (m/s), *ae* is depth of cut (mm), *N* is the grinding pass number and *Fz* the normal force.

Conventional wheels:

0.002 mm/rev qd 0.8:

$$Fz = 400 - 0.088Vw + 564.9ae - 19.27Vc + 10.2N + 0.000052Vw2 - 42.1ae2$$
$$+ 0.220Vc2 - 10.8N2 - 0.0049(Vw.N) + 179.9(ae.N) + 0.66(Vc.N)$$
$$+ 1.251(N3) - 0.000001(ae2.N)$$
$$- 0.00018(Vw.N2) - 82(ae2.N) - 14.45(ae.N2) - 0.051(Vc.N2)$$

0.002 mm/rev qd -0.8:

$$Fz = 408 - 0.088Vw + 564.9ae - 19.27Vc + 5.9N + 0.000052Vw2 - 42.1ae2$$
$$+ 0.220Vc2 - 10.7N2 + 0.0049(Vw.N) + 179.9(ae.N) + 0.66(Vc.N)$$
$$+ 1.251(N3) - 0.000001(ae2.N)$$
$$- 0.00018(Vw.N2) - 82(ae2.N) - 14.45(ae.N2) - 0.051(Vc.N2)$$

0.0005 mm/rev qd 0.8:

$$Fz = 404 - 0.088Vw + 564.9ae - 19.27Vc + 9.8N + 0.000052Vw2 - 42.1ae2$$
$$+ 0.220Vc2 - 11N2 + 0.0049(Vw.N) + 179.9(ae.N) + 0.66(Vc.N)$$
$$+ 1.251(N3) - 0.000001(ae2.N)$$
$$- 0.00018(Vw.N2) - 82(ae2.N) - 14.45(ae.N2) - 0.051(Vc.N2)$$

Hybrid wheels:

0.002 mm/rev qd 0.8:

$$Fz = 89 + 0.138Vw + 506.1ae - 9.21Vc - 4.7N - 0.000009Vw2 - 46.7ae2$$
$$+ 0.065Vc2 - 6.8N2 - 0.0348(Vw.N) + 106.7(ae.N) + 2.43(Vc.N)$$
$$+ 0.629(N3) - 0.000006(ae2.N)$$
$$+ 0.01018(Vw.N2) - 94.6(ae2.N) - 2.91(ae.N2) - 0.379(Vc.N2)$$

0.002 mm/rev qd -0.8:

$$Fz = 130 + 0.138Vw + 506.1ae - 9.21Vc - 36.6N - 0.000009Vw2 - 46.7ae2$$
$$+ 0.065Vc2 - 2.8N2 - 0.0348(Vw.N) + 106.7(ae.N) + 2.43(Vc.N)$$
$$+ 0.629(N3) - 0.000006(ae2.N)$$
$$+ 0.01018(Vw.N2) - 94.6(ae2.N) - 2.91(ae.N2) - 0.379(Vc.N2)$$

0.0005 mm/rev qd 0.8:

$$Fz = 57 + 0.138Vw + 506.1ae - 9.21Vc + 21.8N - 0.000009Vw2 - 46.7ae2$$
$$+ 0.065Vc2 - 12.6N2 - 0.0348(Vw.N) + 106.7(ae.N) + 2.43(Vc.N)$$
$$+ 0.629(N3) - 0.000006(ae2.N)$$
$$+ 0.01018(Vw.N2) - 94.6(ae2.N) - 2.91(ae.N2) - 0.379(Vc.N2)$$

Elongated grit wheels:

0.002 mm/rev qd 0.8:

$$Fz$$
$$= 1461 - 0.381Vw + 130ae - 58.6Vc - 372N + 0.000139Vw2 + 135.9ae2$$
$$+ 0.681Vc2 - 8.7N2 + 0.0557(Vw.N) + 287.7(ae.N) + 17.41(Vc.N)$$
$$+ 1.46(N3) - 0.000023(ae2.N)$$
$$+ 0.00371(Vw.N2) - 150.4(ae2.N) - 17.68(ae.N2) - 0.1937(Vc2.N) - 0.216(Vc.N2)$$

0.002 mm/rev qd -0.8:

$$Fz$$
$$= 1508 - 0.381Vw + 130ae - 58.6Vc - 376N + 0.000139Vw2 + 135.9ae2$$
$$+ 0.681Vc2 - 10N2 + 0.0557(Vw.N) + 287.7(ae.N) + 17.41(Vc.N)$$
$$+ 1.46(N3) - 0.000023(ae2.N)$$
$$+ 0.00371(Vw.N2) - 150.4(ae2.N) - 17.68(ae.N2) - 0.1937(Vc2.N) - 0.216(Vc.N2)$$

0.0005 mm/rev qd 0.8:

$$Fz$$
$$= 1508 - 0.381Vw + 130ae - 58.6Vc - 364N + 0.000139Vw2 + 135.9ae2$$
$$+ 0.681Vc2 - 14.3N2 + 0.0557(Vw.N) + 287.7(ae.N) + 17.41(Vc.N)$$
$$+ 1.46(N3) - 0.000023(ae2.N)$$
$$+ 0.00371(Vw.N2) - 150.4(ae2.N) - 17.68(ae.N2) - 0.1937(Vc2.N) - 0.216(Vc.N2)$$

The equations shown above were compared to the data collected in chapter 4.3 to further assess their prediction accuracy. The graphs are shown in Figure H.1 for the different dressing parameters. The solid markers indicate the predicted model data and the crosses show the actual measured data. These figures demonstrated that the models predicted the pattern of the grinding behaviour for each of the wheels, thus increasing the reliability of the predictions in Figure 5.14.
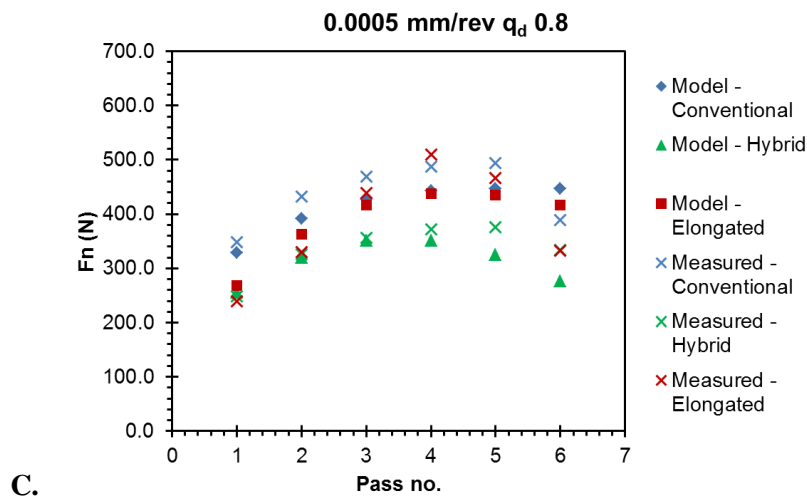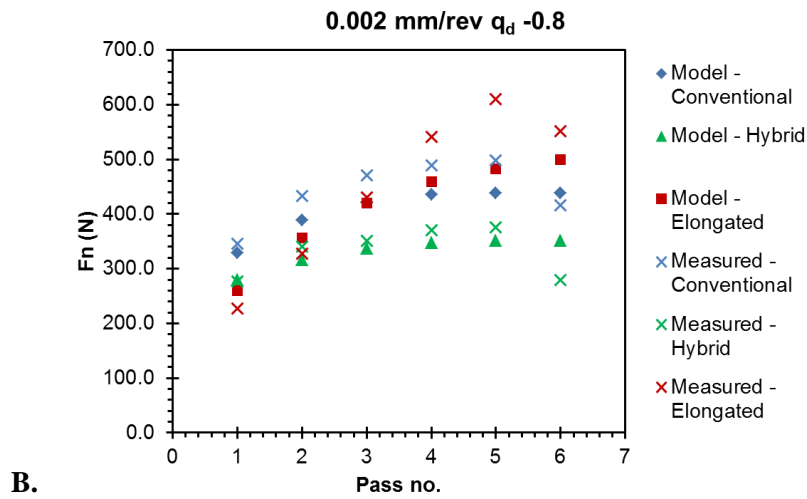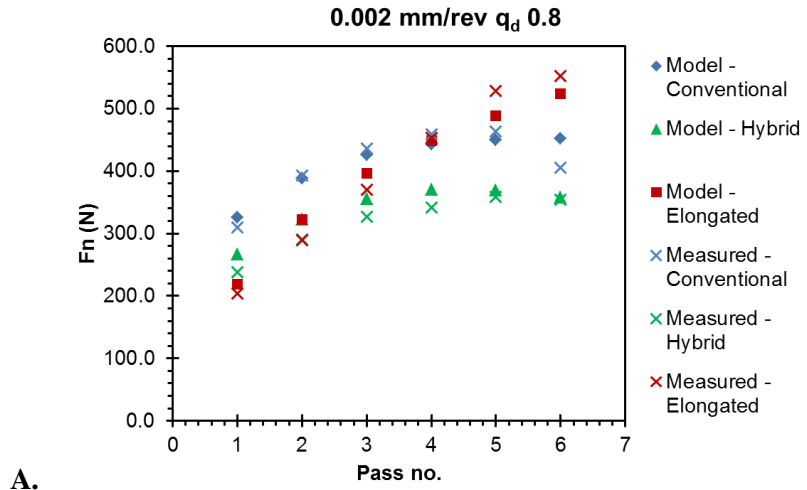
FIGURE H.1 – COMPARISON BETWEEN THE PREDICTED NORMAL FORCE FROM THE GLM MODELS AND THE DATA COLLECTED IN CHAPTER 4.3 (A) 0.002 MM/REV Q_D 0.8 DRESSING PARAMETERS (B) 0.002 MM/REV Q_D -0.8 AND (C) 0.0005 MM/REV Q_D 0.8.

APPENDIX Hii.

Figure H.2 shows the average specific energy plots for each dressing condition and the power equation for each curve. These equations were used to predict the average specific energy at Q' 3.0, 9.0 and 18.0 as shown in Figure 4.40. The colour of the equation corresponds to the same coloured curve on the graph (i.e. blue is the conventional wheel, green is the hybrid and red the elongated grit).
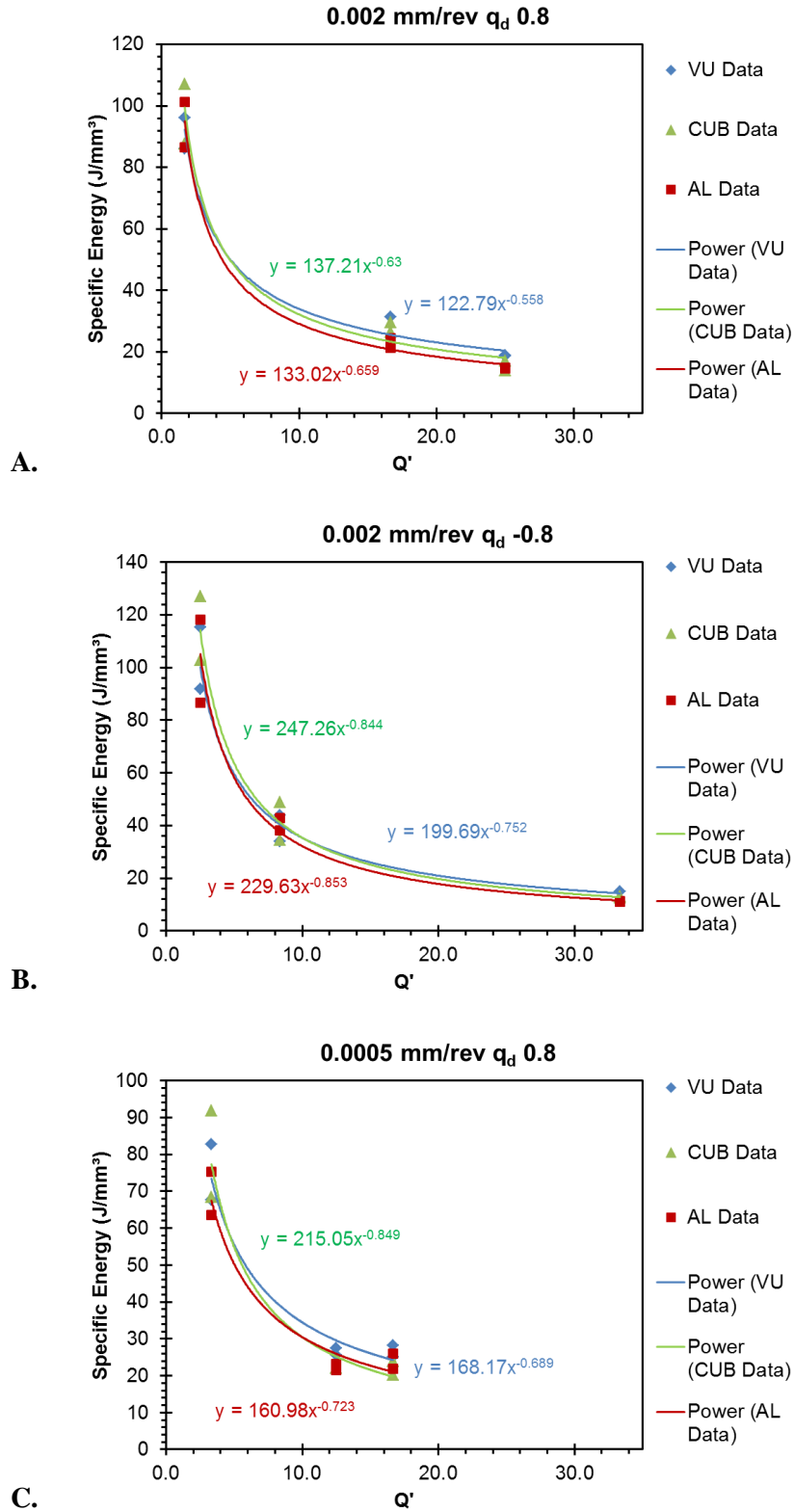
FIGURE H.2 – AVAERGAE SPECIFIC ENERGY CURVES FOR (A) 0.002 MM/REV Q$_D$ 0.8 (B) 0.002 MM/REV Q$_D$ -0.8 AND (C) 0.0005 MM/REV Q$_D$ 0.8.